University of Alberta

Engineering Optical Nanomaterials Using Glancing Angle Deposition

by

Matthew Martin Hawkeye

A thesis submitted to the Faculty of Graduate Studies and Research
in partial fulfillment of the requirements for the degree of

Doctor of Philosophy

in

Micro-Electro-Mechanical Systems (MEMS) and Nanosystems

Electrical and Computer Engineering

Spring 2011
Edmonton, Alberta

Dedicated to Georgina and our family.

Abstract

Advanced optical technologies profoundly impact countless aspects of modern life. At the heart of these technologies is the manipulation of light using optical materials. Currently, optical technologies are created using naturally occurring materials. However, a new and exciting approach is to use nanomaterials for technology development. Nanomaterials are artificially constructed material systems with precisely engineered nanostructures. Many technological revolutions await the development of new nanoscale fabrication methods that must provide the ability to control, enhance, and engineer the optical properties of these artificial constructs.

This thesis responds to the challenges of nanofabrication by examining glancing angle deposition (GLAD) and improving its optical-nanomaterial fabrication capabilities. GLAD is a bottom-up nanotechnology fabrication method, recognized for its flexibility and precision. The GLAD technique provides the ability to controllably fabricate high-surface-area porous materials, to create structurally induced optical-anisotropy in isotropic materials, and to tailor the refractive index of a single material. These three advantages allow GLAD to assemble optical nanomaterials into a range of complex one-dimensional photonic crystals (PCs).

This thesis improves upon previous GLAD optical results in a number of important areas. Multiple optical measurement and modeling techniques

were developed for GLAD-fabricated TiO_2 nanomaterials. The successful characterization of these nanomaterials was extended to engineer PC structures with great precision and a superior degree of control. The high surface area of basic PC structures was exploited to fabricate an optimized colourimetric sensor with excellent performance. This colourimetric sensor required no power source and no read-out system other than the human eye, making it a highly attractive sensing approach. Incorporating engineered defects into GLAD-fabricated PCs established a new level of design sophistication. Several PC defect structures were examined in detail, including spacing layers and index profile phase-shifts. Remarkable control over defect properties was achieved and intriguing polarization-sensitive optical effects were investigated in anisotropic defect layers. The success of these results demonstrates the precision and flexibilty of the GLAD technique in fabricating optical nanomaterials and advanced photonic devices.

Table of Contents

List of Tables

List of Figures

List of Symbols and Abbreviations

Symbols

$\langle \ldots \rangle$	Average
α	Deposition angle
α_H, α_L	High- and low-index sublayer α values
α_{max}, α_{min}	Maximum and minimum rugate α values
β	Column tilt angle
γ	Damping coefficient; liquid surface tension
ΔC	Percieved colour difference magnitude
$\Delta\vartheta$	Relative phase delay
$\Delta\lambda$, $\Delta\omega$, $\Delta\mathcal{E}$	Bandwidth
Δn	Relative index inhomogeneity; Birefringence
$\Delta\phi$	Index profile phase shift
$\Delta\omega$	Normal mode splitting
ε	Dielectric constant
ε_0	Vacuum permittivity
ε_{eff}	Effective medium dielectric constant
ε_i	Incident medium dielectric constant
ε_s	Substrate medium dielectric constant
θ	Propagation angle
θ_0	Angle of incidence
θ_e	Waveplate misalignment angle
θ_m	Optomechanical mount offset
θ_p	Polarizer transmission axis rotation angle
θ_s	Substrate propagation angle
θ_w	Waveplate fast-axis rotation angle
ϑ_x, ϑ_y	Instantaneous field phase factors

$\vartheta(\omega)$	Resonator phase response function
κ	Coupling coefficient
λ	Wavelength
λ_0	Wavelength *in vacuo*; Design wavelength;
λ_b	Short wavelength band edge
λ_B	Bragg resonance wavelength
λ_g	Band gap centre wavelength
λ_p	Peak transmittance wavelength
λ_r	Long wavelength band edge
Λ	Optical path length
μ	Permeability; Distribution mean
μ_0	Vacuum permeability
μ_i	Incident medium permeability
μ_s	Substrate medium permeability
π	Pi (3.14159...)
σ	Standard deviation
τ	Time constant
φ	Substrate polar rotation angle
ϕ	Optical phase; Rugate phase term
Φ	Waveplate phase retardance
χ_e	Electric susceptibility
χ_m	Magnetic susceptibility
ω	Frequency
ω_0, λ_0, $\mathcal{E}_0$	Resonance frequency / wavelength / energy
$\omega_\pm$	Coupled oscillator normal mode frequencies
a_v	Knudsen's evaporation coefficient
A	Zero-order Cauchy dispersion parameter
A_e	Evaporant surface area
A_i, A_r, A_t	Incident, reflected, transmitted wave amplitudes
b	y intercept
B	Second-order Cauchy dispersion parameter
$\mathbf{B}$	Magnetic induction vector
c	Speed of light *in vacuo*
d	Thin film layer thickness

d'	QCM measured thickness
d_H, d_L	High- and low-index sublayer thicknesses
D	Dimensionality; Deposition ratio
D_p	Degree of polarization
$\mathbf{D}$	Electric displacement vector
E_x, E_y	Instantaneous field amplitudes
$\mathcal{E}$	Energy
$\mathbf{E}$	Electric field vector
f	Relative volume fraction
$G(x)$	Gaussian distribution
G_0	Gaussian distribution normalizing constant
h	Planck's constant
$\mathbf{H}$	Magnetic field vector
i	Imaginary unit
I	Oscillator amplitude
$I(\lambda)$	Spectral radiance
k	Extinction coefficient; CIE normalizing constant
k_0	Freespace wave number
L	Total film thickness
$L(\omega)$	Resonator amplitude response (Lorentzian) function
(L^*,a^*,b^*)	CIELAB colour space co-ordinates
m	Molecular weight; Diffraction order; Slope
$\mathbf{M}$	Characteristic matrix; Mueller matrix; Magnetization field
M_{ij}	Element ij of the characteristic matrix
n	Index of refraction
n_a	Average index
n_e	Extraordinary index
n_f	Film index at air interface
n_i	Film index at substrate interface
n_H, n_L	High- and low-index sublayer indices
n_{mid}	Film index at mid-thickness
n_o	Ordinary index
n_p	Peak-to-peak index variation
N	Number of multilayer periods; Number of sublayers
N_e	Molecular evaporation rate

p	Ambient pressure; partial pressure
p_v	Equilibrium vapour pressure
P	Physical period
$\mathbf{P}$	Polarization field vector
Q	Resonator quality factor
r	Fresnel reflection coefficient; Column / nucleus radius
r_m	Mean radius of surface curvature
$\mathbf{r}$	Spatial displacement vector
R	Reflectance; Universal gas constant
$\mathbf{R}$	Lattice vector
s	Ballistic shadow length
$\mathbf{S}$	Stokes vector
S_0, S_1, S_2, S_3	Stokes parameters
$S(\lambda)$	Spectral radiance of reference colour source
$S_{65}(\lambda)$	CIE D65 standard illuminant spectral radiance
t	Time; Fresnel transmission coefficient
T	Transmittance; temperature
T_f	Steady-state transmittance
T_i	Initial transmittance
T_m	Melting point temperature
T_{min}	Band gap minimum transmittance
T_{sub}	Substrate temperature
T_s, T_p	*s*- and *p*-polarized light transmittance
T_x, T_y	*x*- and *y*-polarized light transmittance
u_k	Bloch wave envelope function
U, V, W	Electric and magnetic field amplitude functions
U_0, V_0	Field boundary conditions
V	Liquid molar volume
w_p	Pore width
x, y, z	Global lab frame co-ordinates
x', y', z'	Locally-defined co-ordinates
$(\overline{x},\overline{y},\overline{z})$	CIE standard observer colour matching functions
(X,Y,Z)	CIExyz colour space tristimulus values
(X_w,Y_w,Z_w)	White point tristimulus values

Abbreviations

1D, 2D, 3D	One, two, three-dimensions
CCD	Coupled-charge device
CIE	Commission Internationale de l'Eclairage
DFB	Distributed feedback
DNA	Deoxyribonucleic acid
FWHM	Full-width half-maximum
GLAD	Glancing angle deposition
GRIN	Gradient index
IUPAC	International Union of Pure and Applied Chemistry
LM	Levenburg-Marquardt
M	Magnification
MSE	Mean-squared-error
NIR	Near infrared
p-	Parallel
PC	Photonic crystal
ppm	Parts per million
PTFE	Polytetrafluoroethylene
PVD	Physical vapour deposition
QCM	Quartz crystal microbalance
RH	Relative humidity
s-	*Senkrecht* (German: perpendicular)
sccm	Standard cubic centimeters per minute
SEM	Scanning electron microscope
SZM	Structure zone model
TE	Transverse electric
TM	Transverse magnetic
UV	Ultraviolet
vis	Visible

Chapter 1

Engineered Optical Nanomaterials

1.1 Introduction: Optics and nanoscience

Optics, the study of light and its interaction with matter [1, 2], is a field of fundamental scientific importance and immense technological value. Scientifically, optics has played a significant role in developing our understanding of the natural world. Many early successes of quantum theory involved the interpretation of optical phenomena, such as blackbody radiation, the photoelectric effect, Compton scattering, and Young's double-slit experiment. Contributions from optical research continue to be at the forefront of science, being central to the development of optical trapping and cooling of atoms (Nobel prize in physics, 1997) and laser-based precision spectroscopy (Nobel prize in physics, 2005). Technologically, many industries are completely reliant on optical devices. Consider the widespread use of imaging systems (binoculars, telescopes, microscopes, cameras), flat-panel displays, fibre-optics, lasers, and solid-state lighting. Each of these technologies has fundamentally changed communications, medicine, research, defense, and entertainment.

Just as the field of optics has impacted progress in other disciplines, so too has the development of nanoscale science. A basic, working definition of the nanoscale is between one and one hundred nanometers. More precisely, the nanoscale is defined as the critical dimension where new behaviours emerge due to the relationship between structure and physical properties. At this critical dimension, surface effects compete with volume effects for dominance, quantum mechanical phenomena appear, and the atomistic na-

ture of materials is at the forefront. This greatly impacts the material's thermal, mechanical, chemical, electrical, optical, etc. properties. Nanoscale research has proliferated rapidly due to several factors. Conventional fabrication technologies (e.g., optical lithography) have steadily improved and new methods (e.g., self-assembly) have been discovered. Similarly, the precision of existing characterization methods (e.g., electron beam microscopy) has increased and novel characterization tools (e.g., the scanning probe microscope) have been created. Economic factors also provide significant motivation. The benefits accompanying nanotechnologies include improved efficiency, performance, miniaturization, and integration. Furthermore, breakthrough scientific discoveries may lead to revolutionary new technologies. The forecasted economic and social benefits of nanotechnology innovations provide significant motivation for academic and industrial research.

1.2 Optical nanomaterials

The potential impact of nanoscience on optical research is enormous and the two fields have overlapped greatly. This convergence has led to the development of optical nanomaterials: materials with artificial, nanoscale structure whose properties originate from both the constituent materials and their structure. In a conventional material, the optical properties are determined by the microscopic, atomic-level electromagnetic response. By contrast, the optical properties of nanomaterials are primarily determined by structure-related phenomena, including interference, diffraction, scattering, and resonance. Manipulating the structure to control these phenomena permits tuning and engineering of material optical properties. An ordinary material can thereby be endowed with artifical properties.

The optical nanomaterial field is already broad in scope. Two prominent areas of study are metamaterials [3] and photonic crystals (PCs) [4]. In a metamaterial, the structural inhomogeneity is sub-wavelength in scale; the metamaterial electromagnetic response is therefore treated through an appropriate macroscopic homogeneziation. In a PC, the inhomogeneity is larger (wavelength scale) and periodic. The periodicity leads to constructive and destructive wave interactions, formally analagous to X-ray scattering in crystals and electron propagation in atomic lattices.

The novel properties of nanomaterials allow unprecedented control over light propagation in the material. The careful design and engineering of nanomaterial architecture is creating advanced, and even exotic, new devices for the optics field. For example, PC engineering is developing towards optical computing and information processing [5–8] and metamaterials are begin investigated for sub-diffraction limit imaging [9, 10] and invisibilty devices [10,11]. The theoretical impetus for this research is well-established; realizing these materials remains a technological challenge.

One additional remark is worth considering. Although the adjective "artificial" and the prefix "meta-" are commonly used to describe optical nanomaterials, there are several natural occurrences of these structured media. Opal mineraloids exhibit PC behaviour because they are composed of close-packed, wavelength-scale mineral spheres [12]. Diverse optical nanomaterials are also found in the animal kingdom [13]: the iridescent colouration of many birds and insects is caused by diffraction and PC effects; the eyes of various moth species are covered by reflection-reducing nanostructures; the arms of the brittlestar, a starfish-like marine animal, are covered by microlens-arrays. The biological nanofabrication methods are the product of millions of years of evolution and natural selection pressures. They may someday serve as inspiration for artificial biomimetic processes.

1.3 Nanofabrication

Several outstanding problems exist in optical nanomaterial research. Notable among these is the development of nanofabrication techniques satisfying a myriad range of requirements, such as flexiblity, precision and accuracy, reliablity, robustness, and economic viability.

A multitude of nanofabrication techniques appear in the literature, including refined versions of standard processes, specialized adaptations of other techniques, and entirely novel inventions. These methods are categorized as either top-down and bottom-up. In the top-down approach, nanoscale structures are realized via direct assembly using larger devices. Top-down methods are attractive as they benefit from the great success of traditional microelectronics processing. However, precise sub-100 nm structures are difficult to realize in a cost-effective manner with top-down tech-

niques. Modern optical lithography requires an enormous capital investment. While serial processes such as two-photon and electron-beam lithography are useful for research, they lack the throughput required for low-cost manufacturing. However, promising new top-down techniques [14], such as embossing, contact printing, and molding have the potential to overcome the economic barrier in the future, although they required further development.

In the bottom-up approach, intrinsic long-range (on the nanoscale) interactions are harnessed, causing smaller units to self-organize into desired nanoscale structures [15, 16]. A variety of bottom-up methods exist: prominent techniques include chemical precipitation [17], vapour-liquid-solid growth [18], catalyzed chemical vapour deposition [19], and DNA self-assembly [20]. Bottom-up manufacturing is comparatively inexpensive, but is at an earlier stage of development than top-down approaches.

1.4 Glancing angle deposition

Glancing angle deposition (GLAD), a bottom-up nanofabrication method, has many advantageous qualities. GLAD is based on physical vapour deposition (PVD), a well-studied, scalable, and reliable thin film deposition technique. GLAD is an enormously flexible and adaptable method, compatible with a wide range of materials [21]. A short list of demonstrated materials includes metals (Ag, Al, Au, Co, Cu, Fe, Ni, Pt, Ti), dielectrics (Al_2O_3, CaF_2, MgF_2, Nb_2O_5, TiO_2), semiconductors (Si, Ge), and organics (Alq_3, C_{60}, pentacene). In addition to material flexibility, GLAD can fabricate a wide range of nanoscale geometries. These different geometries can also be combined into intricate architectures. Furthermore, GLAD can achieve the stringent precision required for nanofabrication. These advantages have led to the application of GLAD across a broad spectrum of fields [22], including photovoltaics, fuel cell electrodes, supercapacitors, environmental sensing, catalysis, mechanical resonators, pressure sensors, magnetic recording media, and optical nanomaterials.

1.5 Thesis objectives

The primary objective of this thesis research is engineering basic GLAD-fabricated optical nanomaterials into advanced PC devices. Achieving this objective will not only increase the optical capabilities of the GLAD process, but will hopefully contribute towards economical fabrication of optical nanomaterial devices and widespread applications of these new technologies.

Optical coatings (such as PCs, antireflection layers, colour filters etc.) are used in virtually every optical system. Therefore the challenge is not in finding applications, but rather competing with existing processes currently used by the very mature optical coating industry. Consequently, it is important to select applications which leverage the properties of GLAD-fabricated films. Three such properties are: (1) the ability to control the magnitude and orientation of optical anisotropy through structure; (2) the ability to fabricate optical films with a controllable porosity and high surface area; and (3) the ability to control the refractive index of a single material. These three characteristics are not readily reproducible in traditional thin film manufacturing and represent a unique opportunity for GLAD-fabricated coatings. Significant research efforts have examined the optical anisotropy and many optical devices have been demonstrated. The birefringence properties have been developed into optical waveplates [23]. The circular polarization effects exhibited by helically-structured GLAD nanomaterials are another well-examined subject [24–26]. The second advantage described above has been studied for applications benefiting from enhanced surface areas, such as gas sensing [27, 28], but has seen minimal use for optical devices.

The third advantage is only recently being exploited thanks to improvements in GLAD structural control. Research focused on the third advantage is best described as nascent. Basic refractive index control has been studied and simple optical multilayer devices, such as simple PCs [29] and antireflection coatings [30], have been demonstrated. What is required is further exploration and extension of the capabilities of this GLAD technique. Therefore, this thesis research seeks to achieve the next generation of GLAD-fabricated optical devices. This necessitates a thorough examination of GLAD-enabled refractive index control. These results can then be extended and developed to allow the design and realization of new, ad-

vanced GLAD-fabricated PC devices. Furthermore, by engineering devices that combine all the previously mentioned GLAD advantages, truly novel technologies for the optics field can be demonstrated.

1.6 Thesis structure

Following this introductory chapter, important background material is summarized in CHAPTER 2. The principles of thin film deposition and GLAD fabrication are examined in detail. This discussion covers key topics such as nucleation, column formation, and ballistic shadowing, as well as methods for controlling nanostructure growth. Theory describing the optical properties of nanomaterials is discussed and numerical simulation techniques for thin film optical calculations are derived. The chapter is concluded by a summary of PC optical properties and fabrication techniques.

CHAPTER 3 discusses the experimental techniques used in the thesis. These include the GLAD system and fabrication conditions, the sample characterization tools employed, and the data analysis methods.

The subsequent four chapters constitute the body of original thesis research. CHAPTER 4 examines how the optical properties of nanostructured TiO_2 can be controlled with the GLAD technique. The homogenized properties of the structured optical nanomaterial depend on the amount of TiO_2 in the medium. By manipulating the shadowing effects during film growth the refractive index can be continuously tuned over a wide range. The refractive index measurement is accomplished using homogeneous and gradient-index thin film models, the latter model being shown to provide a superior approximation of the actual nanomaterial.

CHAPTER 5 extends the results of the previous chapter into the fabrication of PC structures. The nanomaterial structure is engineered through *in situ* substrate motion, creating density and index changes in the deposited structure. This work improves upon previously reported results, demonstrating a greater degree of structural precision and PC device control.

As mentioned in the previous section, the increased porosity and surface area of GLAD-fabricated nanomaterials leads to excellent sensor performance. To capitalize on this GLAD advantage, CHAPTER 6 presents the design, fabrication, and characterization of a colourimetric PC humidity

sensor. Water vapour condenses within the porous PC, causing the PC to change colour. This colourimetric sensing approach offers several advantages, and this is the first time it has been adapted to GLAD-fabricated sensors. The quantified colour shift is optimized by appropriate design of PC spectral features.

A prominent topic in PC research is the incorporation of defects in the periodic structure. This is a promising approach to realizing new PC properties and creating advanced PC devices. As such, CHAPTER 7 examines a variety of defect structures inserted into GLAD-fabricated PCs. Defect incorporation in GLAD-fabricated PCs is previously unexamined field and this chapter successfully realizes several complex PC designs. This includes the insertion of optically-anisotropic defect layers, leading to complicated polarization-sensitive resonance phenomena.

The thesis is concluded by CHAPTER 8, wherein the research work is summarized and future experimental directions are suggested. APPENDICES A and B present data from previous chapters omitted for space reasons. Calibration data is also archived in tables as reference for future researchers interested in reproducing and continuing the work presented in this thesis.

Chapter 2

Glancing Angle Deposition and Nanostructured Optics

This chapter presents background material necessary to analyze and interpret the thesis research. A general review of PVD is provided, focusing on aspects central to GLAD, such as nucleation and column formation. The dynamics of GLAD growth are examined in detail, covering topics such as ballistic shadowing, nanocolumn growth and control, film porosity, and competitive growth. These concepts are key to understanding the structure of GLAD-fabricated nanomaterials.

The electromagnetic response, and hence the optical properties, of these nanomaterials can be understood via effective medium theory. Consequently, the principles of these homogenization methods are discussed. As the thesis goal is to develop GLAD-fabricated nanomaterials into advanced PC devices, the general properties of PC materials are summarized and appropriate optical simulation methods are derived. These considerations play a pivotal role in predicting, designing, and optimizing the PC devices.

2.1 Thin film growth

2.1.1 Physical vapour deposition

As a term, PVD is used to describe several related thin film deposition methods. The word *physical* is key as PVD film preparation is based on physical state changes such as evaporation, sublimation and condensation. This differentiates PVD techniques from other deposition methods where films

are deposited through chemical changes, such as chemical vapour deposition and electroplating. Note that PVD approaches can involve chemical reactions, which are often used to correct or alter film stoichiometry [31]. However, these reactive methods rely on vapour condensation for film production and are still classified as PVD.

PVD processes can be divided into three steps [32]. First, a vapour is generated from a (solid) source material. Second, the vapour is transported from the source to the substrate. Third, the vapour condenses into a solid film on the substrate. PVD methods are chiefly distinguished by how the vapour phase is prepared. Resistively heating and vapourizing the source is termed thermal evaporation. Heating the material with a focused electron beam is called electron-beam or e-beam evaporation. Another PVD approach is sputtering, where the source material is bombarded with energetic ions. The ion momentum is transfered to the source atoms, some of which are ejected via a collision cascade process and escape the surface as vapour. Another approach, pulsed laser deposition, uses a focused, high-intensity laser beam to vapourize the source material.

The only PVD method used in this research is e-beam evaporation. The evaporation process (the first step above) can be understood using thermodynamics and the kinetic theory of gases [33]. The evaporation rate (number of evaporated atoms N_e per unit time) from a liquid surface is equal to the rate of atoms leaving the liquid (determined by the equilibrium vapour pressure p_v) minus the rate of atoms impinging on the liquid surface (determined by the ambient pressure p). This leads to the Hertz-Knudsen equation

$$\frac{dN_e}{dt} = A_e a_v \left(2\pi m k_B T\right)^{-\frac{1}{2}} \left(p_v - p\right), \tag{2.1}$$

where A_e is the surface area, a_v is Knudsen's evaporation coefficient, m is the molecular weight, k_B is Boltzmann's constant, and T is the temperature. When p_v is greater than the surrounding pressure p, vapour atoms escape the source.

PVD is performed in high-vacuum environments. At high vacuum, the gas atom mean-free-path is longer than the characteristic dimension of the evaporation chamber. In this molecular or Knudsen flow regime, the evaporated atoms travel in ballistic straight-line paths from source to substrate.

This ballistic vapour transport constitutes the second step of PVD.

2.1.2 Condensation and nucleation

The final PVD step, the vapour-to-solid phase transition at the substrate, proceeds via a nucleation process on the surface [34, 35]. The vapour provides a constant flux of incident atoms to the surface which, once adsorbed onto the substrate, diffuse randomly across the substrate surface. The adsorbed atoms, or adatoms, diffuse until one of three events occur: the adatom may desorb from the surface and escape, it may encounter another adatom and form a nucleus, or it may join a previously formed nucleus. Nucleus stability is determined by the energetics of the system and the size of the nucleus. Below a certain size, it is energetically favorable for adatoms to detach from the nucleus. Once a certain critical size is reached, the energetics change and the rate of adatom detachment is strongly reduced. These critical nuclei quickly grow and become the dominant centres of film growth.

Nucleation occurs following one of three archetypal growth modes depending on the substrate-adatom affinity [36–39]. When the binding between adatoms is stronger than the binding between adatom and substrate, the nuclei form 3D clusters. This is called Volmer-Weber or island growth. If the adatoms are more strongly bound to the substrate than to each other, the nuclei are spread into 2D layers. This is termed Frank-van der Merwe or layer growth. The third growth mode is intermediate between the other two, and proceeds initally by layer growth and then by subsequent islanding. This is called Stranski-Krastanov or layer-plus-island growth.

2.1.3 Column formation: Structure zone models

As deposition progresses beyond the initial stages of nucleation, growth continues as vapour atoms deposit on the film surface. As the nuclei develop, they adopt a columnar structure. Because of the importance of surface diffusion, the substrate temperature T_s plays a significant role in column formation. Experiments by Movchan and Demchishin provided crucial insight into the effect of T_s, when they introduced a film growth concept called a structure zone model (SZM) shown in Fig. 2.1 [40]. As T_s is increased,

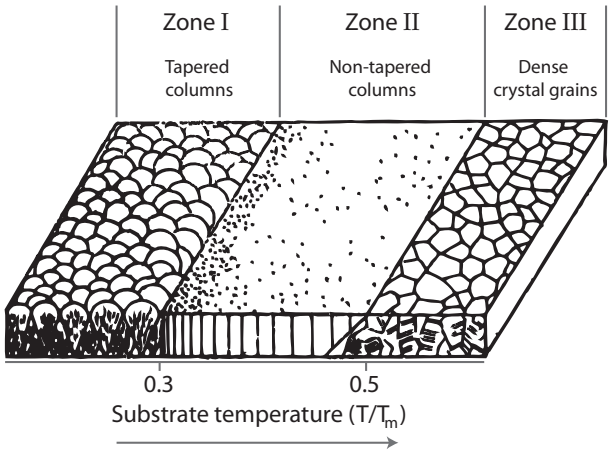

Figure 2.1: The structure zone model proposed by Movchan and Demchishin. Three structural zones are observed: tapered columns, non-tapered columns, and densely-packed crystal grains. The transitions between the zones occur at approximately $T = 0.3T_m$ and $0.5T_m$, where T_m is the material melting's temperature. Adapted from Ref. 40.

three distinct structural regimes were observed, with transitions occuring at temperatures T_1 and T_2. Movchan and Demchishin found that, remarkably independent of material, the transition temperatures occured at $T_1 / T_m \approx 0.3$ and $T_2 / T_m \approx 0.5$, where T_m is the material melting point. In the first zone ($T_s \leq T_1$), the temperature is too low for significant adatom diffusion to occur. The film microstructure consists of tapered columns separated by voids. As T_s is further increased, entering the second zone ($T_1 \leq T_s \leq T_2$), surface diffusion increases the column diameter and reduces the column tapering. In the third zone ($T_2 \leq T_s$), there is sufficient energy for bulk diffusion to occur, leading to crystallization of the deposited material. The columnar features are replaced by densely packed grains. While other researchers have built upon and refined Movchan and Demchishin's SZM, adding more zones [41,42] and other processing variables [43], the basic three-zone model provides insight into film growth.

Vapour condensation is a stochastic process and the columns are not identical. Fluctuations in the local deposition rate combined with the random nature of adatom diffusion lead to a variation in the size of nuclei. In addition, nucleation is enhanced at substrate defects such as impurities, point defects, and edge defects, further increasing this variation [35]. This

randomizes the surface distribution of the columnar features seen in the film.

2.2 Glancing angle deposition

2.2.1 Early history: Oblique deposition

It has long been recognized that oblique deposition, where the incident vapour flux makes an angle $\alpha > 0$ with the substrate normal (see Fig. 2.2a), produces films with intrinsically anisotropic properties. In the earliest reported studies [44–47], obliquely-deposited metals unexpectedly exhibited properties such as dichroism, birefringence, double refraction, and anisotropic resistivity. Kundt correctly deduced that film morphology led to the anisotropic properties rather than the effects of stress or film nonuniformity [44]. Later, the interesting anisotropic magnetic and optical properties prompted significant research, all of which reinforced the importance of microstructure in determining film behaviour [48–52]. Thanks to improved characterization tools, particularly electron microscopy, it was confirmed that these phenomena are indeed a direct result of film structure. A significant contribution came in 1950 when König and Helwig recognized the important role of atomic-scale shadowing during oblique deposition. Because of its importance, this shadowing mechanism will now be explained and examined in more detail.

2.2.2 Ballistic shadowing and controlling column growth

The columnar features seen in PVD films are created by a combination of nucleation and limited diffusion. Of the three nucleation modes, Volmer-Weber growth is the most important case for GLAD as this mode creates microscopic topologies on the substrate surface. At oblique incidence, the 3D clusters intercept incoming vapour and prevent deposition onto the region immediately behind the nucleus, as shown in Fig. 2.2a. Each nucleus effectively creates a ballistic shadow (indicated by the shaded region in Fig. 2.2a) and growth is limited to the nuclei by this shadowing process. Because deposition is limited to the most prominent nuclei, these nuclei are the only features that grow. Surface diffusion will act counter to the shadowing ef-

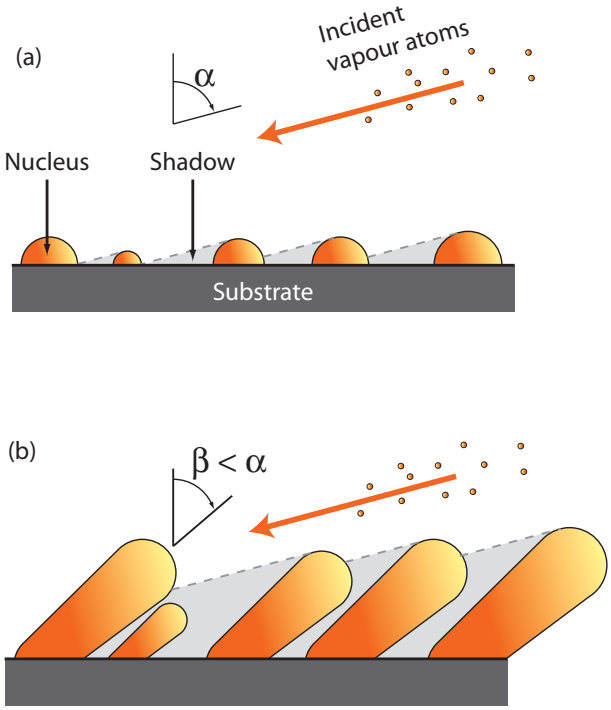

Figure 2.2: An illustration of ballistic shadowing and how it affects film growth. (a) as the vapour nucleates, incident vapour atoms are unable to directly access the region immediately behind the nucleus. This effectively creates shadowed regions of the substrate where no growth occurs. (b) further deposition is limited to the exposed nuclei which develop into columns tilted towards the incident vapour.

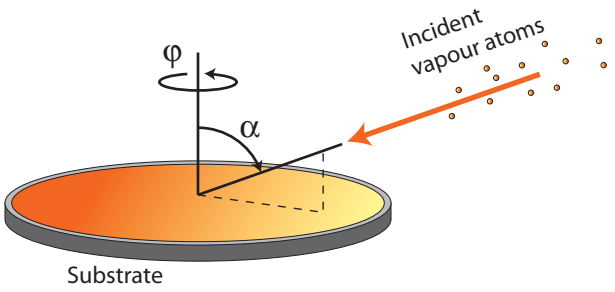

Figure 2.3: The incident vapour flux direction is controlled by two substrate movements: tilting (α) and rotation (φ). Because the columns grow towards the incident vapour, changing these angles during deposition can be used to manipulate the column geometry.

fect, with adatoms diffusing into the shadowed regions. Because it relies heavily on the shadowing process, GLAD operates at low T_s in Zone I of Movchan and Demchishin's SZM.

GLAD tailors the inherent columnar structure of the film by controlling the ballistic shadowing effect. As the nuclei develop into columns, they do so inclined towards the incident vapour as illustrated by Fig. 2.2b [53]. The tilted columns make an angle β with the substrate normal, where $\beta < \alpha$ [53–58]. The columns are initially symmetric about their growth axis. As the columns grow, this symmetry is lost and the columns tend to fan out in a direction perpendicular to the incident vapor direction [50, 59]. This phenomenon, referred to as column broadening or second anisotropy, is a direct product of the anisotropic nature of shadowing which only occurs in the direction parallel to the vapor; there is no mechanism restricting lateral column growth. The columns will continue broadening until they become large enough to chain together. At highly oblique deposition angles, the structural anisotropy can be very pronounced and forms the basis for many of the interesting anisotropic physical properties of GLAD films.

Because the columns grow toward the source it is possible to control their growth direction by changing the source location. This is accomplished in a GLAD system by rotating the susbtrate. Two degrees of rotational control are available: changing the substrate tilt angle α, and rotating the substrate about its normal axis (the azimuthal angle φ), as shown in Fig. 2.3. The angles are adjusted by computer-controlled motors in the vacuum system.

The computer moves the substrate based on feedback from a thickness monitoring element.

Simply by following different substrate motions, a variety of columnar microstructures may be realized. If the substrate is not rotated, tilted columns will form, as previously discussed. If the substrate is rotated by $\varphi = \pi$ radians after fixed growth intervals, a stack of columns with alternating growth direction will result (a chevronic or zig-zag structure) [23, 60]. If the substrate is rotated slowly, the columns adopt a helical shape [25]. As the substrate rotation speed relative to the deposition rate is increased, the pitch of the helix decreases [61]. When the helical pitch is comparable to the column diameter [62], the helical form is lost and the columns degenerate into vertically oriented posts [63]. These different columnar structures are accessed by understanding and controlling the atomistic shadowing dynamics of thin film growth.

2.2.3 Shadowing and film density

While manipulating the φ angle determines the ballistic shadow direction and hence the column orientation, the α angle controls the shadow length and the column separation. As seen in see Fig. 2.4, the shadowing length s of nuceli and columns on the substrate is determined by α according to

$$\cos\alpha = \frac{r}{r+s} \tag{2.2}$$

where hemispherical nuclei are assumed. The one-dimensional fill factor f of this film, defined as the ratio of substrate length covered by film material to the total substrate length, is given by

$$f = \frac{2r}{2r+s} \tag{2.3}$$

where r is the column radius. After simple algebra, substituting Eq. 2.2 into Eq. 2.3 leads to

$$f(\alpha) = \frac{2\cos\alpha}{1+\cos\alpha}. \tag{2.4}$$

Even though the derivation is simplistic and one-dimensional, Eq. 2.4 (originally derived by Tait *et al.* [57]) neatly illustrates how the relative amount of material deposited can be controlled by tilting the substrate. To

fabricate densely packed structures with a correspondingly higher refractive index, low α values are required. A less dense material, having a lower refractive index, requires high α deposition. Therefore, adjusting α provides a simple means of controlling the optical properties of GLAD-fabricated structures. This will be exploited as a technique to tune the properties of GLAD-fabricated optical nanomaterials.

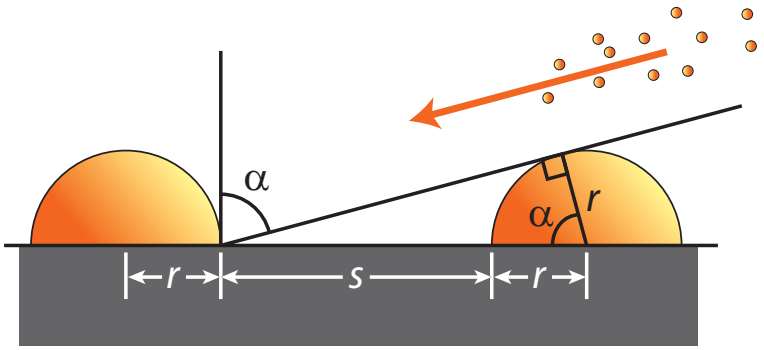

Figure 2.4: A simple model of ballistic shadowing geometry used to derive a relation between α and film density.

2.2.4 Column evolution and competitive growth

The deposition of columnar thin films is a competitive growth process. Since ballistic shadowing leads to the preferential growth of the tallest features on the surface, smaller columns will eventually fall into the shadowed regions cast by larger neighbouring columns. The larger columns then increase in size as they intercept increased amounts of flux. The shadowed column no longer recieves any vapour and stops growing, effectively becoming extinct. This competition and extinction process is characteristic of GLAD films.

Another important aspect of columnar film growth is revealed by the evolutionary growth model [64]. In this model, the columnar structure is hierarchical. A given column is actually a composite of smaller columns bundled together which are composed of subcolumns themselves. The smallest columnar unit is termed a nanocolumn, with a column diameter of 1–3 nm. In very thin films ($\sim$15 nm thick), separate nanocolumns develop. As growth continues, these columns cluster together forming a larger column, which eventually bundle together to form an even larger column, leading

to a structural hierarchy. Such bundled-columnar structures are commonly observed in thin films.

2.3 Optical properties of nanomaterials

The columnar structuring in films produced by PVD creates a nanostructured material, i.e., a nanomaterial. The GLAD technique uses α and φ substrate motions to manipulate the ballistic shadowing effect and control the column growth. Hence, the geometry of the deposited nanomaterial can be flexibily engineered. As was introduced in Sec. 1.2, the structural characteristics of a nanomaterial strongly influence its optical response. *A priori* knowledge of nanomaterial optical properties is crucial for rational design and experimental interpretation. Developing simultaneously accurate and practical models is therefore an important problem.

Common theoretical approaches generally average over the structural inhomogeneities and represent the structured medium with a homogeneous approximation [65, 66]. Solving for the electromagnetic response of this effective, homogeneous material is much simpler. The homogenization process also offers a clear analogue to macroscopic optical measurements. Because the nanostructures are generally small compared to the wavelength, far-field optical measurements sample many nanostructures. Therefore it is the collective optical response that is measured, not the optical response of an isolated nano-element.

2.3.1 Effective medium theory

The effective medium problem in its general form consists of producing a homogeneous medium with the same properties as an arbitrarily arranged collection of arbitrarily shaped-particles. The effective medium representation of an inhomogeneous system depends on the dielectric constants of the constituent particles, the particle structure (shape and size), their geometric distribution throughout the medium, and the nature of the applied field [67, 68]. The first step of all the various effective medium theories is to simplify this general form into a tractable specific case. The original and simplest effective medium theory was developed by Maxwell Garnett [69].

It is based on Lorentz's derivation of the Clausius-Mossotti equation[1], relating the macroscopic dielectric response to the constituent molecular dipole fields. Maxwell Garnett recognized that the field scattered by a subwavelength sphere is equivalent to the field radiated by an electric dipole. This equivalence prompted him to adapt the local field approach into an effective medium theory describing the optical properties of subwavelength metallic spheres. Given a mixture of material 1 (with dielectric constant ε_1) embedded in material 2 (with dielectric constant ε_2), with relative volume fractions f_1 and $f_2 = 1 - f_1$, the Maxwell-Garnett effective dielectric constant ε_{eff} is given by

$$\frac{\varepsilon_{\text{eff}} - \varepsilon_2}{\varepsilon_{\text{eff}} + (D-1)\varepsilon_2} = f_1 \frac{\varepsilon_1 - \varepsilon_2}{\varepsilon_1 + (D-1)\varepsilon_2}. \tag{2.5}$$

The constant D is the system dimensionality: for $D = 3$, spherical particles of ε_1 are embedded within a volume of ε_2. For $D = 2$, circular inclusions of ε_1 are embedded in a planar area of ε_2. Despite assumptions on the particle shape (spherical/circular), arrangment (highly symmetric), and size (vanishingly small), the Maxwell Garnett approach can be a useful and accurate approximation.

Another important effective medium theory was developed by Bruggeman [70]. Like the Maxwell Garnett theory, Bruggeman's theory is based on subwavelength spherical particles. However, in the Bruggeman approach, both materials ε_1 and ε_2 contribute to the local field [71]. Bruggeman's approach leads to

$$f_1 \frac{\varepsilon_1 - \varepsilon_{\text{eff}}}{\varepsilon_1 + (D-1)\varepsilon_{\text{eff}}} + f_2 \frac{\varepsilon_2 - \varepsilon_{\text{eff}}}{\varepsilon_2 + (D-1)\varepsilon_{\text{eff}}} = 0. \tag{2.6}$$

For the same input parameters, the theories predict different ε_{eff} as shown in Fig. 2.5. This figure plots the effective index ($\sqrt{\varepsilon_{\text{eff}}}$) for three cases. The first, labelled 'MG1', is the Maxwell Garnett prediction for ε_1 embedded in ε_2. The second, labelled 'MG2', is the reverse of 'MG1' i.e. the Maxwell Garnett prediction for ε_2 embedded in ε_1. The third, labelled 'Bruggeman', is the Bruggeman prediction for ε_1 in ε_2. In all three cases, the inclusions are circular ($D = 2$), ε_1 = 4.0 and ε_2 = 1.0.

The discrepancy between the predictions stems from the different mi-

[1]This equation is often connected with different scientists: Clausius, Mossotti, Lorenz, and Lorentz. All made contributions in developing the local field concept [65].

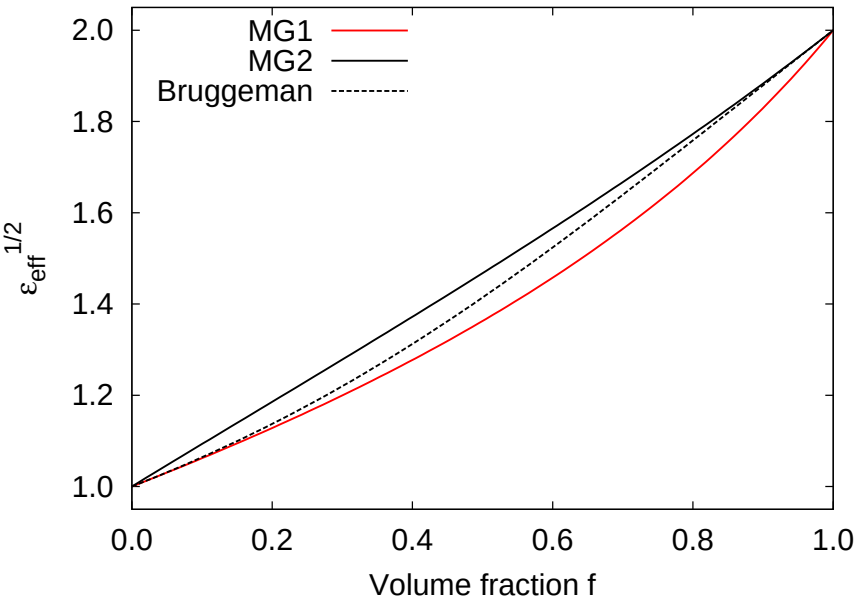

Figure 2.5: The calculated Maxwell-Garnett (Eq. 2.5) and Bruggeman (Eq. 2.6) effective indices for $D = 2$, $\varepsilon_1 = 4.0$ and $\varepsilon_2 = 1.0$. The MG1 and MG2 curves are the Maxwell-Garnett predictions for ε_2 embedded in ε_1 and ε_1 in ε_2, respectively.

crostructures assumed in deriving the theories [72]. The two Maxwell-Garnett predictions represent equivalent (but inverted) separated circular-grain microstructures. The Bruggeman prediction represents an aggregate microstructure that is symmetric upon inversion. The Bruggeman effective index lies between the two Maxwell Garnett predictions. At small f and large f, the 'Bruggeman' curve approaches the 'MG1' and the 'MG2' curves, respectively. For the purposes of this thesis, the main point to recognize is the monotonic relationship between the effective index and the relative volume fraction. Therefore controlling the relative volume fraction, as discussed in Sec. 2.2.3, amounts to tailoring the refractive index.

2.3.2 Non-spherical particles

In optical nanomaterials, the particles are often anisotropically structured. This is certainly the case for GLAD-fabricated columns. For vertically oriented columns, the planar cross-section is approximately circular and Eqs.

2.5 and 2.6 can be applied with $D = 2$ to examine electric fields oriented in the substrate plane. However, this symmetry is generally unsatisfied. For example, tilted columns (deposited at fixed α and φ, see Sec. 2.2.2) broaden into fan-like shapes during growth due to the anisotropic nature of the shadowing mechanism.

Generalizations of the Maxwell Garnett and Bruggeman effective medium theories have been created based on ellipsoidal particle shapes [73, 74]. These theories are used to explain the optical anisotropy of GLAD structures [58, 75–77]. In these theories, the altered screening of the ellipsoidal particles is accounted for by the depolarization factor [78]. The effective medium theories can then be rederived using these alternatively polarized particles. The generalized theories provide expressions for the principal axes of the rank-2 dielectric tensor. The fan-like tilted columns can be analyzed in two- or three-dimensions. In 2D, the planar cross-section of these structures is roughly elliptical, with the semi-minor elliptic axis pointing in the source direction and the effective dielectric tensor is a 2x2 matrix. In 3D, the column is represented by a scalene ellipsoid and the effective dielectric tensor is a 3x3 matrix. In both cases, the tensor principal axes are aligned with the ellipsoidal axes.

2.3.3 Larger particles

A key approximation in these effective medium theories is the assumption of subwavelength particles. When the particles are very small, the applied field is essentially constant across the entire particle diameter even at optical wavelengths. The particle then responds equivalently to an electric dipole, as noted above. As the particle size increases relative to the wavelength, this electrostatic approach becomes a poorer approximation. The full electrodynamic treatment of spherical particles was solved by Mie [79] and by Debye [80]. The scattered field can be expressed as a series expansion of Bessel functions. The first term of the expansion reproduces the electric dipole field. Including the next higher term (magnetic dipole contribution) in a homogenization approach leads to a dynamical effective medium theory [81, 82]. Incorporating additional higher-order terms rapidly increases the complexity of the theory [83]. Furthermore, it should be noted that all the above effective medium theories (except [83]) ignore multiple scat-

tering effects and the particles do not interact. This becomes a less-valid approximation when the particles are large (and hence the scattered fields are greater) and/or when the particles are densely packed.

The range of validity of the electrostatic theories (Eqs. 2.5 and 2.6) is obviously questioned by these considerations. Maxwell Garnett suggested that the particles be "an order of magnitude so small as a wave-length of light" [69]. More recently, experimental results have shown the theories are adequate for particle-diameter to wavelength ratios of 0.25 [82]. (Note that these ratios refer to the field inside the material i.e. λ_0/n.) As the particle size increases beyond these values, the electrostatic assumption is broken and waveguiding effects concentrate the field inside the higher ε material [66]. Consequently, the actual ε_{eff} will be greater than the predicted ε_{eff}.

2.4 Properties of optical thin films

The effective medium considerations of the preceeding section motivate treating GLAD-fabricated nanostructures as a homogeneous medium. This allows GLAD-films to be analyzed using optical thin film approaches. These calculation methods are presented and explained in this section.

2.4.1 A single homogeneous layer: the Airy summation

Calculating the optical properties of a thin layer is a historic problem. A light beam incident upon a layer of thickness d and constant refractive index n, will experience reflection every time it encounters an interface, leading to an infinite series of reflected waves. When the layer thickness is much smaller than the optical coherence length, these multiply reflected waves sum coherently and the total reflected intensity is

$$R = \frac{r_{12}^2 + r_{23}^2 + 2r_{12}r_{23}\cos 2\phi}{1 + r_{12}^2 r_{23}^2 + 2r_{12}r_{23}\cos 2\phi}, \tag{2.7}$$

a result originally found by G. B. Airy [84]. In this equation, r_{12} and r_{23} are the Fresnel reflection coefficients at the two bounding interfaces and $\phi = 2\pi nd\cos\theta/\lambda_0$ (where θ is the propagation angle of light in the film, measured from the normal) is the phase change of the light as it propagates

through the film. For a non-absorbing film, energy conservation implies the transmitted intensity is $T = 1 - R$. From Eq. 2.7, it can be seen that the intensity of the layer reflection varies periodically with 2ϕ due to the constructive and destructive interference between the multiply reflected light. For varying λ, the oscillating spectral reflectance forms Fabry-Perot interference fringes [85]. If the interfaces are not parallel d is spatially varying and interference fringe patterns are created, such as Newton's rings[2] or Fizeau fringes [86].

2.4.2 Multiple homogeneous layers: characteristic matrices

Extending Airy's method to multiple layer systems quickly becomes impractical and a different approach is required [87]. Developing a general theory capable of calculating the optical response of such systems begins, as do most problems in physical optics, with Maxwell's equations. These equations relate the four electromagnetic field vectors, the electric field **E**, the magnetic field **H**, the electric displacement **D**, and the magnetic induction **B**, through spatial and time derivatives. In the absence of charges and currents, Maxwell's equations in matter are [2]

$$\nabla \times \mathbf{H} - \frac{\partial}{\partial t}\mathbf{D} = 0, \tag{2.8a}$$

$$\nabla \times \mathbf{E} + \frac{\partial}{\partial t}\mathbf{B} = 0, \tag{2.8b}$$

$$\nabla \cdot \mathbf{D} = 0, \tag{2.8c}$$

$$\nabla \cdot \mathbf{B} = 0. \tag{2.8d}$$

The fields are further interelated by the constitutive equations

$$\mathbf{D} = \varepsilon_0 \mathbf{E} + \mathbf{P}, \tag{2.9a}$$

$$\mathbf{H} = \frac{1}{\mu_0}\mathbf{B} - \mathbf{M}, \tag{2.9b}$$

where ε_0 = 8.854$\times 10^{-12}$F/m and μ_0 = $4\pi \times 10^{-7}$H/m are the vacuum permittivity and permeability. The field quantities **P** and **M** are the polarization

[2] Although called Newton's rings, the effect was first observed independently by Robert Boyle and by Robert Hooke [1]. Newton recieves credit for his subsequent explanation of the phenomena

and magnetization of the material medium. **P** and **M** represent the electric and magnetic dipole moments[3] in the material, which may be either permanent or induced. The electric and magnetic susceptibilities χ_e and χ_m relate **P** to **E** and **M** to **H**. In linear materials, $\mathbf{P} = \varepsilon_0 \chi_e \mathbf{E}$ and $\mathbf{M} = \mu_0 \chi_m \mathbf{H}$. The material dielectric constant ε and magnetic permeability μ are correspondingly defined as $\varepsilon = 1 + \chi_e$ and $\mu = 1 + \chi_m$.

By a series of substitutions and applying vector identities[4] Maxwell's equations can be transformed into wave equations [1]

$$\nabla^2 \mathbf{E} - \frac{\varepsilon\mu}{c^2}\frac{\partial^2 \mathbf{E}}{\partial t^2} + (\nabla \ln \mu) \times (\nabla \times \mathbf{E}) + \nabla (\mathbf{E} \cdot \nabla \ln \varepsilon) = 0, \tag{2.10a}$$

$$\nabla^2 \mathbf{H} - \frac{\varepsilon\mu}{c^2}\frac{\partial^2 \mathbf{H}}{\partial t^2} + (\nabla \ln \varepsilon) \times (\nabla \times \mathbf{H}) + \nabla (\mathbf{H} \cdot \nabla \ln \mu) = 0. \tag{2.10b}$$

where $c = (\varepsilon_0 \mu_0)^{-1/2}$ is the speed of light in vacuum. When ε and μ are spatially non-varying, $\nabla(\ln \varepsilon)$ and $\nabla(\ln \mu)$ are zero and these equations reduce to the more commonly derived two-term wave equations:

$$\nabla^2 \mathbf{E} - \frac{\varepsilon\mu}{c^2}\frac{\partial^2 \mathbf{E}}{\partial t^2} = 0, \tag{2.11a}$$

$$\nabla^2 \mathbf{H} - \frac{\varepsilon\mu}{c^2}\frac{\partial^2 \mathbf{H}}{\partial t^2} = 0. \tag{2.11b}$$

The reduced dimensions of the thin film problem lead to some additional simplifications. If the *z*-axis is taken parallel to the layer normal and the plane of incidence is the *yz*-plane, the incoming plane wave can be resolved into two orthogonal components of different polarization. In the first, **E** and the *x*-axis are co-parallel (the TE- or *s*-polarization). In the second, **H** and the *x*-axis are co-parallel (the TM- or *p*-polarization). As pointed out by Born and Wolf [1], Maxwell's equations are unchanged by the substitution $(\mathbf{E}, \varepsilon) \rightarrow (\mathbf{H}, -\mu)$. Any result derived for the TE-wave can be quickly transformed to the corresponding TM-wave result using this transformation. For

[3] Higher-order moments are invariably negligible [2].

[4] Three vector identities are required:

$$\nabla \times \nabla \times \mathbf{v} = \nabla (\nabla \cdot \mathbf{v}) - \nabla^2 \mathbf{v}$$

$$\nabla \times u\mathbf{v} = u \nabla \times \mathbf{v} + \nabla u \times \mathbf{v}$$

$$\nabla \cdot u\mathbf{v} = u \nabla \cdot \mathbf{v} + \mathbf{v} \cdot \nabla u$$

.

the TE-wave, only E_x is non-zero and Eq. 2.11a is solved by separation of variables. This solution combined with Eq. 2.8b characterizes the propagating **E** and **H** fields:

$$\begin{aligned} E_x &= U(z)\exp\left[i(k_0 n\sin\theta y - 2\pi\omega t)\right], \\ H_y &= V(z)\exp\left[i(k_0 n\sin\theta y - 2\pi\omega t)\right], \\ H_z &= W(z)\exp\left[i(k_0 n\sin\theta y - 2\pi\omega t)\right], \end{aligned}$$

where $k_0 = 2\pi/\lambda_0$ is the freespace wavenumber, θ is the propagation angle in the layer, ω is the frequency, and t is time. On account of Eqs. 2.8a and b, the field amplitude functions U, V, and W are inter-related by first-order differential equations. By elimination between these equations, the following second-order differential equations are produced

$$\begin{aligned} \frac{d^2U}{dz^2} + k_0^2 n^2\cos^2\theta U = 0, \\ \frac{d^2V}{dz^2} + k_0^2 n^2\cos^2\theta V = 0. \end{aligned}$$

The propagating TE wave is therefore described by the solutions

$$\begin{aligned} U(z) &= A\cos\phi + B\sin\phi, \\ V(z) &= -i\sqrt{\frac{\varepsilon}{\mu}}\cos\theta\left[B\cos\phi - A\sin\phi\right] \end{aligned}$$

where $\phi = k_0 nz\cos\theta$. Taking $U(0)$=U_0=A and $V(0)$=V_0=$-i\sqrt{(\varepsilon/\mu)}\cos\theta B$ allows the solutions to be expressed as

$$\begin{aligned} U(z) &= U_0\cos\phi + V_0\frac{i}{\cos\theta}\sqrt{\frac{\mu}{\varepsilon}}\sin\phi, \\ V(z) &= U_0 i\cos\theta\sqrt{\frac{\mu}{\varepsilon}}\sin\phi + V_0\cos\phi. \end{aligned}$$

This can be compactly written in matrix form:

$$\begin{bmatrix} U(z) \\ V(z) \end{bmatrix} = \begin{bmatrix} \cos\phi & \frac{i}{\cos\theta}\sqrt{\frac{\mu}{\varepsilon}}\sin\phi \\ i\cos\theta\sqrt{\frac{\mu}{\varepsilon}}\sin\phi & \cos\phi \end{bmatrix} \begin{bmatrix} U_0 \\ V_0 \end{bmatrix}$$

which is typically inverted for convenience to yield

$$\begin{bmatrix} U_0 \\ V_0 \end{bmatrix} = \begin{bmatrix} \cos\phi & -\frac{i}{\cos\theta}\sqrt{\frac{\mu}{\varepsilon}}\sin\phi \\ -i\cos\theta\sqrt{\frac{\mu}{\varepsilon}}\sin\phi & \cos\phi \end{bmatrix} \begin{bmatrix} U(z) \\ V(z) \end{bmatrix}. \tag{2.12}$$

This matrix, pertaining to the *s*-polarized fields, is denoted $\mathbf{M}_s$. The corresponding matrix for the *p*-polarization is

$$\mathbf{M}_p = \begin{bmatrix} \cos\phi & -\frac{i}{\cos\theta}\sqrt{\frac{\varepsilon}{\mu}}\sin\phi \\ -i\cos\theta\sqrt{\frac{\varepsilon}{\mu}}\sin\phi & \cos\phi \end{bmatrix}. \tag{2.13}$$

These matrices relate the electromagnetic field between any two points in the layer and completely determine the propagation of the fields in the medium. Because these matrices encode the layer characteristics, they are called the characteristic matrices.

While deriving this single layer solution is more difficult than the Airy summation, the matrix method quickly and easily computes the properties of multiple layers. Assuming isotropic materials, the most general multilayer case is a series of N layers extending from $0 \leq z \leq z_1$, $z_1 \leq z \leq z_2, \cdots, z_{N-1} \leq z \leq z_N$, having characteristic matrices $\mathbf{M}_1$, $\mathbf{M}_2, \cdots, \mathbf{M}_N$. The characteristic matrix $\mathbf{M}$ of the assembled layers is simply

$$\mathbf{M} = \prod_{j=1}^{N} \mathbf{M}_j. \tag{2.14}$$

2.4.3 Calculating reflection and transmission coefficients

In a multilayer calculation, the properties of interest are typically the reflectance R and transmittance T. Calculating these quantities from the internal multilayer fields requires applying boundary conditions. The field amplitudes of the incident, reflected, and transmitted waves are respectively defined as A_i, A_r, and A_t. The regions bounding the multilayer have dielectric constants ε_i, ε_s and magnetic permeability μ_i, μ_s, where the subscripts refer to the incident (i) and substrate (s) media. The incident and reflected waves propagate at angles θ_0 to the layer normals and the transmitted light at an angle θ_s (related by Snell's law to θ_0).

The electromagnetic boundary conditions require that the tangential components of **E** and **H** remain continuous across the bounding interfaces. For plane waves, **E** and **H** are further related by $\mathbf{E} = -\sqrt{\mu/\varepsilon}(\hat{z} \times \mathbf{H})$ and $\mathbf{H} = \sqrt{\varepsilon/\mu}(\hat{z} \times \mathbf{E})$ (which follow from Eqs. 2.8a and 2.8b). The incident ($z = 0$) and transmitted ($z = z_N$) fields can then be written, for the *s*-wave, as

$$U_0 = A_i + A_r, \tag{2.15}$$

$$V_0 = \left(\cos\theta\sqrt{\varepsilon_s/\mu_s}\right)(A_i - A_r), \tag{2.16}$$

$$U(z_N) = A_t, \tag{2.17}$$

$$V(z_N) = \left(\cos\theta\sqrt{\varepsilon_s/\mu_s}\right)A_t. \tag{2.18}$$

The corresponding *p*-wave fields are found by replacing ε/μ with μ/ε. These fields are connected by Eq. 2.12

$$\begin{aligned} A_i + A_r &= \left(M_{11} + M_{12}\cos\theta\sqrt{\varepsilon_s/\mu_s}\right)A_t, \\ \cos\theta\sqrt{\varepsilon_i/\mu_i}(A_i - A_r) &= \left(M_{21} + M_{22}\cos\theta\sqrt{\varepsilon_s/\mu_s}\right)A_t. \end{aligned}$$

Solving these equations to obtain the reflection ($r = A_r/A_i$) and transmission ($t = A_t/A_i$) coefficients gives

$$r = \frac{(M_{11} + M_{12}p_s)\,p_i - (M_{21} + M_{22}p_s)}{(M_{11} + M_{12}p_s)\,p_i + (M_{21} + M_{22}p_s)}, \tag{2.19a}$$

$$t = \frac{2p_i}{(M_{11} + M_{12}p_s)\,p_i + (M_{21} + M_{22}p_s)}, \tag{2.19b}$$

where $p_i = \cos\theta_i\sqrt{\varepsilon_i/\mu_i}$ and $p_s = \cos\theta_s\sqrt{\varepsilon_s/\mu_s}$. The reflectance R and transmittance T are given by $R = |r|^2$ and $T = (p_s/p_i)\,|t|^2$.

2.5 Periodic structures: Photonic crystals

The stated objective of this thesis is to develop GLAD-fabricated nanomaterials into photonic crystal technologies. As with effective medium theory, reviewing the relevant aspects of photonic crystal theory is necessary for interpretation of experimental findings. Given the wide-spread interest in photonic crystals, there has been significant theoretical examination of their

properties. The characteristic matrix approach developed in Sec. 2.4.2 is powerful and can predict the properties of general one-dimensional optical systems including photonic crystals. However, significant physical intuition is gained by considering the propagation of optical waves in a periodic system.

2.5.1 Wave propagation in periodic structures

A periodic optical system is one where the spatial dependence of the dielectric constant $\varepsilon(\mathbf{r})$ is invariant after being displaced by some $\mathbf{R}$, i.e.

$$\varepsilon(\mathbf{r}) = \varepsilon(\mathbf{r} + \mathbf{R}). \tag{2.20}$$

The physics of this problem, in one-dimension, was first studied by Lord Rayleigh [88, 89]. Central to the solution is the constructive interference of scattered waves. Rayleigh noted that at every $\varepsilon(\mathbf{r})$ interface a reflected wave is produced. When the optical path length between interfaces is a half-wavelength, Rayleigh concluded that "...the partial reflexions from the various [interfaces] will all concur in phase, and the result must be a powerful aggregate reflexion, even though the effect of an individual [interface] may be insignificant" [88]. This is essentially the Bragg condition

$$m\lambda_B = 2\Lambda \sin\theta \tag{2.21}$$

arrived at by von Laue, W. H. Bragg and W. L. Bragg in developing X-ray diffraction theory [90]. In Eq. 2.21, λ_B is the optical wavelength, θ is the propagation angle, Λ is the optical path length of the unit cell, and m is the diffraction order. The large reflection is known interchangably as a Bragg diffraction, interference, or reflectance peak. The width of the reflectance peak is determined by the scattering strength of the interfaces.

Further understanding of wave propagation in periodic structures came with the results of Felix Bloch [91]. Bloch explained the behaviour of electron waves in crystalline solids by solving the Schrödinger equation with periodic coefficients. The key insight is that the field[5] propagates through the periodic system as a Bloch wave: a time-harmonic plane wave multiplied

[5] Although the electron wavefunction is a scalar field, electromagnetic vector fields obey the same principle [4].

by a periodic envelope $u_k(\mathbf{r})$. The function $u_k(\mathbf{r})$ has the same period as the underlying structure and represents the coherent interference of all the scattering events in the system. For electrons propagating in a crystal lattice, the periodicity of the atomic potential creates a band gap in the electronic dispersion relation. For frequencies within this band gap, no purely real wave vectors exist. Electrons cannot occupy these states and propagation within the band is forbidden.

The optical Bragg diffraction peak and the electronic band gap have similar origins: constructive and destructive interference of waves scattered by a periodic medium. Because of this parallel, the optical diffraction peak is commonly called the photonic band gap and periodic optical systems are referred to as photonic crystals [92, 93]. The intense research effort surrounding PCs in recent years has been driven by this parallel. If the control over electron propagation achieved using semiconductor technology could be adapted to photon propagation in photonic crystals, tremendous impacts on physics and electrical engineering would follow.

2.5.2 One-dimensional photonic crystal structures

While a major goal in PC research is a complete, three-dimensional photonic band gap, functional demonstrations of this objective has only been achieved using intricate top-down microfabrication processing [94]. Alternatively, one-dimensional periodic systems retain many of the interesting and useful photonic band gap properties while being simpler to fabricate.

In a 1D system, Eq. 2.20, written in terms of the index $n = \sqrt{\varepsilon}$, simplifies to

$$n(z) = n(z + P), \tag{2.22}$$

where P is the physical period of the system. This periodicity condition can be realized with either a discrete or continuous index profile. In the discrete case, the system is composed of alternating layers of different materials. The layer refractive indices are respectively n_1 and n_2. At every layer interface a portion of the wave is reflected according to the Fresnel formulae. To satisfy the Bragg condition (Eq. 2.21) at normal incidence and wavelength λ_0, the

layer thicknesses d_1 and d_2 are required to be

$$n_1 d_1 + n_2 d_2 = \frac{\lambda_0}{2}. \tag{2.23}$$

This refractive index profile $n(z)$ can be expressed as a piecewise function

$$n(z) = \begin{cases} n_a & \text{if } mP < z < (mP + d_1) \\ n_b & \text{if } (mP + d_1) < z < (mP + d_1 + d_2) \end{cases} \tag{2.24}$$

where m is an integer. Materials with this refractive index structure are called Bragg multilayers [4]. The band gap effects (band gap depth, width) are maximized when both sublayers have quarter-wave optical path lengths ($n_1 d_1 = n_2 d_2 = \lambda_0 / 4$), which is the usual case. At λ_0, the optical transmittance T through a finite Bragg multilayer is [95]

$$T = 4n_1^2 \left(\frac{n_1}{n_2} \right)^{N-1}, \tag{2.25}$$

where N is the total number of periods in the multilayer and the derivation assumes $n_1 < n_2$. As can be seen, the transmittance approaches zero rapidly as the number of interfaces (i.e. scatterers) in the PC increases. The transmittance also decreases when the interface reflection (i.e., scattering potential) increases. The photonic band gap (FWHM) bandwidth $\Delta\lambda$ produced by this structure is equal to

$$\frac{\Delta\lambda}{\lambda_0} = \frac{4}{\pi} \arcsin \left(\frac{n_1 - n_2}{n_1 + n_2} \right). \tag{2.26}$$

In the continuous case, the index profile changes smoothly from point-to-point. The most common periodic realization of such a profile is the rugate[6] structure. In the rugate structure, the refractive index profile follows a sine variation:

$$n(z) = n_a + \frac{1}{2} n_p \sin \left(2\pi \frac{z}{P} + \phi \right), \tag{2.27}$$

where n_a is the average index, n_p is the peak-to-peak index variation amplitude, and ϕ is the starting phase. The Bragg condition for this index profile

[6] From the latin 'ruga', meaning wrinkle

is satisfied for

$$n_a P = \frac{\lambda_0}{2}. \tag{2.28}$$

The band gap properties of the rugate structure were calculated using coupled mode theory by Southwell [96]. At λ_0, the transmittance through an N period rugate multilayer is

$$T = 1 - \tanh^2\left(\frac{\pi n_p N}{4 n_a}\right). \tag{2.29}$$

As the argument of the hyperbolic tangent in Eq. 2.29 increases (i.e., as n_p and / or N increases), the transmittance through the rugate structure quickly approaches zero. The rugate's photonic band gap bandwidth is

$$\frac{\Delta\lambda}{\lambda_0} = \frac{n_p}{2 n_a}. \tag{2.30}$$

2.5.3 One-dimensional photonic crystal fabrication methods

To realize one-dimensional PCs, a fabrication technique must be able to vary the refractive index of a thin film system. The simplest method is to deposit layers of different materials. This is the approach taken in conventional thin film processing. Alternate deposition of quarter-wave layers of a low- and a high-index material (such as cryolite / ZnS or SiO_2 / Nb_2O_5) produces a two-material Bragg multilayer. State-of-the-art optical thin film fabrication is an automated process [97], with excellent quality control accomplished through rapid design techniques [98–100], continuous deposition monitoring [101], and *in situ* error compensation [102, 103]. As mentioned in Sec. 1.5, competing with conventional thin film methods requires leveraging properties unique to GLAD fabricated films, such as porosity and anisotropy.

Creating PCs with a continuous index variation is more difficult. Correspondingly, the methods are less well-studied and have not reached the same level of sophistication as conventional manufacturing. Techniques used to realize continuous index variations include simultaneous evaporation [104] or sputtering [105] of two materials, plasma-enhanced chemical vapour deposition [106, 107] and ion-beam controlled compositional gradients in evaporated films [108].

Various bottom-up nanofabrication techniques have also been applied

to PC fabrication. Whereas the previously mentioned fabrication methods achieve index contrast via combining different materials, the nanofabrication techniques realize index contrast through structural control. A prominent approach introduces porosity into crystalline Si via controlled electrochemical etching [109]. Refractive index gradients are realized by varying the pore sizes, which are determined by the etch current.

Another PC fabrication approach uses spin casting of nanoparticle colloids to produce porous, structured layers [110]. Layers are fabricated from different colloidal solutions, which are sequentially spin-cast on top of one another. A drawback of this approach however is that after each layer is prepared, a high-temperature annealing treatment is required. For complicated optical devices with many layers, the number of processing steps increases rapidly, limiting sample throughput and yield.

One-dimensional PCs have also been fabricated using diblock copolymers [111]. In this approach, the copolymer phases (such as, polystyrene and polyisoprene) spontaneously separate into a lamellar structure. Many layers can be produced and the technique can be extended into two- and three-dimensions. However only discrete index changes can be created and there is no clear route to PC defect introduction.

While these are all promising bottom-up nanofabrication techniques, they do not possess the same fabrication advantages as GLAD. As a fabrication method, GLAD provides greater material flexibility. The ability to introduce and control optical anisotropy is not provided by these other techniques. Additionally, GLAD can realize both discrete and continuous index variations.

2.6 Summary

This chapter reviewed and discussed a number of background topics. The basics of thin film deposition and PVD were covered, in particular the condensation, nucleation and column growth phases. These three phases are highly relevant, being central to the GLAD process. Key aspects of GLAD were introduced, such as ballistic shadowing, controlling column growth and orientation, the link between shadowing and film density, and the competitive nature of GLAD growth. Reviewing these topics provides important

understanding of the principles of GLAD growth. These principles determine the morphology of GLAD-fabricated nanomaterials and indicate how the morphology can be engineered.

The relationship between nanoscale morphology and the nanomaterial optical properties is explained using effective medium theories. In these theoretical approaches, a complicated structured medium is replaced by a homogeneous counterpart with an approximately equivalent electromagnetic response. Justified by these approaches, the optical properties of GLAD nanomaterials can be simulated using conventional techniques, including the powerful characteristic matrix technique.

The general properties of waves propagating in a periodic system are common to many phenomena including PCs, the basic optical device fabricated in this research. The concepts introduced, such as Bragg interference and Bloch waves, are used in later chapters to interpret experimental findings. Various theoretical and experimental realizations of PCs were summarized.

The background summarized in this chapter is used throughout this research. The concepts are used to analyze and interpret experimental findings as well as predict and design the properties of PC devices. The next chapter provides an overview of research methodology, discussing fabrication and characterization tools used to collect experimental data.

Chapter 3

Experimental Methods and Characterization Techniques

A range of experimental methods are employed in this thesis research. These methods can be divided into three categories: (1) fabrication and preparation of samples using PVD and GLAD techniques, (2) measurement of sample optical and structural properties, and (3) reduction and model-fitting of the measured data. The main sections of this chapter present and discuss these three aspects of the research methodology.

3.1 Sample fabrication

3.1.1 Description of vacuum system

A typical, GLAD-modified PVD apparatus is presented schematically in Fig. 3.1. Basic components common to PVD systems are shown. The chamber is attached to a system of vacuum pumps, used to prepare the requisite high-vacuum environment. The source material is heated by an electromagnetically focused and rastered electron beam. The electrons are accelerated by a 9 kV potential. The source material is heated, increasing the material vapour pressure p_v. When p_v is greater than the ambient chamber pressure p (Eq. 2.1), the material evaporates into the chamber. A substrate platform is positioned above the vapour source. Substrates mounted on this platform intercept the vapour and the deposit is formed as described in Sec. 2.1.2.

A quartz crystal microbalance (QCM) is used to measure deposition rate. By vibrating a quartz crystal and monitoring shifts in resonance, the QCM

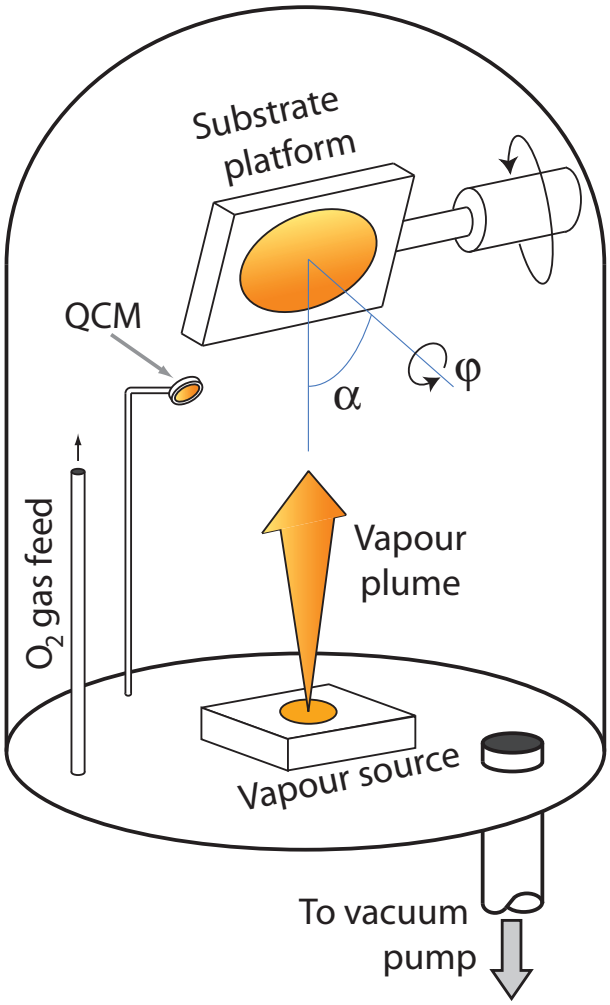

Figure 3.1: A typical PVD system modified for GLAD use. The substrate platform is attached to motors adjusting the (α, ϕ) substrate position. A vapour source is positioned beneath the substrate platform and a quartz crystal microbalance (QCM) monitors the deposition rate.

is able to accurately measure deposited mass. This is converted to thickness using the inputted material density and Z-ratio. The tooling factor is a calibration parameter used to account for the geometric deposition rate difference between the QCM and the substrate.

Unique to the GLAD process are the motors attached to the substrate platform. These motors control the substrate position via α and φ rotations, as indicated on Fig. 3.1 and defined in Sec. 2.2.2. The motor-determined substrate position is controlled by a computer. The computer simultaneously monitors the QCM measured deposition rate and adjusts the substrate position following a user-inputted motion algorithm. This motion algorithm consists of a three column table instructing the computer what the α and ϕ positions should be at a given QCM thickness.

3.1.2 Deposition ratio

The film thickness at the substrate is determined by the mass and density of the deposited film. As discussed in Sec. 2.2.3, there is a monotonically decreasing relationship between α and the deposited film density. This implies that the deposited film thickness is α-dependent. Films deposited at higher α will correspondingly be thicker than expected.

To reliably deposit a target thickness, the effect must be accounted for. This is done through an experimental calibration factor called the deposition ratio D. It is defined as

$$D(\alpha) = \frac{d(\alpha)}{d'} \tag{3.1}$$

where d is the film thickness and d' is the QCM-measured thickness. The system tooling factor described above is incorporated into this definition. D depends on several factors other than α including the system geometry, vapour plume distribution, deposition pressure, substrate temperature, substrate sticking coefficient, and QCM accuracy.

3.1.3 Titanium dioxide (TiO_2)

Titanium dioxide (TiO_2), also known as titania, is a geologically abundant mineral and is the chief source material used in this research. TiO_2 has useful electronic [112], optical [113, 114], and surface chemical [115] properties and has found application in a long list of areas: decorative and functional

pigments [116], sunscreens [117], solar energy [118], photocatalysis [119], transparent magnetic materials [120], memristive circuit elements [121, 122], and lithium-battery electrodes [123, 124]. Most notably for this work, TiO_2 is commonly used in optical interference coatings thanks to its high refractive index, mechanical hardness, chemical resistance, and visible transparency [125–127]. For these reasons, it was selected for this research. However, many of the results could be replicated using other materials given the flexibilty of the GLAD process.

TiO_2 thin films can be prepared using most standard coating techniques. For evaporation PVD processes, electron-beam evaporation is generally used for rapid growth of high quality films [128]. Realizing thin films of oxide compounds often requires depositing in an oxygen environment as the original source material partially dissociates upon evaporation [31]. Ideally, the condensing sub-oxide vapour then reacts with ambient O_2 at the substrate to reform the fully oxidized compound.

TiO_2 film optical properties are well known to be highly sensitive to numerous deposition conditions [129]. Key deposition parameters include [126–128, 130]: source material composition, O_2 partial pressure during deposition, substrate temperature, and deposition rate. Considering these factors is important in formulating the general deposition process used in this research.

3.1.4 General deposition conditions and process

A TiO_2 deposition process was developed, combining the considerations of Sec. 3.1.3 with previous work by research colleagues. The wide range of deposition variables provides a large parameter space. In developing this process, the primary goal was consistency, not necessarily optimality. This process could subsequently be optimized to various application requirements.

The chamber was pumped to a base pressure of at least 10^{-6} Torr, where 1 Torr = 133.3 Pa. The starting source material was TiO_2 (rutile form: 99.9% purity, supplied by Cerac Inc. and Kurt J. Lesker Company) placed in a Cu crucible liner. The same liner would be used over several process runs as a single deposition would not fully consume the source. Depleted material was replensihed with fresh material between each run. Small quantities of O_2 gas were introduced to the chamber at low flow rate using a mass flow

controller. The flow rate was manually varied to maintain an O_2 partial pressure of $(9 \pm 1) \times 10^{-5}$ Torr. In early deposition, the O_2 partial pressure was estimated from the total chamber pressure measured using the ion gauge. Later, a residual gas analyzer was made available, providing greater detail about the chamber atmosphere. Superior O_2 pressure control could therefore be attained. The electron-beam was focused onto the source material and swept across the entire crucible. The electron-beam current was manually varied to achieve a QCM-measure deposition rate of 0.9 ± 0.1 nm/s. Glass and Si substrates were mounted on the deposition platform (Fig. 3.1). The glass substrates used were 1"x1" squares of B270, a high-transmittance crown glass fabricated by Schott. The Si substrates were test-grade, p-doped 3" diameter wafers. No attempt was made to control the substrate temperature as the deposition system had no substrate heating or cooling apparatus.

Previous investigations have found that TiO_2 films prepared under similar conditions are amorphous [61, 131]. Although annealing treatments can be used to modify the crystal phase post-deposition [61, 131–134], no such experiments were conducted in this thesis research. Future work could use temperature annealing to modify films post-deposition [135].

3.2 Sample characterization

3.2.1 Structural measurements

To examine film micro- and nanostructure, the fabricated samples were examined using a scanning electron microscope (SEM). The primary SEM used was a field-emission Hitachi S-4800. A lower-resolution JEOL field-emission SEM was also used when the Hitachi SEM was unavailable. SEMs measure the secondary electrons emitted by the sample as an electron-beam is rastered across the surface. No back-scattered electron measurements were performed. Contrast arises in these SEM images from differences in secondary electron emission across the sample. Secondary electron emission depends on the beam current and voltage, the sample atomic composition, and the sample topography. This last factor allows the sample structural variation to be determined in the case of single-material structures like those fabricated in this research. Images could be obtained from several perspectives: top-down surface views, oblique views, and cross-sectional

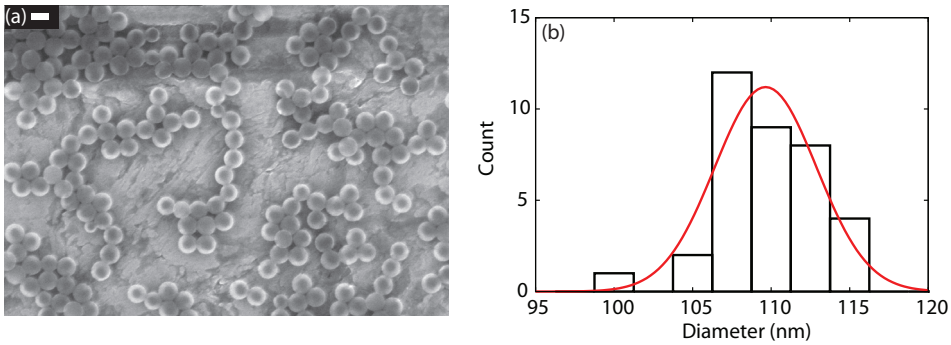

Figure 3.2: (a) top-down SEM view of calibrated monodisperse polystyrene microspheres at 50,000x magnification. (b) the frequency histogram obtained from thirty-six measured microsphere diameters. The red line is a Gaussian distribution fit to the measurements. The distribution mean agrees with the expected mean to within the calibration accuracy ($\pm$ 5 nm).

side views. For cross-sectional imaging, samples deposited on Si substrates were cleaved carefully to expose the internal film structure.

The SEM is an excellent tool for both qualitative and quantitative structural measurements. For the latter, measurement errors may arise from numerous factors: difficulty in determining a structural edge (due to sample charging, limb darkening and electron beam interaction volume effects), the image digitization (non-zero pixel size), electron-beam aberrations, and the calibration of the SEM field-of-view.

To estimate the accuracy of SEM measurements, monodisperse polystyrene microspheres were obtained from Sigma-Aldrich. The average microsphere diameter was NIST-traceably calibrated to be 105 $\pm$ 5 nm (65% confidence interval). The calibrated standard deviation of the microsphere diameters was 6 nm. The microspheres were provided in a 2% wt. suspension. To prepare the microspheres for SEM observation, a drop of the suspension was diluted by a factor of approximately 100. A drop of the diluted suspension was placed on a bare steel SEM stub and allowed to dry overnight. The uncoated spheres were then imaged top-down via SEM (S-4800) at a magnification of 50000 times, producing the image shown in Fig. 3.2(a).

From Fig. 3.2(a), thirty-six microsphere diameters were measured. Fig. 3.2(b) presents the frequency histogram of the measured diameters. The

histogram bin size is 2.5 nm. A Gaussian distribution function

$$G(x) = \frac{G_0}{2\pi\sigma^2} \exp\left[-\frac{(x-\mu)^2}{2\sigma^2}\right] \tag{3.2}$$

was fit to the histogram by adjusting the distribution mean μ, standard deviation σ, and the normalizing constant G_0. The fit was performed numerically using the Levenberg-Marquardt algorithm (Sec. 3.3) and the best-fit curve is shown as a red line on Fig. 3.2(b). The best-fit mean and standard deviation are μ = 109.6 $\pm$ 0.5 nm and σ = 3.2 $\pm$ 0.5 nm. The measured and expected average diameter agree to within the calibration accuracy. Therefore, it can be confidently stated that the SEM measurements are accurate to within 5 nm at this level of magnification.

3.2.2 Optical measurements

Optical data was collected using transmittance and reflectance white-light spectroscopy. This is a simple yet powerful means of characterizing the optical behaviour of samples fabricated in this research. Generally speaking, the measuring apparatus contains a broadband light source, collection and collimation optics, a monochromator, a broadband detector and the sample under examination. Two commercially built spectral characterization tools were used: a Perkin-Elmer Lambda 900 UV/vis/NIR spectrophotometer (henceforth called the spectrophotometer) and a J. A. Woollam Co., Inc. V-VASE variable angle spectroscopic ellipsometer (henceforth called the ellipsometer). The operation of each is now reviewed in turn.

The spectrophotometer was operated exclusively in transmittance mode. It uses a tungesten-halogen bulb as a visible and infrared wavelength source and a deuterium arc lamp as a UV source. Wavelength selection is performed by a double-pass grating monochromator. One set of gratings is used at UV and visible wavelengths, a different set at infrared. The monochromator slit-width is automatically adjusted based on the measured signal levels. The (nearly) monochromatic beam is split along two paths, one passing through the sample (the sample arm) and the other passing through freespace (the reference arm). The intensity of both arms is measured by either a photomultiplier tube (UV and visible wavelengths) or a PbS pho-

todiode (infrared wavelengths). The sample-to-reference intensity of both arms is calculated to provide the relative sample transmittance. The sample and reference arm configuration is beneficial as it minimizes systematic errors due to bulb drift.

The ellipsometer is different from the spectrophotometer in several respects. It does not split the beam into sample and reference paths. Rather the baseline "100%" signal must be measured prior to the sample measurement. The ratio of sample to baseline is calculated afterwards. The ellipsometer uses a Xe-arc lamp as a white light source. Si and InGaAs photodiodes measure the signal at visible and infrared wavelengths, respectively. The double-pass monochromator has two gratings sets for the different spectral regions. The ellipsometer follows a typical rotating-analyzer design. A pre-sample polarizer and retarding element are used to illuminate the sample with different polarization states. A rotating polarizer is positioned after the sample. These high-quality polarization optics make the ellipsometer very useful for polarization-resolved transmittance and reflectance measurements. The ellipsometer also benefits from a precise mechanical goniometer system, allowing reflectance measurements at incidence angles from 20° to 89°. Transmittance measurements are restricted to normal-incidence.

The spectrophotometer and the ellipsometer provide several measurement advantages, namely automation, internal calibration, and repeatability. They also provided high-quality, internally aligned optical components. However, they are inflexible and incapable of performing certain specialized measurements. Therefore, custom spectroscopic experiments were constructed when needed. These apparatus used free-standing optical elements (lenses, polarizers, etc.) assembled and aligned on an optical table. An optical-fibre-coupled tungsten-halogen bulb (Ocean Optics HL-2000) was used as white light source and a CCD-grating spectrometer (Ocean Optics USB2000 and HR4000) was used as a monochromator and detector. The details of these specialized measurement apparatus are discussed later in the relevant chapters.

3.3 Data reduction and fitting

There are several instances in the forthcoming research where models are numerically fit to observed data. As such, a brief review of the technique is warranted. The general proceedure consists of numerically minimizing the difference between the observed data ($\mathbf{y}$) and the model prediction ($\mathbf{Y}$). The data-model difference is calculated as the mean-squared-error (MSE)

$$MSE = \frac{1}{J}\sum_{i=1}^{J}(y_i - Y_i)^2, \tag{3.3}$$

where J is the number of data points. The minimization is performed by adjusting the model parameters, yielding the best-fit parameter set. When the model is linearly related to the parameters, the standard least-squares method can be used. However, more often in this research the model is nonlinear and a more general least-squares technique is required.

The Levenberg-Marquardt (LM) method [136, 137] is the standard nonlinear least-squares optimization algorithm [138]. The LM algorithm combines the least-squares (second-derivative) approach with a steepest descent (first-derivative) calculation. Two different implentations of the LM method were used, depending on the model complexity. The Gnuplot[1] graphing software contains a LM routine called via the *fit* command. This routine can accomodate simpler models based on algebraic, real-valued functions. For more complicated models, such as the characteristic matrix method (Sec. 2.4.2) which requires matrix computations and complex-valued functions, the *nlinfit* function in MATLAB® was used[2].

The uncertainties in the best-fit parameters are determined from the curvature (expressed by the Hessian matrix) of the MSE hypersurface [139]. The covariance matrix, providing estimates of the parameter uncertainties, is the inverse of the Hessian matrix [138]. Note that the uncertainties are not a goodness-of-fit value, nor do they indicate the accuracy of the model. They are simply an estimate of the numerical precision of the fit, i.e., how close the calculated best-fit parameters are to the *true* best-fit parameters.

[1] Version 4.4.0, available online at http://www.gnuplot.info/

[2] Release R2009a with the Statistics Toolbox.

3.4 Summary

This chapter has reviewed the main experimental methods and techniques used in performing the thesis research. The GLAD apparatus has been discussed and the general process flow has been presented. Attempts to reproduce and/or extend the results of this thesis should be mindful of this information. The structural and optical characterization tools used to gather data have been examined. The SEM measurement accuracy at high magnification is estimated to be better than 5 nm. Finally, the numerical optimization routines used later in the thesis have been reviewed. To avoid repetition of these details, the discussions of later chapters make reference to the relevant sections of this chapter.

Chapter 4

Controlling the Optical Properties of Nanostructured TiO_2 Films

4.1 Thin film optical properties

The optical properties of a thin film are determined by two parameters: the refractive index n and its thickness d. Together, these define the optical path length of the film $\Lambda = nd$. The refractive index n provides a fundamental characterization of light-matter interaction. Consequently, measuring n is an important experimental task in optical science. n is always measured indirectly by means of measuring an optical quantity (such as reflected or transmitted intensity) and calculating n from a chosen model. This model inevitably makes a series of assumptions and approximations. Therefore, the accuracy and precision of the measurement depends on how well the model corresponds to the actual system. As point out by Borgogno *et al.* [140], "No matter how accurate the measurements, the optical constants obtained are only as good as the model used for their derivation". This is nicely demonstrated by a large collaborative study conducted by Arndt *et al.* [141]. In this report, a set of nominally identical films (Sc_2O_3 and Rh) were distributed to twelve different research groups. These groups then measured n, each using a different method. For the Sc_2O_3 films, the variance of the measured indicies was 1.5% across all twelve groups. For the Rh films, the variance was much larger, being 13%. The increased variance found for the Rh films was attributed to the inaccuracy of the models used.

Accurately fabricating optical films using GLAD requires knowing n and

Table 4.1: A summary of reported optical characterizations of GLAD-fabricated structures.

Technique	Reference	Material(s)	Structure	α range ($^\circ$)
Ellipsometry	[58]	Ta_2O_5, TiO_2, ZrO_2	Tilted	0-70
	[143]	Si	Vertical	0-85
	[77]	MgF_2, SiO_2	Tilted	60-86
	[144]	ITO	Tilted	0-75
	[145]	ITO	Tilted	0-85
	[146]	ITO	Tilted, helical	0-80
	[147]	Alq_3	Tilted	65-87
	[148]	Co	Tilted, helical	85
	[149]	Ti	Tilted	85
Photometry	[23]	Ta_2O_5, WO_3	Tilted	0-75
	[76]	Cr, Al, Ti, W	Tilted	79-89
	[150]	SiO_2	Tilted	80
Swanepoel's method	[151]	As_2S_3	Tilted	0-80
	[152]	As_2S_3, As_2Se_3	Tilted	80
	[153]	ZnS	Tilted	0-85
	[154]	ZrO_2	Tilted	0-80
	[155]	TiO_2	Tilted	0-75
	[156]	$GeSe_2$	Tilted	0-80
	[157]	Nb_2O_5	Tilted	0-80

d. While *d* is nearly always measured while making structural observations via SEM, a variety of techniques have been used to study the optics of GLAD-fabricated columns of different materials and structures. Following Abelès [142], these optical characterization methods can be divided into two categories: photometric, where an optical intensity is measured, or polarimetric, where the polarization-state change is measured. The former amounts to a reflectance and/or transmittance measurement, while the latter is an ellipsometry measurement. The application of these techniques are summarized in Table 4.1.

Regardless of the technique, these refractive index measurements assume that the films are well-approximated as a continuous and homoge-

neous medium. This greatly simplifies the mathematical treatment of the system and has been shown to be a valid approximation so long as the column sizes remain small ($< \lambda/4$ [82]). Some authors also make the assumption that the films are isotropic. For instance, the Swanepoel method was derived from an isotropic model and it is commonly used to measure n of isotropic films. However, the optical properties of GLAD-fabricated films are inherently anisotropic and this must be taken into consideration when choosing a characterization approach. This is why generallized ellipsometry is so commonly used, since ellipsometry measures polarization-state changes and is therefore sensitive to sample anisotropy [158, 159].

For vertical columns, the structure studied in this work, the anisotropy is uniaxial. The two principal indices are oriented along the column axis (n_e) and in the substrate plane (n_o). The technique developed for this work is based on measuring the reflectance of *s*-polarized light. Because the electric field of *s*-polarized light is perpendicular to the plane of incidence, the field only couples to n_o and the film behaves isotropically. This means that 2x2 matrix calculations can be used to model the film, a simpler approach than the 4x4 matrix framework required for ellipsometric measurements [160, 161]. Thesis research presented in this chapter has been published in *Physica Status Solidi A* [162].

4.2 Obtaining calibration data

As discussed in Sec. 4.1, the optical properties are determined by n and d. Accurately fabricating optical films at different α therefore requires knowing how n and d depend on α. To experimentally determine these calibration functions, $n(\alpha)$ and $d(\alpha)$, a series of vertical-column TiO_2 films were deposited over a wide α range.[1] The film parameters are summarized in Table 4.2. This series can be loosely divided into two sets, thin (< 250nm) and thick (> 500nm), depending on the final QCM thickness d'. The ratio of film thickness d to d' defines the deposition ratio D and permits accurate layer deposition to a target thickness. Note that while the primary objectives of this calibration film set are to obtain estimates of $D(\alpha)$ and $n(\alpha)$, it will also be possible to examine α-dependent structural trends from

[1] This film set was prepared in collaboration with John J. Steele.

Table 4.2: The deposition angle α and the QCM thickness parameters for the film set fabricated in this study. The films can be divided into two sets, thin ($<$ 250nm) and thick ($>$ 500nm), depending on the final QCM thickness.

Film	$\alpha(^\circ)$	QCM (nm)	Film	$\alpha(^\circ)$	QCM (nm)
m=1	40	250	10	65	575
2	60	150	11	70	620
3	70	200	12	75	660
4	75	200	13	78	680
5	80	125	14	80	633
6	86	150	15	81	500
7	40	515	16	83	700
8	50	520	17	83	780
9	60	500	18	85	725

SEM observations. Because the experimental parameter space systematically covers only α, there will not be enough points to make strong conclusions about thickness-dependent trends. However, preliminary observations can be made that may guide future experiments.

4.2.1 Fabrication details

These films were deposited by e-beam evaporation of TiO_2 following the procedure described in Sec. 3.1.4. The substrate was held at the desired α position and φ was rotated through 360° every 10 nm of growth (at the QCM). The films were only deposited onto p-doped Si wafers. This substrate choice was based on three reasons. One, samples prepared on Si wafers are easy to cleave for SEM imaging. Two, there will be no backside reflection to complicate the analysis since Si absorbs light in the spectral region of interest. Three, the large refractive index of Si provides significant index contrast with respect to the TiO_2 film. This leads to greater interfacial reflection and provides larger interference fringes. This will aid in the numerical determination of n from the thin film model.

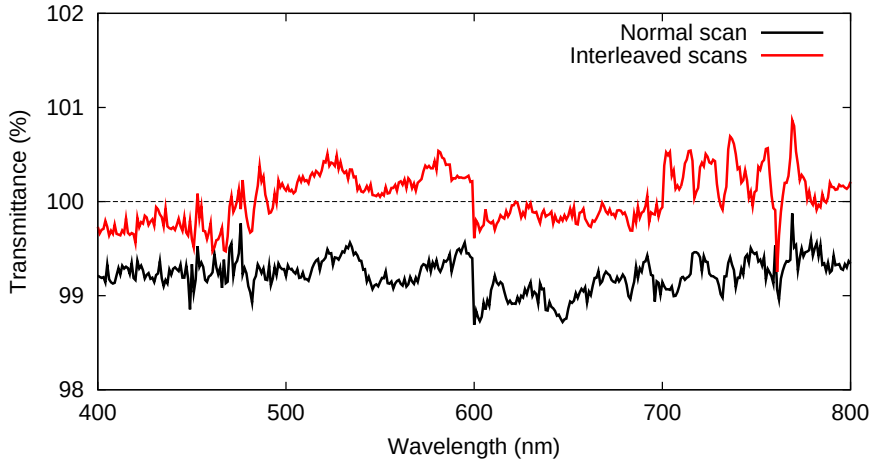

Figure 4.1: By breaking up a longer scan (Normal) into shorter sub-scans that are recombined after the measurement (Interleaved), the systematic error due to bulb drift can be minimized.

4.2.2 Measurement details

Every sample was examined by SEM to measure the film thickness as well as to observe the film columnar structure. A portion of each Si wafer was cleaved in two, and the exposed edge was imaged. Top-down images of the same cleaved samples were also obtained.

The spectral reflectance of *s*-polarized light incident at 30° from the substrate normal was measured for wavelengths between 400 nm and 700 nm, in 1 nm increments. This measurement was performed using the ellipsometer (Sec. 3.2.2), operating in intensity mode. In this mode, the ellipsometer first measures the transmittance with no sample (baseline 100% signal) and then measures the signal reflected from the sample. The ratio between the two is then calculated to obtain the relative spectral reflectance. Because of the time delay between the reference and sample scans, any bulb drift will introduce a systematic error in the measurement. As discussed by Tikhonravov *et al.*, determining *n* from photometric intensity measurements is particularly sensitive to systematic errors [163]. Therefore, the accuracy of the apparatus was tested by measuring the free-space transmittance (transmittance with no sample) for a series of different scan lengths. It was found that breaking-up a longer scan into multiple shorter scans can eliminate bulb drift error,

as shown in Fig. 4.1. Here, rather than performing a single scan from 400 nm to 800 nm, three sub-scans were performed, covering 400-499 nm, 500-699 nm, and 700-800 nm, respectively. These scans are then recombined (interleaved) post-measurement. The mean transmittance values (with one standard deviation uncertainties) of the two scans were T_{normal} = 99.4±0.5% and $T_{\text{interleaved}}$ = 100.0±0.6%.

4.2.3 Calculation details

The refractive index was obtained by numerically minimizing the squared difference between the modeled and measured reflectance data. The model reflectance was calculated using the standard matrix technique (Sec. 2.4.2). This minimization was carried out using the LM algorithm (Sec. 3.3). To account for the wavelength-dispersion of the material, a two-term Cauchy model was used

$$n(\lambda) = A + B/\lambda^2. \tag{4.1}$$

The coefficients A and B were the only fitting parameters and d was fixed to the SEM measured value. The indices were constrained to be real meaning that the films do not scatter or absorb.

4.2.4 Substrate characterization

Thin film optical measurements require knowing the substrate optical constants as inputs to the optical modeling. The substrate properties were therefore calculated by measuring the reflectance spectra (for both *s*- and *p*-polarized light) at incident angles of 30°, 45°, and 60°. The substrate dielectric function ε was parameterized by a two-term oscillator function

$$\varepsilon(\mathcal{E}) = \varepsilon_\infty + \frac{I_1}{\mathcal{E}_1^2 - \mathcal{E}^2 - i\gamma_1\mathcal{E}} + \frac{I_2}{\mathcal{E}_2^2 - \mathcal{E}^2 - i\gamma_2\mathcal{E}} \tag{4.2}$$

where $\mathcal{E}$ is the photon energy, ε_∞ is the long-wavelength dielectric response, and I_i, E_i, and γ_i are respectively the strength, energy, and damping of the i^{th} oscillator. The relationship between (complex) index and dielectric constant is given by $n + ik = \sqrt{\varepsilon}$, where k is the extinction coefficient. The model reflectance was calculated using Fresnel's equations. These seven parameters were numerically fit to the entire experimental data set simultaneously

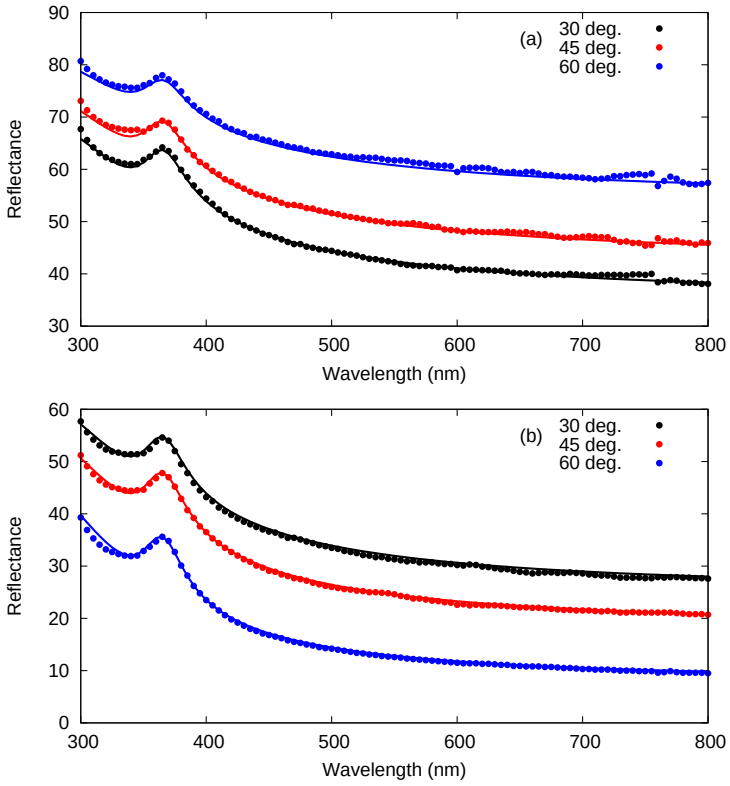

Figure 4.2: Measured (data points) and fitted (solid lines) reflectances from a bare p-doped Si substrate. The spectra in (a) and (b) show the *s*- and *p*-polarized reflectances.

Table 4.3: Fitted parameters for the p-doped Si dielectric function. The parameters correspond to Eq. 4.2.

ε_0	I_1 (eV^2)	$\mathcal{E}_1$ (eV)	γ_1 (eV)	I_2 (eV^2)	$\mathcal{E}_2$ (eV)	γ_2 (eV)
1.53	20.17	3.36	0.29	133.09	3.94	1.48

using the LM algorithm. The results are shown in Fig. 4.2. The calculated optical constants are presented in Fig. 4.3 alongside reference values for undoped Si [164]. Good agreement is observed between the measured and reference *n*-values. The p-doped Si has a higher extinction coefficient (*k*) than undoped Si due to increased absorption by free charge carriers. Another small source of deviations is the native oxide layer present on the Si wafer which is unaccounted for in the analysis. Future experiments requiring a more accurate substrate representation could use a Drude-like term to model free-carrier effects and incorporate a thin SiO_2 layer to represent the native oxide. However for the present work, this model is sufficiently accurate as evident by the good agreement in Fig. 4.2.

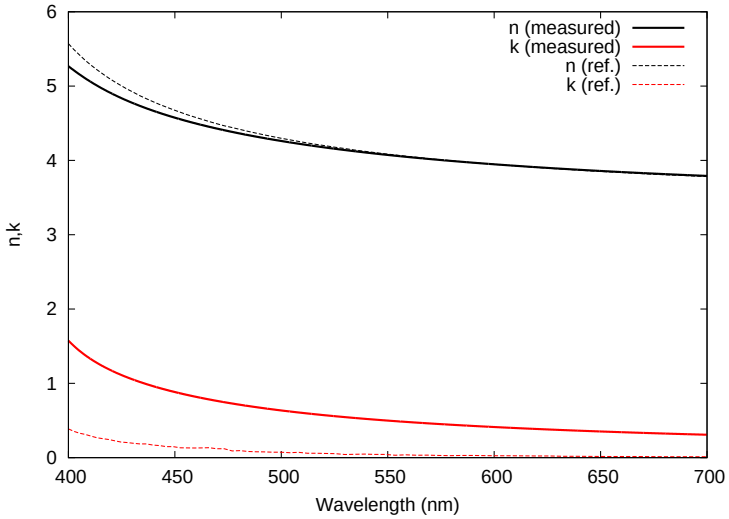

Figure 4.3: Optical constants, n (black) and k (red), of p-doped Si substrates calculated from reflectance measurements. Also shown (dashed lines) for comparison are reference optical constants of undoped Si.

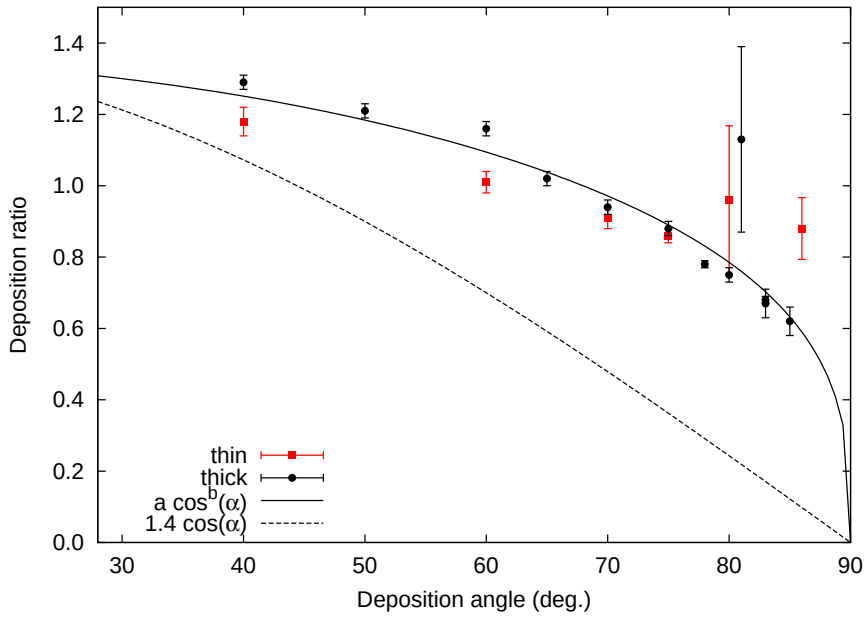

Figure 4.4: The measured deposition ratios for the TiO_2 vertical post films fabricated in this study. This data is available in tablular form in Appendix A (Table A.1). A cosine-power law was fit to the data (solid line). The dashed line is $1.4\cos(\alpha)$, which corresponds to the α-dependent substrate geometric cross-section. The measured deposition ratios lie above this line, indicating a decrease in film density with increasing α.

4.3 Structural characterization results

4.3.1 Measured deposition ratios

The deposited film thicknesses were measured from the cross-sectional SEM images, like those shown in Fig. 4.6. Measurement uncertainty arises from subjective estimation of the film / substrate and film / air interfaces and the SEM accuracy. In particular, determining the film / air interface is more difficult because of surface roughness. However, it is straightforward to determine an upper and lower boundary for both interfaces. Adding these intervals in quadrature then provides an estimate of the total measurement uncertainty. Dividing the measured thickness d by the QCM measured thickness for that deposition d' calculates the deposition ratio D. These results are shown in Fig. 4.4.

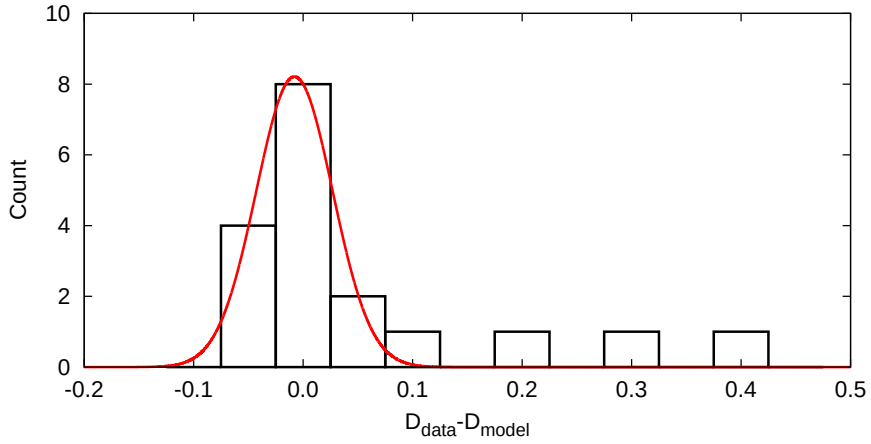

Figure 4.5: Frequency histogram of the difference between the deposition ratio data (see Fig. 4.4) and the phenomenological model $D_{\text{model}}(\alpha) = a\cos^b(\alpha)$. A normal distribution was fit to the residuals and is shown as a red curve.

The deposition ratio clearly shows a non-linear, monotonically decreasing relationship with α. Such behaviour is expected due to the decreasing geometric substrate cross-section. Less vapour flux therefore deposits on the substrate and the resulting film will be thinner, decreasing D. The cross-section follows $\cos(\alpha)$, shown as a dashed line on Fig. 4.4. The deposition ratio does not however follow this geometric effect, but rather lies above this line. This is because the film density decreases with α, as described in Sec. 2.2.3, increasing the deposited film thickness and increasing D.

As α approaches 90°, the deposited film thickness should vanish since no vapour flux will reach the substrate. It can be seen that data points are not approaching this limit. However, the data set is limited to films deposited at $\alpha < 86°$ and does not examine extremely glancing deposition angles. Even so, in seeking a phenomenological expression with which to fit and describe the data, this limit should still be satisfied. A cosine-power-law meets this requirement and the data was fit with the equation $D_{\text{model}}(\alpha) = a\cos^b(\alpha)$. The resulting fit is plotted as a solid line on Fig. 4.4. The fitted parameters are $a = 1.36 \pm 0.08$ and $b = 0.31 \pm 0.04$. This equation provides a good visual fit of the data points. Fig. 4.5 shows the residual distribution of the data and model. A Gaussian distribution (Eq. 3.2, red curve) was

also fit to the residuals, yielding best-fit parameters $\mu = (-8 \pm 4) \times 10^{-3}$ and $\sigma = 0.035 \pm 0.003$. The majority of the residuals cluster around zero (15 of 18 points lie within 3σ of the mean), an indication that the model provides a satisfactory description the data. The three points falling outside 3σ correspond to the data with the largest uncertainty. It is likely that the measurement uncertainty is responsible for the large residual. Therefore, the standard deviation provides an estimate of random variation of the deposition process. Further experiments would be required to check if D possess a thickness dependence. The present data does indicate that this potential dependence is small when compared to the effect of α.

4.3.2 Structural observations: film cross-section

Figs. 4.6a-f show cross-sectional SEM images of six of the films described in Table 4.2 (a-f correspond to films m=1, 3, 6, 7, 9, and 11). The vertically oriented columnar structure of the films can be observed in these images. Furthermore, the film structure changes significantly with α. At $\alpha = 40°$, the film appears very dense with little discernable void structure. As α is increased to 60°, the columnar structure is more apparent, although still densely packed. At 75°, the inter-column void is observable and larger columns are present. Column broadening, where the column diameter increases with film thickness, and column extinction is apparent at this α, a clear indication of competitive growth as was described in Sec. 2.2.4. At 78°, the inter-column voids are larger indicating the decrease in film density due to the increased shadow length. At $\alpha = 81°$ and 83°, the trends continue: larger columns, increasing amounts of inter-column void, more extinct columns and increased column broadening (greater degree of competitive growth).

4.3.3 Structural observations: top-down

Examining the film surface in top-down SEM images leads to similar observations as were found in Sec. 4.3.2. For top-down images, it is important to compare films of similar thickness as column broadening and extinction effects change the structure as film growth progresses. Figs. 4.7a-d shows top-down SEM images of films deposited at 60°, 75°, 85°, and 86°. The

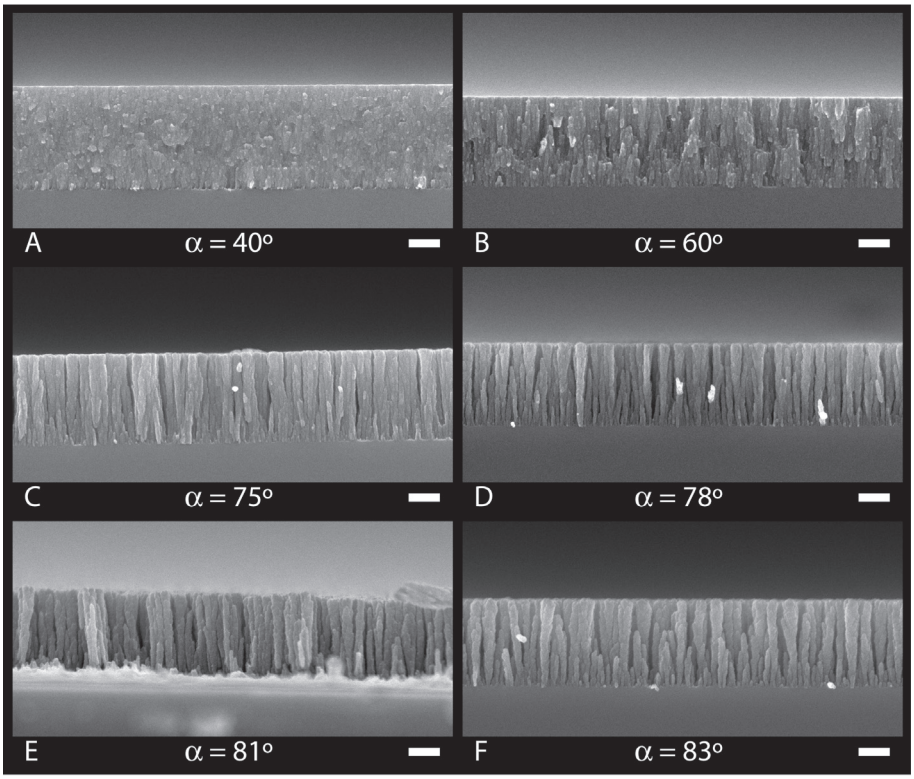

Figure 4.6: Cross-sectional SEM images of TiO_2 vertical post nanostructures fabricated at α = 40° (A), 60° (B), 75° (C), 78° (D), 81° (E), and 83° (F). The scale bar on each image indictates 200 nm.

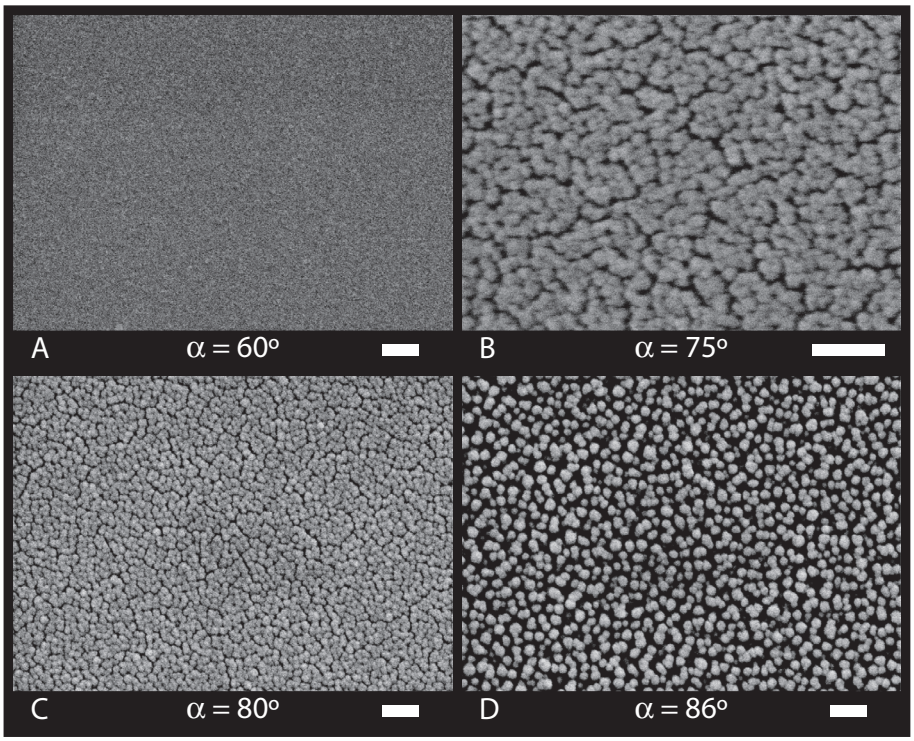

Figure 4.7: Top-down SEM images of TiO_2 vertical post nanostructures fabricated at α = 60° (A), 75° (B), 85° (C), and 86° (D). The scale bar on each image indictates 200 nm.

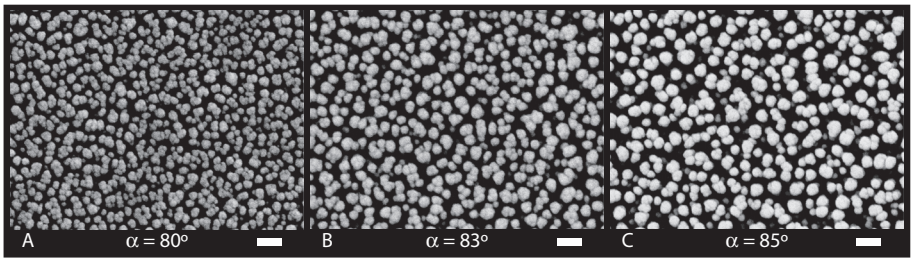

Figure 4.8: Top-down SEM images of TiO_2 vertical post nanostructures fabricated at α = 80° (A), 83° (B), and 85° (C). The scale bar on each image indictates 200 nm.

thicknesses of these films are all comparable, being 152 ±5 nm, 171 ± 4 nm, 120 ± 26 nm, and 132 ± 13 nm, respectively.

At such small thicknesses, columnar structures are very small and high magnification (M) SEM images are required to observed any film features. At 60° (M=50,000), the top-down image is essentially noise-dominated and featureless. At 75° (M=100,000), intercolumn void regions can be observed. The columns are not separated at this α and are instead found bundled together. By 80° (M=50,000), the columns are still bundled together although the separation has increased. Finally at 86° (M=50,000), the columns are distinctly separated. Although many of the columns are still touching they would be more appropriately described as dimer or trimer columnar units than as bundled columns. Separated columnar structures are more apparent in thicker films. Figs. 4.8a-c show top-down SEM images of films deposited at α = 80°, 83°, and 85°. The corresponding film thicknesses are 475 ± 13 nm, 471 ± 25 nm, and 451 ± 30 nm, respectively. As α is increased, the columns becomes larger and the film density decreases.

4.4 Optical characterization results

4.4.1 Measured and modeled reflectance spectra

For space reasons, only spectra for eight of the eighteen films are presented in this section. These spectra are shown in Fig. 4.9. These were selected to provide a representative cross-section of the complete result set. All spectra are provided in Appendix A for closer inspection (Fig. A.1). The first four

spectra are taken from the 'thin'-set and are deposited at low-α, (a) and (b), and high-α, (c) and (d). The fifth through eighth spectra are taken from the 'thick'-set and are deposited at low-α, (e) and (f), and high-α, (g) and (h). In reference to Table 4.2, the subfigures correspond to (a) m=1, (b) m=2, (c) m=5, (d) m=6, (e) m=7, (f) m=9, (g) m=14, and (h) m=17. In all the figures, the circles correspond to the measured reflectance (R_{data}) and the blue curve is the model reflectance after fitting (R_{slab}).

As can be seen from Fig. 4.9, the homogeneous slab model provides a satisfactory approximation to the measured data. Qualitatively, the model nicely reproduces the measured thin film interference fringes. However, there is a varying degree of agreement over the entire data set. Examining the quantitative agreement, given by the *MSE* (Eq. 3.3), facilitates the fit evaluation. The *MSE* between the measured and simulated spectra varies as shown in Fig. 4.10. Across the entire data set the best and worst data-model agreements are found in Fig. 4.9h (*MSE*=0.73) and Fig. 4.9c (*MSE*=61.2). No α-dependent trend can be discerned in the *MSE* data, nor can a significant difference between the thin and thick *MSE* values be observed. However, even in the previously mentioned worst case the root-mean-squared error is 7.8%.

4.4.2 Measured dispersion parameters

Fig. 4.11 shows the parameters *A* and *B* obtained from the model-fitting. The α dependence of *A* and *B* is clear: both parameters monotonically decrease as α increases. This behaviour is expected because the index is determined by the density and depositing at higher α produces a less dense film. The estimated *B*-coefficient uncertainties are notably larger for the thin film set (red open squares) than for the thick film set (black open circles). This is likely because the short optical path length of the thinner films creates fewer interference fringes over the measured wavelength range (compare Figs. 4.9a-d with Figs. 4.9e-h). Small changes in *B* therefore have less impact on the *MSE* value, increasing the uncertainty of the numerical optimization.

From the *A* and *B* results, the refractive index at λ = 600 nm was calculated. This result is shown in Fig. 4.12 and demontrates one of the primary accomplishments of this chapter. By varying the deposition angle α the relative proportions of TiO_2 and air can be varied, which ultimately allows

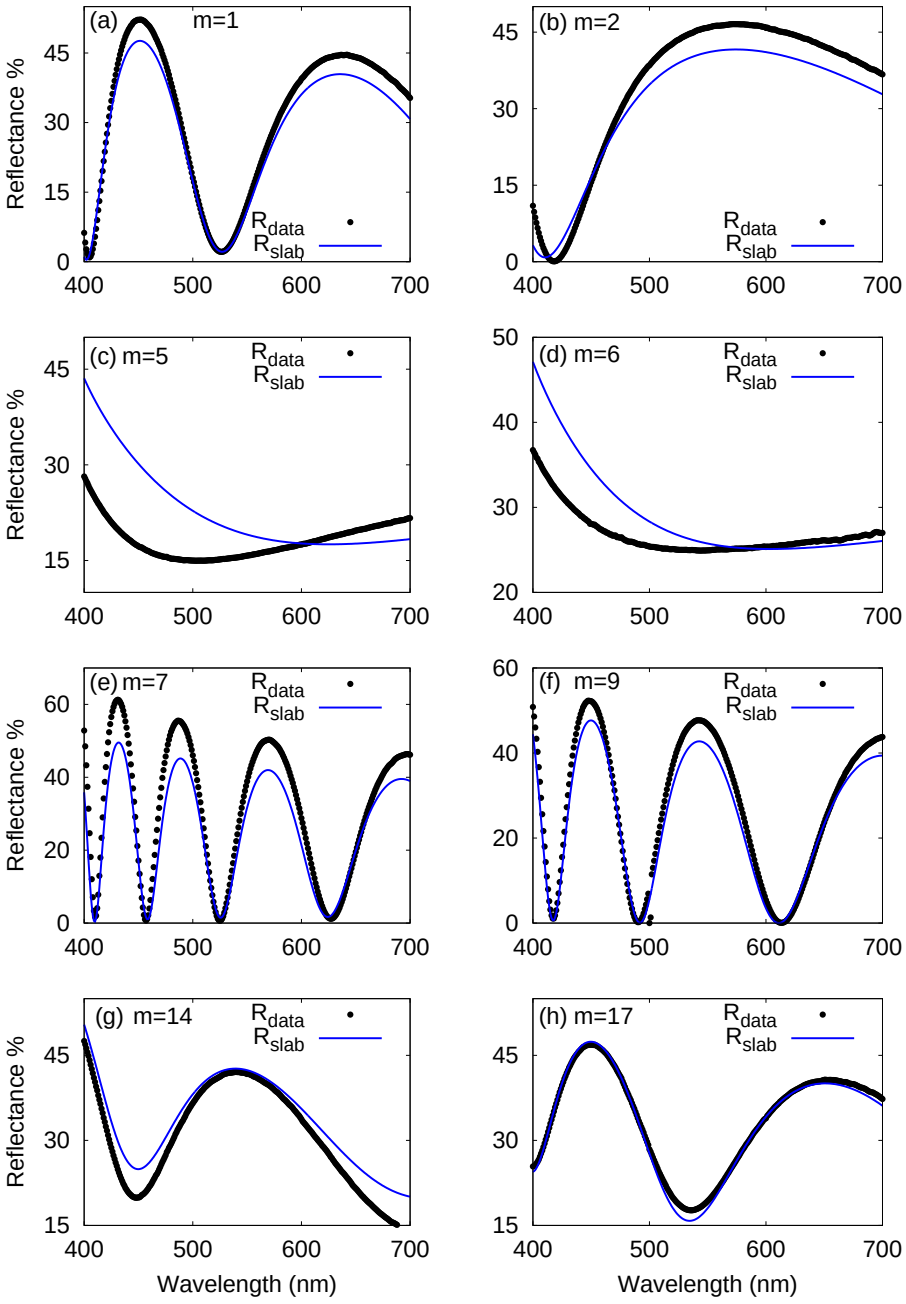

Figure 4.9: Measured (circles) and fitted-model (blue line) reflectance spectra for eight of the films fabricated in this study. In reference to Table 4.2, the subfigures correspond to (a) m=1, (b) m=2, (c) m=5, (d) m=6, (e) m=7, (f) m=9, (g) m=14, and (h) m=17.

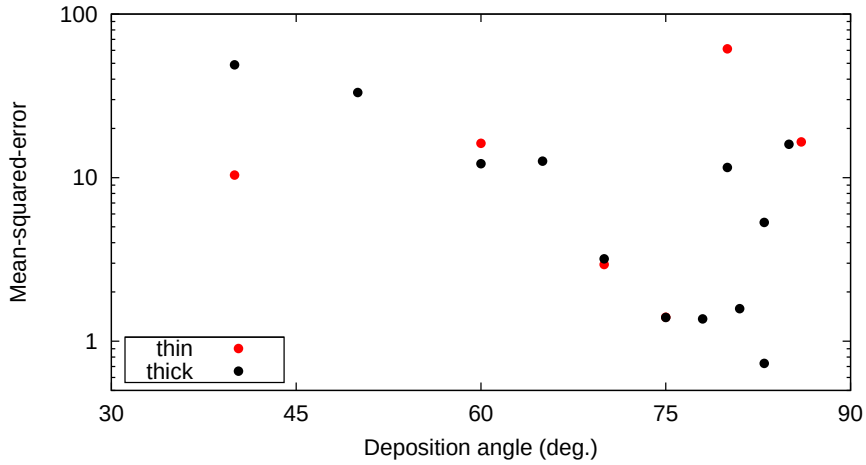

Figure 4.10: The mean-squared-error (*MSE*) between the measured and simulated reflectance spectra, for thin (red points) and thick (red points) film sets. A lower MSE value indicates better data-model agreement.

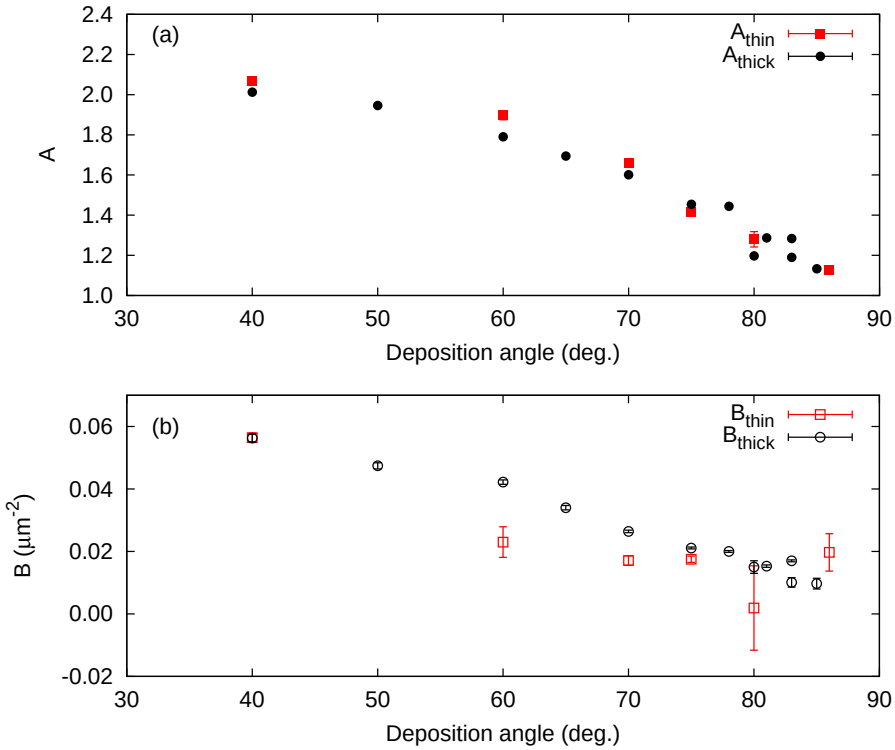

Figure 4.11: The fitted parameters (a) *A* and (b) *B* corresponding to the Cauchy dispersion equation (Eq. 4.1).

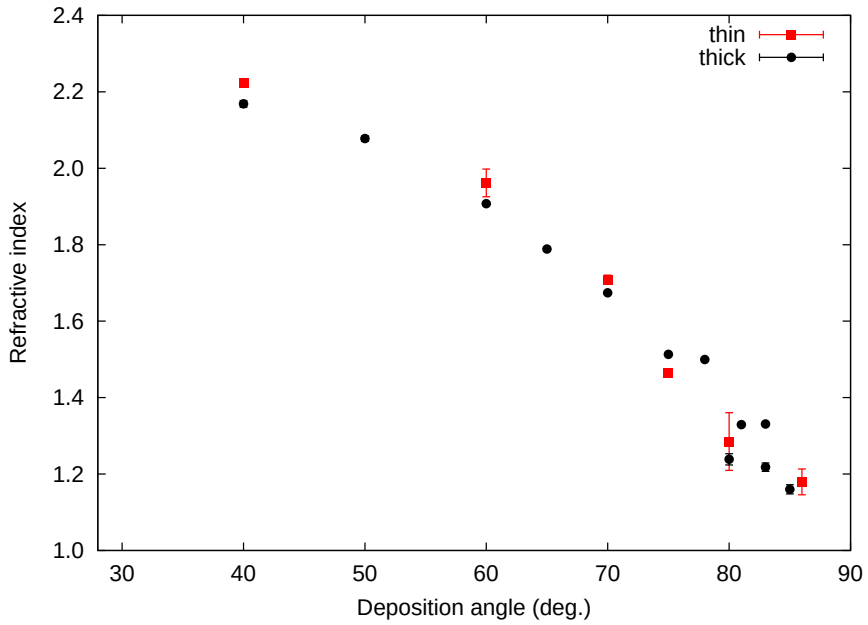

Figure 4.12: The refractive index n at λ = 600 nm as calculated from the fitted Cauchy dispersion coefficients (Fig. 4.11).

the refractive index of the deposited medium to be controlled. This also provides the second portion of the calibration data required to accurately deposit a layer of a given optical path length *nd*.

4.5 Improved optical modeling: index gradients

As stated in Sec. 4.1, the accuracy of the index measurement depends on the model accuracy. While the agreement between the experimental data and the homogeneous slab model is acceptable, certain observations suggest how the model may be improved. Note that even though the thin film interference fringes are reasonably well matched, in several cases the model is more successful in reproducing the fringe spectral period than the reflectance amplitude variation (see Figs. 4.9a, e, and f). This occurs when a homogeneous slab model is applied to a layer with a refractive index thickness gradient, i.e. $n = n(z)$ [140, 165]. Therefore, utilizing a graded-index (GRIN) model should provide a more complete and accurate description of the GLAD-fabricated nanostructured TiO_2 in this study.

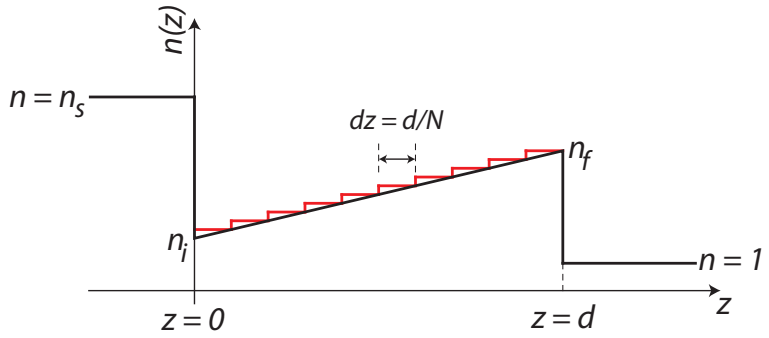

Figure 4.13: A thin film with a linear refractive index gradient parameterized by Eq. 4.3. Optical simulations require digitizing the gradient into thin homogeneous layers, as represented by the red line.

4.5.1 A simple GRIN model

The model developed here is based on a linear index gradient [140]. Although this is a simplistic approach it is a good starting point as only one additional fitting parameter is introduced. In this model, $n(z)$ is given by

$$n(z) = n_i + (n_f - n_i)\frac{z}{d}, \tag{4.3}$$

where n_i and n_f are the film index at the substrate and air interfaces, respectively. As before, d is the film thickness. It is also useful to add the definition

$$\Delta n = \frac{n_f - n_i}{n_i}, \tag{4.4}$$

where Δn measures the relative index inhomogeneity through the film.

This linear $n(z)$ model is depicted in Fig. 4.13. The optical reflectance of this $n(z)$ profile cannot be calculated exactly. Rather, the linear index profile must be discretized into N homogeneous sublayers. In the $d/N \rightarrow 0$ limit, this approach is exact [1]. For these modeling calculations, N=50 was selected. The numerical fitting now minimizes the data-model MSE via the parameters A, B, and Δn (Δn is assumed to be wavelength independent.)

4.5.2 Index gradient: modeling results

Eight of the eighteen results are presented in Fig. 4.14. All spectra are provided in Appendix A for closer inspection (Fig. A.1). These spectra corre-

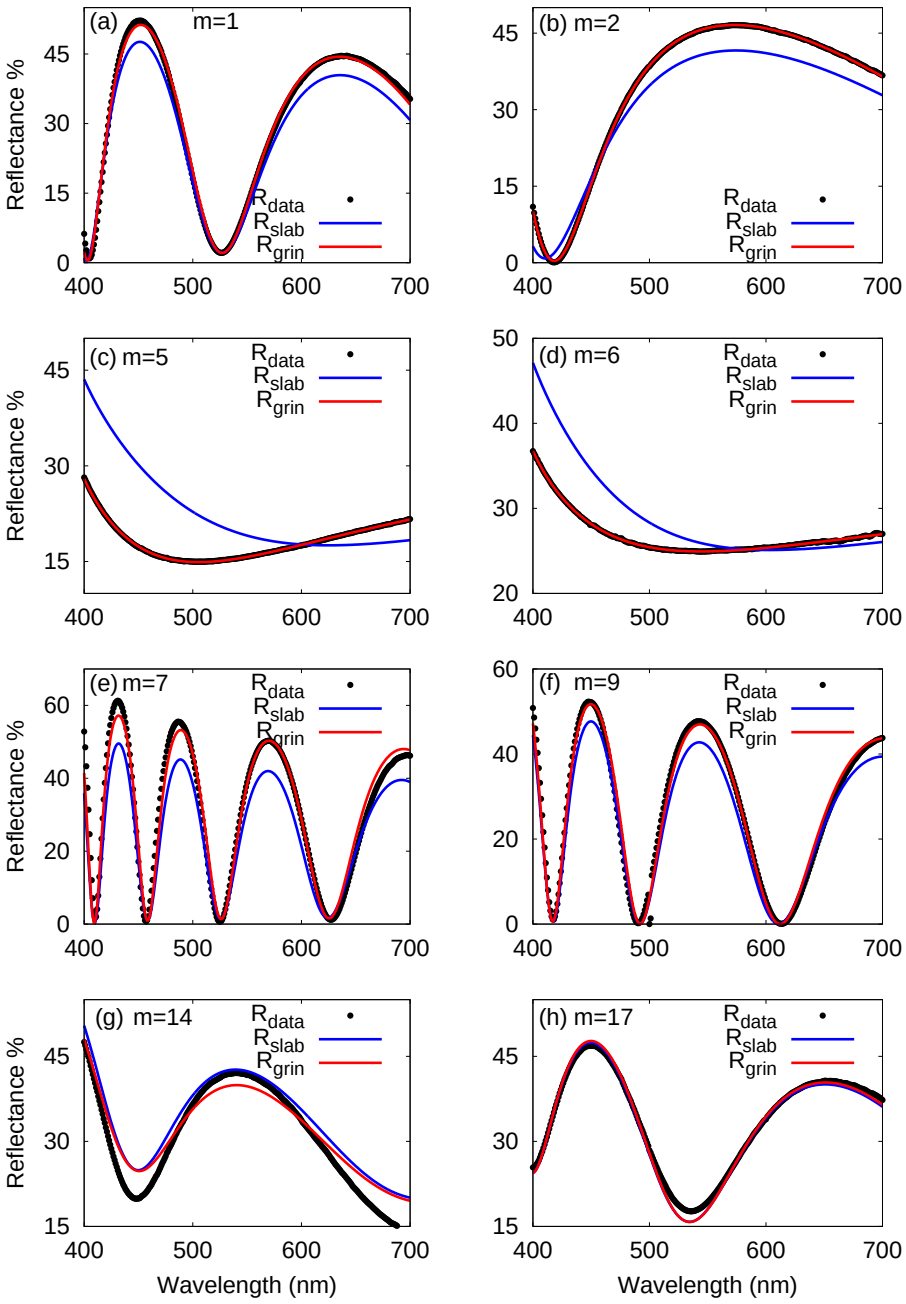

Figure 4.14: The three reflectance spectra shown are the measured data (circles), fitted homogenous-slab model (blue line), and fitted linear index-gradient model (red line). In reference to Table 4.2, the subfigures correspond to (a) m=1, (b) m=2, (c) m=5, (d) m=6, (e) m=7, (f) m=9, (g) m=14, and (h) m=17.

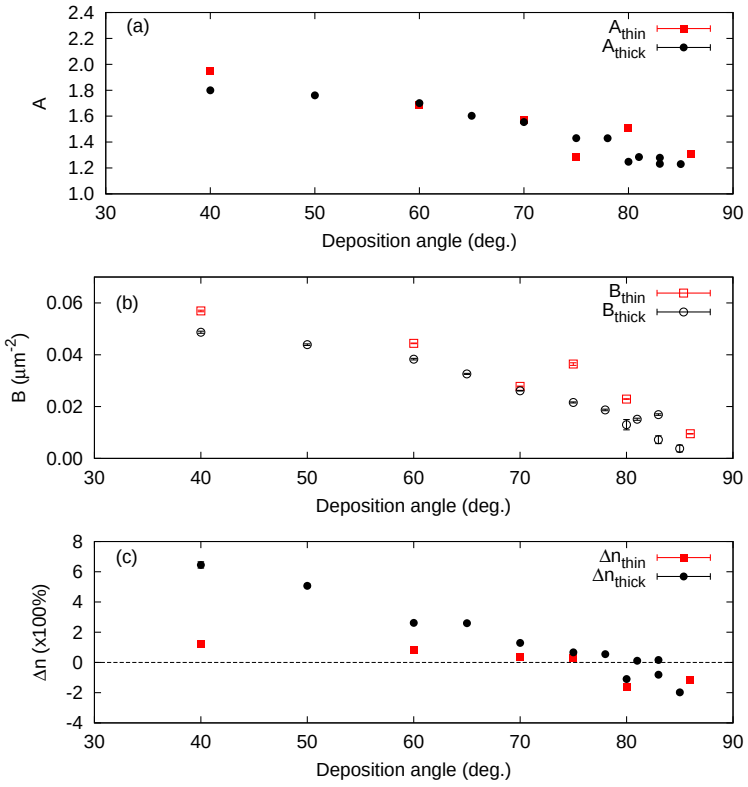

Figure 4.15: The fitted parameters for the linearly graded index model. (a) and (b) respectively correspond to the dispersion coefficients *A* and *B*. (c) shows the relative index inhomogeneity through the film Δn.

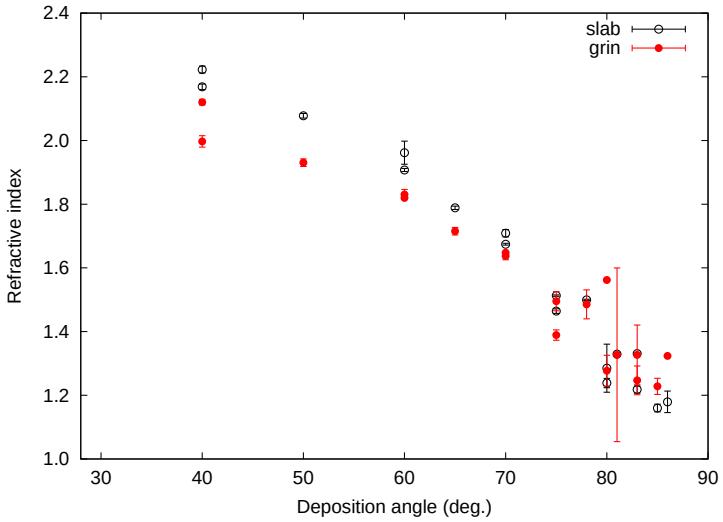

Figure 4.16: The refractive indices calculated from the slab-model (open circles) and the mid-thickness ($0.5(n_i + n_f)$) refractive indices calculated from the gradient-index model. Both indices are at λ = 600 nm. For clarity of presentation, the thin and thick film sets are combined.

spond to the same films as shown Fig. 4.9. The three reflectance spectra plotted in each figure are the measured data (black circles), the homogeneous-slab model result (blue line), and the GRIN model result (red line). As can be observed from these results, the agreement between theory and experiment is significantly improved by using the GRIN model. The new model reproduces both the fringe period and amplitude more accurately, avoiding this deficiency of the slab model result.

The A, B, and Δn parameters obtained from the fitted model are shown in Fig. 4.15. As with the slab-model A and B parameters (Fig. 4.11), the dispersion coefficients decrease as α increases. The refractive index change in the film, as quantified by Δn, is shown in Fig. 4.15c. At low-α, the refractive index increases with film thickness ($\Delta n > 0$). The magnitude of this increase is also α-dependent, with larger, positive index gradients occuring at lower α. With increasing α, the index gradient becomes smaller. At approximately $\alpha = 80^\circ$, the gradient is near-zero. For $\alpha > 80^\circ$, the gradient returns although it is now negative, indicating that the index decreases with film thickness.

Fig. 4.16 compares the indices (at λ = 600 nm) found for both the slab and GRIN models. For the GRIN model, this index value is taken at the film

mid-thickness point, i.e., $n_{\text{mid}} = (n_i + n_f)/2$. Little difference between the two data sets is observed around α = 80°, as would be expected given that the gradient is nearly zero in this region. At low-α, the GRIN model index is smaller than the slab model index because of the positive index gradient. At high-α, the GRIN model index is slightly larger than the slab model index because of the small negative gradient.

4.5.3 Index gradients: physical mechanisms

The success of the GRIN model provides compelling evidence that n varies with thickness in the prepared TiO_2 nanostructured layers. Obviously, this implies some physical aspect of the layer is changing during deposition. The observed column broadening discussed in Sec. 4.3.2, could be responsible for index gradient. However, this is unlikely given that column broadening is only observed at higher α and the largest index gradients occur at low α. Previous X-ray diffraction studies of similarly prepared TiO_2 layers have shown that these films are amorphous and that crystal phase changes do not occur without prolonged annealing at 400°C [61,131,134]. This rules out a crystal-phase change that would affect n. A more reasonable suggestion is that the film density ρ is changing. An increase in ρ (and consequently an increase in n) is associated with the increased packing-density of micro-columns [166] and/or an increase in the atomic density [167].

It is well-established that TiO_2 film density is sensitive to deposition parameters, most notably substrate temperature, oxygen partial pressure, and starting material [126, 127, 129, 130, 167]. While the starting material and oxygen partial pressure are controlled, the substrate temperature is not. The refractive index of deposited TiO_2 films increases with substrate temperature. Thermal radiation, from the molten TiO_2 source (melting point: 1843°C [168]), and enthalpy contributions, from vapour condensation and TiO_2 formation, heat the substrate during deposition. Correspondingly, this creates a positive index gradient in the deposited film. Because radiative heating depends on the substrate geometric cross-section and the enthalpy contributions depend on deposition rate (also dependent on the geometric cross-section), the substrate experiences greater heating at lower α. Therefore, more significant index gradients are seen at lower α.

Because the substrate cannot cool during deposition, substrate tempera-

ture change is not a valid explanation for the small, negative index gradients seen at high α. It is unclear what is driving this density change although several possible mechanisms can be suggested. One possible mechanism is that competitive growth decreases the column packing density as the film develops. Another possibility is that increased surface roughness is reducing the air-film interfacial reflection [169], mimicing the effect of a negative index gradient. Also, columnar structures deposited at high α are significantly larger are correspondingly have increased scattering cross-sections. These large structures also violate the quasi-static limit of basic effective medium theories. Further experiments, more accurate characterization, and optical models incorporating these effects are required to better understand the optical properties structures deposited at large α.

4.6 Summary and Conclusions

These results further demonstrate how GLAD can be used to control the structure and optical properties of columnar films in a simple bottom-up nanofabrication process. The ordinary index of vertically oriented TiO_2 columns has been measured using reflectance measurements and two modeling approaches. The first approach, a traditional homogeneous-slab model, while simple, is a good first-order approximation to the actual nanostructured films. The second approach is a refinement of the first, describing the films as having a thickness-dependent refractive index. The second model provides a superior agreement to the experimental data and hence, provides a more complete picture of the optical characteristics of these nanostructured films. Calibration data such as obtained in this chapter is necessary for the design of more complex optical coatings, as described in the following chapters.

Chapter 5

GLAD-fabricated Optical Multilayers

5.1 Introduction

Thin films are commonly used to change the surface properties in an optical system and improve its performance. While single layers are often used, for example to fabricate simple antireflection coatings [170], advanced surface engineering often requires depositing multiple layers [95]. Therefore there is an important technological impetus to extend the results of the previous chapter to the fabrication of more complicated layer assemblies. This extension is straightforward: α is dynamically varied during deposition, creating density and index changes in the deposited film. Because n varies continuously with α, there is great design flexibilty using this process.

The first report of fabricating optical multilayers in this manner is by Robbie *et al.* [29]. In this work, α was varied sinusoidally between 51° and 81° and the substrate was quickly rotated during the deposition of MgF_2. This created a vertically oriented columns with a continuous, periodic density variation leading to the sinusoidal index profile of a rugate interference filter [96]. Using this method but without substrate rotation McPhun *et al.* generated a birefringent rugate filter out of ZrO_2, combining column density variation with tilted column form birefringence [171]. Several papers published by the Robbie group at Queen's University, Canada extended the rugate filter work, this time using Si. Calibration refinements improved the technique accuracy [143], deposition and optical modeling were used to bet-

ter understand the filter properties [172], and post-deposition annealing was used to oxidize the filters for operation in the visible wavelength [173]. This GLAD-approach was also used to realize discrete index changes and fabricate a Bragg stack multilayer [174]. Aside from interference filters, Kennedy and Brett employed the α-variation technique to generate Gaussian index profiles in SiO_2 [30]. These tapered columnar structures act as antireflection coatings by providing index-matching between the air and glass substrates.

The research presented in this chapter seeks to develop GLAD multilayer structures in TiO_2 based on the previous chapter's results. Given the prior demonstrations of rugate structures in the literature, realizing this structure in TiO_2 and demonstrating device tunability is an obvious starting point. From there, this chapter examines the less-studied periodic Bragg multilayer. Because the Bragg structure is simpler than the rugate structure, it is more amenable to simulation and numerical data fitting. It therefore serves as a better test case for GLAD optical engineering. Thesis research presented in this chapter has been published in *Journal of Physics D* [175].

5.2 Gradient-index multilayer structures

5.2.1 Substrate motion algorithm

Among the primary results of chapter 4 is the experimentally measured relationships $n(\alpha)$ and $D(\alpha)$. From these two quantities, layers of a given n can be deposited with a target thickness d. To realize the sinusoidal rugate index profile, Eq. 2.27 is discretized into N-sublayers with index and thickness (n_j, d_j). Depositing the j^{th}-layer then requires holding at α_j, such that $n(\alpha_j) = n_j$, and depositing a QCM-measured thickness d'_j, such that $d'_j = D(\alpha_j)d_j$. The required α_j was estimated by fitting second-order polynomials $f(n)$ and $g(D)$ to the inverted data sets. Sequentially depositing sublayers $j = 1$ to $j = N$ constructs the rugate multilayer. In the limit $N \to \infty$, this reproduces the continuous index variation of the rugate profile. However, in practice d_j was never set smaller than 10 nm, allowing sufficient time for accurate motor movement. The substrate was rotated continuously during deposition, completing one revolution every 10 nm of deposition at the QCM. This ensures that vertically oriented columnar structures are produced with no optical birefringence at normal incidence.

Table 5.1: Gradient-index rugate structures fabricated in this study

Film	$\alpha_{\min}$ (°)	$\alpha_{\max}$ (°)	λ_0 (nm)
A	30	80	450
B	30	80	530
C	30	80	600
D	30	80	750
E	45	65	530
F	37.5	72.5	530

5.2.2 Rugate structure film set

A series of sixteen-period TiO_2 rugate structures were fabricated. Multilayers were deposited onto B270 glass, for optical characterizations, and p-doped (100) Si substrates, for structural characterizations. The depositions were performed in an e-beam evaporation system specifically modified for GLAD use following the procedure described in Sec. 3.1.4.

The main parameters determining the optical properties of a rugate filter are the peak-to-peak index variation n_p, the average index n_a, and the physical period P. The first two parameters, n_p and n_a, are determined by α. During deposition, α is varied between $\alpha_{\min}$ and $\alpha_{\max}$. P is determined by the thickness deposited during one α cycle. However, P is rarely designed for, but is instead calculated to produce a band gap at a target wavelength λ_0, where $\lambda_0 = 2n_aP$ (Eq. 2.28). Six films were fabricated to examine the effects of these parameters. The films and their corresponding deposition parameters are summarized in Table 5.1. The first four (films A-D) have the same α variation, ($\alpha_{\min}$, $\alpha_{\max}$)=(30°, 80°), but different λ_0. The design wavelengths, 450 nm, 530 nm, 600 nm, and 750 nm, respectively correspond to blue, green, red, and near-infrared wavelengths. Films E and F have the same λ_0 as film B, but with decreasing α variation.

5.2.3 Rugate multilayer structural characterization

Samples deposited on Si substrates were cleaved and the exposed edge was imaged with a SEM. The cross-sectional SEM images obtained for films A-D are shown in Fig. 5.1, where (a) is an image of film A, (b) of film B, (c) of film

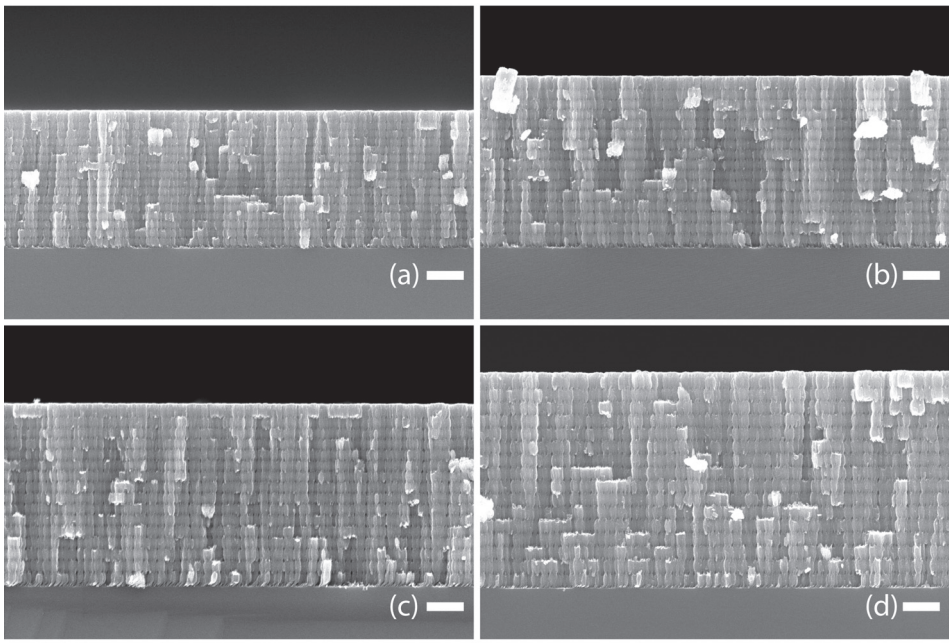

Figure 5.1: Cross-sectional SEM images of GLAD-fabricated rugate multilayer structures. In reference to the film set shown in Table 5.1, (a) is film A, (b) is film B, (c) is film C, and (d) is film D. The white scale bars indicate 500 nm.

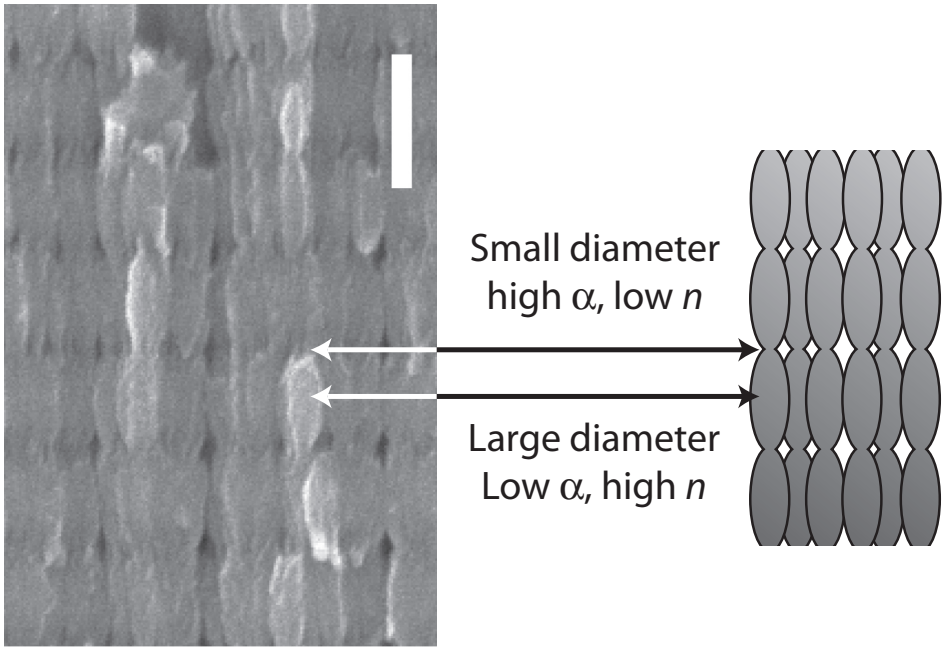

Figure 5.2: Enlarged SEM image of a GLAD-fabricated rugate multilayer revealing greater structural detail. The white scale bar indicates 200 nm. The accompanying diagram illustrates the periodic variation of the column diameter.

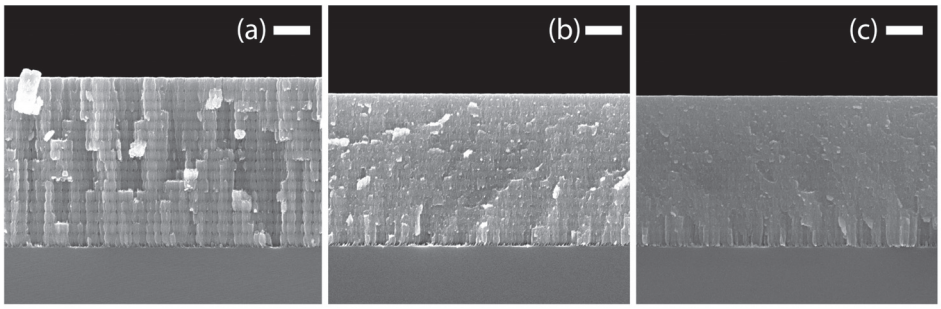

Figure 5.3: Cross-sectional SEM images of films (a) B, (b) E, and (c) F. The α-variation during deposition progressively decreases in these samples (see Table 5.1). The scale bar indicates 500 nm.

C, and (d) of film D. The image greyscale brightness is determined by the local film morphology: brighter/darker areas correspond to denser/less-dense structural regions. A periodic structural variation introduced by α changes during deposition can be clearly seen in the micrographs. From the micrographs, P for each film was estimated by dividing the multlayer's total thickness by sixteen. This measurement yields $P_A = 114 \pm 1$, $P_B = 146 \pm 1$, $P_C = 152 \pm 2$, and $P_D = 181 \pm 3$.

Fig. 5.2 shows an enlarged section taken from an SEM image of film C. From this image, the structural variation in one period can be examined in greater detail. The film is composed of columnar structures with a periodically varying diameter, as indicated by the accompanying illustration. At low α the column diameter is largest, while at high α the column diameter is smaller. In between these two α endpoints, the column diameter changes smoothly following the continuous α-variation. The density gradient caused by the column diameter variation is the source of the refractive index gradient.

The SEM images examined thus far all have α bounds of 30° and 80°, and therefore exhibit similar structural variation. Fig. 5.3 shows cross-sectional SEM images of films (a) B, (b) E, and (c) F, which all have different α-bounds. The structural variation in film B is immediately apparent due to the signficant difference between the dense and porous structures. This structural constrast is present in the SEM of film E, although it is diminished and less apparent. In film F, the structural variation is subtle and difficult to observe

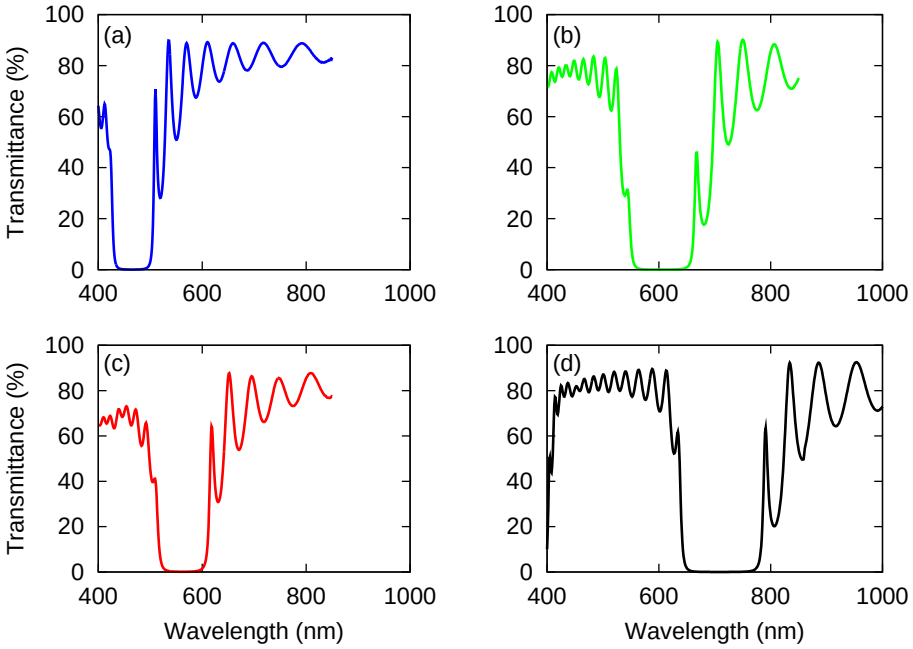

Figure 5.4: The normal incidence transmittance spectrum measured for films (a) A, (b) B, (c) C, and (d) D. The progressively increasing film period redshifts the stopband, causing films A, B, C, and D to respectively reflect blue, green, red, and near-infrared wavelengths, respectively.

beyond the first few periods. This is due to the much smaller α-variation during deposition. As was done with films A-D, P for these films is estimated to be $P_E = 130 \pm 2$ and $P_F = 129 \pm 2$.

5.2.4 Controlling the band gap spectral location

The normal-incidence spectral transmittance of rugate multilayers A through D were measured using the spectrophotometer. These transmittance spectra are shown in Fig. 5.4, where (a) corresponds to A, (b) to B, (c) to C, and (d) to D. A well-formed band wherein transmittance is strongly reduced is observed in each spectrum. This indicates the presence of a photonic band gap created by the destructive interference of light over this wavelength band. Outside the band gap, smooth and regular variation of the transmitted intensity can be seen, consistent with thin film interference fringes. At long wavelengths, the interference fringe peaks approach 96% transmittance. This corresponds to near-perfect constructive interference of

Table 5.2: Measured band gap parameters of the fabricated rugate multilayer structures.

	Film	$\lambda_g \pm 0.5$ (nm)	$\Delta\lambda \pm 0.5$ (nm)	$\frac{\Delta\lambda}{\lambda_g}$
Different λ_0	A	467.2	80.2	0.172
	B	564.1	100.7	0.178
	C	605.7	119.3	0.197
	D	713.8	147.2	0.206
Different $\Delta\alpha$	B	564.1	100.7	0.178
	E	559.4	67.8	0.121
	F	563.8	52.6	0.093

the forward propagating light, and the 4% loss is caused by the backside reflectance. At shorter wavelengths, the transmittance is reduced from this limit even when substrate index dispersion is included. This indicates an additional wavelength-dependent loss mechanism. Likely, this is due to scattering by the film surface or volume.

The band gap centre wavelength λ_g and bandwidth $\Delta\lambda$ of each spectrum was measured. Because the maximum transmittance points on either side of the band gap are different, determining a FWHM for the band is ambiguous. Therefore, $\Delta\lambda$ was calculated as the spectral distance between points of 30% transmittance on the bandedges. Additionally, λ_g was also calculated by taking the midpoint between these values. The bandedge steepness was determined by calculating the transmittance-spectrum slope at both the 30% bandedge points. For films A, B, C, and D, the long-wavelength bandedge slopes are 12.6 %/nm, 8.1 %/nm, 7.8 %/nm, and 8.6 %/nm, repectively. The corresponding short-wavelength bandedge slopes are -7.9 %/nm, -4.8 %/nm, -2.7 %/nm, and -7.7 %/nm. Note that the short-wavelength bandedge of film C contains an interference fringe near the 30% transmittance point, reducing the calculated slope in comparison to the other values. As can be seen, the bandedge steepness means that selecting different points on the bandedges (with which to obtain λ_g and $\Delta\lambda$) will make a small but negligible difference to the result.

The measured λ_g and $\Delta\lambda$ values are summarized in Table 5.2. The ratio $\Delta\lambda/\lambda_g$ is shown as well. Because of the progressively larger P in this

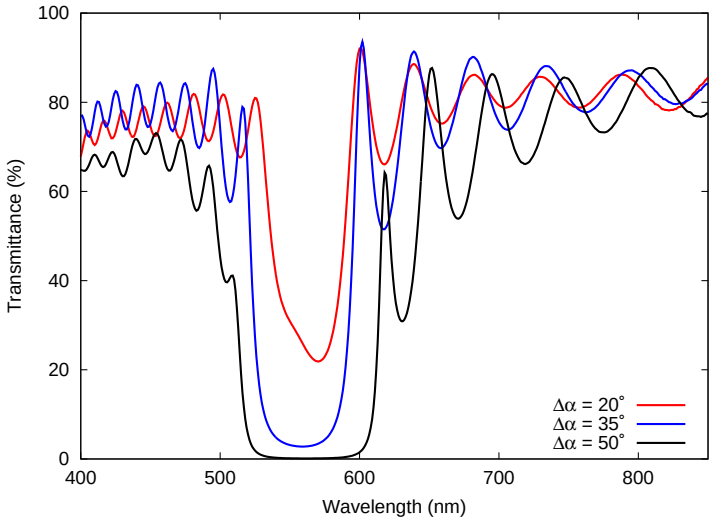

Figure 5.5: The normal incidence transmittance spectrum measured for films B (black line), E (blue line), and F (red line). Changing the α bounds affects the index contrast n_p of the rugate multilayer and alters the resulting band gap.

film series, the band gap appears at increasingly longer wavelengths. Both the bandwidth and the $\Delta\lambda/\lambda_g$ ratio increase as well. Coupled-wave theory predicts (Eq. 2.30)

$$\frac{\Delta\lambda}{\lambda_g} = \frac{n_p}{2n_a}.$$

$\Delta\lambda/\lambda_g$ should therefore be independent of P. However, because of dispersion, the index increases as the TiO_2 absorption band is approached. Since n_p is the difference between two indices, it is minimally affected by dispersion. Dispersion increases n_a which consequently reduces the relative stopband width at shorter wavelengths, as observed.

The normal-incidence transmittance spectra of films E and F were also measured using the spectrophotometer and are shown in Fig. 5.5. The measured transmittance spectrum for film B is also provided (repeated from Fig. 5.4b). The effect of changing the α bounds on the band gap can be clearly seen in the spectra. As $\Delta\alpha$ increases, the band gap width increases and the minimum reflectance decreases. This behaviour occurs because $\Delta\alpha$ determines n_p. Increased index contrast in the rugate multilayer increases the strength of the interference causing the observed band gap changes. Note

that the amplitude of interference fringes nearest the band gap depends on $\Delta\alpha$ as well. This is also caused by decreased interference.

The same band gap parameters, λ_g and $\Delta\lambda$, were measured for films E and F. However, because the band gap transmittance of film F is significantly higher, defining λ_g and $\Delta\lambda$ in terms of 30% transmittance points is inappropriate. The bandedge 50% transmittance points were used instead. The measured band gap parameters are shown in Table 5.2. The B, E, and F band gaps occur within 5 nm of the average $\langle\lambda_g\rangle$ = 562.4 nm. This suggests the fabrication process is highly repeatable, although more points are required to estimate fabrication tolerances.

5.2.5 Optical measurements at non-normal incidence

Thus far, all the optical measurements have been performed at normal incidence. At non-normal incidence, two effects are observed. First, the symmetry between *s*- and *p*-polarization is broken by differences in the Fresnel reflection/transmission equations. Therefore, two band gaps, one for each polarization, will be observed and the measurement must be polarization-resolved. The second effect is a blue-shifting of the interference fringes and the band gaps. This can be seen from the theory developed in Sec. 2.4.2, where the optical phase ϕ is proportional to $\cos\theta$.

Rather than measure the transmittance spectra using the spectrophotometer, which lacks polarizers, a custom measurement apparatus was constructed. The collimated output from a fibre-coupled tungsten-halogen lamp was passed through a small aperture ($\approx$ 1 mm diameter) and then polarized using a Glan-Taylor prism. The sample was mounted on a 360° rotation stage, although in practice, measurements were limited to below θ_i = 85° by the relative size of the beam spot on the sample. The light transmitted through the sample was focused into a fibre-coupled spectrometer. The detected spectral intensity was normalized to the intensity measured when the sample was removed.

Fig. 5.6 shows (a) the *s*-polarized transmittance (T_s) and (b) the *p*-polarized transmittance (T_p) spectra measured from θ_i = 0° to 85° in 5° intervals. At normal incidence, T_s and T_p are essentially identical. As θ_i increases, spectral changes are observed following the previous discussion. The thin film interference fringes gradually shift to shorter wavelengths, as does the

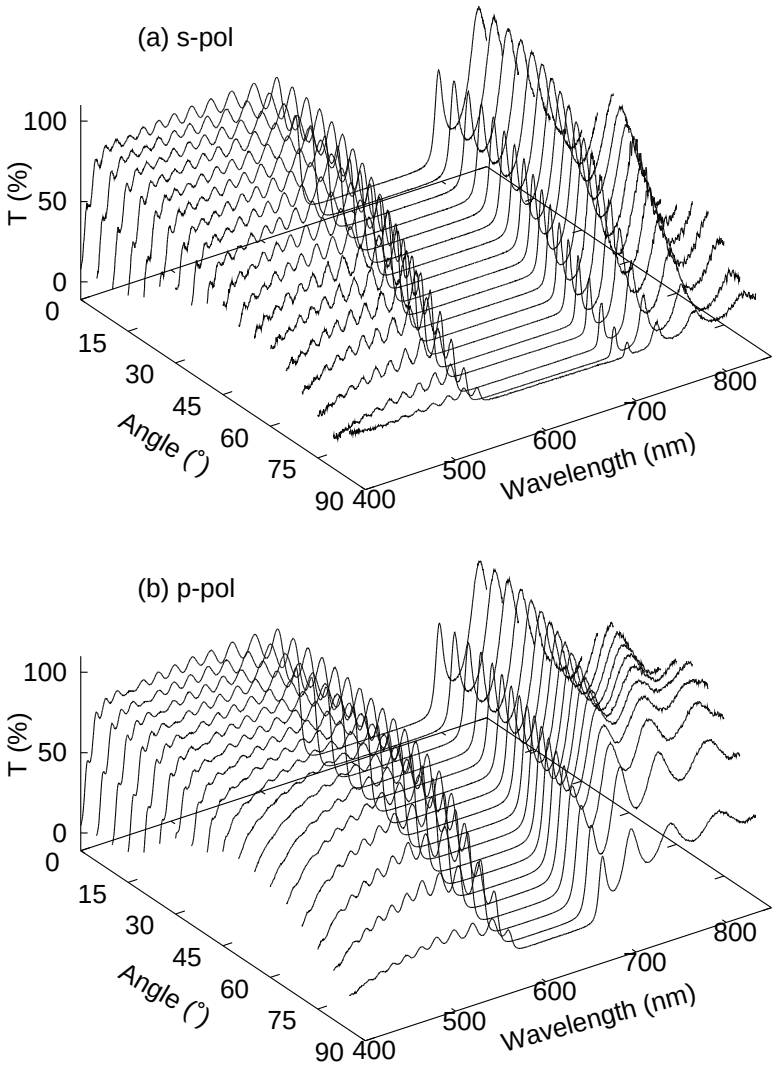

Figure 5.6: The transmittance spectra measured for light incident at different angles. Graphs (a) and (b) respectively correspond to the measured transmittance of *s*- and *p*-polarized light.

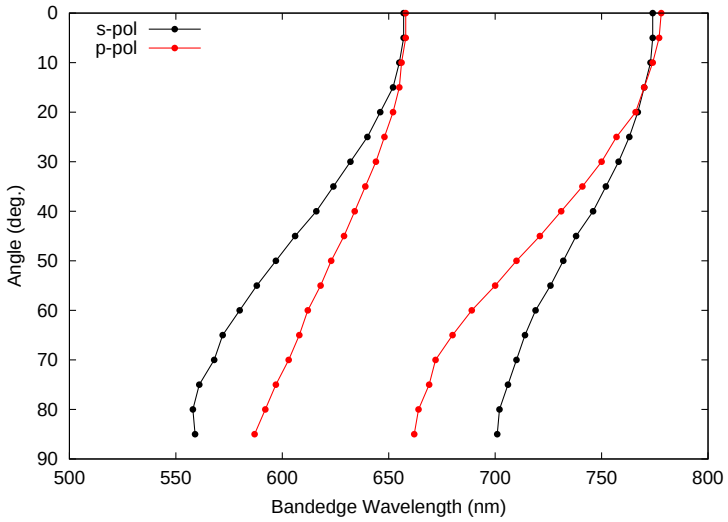

Figure 5.7: The long and short-wavelength bandedges vary as a function of θ_i. The black and red points respectively denote the *s*- and *p*-polarizations.

band gap. The band gap shape changes differently depending on the polarization. The *s*-polarized band gap widens (due to increased interface reflection) while the *p*-polarized band gap becomes narrower (due to decreased reflection nearer the Brewster angle [95]). The long- and short-wavelength bandedges were measured at points of 9% transmittance. These are plotted in Fig. 5.7 as a function of θ_i. The black and red points respectively denote the *s*- and *p*-polarizations. The band gap blueshifting and the changing bandwidth can be clearly seen in this data.

5.2.6 Reducing interference fringes by apodization

Often, the spectral profile of an "ideal" filter is flat: the band gap should be completely reflecting (T = 0%) and the transmittance outside the band gap should be 100% for all wavelengths. Decreasing the band gap transmittance requires increasing the index contrast and/or the number of periods in the multilayer. However, this also increases the interference fringe amplitude near the bandedges. To mitigate these fringes, the refractive index $n(z)$ profile must be apodized by an envelope function [176]. A typical envelope

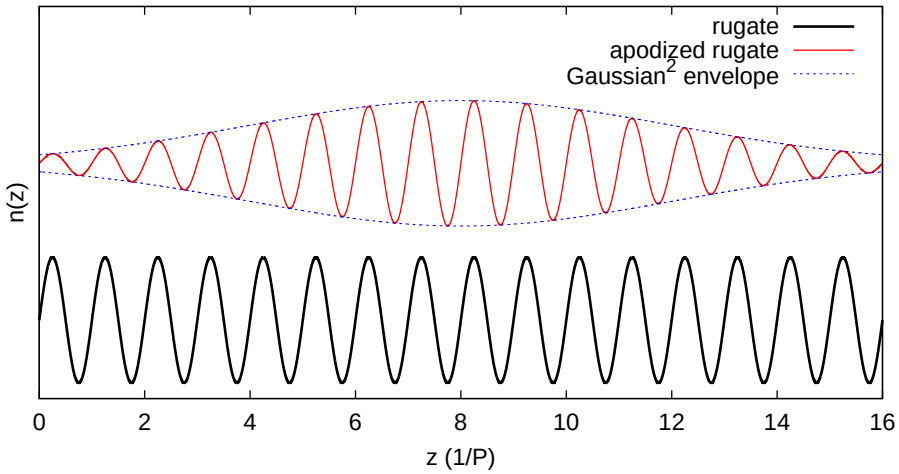

Figure 5.8: Refractive index profiles of a normal rugate structure (black line) and an apodized rugate structure (red line). The apodized rugate profile is created by applying a squared Gaussian envelope (dashed blue line) to the $\sin(z)$ rugate profile.

choice is based on a Gaussian function

$$n(z) = n_a + 0.5 n_p \sin\left(\frac{4\pi n_a z}{\lambda_0}\right) \exp\left[-2\frac{(z - L/2)^2}{(L/2)^2}\right]. \qquad (5.1)$$

In Eq. 5.1, the standard rugate sinusoidal index profile is modified by a squared-Gaussian envelope centred at the film midpoint ($z = L/2$). This index profile is plotted in Fig. 5.8 alongside an unmodified rugate index profile.

Using GLAD, this multilayer structure was constructed by appropriately changing the substrate motion algorithm. At the start of film deposition, the α-variation is small. The α-variation gradually increases reaching a maximum at the film midpoint, then gradually decreases until the film is completed. The parameters of this new multilayer were chosen to fabricate an apodized version of film B in Table 5.1. The cross-sectional SEM image obtained for the apodized multilayer is shown in Fig. 5.9b to the right of an image of film B (Fig. 5.9a). The altered α movements significantly change the film structure. Over the entire film thickness the apodized multilayer structure interpolates from small-to-large-to-small structural variation. Near the film endpoints, the structural contrast is minimal and similar to that ob-

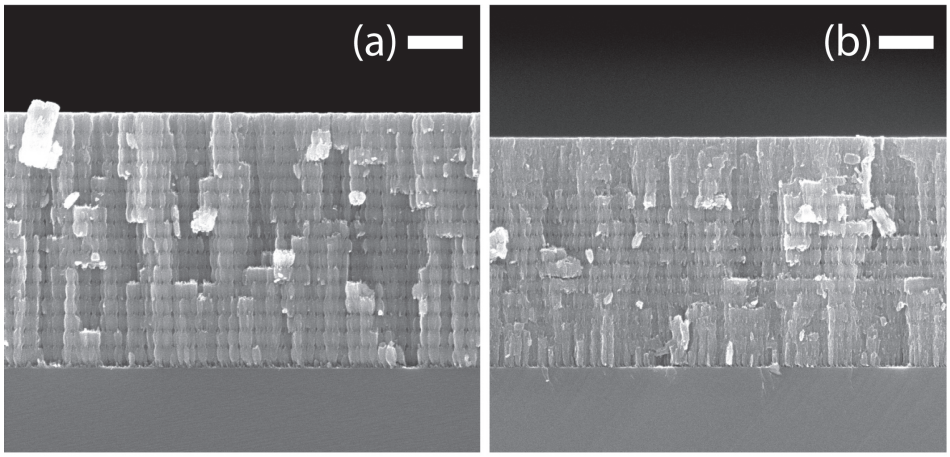

Figure 5.9: SEM images of (a) a normal rugate multilayer structure and (b) an apodized-rugate multilayer structure. The scale bar indicates 500 nm.

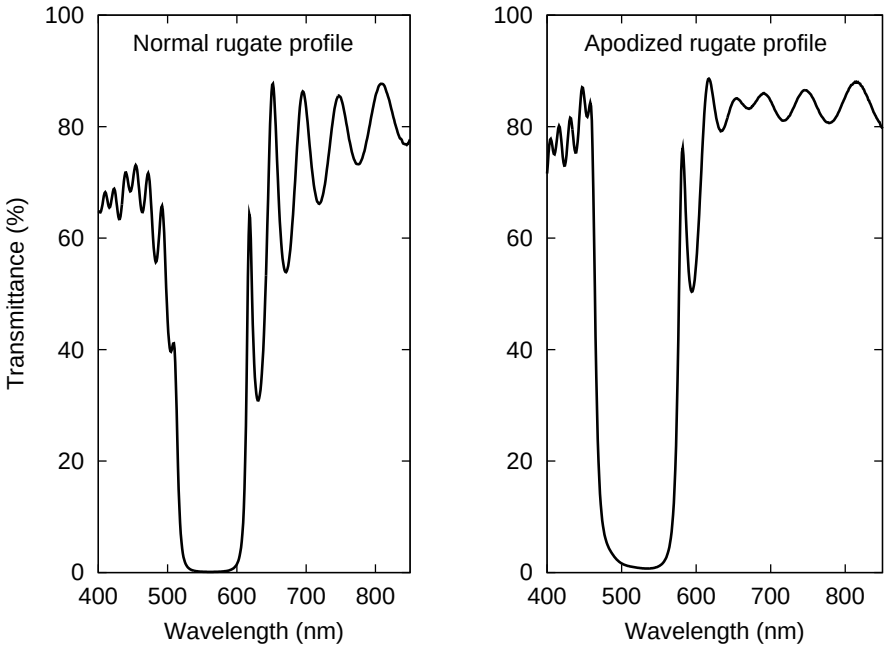

Figure 5.10: Transmittance spectra measured for the normal-rugate (left) and the apodized-rugate (right) index profiles (see Fig.5.8).

Table 5.3: Index parameters n_a and n_p calculated using the coupled-wave theory results and the measured values of P, λ_g, and $\Delta\lambda$.

	Film	λ_g (nm)	n_a	n_p
Different λ_0	A	467.2	2.04 ± 0.03	0.57 ± 0.02
	B	564.1	1.94 ± 0.02	0.57 ± 0.01
	C	605.7	1.99 ± 0.03	0.66 ± 0.02
	D	713.8	1.98 ± 0.03	0.69 ± 0.02
Different $\Delta\alpha$	B	564.1	1.94 ± 0.02	0.57 ± 0.01
	E	559.4	2.20 ± 0.02	0.39 ± 0.01
	F	563.8	2.18 ± 0.04	0.26 ± 0.01

served in Fig. 5.3c. Towards the film midpoint however, the structural variation is increased and the film structure resembles that of film B.

The normal-incidence transmittance spectrum of the apodized multilayer was measured using the spectrophotometer. This is shown on the right side of Fig. 5.10. To the left of this spectrum is the measured film B transmittance. As can be seen, the films exhibit band gaps of similar depth and width. However, the interference fringe amplitude of the apodized multilayer is significantly reduced, as expected.

5.2.7 Estimating refractive index parameters

From the measured values of P, λ_g, and $\Delta\lambda$, the refractive index parameters n_a and n_p can be calculated using Eqs. 2.28 and 2.30, repeated here for convenience

$$\lambda_g = 2n_aP \quad \text{and} \quad \tfrac{\Delta\lambda}{\lambda_g} = \tfrac{n_p}{2n_a}.$$

Solving these two equations for the two unknowns n_a and n_p yields the results presented in Table 5.3.

Comparing these index parameters with the previously measured single layer indices is difficult because the coupled-wave equations do not account for dispersion. However, index estimates of $n = n_a + 0.5n_p \approx 2.3$ at α = 30° and $n = n_a - 0.5n_p \approx 1.7$ at α = 80° can be obtained. These estimated values are greater than expected when compared to the single layer indices presented in Fig. 4.16. It is unclear if this discrepancy is actually

due to increased refractive indices or if it is related to an insufficiency of the coupled-wave model, such as material dispersion and / or non-sinusoidal index profile.

5.3 Quarter-wavelength Bragg multilayers

With the intent of closely examining the fabrication method accuracy, the rugate structure is not a suitable first choice because it is difficult to verify the design goal has been achieved. While parameters such as P, n_a, and n_p were estimated in Sec. 5.2.7, it is difficult to confirm that the index profile follows a true sine function and not some sine-like variation. Because resonant wave reflection is a general property of periodic systems, similar behaviour would be expected for a profile with, for example, a sine-squared dependency. To more precisely examine the index profile optical simulations are required, as was done in chapter 4. With a rugate structure, many layers are required in the index profile digitization. Calculating optical properties over a wide wavelength range therefore requires many thousands of matrix multiplication steps. If numerical fitting is required, the number of multiplications increases many times over again. It is therefore logical to examine a simpler system, such as the Bragg multilayer discussed in Sec. 2.5.2, and attempt to observe deviations from the target design.

5.3.1 Substrate motion algorithm

The substrate motions required to fabricate Bragg multilayers are simpler than those presented in Sec. 5.2.1 to deposit graded-index structures. The target Bragg structure consists of alternating high index n_H and low index n_L sublayers, each having a quarter-wave optical thickness at a design wavelength λ_0. This corresponds to

$$n_H d_H = n_L d_L = \frac{\lambda_0}{4}, \tag{5.2}$$

where d_H and d_L are the H- and L-sublayer physical thicknesses, respectively. The H- and L-sublayers are deposited at deposition angles α_H and α_L. From the $n(\alpha)$ and $D(\alpha)$ calibration data, this corresponds to indices $n_H = n(\alpha_H)$ and $n_L = n(\alpha_L)$ and QCM thicknesses $d'_H = D(\alpha_H)\lambda_0 / 4n_H$

Table 5.4: Bragg multilayer structures fabricated in this study.

Film	α_H (°)	α_L (°)	λ_0 (nm)	N	Film	α_H (°)	α_L (°)	λ_0 (nm)	N
A	45	78	700	8	J	40	80	650	8
B	45	78	700	16	K	40	80	650	8
C	45	78	700	8	L	40	80	670	12
D	45	78	700	8	M	40	80	670	16
E	45	78	700	8	N	60	80	560	12
F	45	78	700	8	P	60	80	560	12.5
G	40	80	725	5	Q	60	80	560	12.5
H	40	80	725	5	R	60	80	560	12.5

and $d_L' = D(\alpha_L)\lambda_0/4n_L$. To achieve polarization insensitive properties at normal-incidence, the vertical post structure was deposited. At the interface between sublayers, a 2 nm transition layer was included to account for the finite speed of the substrate motors.

5.3.2 Bragg multilayer film set

A series of Bragg multilayer structures were fabricated in an e-beam evaporation system specifically modified for GLAD use following the process described in Sec. 3.1.4. Multilayers were deposited onto B270 glass, for optical characterizations, and p-doped Si substrates, for structural characterizations. In designing the Bragg multilayer structure, the main fabrication parameters are the sublayer deposition angles α_H and α_L, the target wavelength λ_0, and the number of periods in the film N. The parameters of this film series are shown in Table 5.4. The films are labelled alphabetically A-R, although letters I and O are not used to avoid typographic confusion with 1 (one) and 0 (zero).

5.3.3 Structural characterization of Bragg multilayers

Samples deposited on Si were carefully cleaved and the exposed edges were imaged using a SEM. Fig. 5.11 shows these cross-sectional SEM images for films G, K, L, and M. The SEM magnification was chosen to fit the entire film thickness in the field of view; the white scale bar in each image indi-

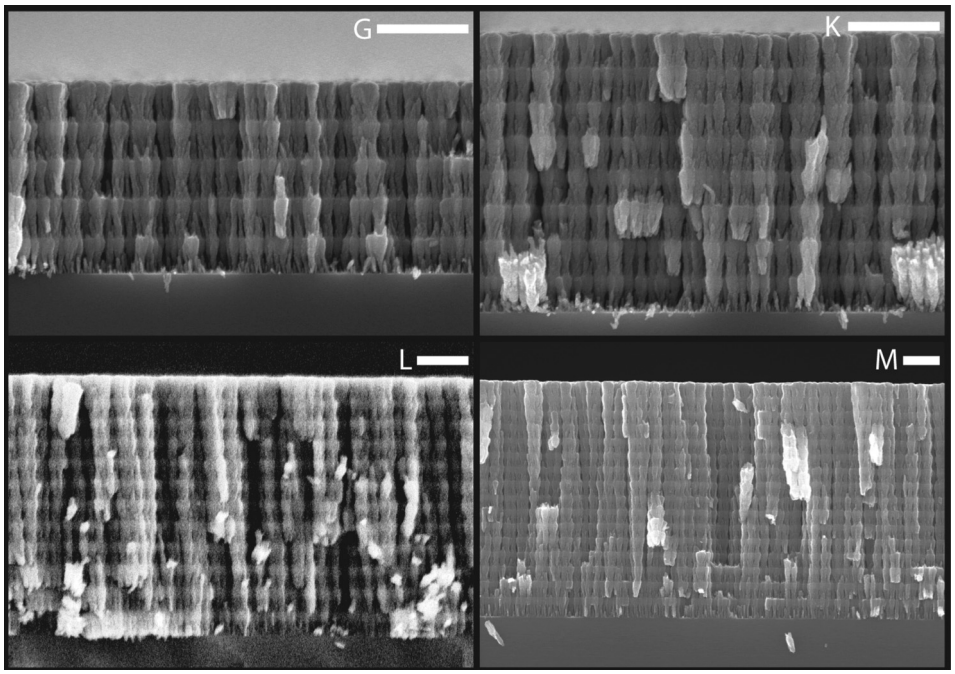

Figure 5.11: Cross-sectional SEM images of GLAD-fabricated TiO_2 Bragg multilayers. The images are labeled G, K, L, and M in correspondence with Table 5.4. The scale bar in each image measures 500 nm.

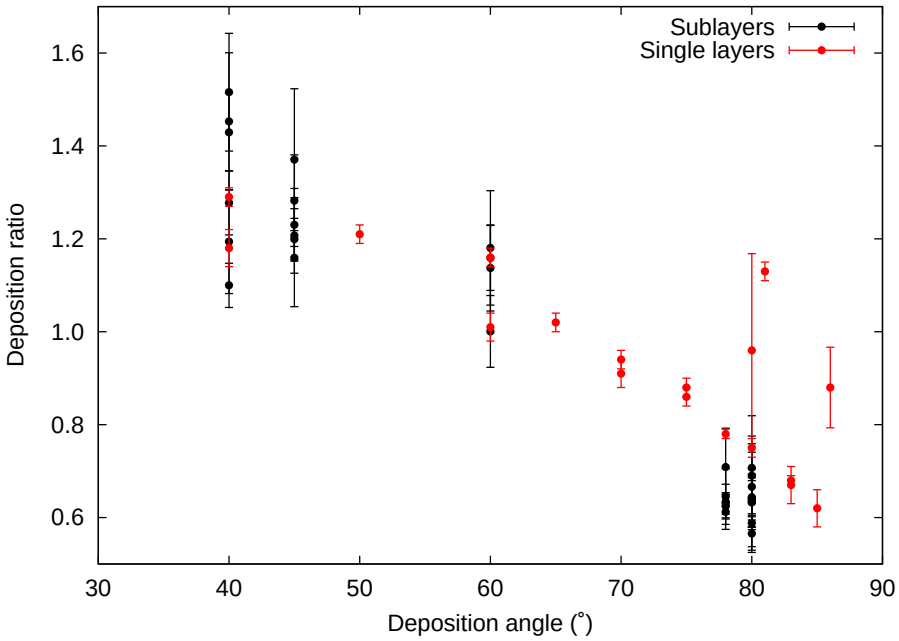

Figure 5.12: Measured Bragg sublayer (black points) and single layer (red points) deposition ratios.

cates 500 nm. These structures were deposited with the same α_H and α_L, but have different N. From these SEM images, the coarse structure of the Bragg multilayers can be observed. The grayscale contrast originates from the topography of the sample. Structural stratification resulting from changing film density can be clearly seen in the images: brighter / darker areas correspond to structurally denser / less-dense regions of the multilayer.

From these SEM images, the thickness of every sublayer was measured and the deposition ratio was calculated using the corresponding QCM thickness. Fig. 5.12 shows the mean sublayer deposition ratios (black points) with error bars equal to the standard deviation of the measured values. Also shown on this plot are the single layer deposition ratios (red points) measured in Sec. 4.3.1. Although the uncertainties are large, there appears to be a slight difference between the single and multilayer deposition ratios at large α. This difference could arise from several sources. A possible cause is systematic measurement error stemming from inaccurately determining the sublayer interfaces. However, this is unlikely since the data sets agree for $\alpha \leq 60^\circ$ and the same inaccuracy exists for all sublayers. Assuming

therefore the effect is real, this difference could indicate a deposition ratio thickness-dependence given that the Bragg sublayers are thinner than the single layer films. Another possible cause is surface related. The high-α single layer are films deposited on Si, whereas the sublayers are deposited onto a previously-deposited structured TiO_2 surface. A third potential cause is substrate heating, as was discussed in Sec. 4.5.3. Further experiments are required to fully investigate and understand this effect.

5.3.4 Bragg multilayer: fine structure

To examine the multilayer structure in greater detail, a series of high magnification SEM images were taken from a single film at different points along the film thickness. The field of view of each successive image overlapped by approximately 20%, allowing the images to be combined into a single composite panorama. This composite is shown in Fig. 5.13. From this image, the Bragg multilayer structure can be viewed at high resolution from start to finish. Throughout the film, the structural distinction between H- and L-sublayers is readily apparent. However, the sublayer structure, particularly the L-sublayer, changes with film thickness. The two diagrams alongside the SEM image illustrate the changing structure. The first few L-sublayers consist of multiple small columnar structures separated by interstitial void regions. The L-sublayer structure differs significantly from the relatively featureless H-sublayer. Because of its higher density, the H-sublayer is more structurally uniform. Further along the film thickness, the H- and L-sublayer structural differences have changed. In the final few film periods, the L-sublayer structure is no longer characterized by multiple small columns. Instead, the film appears to consist of single, larger columns. This process resembles the evolutionary film growth model where the smaller columns bundle together as deposition progresses. The H- and L-sublayers are distinguishable by the changing column diameter: the H-sublayer columns are larger than the L-sublayer columns. The transistion between these structures is not sudden, but instead a gradual transformation occurs from one period to the next.

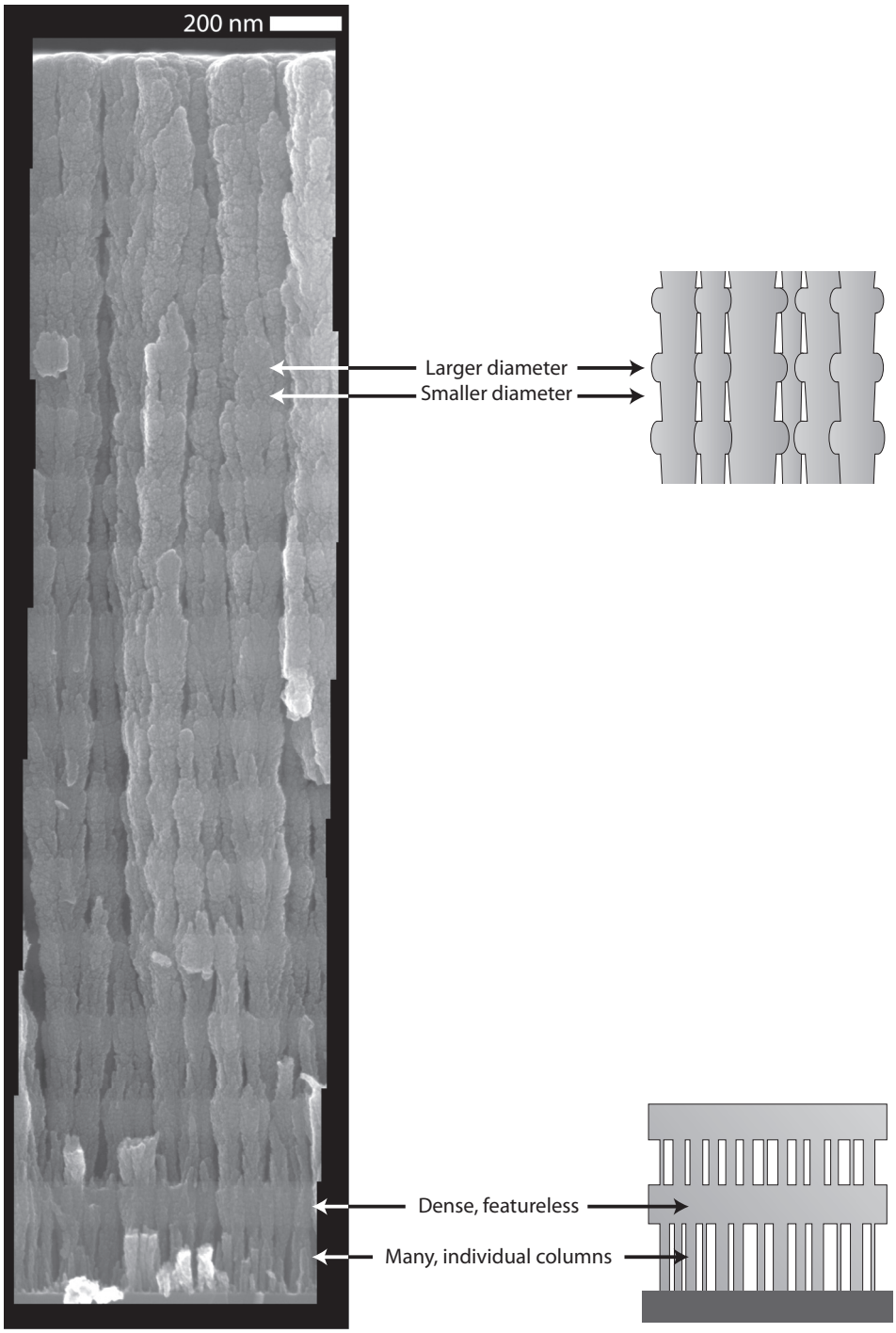

Figure 5.13: Composite image constructed from high (150,000) magnification SEM images taken at different points along the thickness of a Bragg multilayer.

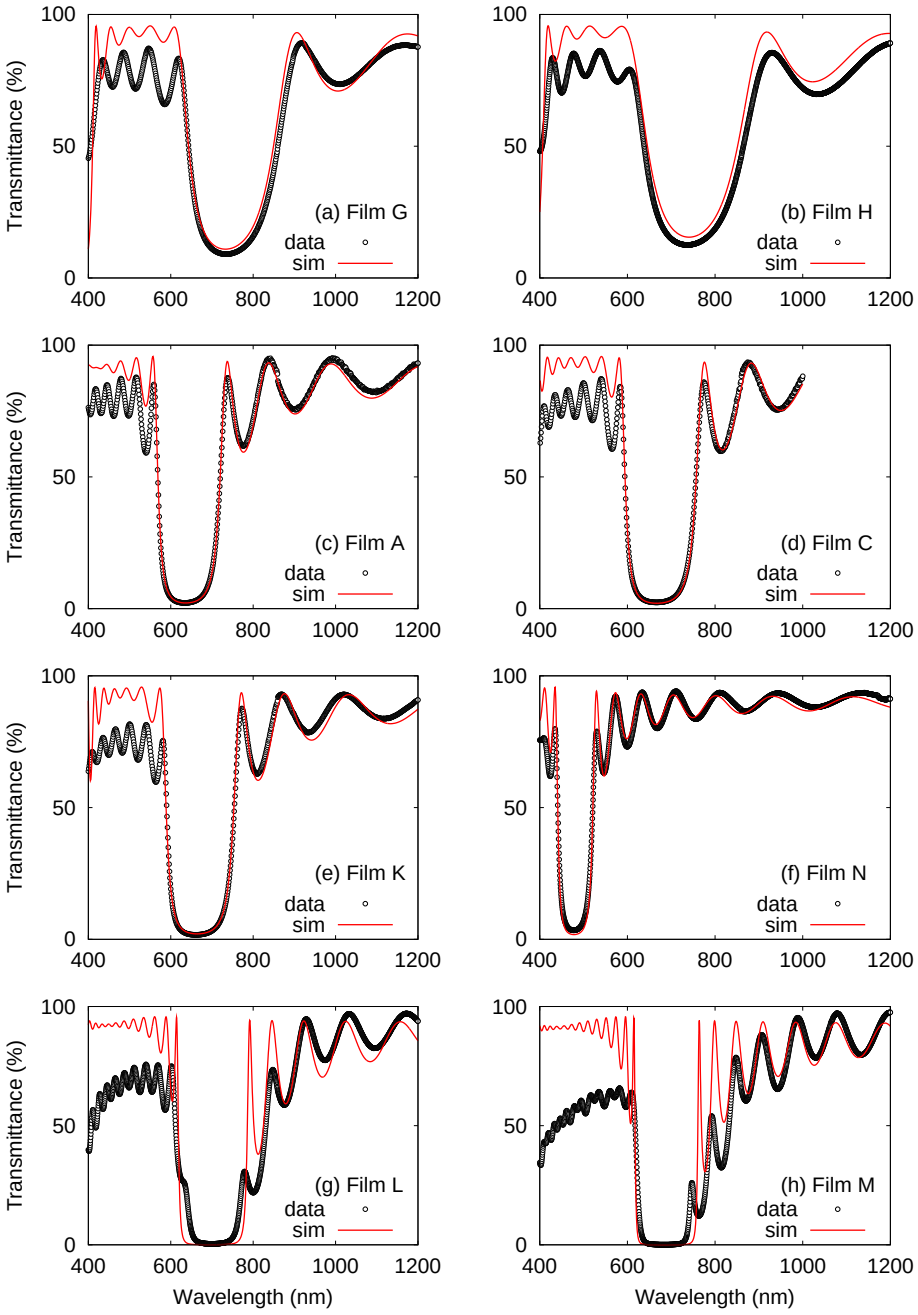

Figure 5.14: Measured (data points) and simulated (red curve) transmittance spectra of GLAD-fabricated Bragg multilayers. The alphabetic film labels correspond to Table 5.4.

5.3.5 Bragg multilayer optical properties

The optical transmittance of each film was measured at normal incidence using the spectrophotometer. Characteristic matrix calculations were also performed to simulate the multilayer optical response. The model developed assumes that the sublayers are homogeneous, lossless, isotropic slabs. While in Sec. 4.5, small index gradients were found in GLAD-deposited layers, the present simulations neglect this effect. Given the small sublayer thicknesses, gradient-index effects will be small and ignoring them provides good preliminary results. In the simulation, the L- and H-sublayer indices were modeled by two-term Cauchy dispersion equations

$$n_L(\lambda) = A_L + B_L/\lambda^2, \tag{5.3a}$$

$$n_H(\lambda) = A_H + B_H/\lambda^2. \tag{5.3b}$$

The mean thicknesses obtained from SEM measurements were used as sublayer thicknesses d_L and d_H. The simulated transmittance was numerically fit to the measured spectrum using the LM algorithm. The only fitting parameters were the Cauchy dispersion coefficients (A_L, B_L, A_H, and B_H).

Fig. 5.14 shows eight of the measured (data points) and simulated (red curve) transmittance spectra. In reference to Table 5.4, Fig. 5.14 (a) corresponds to film G, (b) to H, (c) to A, (d) to C, (e) to K, (f) to N, (g) to L, and (h) to M. The results are presented in this order as they then correspond to an ascending series in terms of N. These eight sets were selected as representative of the set of entire results. All the spectra are provided for inspection in Appendix B (Fig. B.1). In every spectrum, the presence of a photonic band gap is confirmed by a band of strongly decreased transmittance. This band gap is created by the destructive interference of light waves propagating in the periodically structured Bragg multilayer. Outside of the band gap, thin film interference fringes are observed as expected. From the fitted Cauchy dispersion coefficients, the sublayer indices were calculated at λ = 600 nm. Fig. 5.15 shows these values (black points) as well as the single layer indices obtained from the graded-index model[1] in Sec. 4.5.2. There is no significant difference between the single layer and Bragg sublayer indices. The Bragg

[1]Because the Bragg sublayers are relatively thin, the gradient-index single layer indices were calculated from Eq. 4.3 with z = 0.

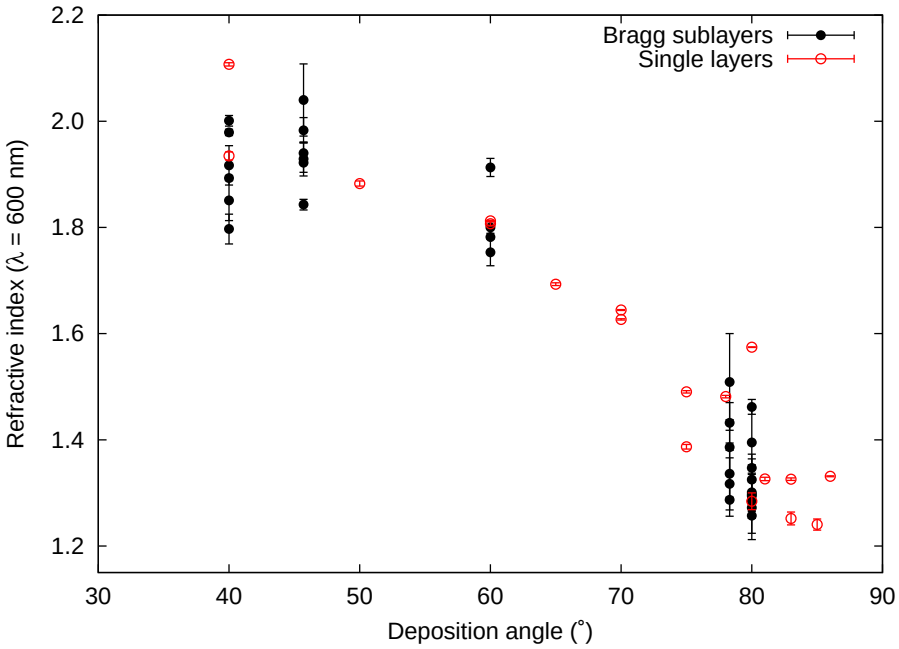

Figure 5.15: The measured refractive indices (at λ = 600 nm) of Bragg sublayers (black points) and single layers (red points) deposited at different deposition angles. No significant difference is observed between the two data sets.

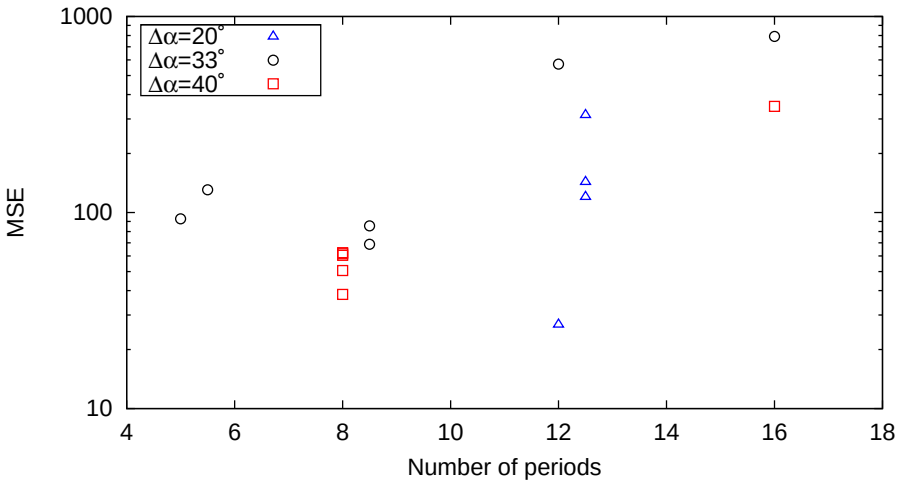

Figure 5.16: The mean-squared-error (*MSE*) between the measured and simulated Bragg multilayer transmittance spectra plotted against the number of multilayer periods. Greater discrepancy between measurement and simulation is seen in thicker films.

sublayer uncertainties are larger however, which is understandable given the greater model complexity used in their determination.

5.3.6 Bragg multilayers: Experiment versus simulation

Visually, the agreement between data and simulation is better for films with fewer periods (for example, compare (c) and (h) in Fig. 5.14). In thinner films, such as Figs. 5.14(a)-(e), the band gap depth and width are accurately fitted. The amplitude and period of interference fringes at the bandedges are also well reproduced. However, the data-simulation agreement for films L and N, respectively having 12 and 16 periods, is not as good except at long wavelengths far from the band gap. Two main discrepancies can be noted. The first is the decreasing transmittance at short wavelengths ($\lambda <$ 500 nm). The second is the reduced transmittance of interference fringes near the bandedges. The *MSE* between data and simulation provides a quantitative expression of agreement and is shown in Fig. 5.16. The *MSE* values are plotted against N and divided into three categories depending on $\Delta\alpha$. As can be seen in this semilog plot, thicker films tend to have larger *MSE* values and correspondingly less accurate fits.

To examine the band gap properties, the bandwidth $\Delta\lambda$, band gap centre

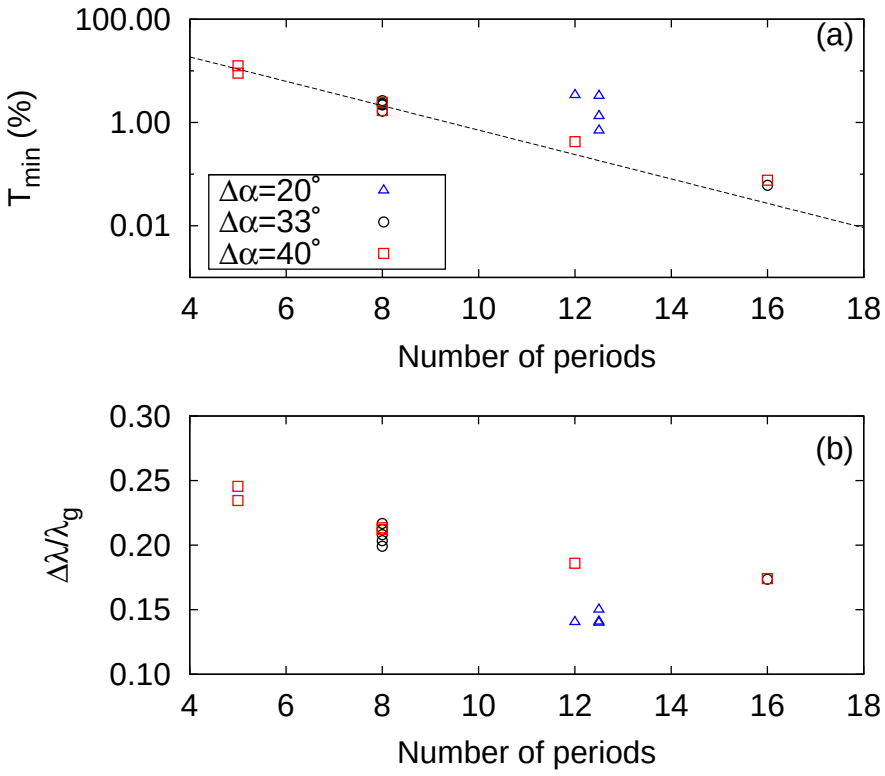

Figure 5.17: The measured (a) minimum band gap transmittance ($T_{\min}$) and (b) relative bandwidth ($\Delta\lambda/\lambda_g$) plotted against number of periods in the Bragg multilayer. The coloured data points correspond to Bragg multilayers with different sublayer index contrasts (determined by $\Delta\alpha = \alpha_L - \alpha_H$). The black dashed line is the function $T_{\min} = b \cdot a^N$ numerically fit to the $\Delta\alpha$ = 33° and 40° data sets.

wavelength λ_g, and the minimum band transmittance $T_{\min}$ were measured for every film. Determining the bandwidth presents the same subtleties as discussed in Sec. 5.2.4. In this instance, $\Delta\lambda$ is measured between points along the bandedge where the transmittance is 20% greater than $T_{\min}$. Fig. 5.17 shows $T_{\min}$ and the ratio $\Delta\lambda/\lambda_g$ plotted against N. The data are also subdivided according to $\Delta\alpha = \alpha_L - \alpha_H$. As N is increased, $T_{\min}$ decreases due to greater destructive interference of the propagating wave. In an ideal Bragg multilayer with quarter-wavelength sublayers, $T_{\min}$ is determined by Eq. 2.25. $T_{\min}$ should therefore be proportional to a^{N-1}, where a is a constant. A function of this proportionality was fit to the combined $\Delta\alpha$ = 33° and 40° sets and is shown as a black dashed line on Fig. 5.17(a). As can be seen, the data deviates from the expected relationship at larger N, indicating that the fabricated Bragg multilayer differs from the ideal Bragg structure. This indication is also supported by the data in Fig. 5.17(b). In the ideal Bragg structure the ratio $\Delta\lambda/\lambda_g$ is independent of N, as shown by Eq. 2.26. However the measured values of this ratio clearly decrease with N, further indicating a deviation from the ideal Bragg structure.

The greater discepancy between data and model observed in thicker films could be related to multiple factors. Following the Beer-Lambert law, optical loss scales exponentially with thickness. Because the simulation assumes lossless sublayers, this would imply poorer fitting as thickness increases. Relatedly, the magnitude of optical losses could increase with thickness. For example, the increasing size of columnar features with film thickness (c.f. Fig. 5.13) would cause greater scattering losses. Another factor is the structural changes discussed in Sec. 5.3.4 causing optical effects not accounted for in the model.

5.4 Short and long term film stability

While characterizing the Bragg multilayers, a small time-dependence of the measured film transmittance was noticed. For example, Fig. 5.18 shows film J's measured transmittance spectra 3 hr (black line), 49.3 hr (red line), and 99.8 hr (blue line) after being removed from the deposition system. Several aspects of the time-dependence were observed to be universal. One, the transmittance changes were always transient and transmittance spectra

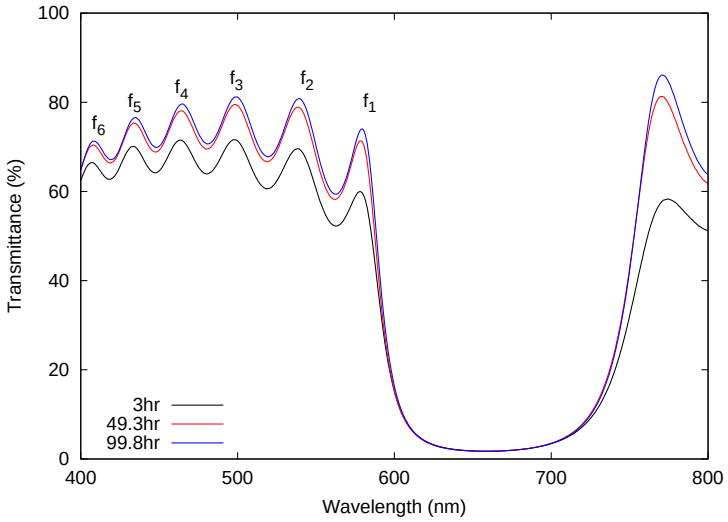

Figure 5.18: Measured transmittance spectra of Bragg multilayer (film J) taken at different times after removal from the deposition system. The transmittance increases slowly over time.

would stabilize after a few days. Two, the transmittance would always increase. Three, the transmittance change began once the film was removed from the deposition system (vacuum environment).

To quantify the transmittance change and study film stability, the optical transmittance of film J was measured several times. The time since removal from the deposition system was noted for every measurement. The interference fringe peak transmittances (labelled in Fig. 5.18) are shown in a semilog time plot in Fig. 5.19. To determine the time constant τ associated with the spectra stabilization, the expression

$$T(t) = T_f - (T_f - T_i) \exp\left(\frac{-t}{\tau}\right) \tag{5.4}$$

was fit to the data, where T_i is the initial transmittance and T_f is the steady-state transmittance. The fitted parameters are presented in Table 5.5. The error-weighted-mean time constant is $\langle\tau\rangle$ = 30.9 $\pm$ 0.2 hr.

These results indicate that there is a short-term transient variation in the multilayer optical properties. After this initial change however, the transmittance is stable for greater than 2600 hr (samples were stored in covered petri dishes under ambient conditions). Given that the transmittance always

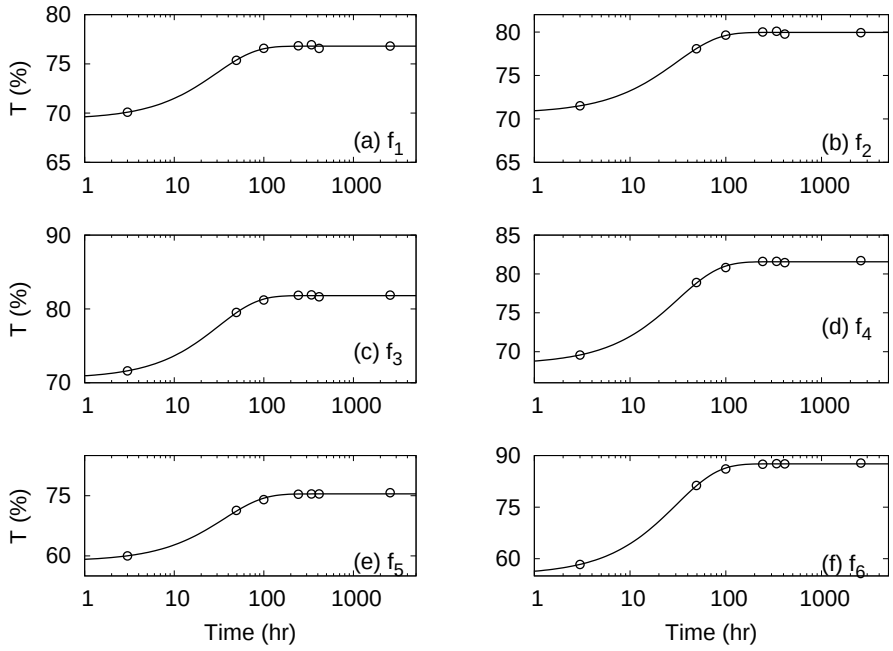

Figure 5.19: Time-dependent transmittance of the six fringe peaks f_1 through f_6 (labelled in Fig. 5.18). The circles correspond to measured transmittance values and the solid line is Eq. 5.4 fit to the data.

Table 5.5: The fitted parameters of the fringe peak transmittance exponential aging (Eq. 5.4). The fringes are labelled in Fig. 5.18.

Fringe	T_i (%)	T_f (%)	τ (hr)
f_1	69.4 ± 0.2	76.80 ± 0.06	30 ± 2
f_2	70.6 ± 0.2	79.96 ± 0.2	31 ± 1
f_3	70.6 ± 0.1	81.90 ± 0.06	31 ± 1
f_4	68.4 ± 0.2	81.7 ± 0.1	31 ± 1
f_5	58.7 ± 0.3	75.4 ± 0.1	36 ± 2
f_6	55.3 ± 0.2	87.59 ± 0.09	30.5 ± 0.6

increases (implying decreasing optical absorption), a likely explanation for the short-term aging is oxygen depletion of the as-deposited TiO_2 films. Oxygen deficiencies are common in TiO_2 films deposited on unheated substrates [130]. Oxygen deficiencies act as electron-donors in TiO_2 and sub-stoichiometric TiO_2 possesses free electrons causing optical absorption at sub band-gap visible wavelengths [177]. Once removed from the vacuum system, the films are exposed to ambient oxygen. The absorption slowly decreases as the oxygen molecules diffuse into the bulk, columnar material and the free carrier concentration decreases. Heating the films hastens this process: film optical properties reached steady-state after an overnight anneal at 70 °C in an ambient atmosphere.

5.5 Summary and Conclusions

The single-layer optical nanomaterial results of chapter 4 have been extended to create PC multilayer structures. GLAD-fabricated TiO_2 rugate PCs were successfully prepared and characterized. The photonic band gap created by the rugate sinusoidal index variation can be controlled by adjusting the α-motions during deposition. Slowing the α-variation increases the physical period, shifting the Bragg resonance to longer wavelengths. Decreasing the α-variation amplitude correspondingly decreases the peak-to-peak index variation, producing a narrower band gap. This latter technique was extended to realize an apodized version of the rugate multilayer. Excellent photonic band gap control is demonstrated by this work, greater than that shown in previous research.

To further improve the technique, optical modeling techniques are required to better assess the fabrication accuracy. Therefore, a large set of Bragg multilayer PCs were fabricated. Precise modeling of the Bragg structure requires fewer layers than the rugate structure, rendering the Bragg PC more suitable for numerical calculation and iterative data fitting. The optical modeling accurately reproduces key aspects of the measured Bragg PC spectra, including the band gap depth and bandwidth, and the interference fringe amplitude and period. The optical simulations reveal that the model is less accurate when applied to thicker multilayers. This conclusion is supported by a detailed analysis of band gap parameters, showing that

the bandwidth and minimum-transmittance thickness-scaling deviates from the expected behaviour. These discrepancies are related to factors not incorporated in the model. Possible factors include optical losses (scattering and absorption) and effects related to structural changes. Developing more precise representations of the multilayer structures is a key step towards removing deficiencies and improving the fabrication technique. Future theoretical work will also require continued sample fabrication and experimentation to verify improved models.

In this chapter, PC structures have been successfully realized to a good degree of accuracy. The important ability to design and tune the PC band gap properties has also been demonstrated. These are essential achievements towards creating the next generation of GLAD PC devices, providing a strong foundation for further work. The remainder of this thesis extends the results of this chapter towards functional, rationally designed PC devices.

Chapter 6

Colourimetric Porous Photonic Crystal humidity sensor

6.1 Optical sensing and photonic crystal sensors

PCs achieve their unique properties through their structure, which creates a periodic spatial variation of the refractive index $n(z)$. Because of this, the interaction between light and the PC is very sensitive to $n(z)$. Slight perturbations, such as structural distortions or refractive index changes, lead to measurable changes of the PC optical properties. PCs are often porous and the internal structure of such PCs are open to their surroundings. Fluids can penetrate into the PC and create the aforementioned $n(z)$ changes. This inherent environmental sensitivity can be mitigated, for example by hermetic encapsulation or surface functionalization. However, this sensitivity can be exploited allowing the PC to transduce the presence of an analyte into an optical signal.

Significant research effort has focused on maximizing the sensitivity and detection limits of optical based sensors. This has led to the development of ultra-high quality optical resonators. For example, microscale ring-resonator structures have been used to sense ppm concentrations of D_2O in H_2O [178] and detect single protein molecules [179]. Microcavities in 2D PC structures have been able to detect index changes as small as 10^{-4} [180]. While the performance of these devices is impressive, they require both precise fabrication and highly-sensitive optical read-out equipment. Alternatively, the PC sensor can be optimized for cost and simplicity. For example, as the PC

band gap shifts in the presence of the analyte, the PC colour changes. The PC can therefore act as a simple, colourimetric sensor responding visually to the environment. This approach requires no power source and no read-out system other than the human eye, making colourimetric sensing highly attractive. Combining colourimetric sensing with a self-assembly technique for PC fabrication would reduce the PC sensor cost and complexity and improve the large-scale manufacturability of the device.

6.1.1 Self-assembled PC structures and sensing

Several approaches have been used to fabricate 1D PC structures, as reviewed in Sec. 2.5.3. Many of these techniques have also been adapted to realize PC sensing devices. One such method uses electrochemical etching of crystalline Si to produce porous Si [109]. By varying the etch current, the density of the porous Si can be controlled and different 1D PCs can be realized. Molecules can infiltrate the porous Si and create optical changes. A range of organic solvent vapours have been detecting using 1D PCs [181–184] and 1D PCs with microcavity resonators [185, 186]. While sensing with porous Si PCs has been successful, its primary drawback is that the technique is limited to Si, which is absorbing in the visible spectrum. This restricts its use to longer wavelengths or operation in a reflectance configuration.

Another PC fabrication approach uses spin casting of nanoparticle colloids to produce a porous, structured layer [110]. Sequential deposition of alternating colloid layers then produces a PC multilayer. Layers can be fabricated from different colloids, including SiO_2 [110], TiO_2 [110] and Laponite [187]. These PC structures have been used to detect water and isopropanol vapours [188], ionic solutions [189], and organic solvent mixtures and bacteria [190]. However, this approach requires a 15 minute high temperature (450°C) annealing step between every layer deposition in order to produce high quality PCs. Because of the length of time required to fabricate samples, experimental results have only been reported for PCs with six [110], eight [188, 190], and thirteen [188] sublayers.

A third approach assembles spherical microparticles into 3D PC structures. By carefully controlling the sedimentation of the particles in solution, the particles will settle into a close-packed arrangment [191, 192]. This cre-

ates 3D refractive index periodicity and corresponding Bragg diffraction. However, the PC index contrast is not sufficient to create a full 3D photonic band gap. For sensing applications, a hydrogel network can be polymerized around the 3D structure [193]. Hydrogels are 3D networks of polymer molecules that alter their shape in response to changes (for example, in temperature, pH, ionic concentrations) in their aqueous surroundings [194]. By fabricating a hydrogel into a 3D PC structure, these shape changes alter the optical Bragg reflectance. These hydrogel 3D PCs have been used to measure solution pH and ion concentration [193, 195], glucose [196], and organic solvents [197]. However, an inherent limitation of hydrogel-based PC sensors is that they are restricted to aqueous environments.

6.1.2 Advantages of GLAD-fabricated structures

Although each technique reviewed above is able produce colourimetric PC sensors, they all have drawbacks limiting their wide-spread application. The GLAD technique however, solves many of these issues and is an excellent sensor technology platform. GLAD offers several advantages as a fabrication technique, including compatibility with a wide range of materials, ability to produce very high surface area structures, ability to flexibly deposit different structural geometries, and ability to operate in or out of liquid environments. The combination of these advantages provides great flexibility, making GLAD sensors tailorable to a number of sensing approaches. GLAD has been used to fabricate electrical [28] and optical [198–200] fluid sensors, porous electrodes for electrochemical sensing [201], nanostructured metals for surface enhanced Raman scattering [202] and localized surface plasmon resonance sensors [203], and chromatographic separation media [204, 205].

6.1.3 Target analyte: water vapour

In these experiments, the PC sensor was tested for its response to water vapour. This analyte was chosen for the following reasons. First, water vapour sensors are important components in a broad spectrum of applications [206–208] including weather and climate measurement, industrial process control, medical monitoring, and home appliances. Second, because TiO_2 surfaces have hydroxyl groups they have a strong chemical affinity

for water vapour [209]. Therefore, the porous TiO_2 surface will be highly receptive to water vapour, improving the device sensitivity. Third, a well-characterized test apparatus was available for this work [28, 199]. Fourth, the demonstration of water vapour sensing is a proof-of-principle result that can be extended to other important gases (such as H_2S, NO, CO_2, organic solvents) and biochemical compounds (such as protein enzymes, DNA).

The amount of water vapour in air determines its partial pressure p. The relative humidity RH is the ratio of p to the saturation pressure p_v of water vapour. At 0% RH, air is completely water-free, while at 100%RH, the air is saturated. The refractive index difference between these two points however is less than 10^{-6} [210]. Therefore, for the presence of water vapour to cause an appreciable change in the PC sensor, it must condense into liquid form (where n=1.33) at a pressure below p_v. This requires capillary condensation of water vapour into the internal pore surfaces of the PC. Capillary condensation is a surface-mediated, gas-to-liquid phase transition occuring at pressures below the saturation vapour pressure [211]. The equilibrium partial pressure of the gas phase above a liquid meniscus is given by the Kelvin equation

$$\ln \frac{p}{p_v} = -\frac{2\gamma V}{r_m RT}, \tag{6.1}$$

where γ is the liquid surface tension, V is the liquid molar volume, r_m is the mean radius of curvature of the liquid surface, R is the universal gas constant, and T is the temperature. Eq. 6.1 predicts that, when confined in a pore, vapours condense at a pressure determined by the pore size and structure (which in turn determines r_m). In a porous PC structure, this condensation mechanism allows the realization of measureable optical changes even at small p.

6.2 Colour measurement science

The electromagnetic properties of light are well-understood. However, the human perception of light is a more difficult topic to understand and its interpretation is a long-standing problem [212]. To investigate the colourimetric response of the PC sensor, the properties of colour must be examined. The perception of a "colour" can crudely be broken down into three

parts [213]:

1. the spectral power distribution (spectral radiance) $I(\lambda)$ (power per unit area per unit wavelength) of the light reaching the retina,

2. the conversion of the incident light energy into nerve signals by photoreceptors (rods and cones) in the retina, and

3. the psychological interpretation of these nerve signals by the brain.

The modern understanding of colour perception stems from investigations conducted in the 1920s [214]. These experiments examined the correlation between physical stimulus (light) and psychological response (perceived colour) using colour-matching experiments.

Standardized methods of reporting colour have been developed by the Commission Internationale de l'Eclairage (CIE) based on the results of these psycho-physical experiments [215]. In the CIE system, any particular colour is represented as a mixture of three primary colours, known as primaries or colour matching functions. Together, these functions $\overline{x}(\lambda)$, $\overline{y}(\lambda)$, and $\overline{z}(\lambda)$ numerically describe the photometric response of a standardized human eye, called the CIE 1931 standard observer [216]. These functions are shown in Fig. 6.1. The CIE provides tabulated values of $\overline{x}(\lambda)$, $\overline{y}(\lambda)$, and $\overline{z}(\lambda)$ at 5 nm intervals.[1] The solid lines on this plot are spline interpolations to a finer wavelength resolution required for later calculations. To numerically describe a given colour with spectral radiance $I(\lambda)$, a tristimulus value (X, Y, Z) is specified:

$$X = k \int_0^\infty I(\lambda)\overline{x}(\lambda)d\lambda, \tag{6.2a}$$

$$Y = k \int_0^\infty I(\lambda)\overline{y}(\lambda)d\lambda, \tag{6.2b}$$

$$Z = k \int_0^\infty I(\lambda)\overline{z}(\lambda)d\lambda, \tag{6.2c}$$

where k is a normalizing constant given by

$$k = \frac{100}{\int_0^\infty S(\lambda)\overline{y}(\lambda)d\lambda}.$$

[1] At the time of writing, tabulated values of $\overline{x}(\lambda)$, $\overline{y}(\lambda)$, and $\overline{z}(\lambda)$ are available at the CIE website (http://www.cie.co.at)

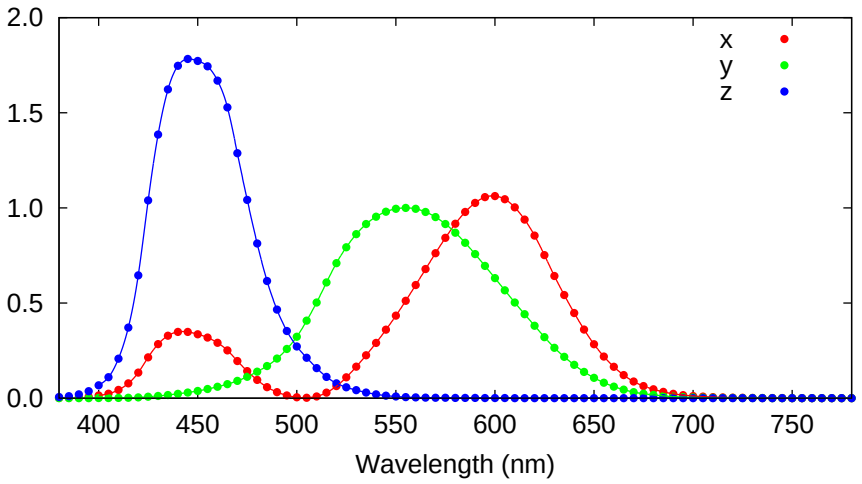

Figure 6.1: The colour matching functions of the CIE 1931 standard observer. The data points are the CIE standard values (specified in 5 nm intervals) and the solid lines are spline interpolated values to the wavelength resolution required in later calculations.

The constant k is defined to set $Y = 100$ when the colour specified by $I(\lambda)$ is equal to a reference colour source $S(\lambda)$, typically white light. The functions $\overline{x}(\lambda)$, $\overline{y}(\lambda)$, and $\overline{z}(\lambda)$ are unitless and (X, Y, Z) carry the same units as $I(\lambda)$.

This approach defines the CIE 1931 XYZ colour space, one of the most common mathematical models for colour. However, one of the main drawbacks of this colour space is its lack of perceptual linearity. In a perceptually linear colour space, the Euclidean distance between two tristimulus points in the colour space would be proportional to the percieved colour change. This shortcoming led to the development of the CIELAB model which is more perceptually linear [217]. As with the XYZ colourspace, colour in the CIELAB model is specified by three co-ordinates (L^*, a^*, b^*) which can be calculated from the (X, Y, Z) co-ordinates using the following equations

$$L^* = 116 f\left(Y / Y_w\right) - 16, \tag{6.3a}$$

$$a^* = 500\left[f\left(X / X_w\right) - f\left(Y / Y_w\right)\right], \tag{6.3b}$$

$$b^* = 200\left[f\left(Y / Y_w\right) - f\left(Z / Z_w\right)\right], \tag{6.3c}$$

where

$$f(t) = \begin{cases} t^{1/3}, & \text{for } t > (6/29)^3 \\ \frac{1}{3}\left(\frac{29}{6}\right)^2 t + \frac{4}{29}, & \text{otherwise} \end{cases}$$

and (X_w, Y_w, Z_w) specify the white point. Whereas the XYZ colour space is an additive representation of colour, the LAB space is a subtractive representation. L^* specifies the lightness of the colour (with $L^* = 0$ being black and $L^* = 100$ being diffuse white), a^* represents the colour's redness or greeness ($a^* > 0$ is red, $a^* < 0$ is green), and b^* is the colour's yellowness or blueness ($b^* > 0$ is yellow, $b^* < 0$ is blue).

The CIELAB system provides a simple means of calculating colour differences. Given two colours (L_1^*, a_1^*, b_1^*) and (L_2^*, a_2^*, b_2^*), the percieved colour difference magnitude ΔC is

$$\Delta C = [(L_2^* - L_1^*) + (a_2^* - a_1^*) + (b_2^* - b_1^*)]^{1/2}. \tag{6.4}$$

However, there are other variables impacting colour perception [218]. These include sample size, the surrounding visual field and the type and intensity of the illumination light source. There is also the important factor of observer subjectivity. These factors, acting alone or in combination, can conspire to skew the actual visual colour difference from the computed ΔC. That said, the CIELAB colour space does provide a mathematical standard with which to approximately quantify colour. Additionally, appropriate design and packaging of the PC sensor can be used to control the viewing conditions and eliminate some of the environmental variability.

6.3 Optimizing the colour change of a PC sensor

Possessing a mathematical model for describing colour, it is possible to calculate the colour of the PC from the measured transmittance spectrum $T(\lambda)$. For a given illumination source with spectral radiance $S(\lambda)$, the spectral radiance of the light passing through the PC is $I(\lambda) = T(\lambda)S(\lambda)$. Using $I(\lambda)$ and the equations above the PC colour can be calculated. Obviously, this colour depends on the source $S(\lambda)$. In the interests of standardization, the CIE provides tables of illuminants to mimic a variety of conditions, includ-

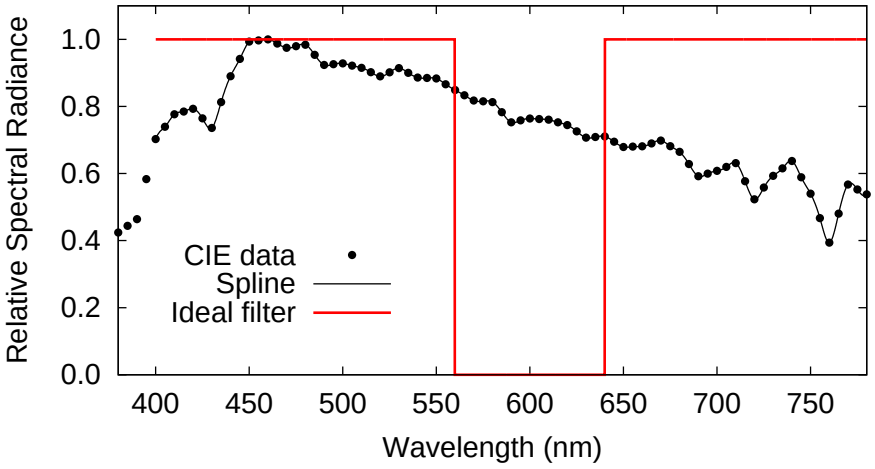

Figure 6.2: The CIE defined D65 illuminant specifying the relative spectral radiance of a standard daylight. The data points are the CIE standard values (specified in 5 nm intervals) and the solid black curve shows the spline interpolated values to the wavelength resolution required in later calculations. The red curve shows the transmittance profile of an idealized "top-hat" PC stopband used in design calculations for a PC sensor.

ing incandescent lighting and sunlight.[2] For these calculations, the standard D65 illuminant $S_{65}(\lambda)$ was selected as it approximates average daylight [219]. The relative spectral radiance of the D65 standard is shown in Fig. 6.2.

The spectral location λ_0 of a PC stopband is linearly related to the optical path length of the unit cell (Eq. 2.21). The wavelength shift $\Delta\lambda_0$ is therefore proportional to the index change caused by water vapour condensing in the PC sublayers. However, the percieved colour change is not proportional to $\Delta\lambda_0$ because colour is not a linear function of λ. It is therefore important to consider what PC design will produce a maximal colour change with minimal $\Delta\lambda_0$. The CIELAB space, with its perceptual linearity, allows for a quantification of colour change. Consider a source (D65) filtered through an idealized "top-hat" stopband with an 80 nm bandwidth (red line in Fig. 6.2). Fig. 6.3a shows the calculated (L^*,a^*,b^*) co-ordinates for light transmitted through filters with different λ_0.

[2]Tabulated values of the standard illuminants are also available at the CIE website (http://www.cie.co.at)

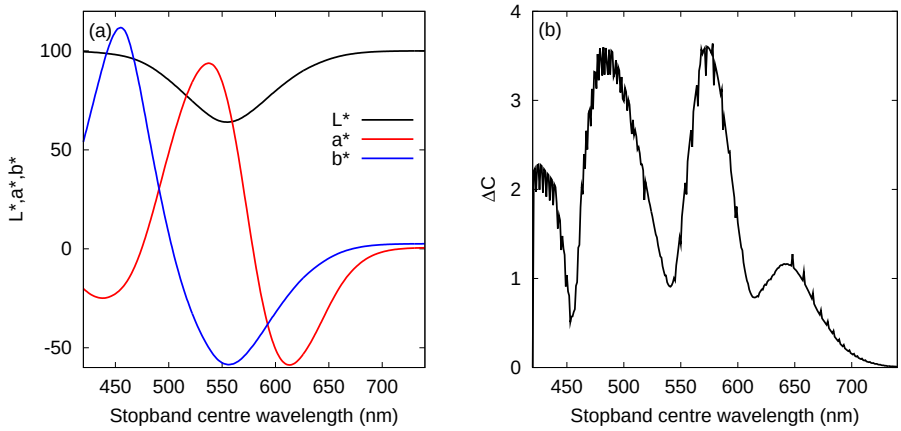

Figure 6.3: (a) The calculated CIELAB co-ordinates (L^*, a^*, b^*) describing the colour of light transmitted through the ideal stopband filter. (b) The Euclidean distance ΔC between successive (L^*, a^*, b^*) points in (a). Because of CIELAB's approximate perceptual linearity, this distance is proportional to the perceived colour change.

This numerical data can be translated into the following qualitative description of the transmitted colour (λ_0 transitions are approximate):

1. $\lambda_0 < 475$ nm: the filter blocks blue light and the transmitted light is a mixture of longer wavelengths. This produces a mixture of red, green and yellow light ($a^* \approx 0$, $b > 0$).

2. 475 nm $< \lambda_0 <$ 500 nm: the filter starts blocking green light, and the transmitted light is a mixture of red and yellow ($a^* > 0$,$b^* > 0$).

3. 500 nm $< \lambda_0 <$ 520 nm: the filter starts passing blue light and blocks predominantly green light. The transmitted light is blue, yellow, and red ($a^* > 0$ and $b^* \approx 0$).

4. 520 nm $< \lambda_0 <$ 550 nm: the filter blocks yellow in addition to green light. The transmitted light is red and blue ($a^* > 0$,$b^* < 0$).

5. 550 nm $< \lambda_0 <$ 570 nm: the filter starts blocking red light and starts passing green light. The transmitted colour is blue and green ($a^* \approx 0$,$b^* < 0$).

6. 570 nm $< \lambda_0 <$ 650 nm: the filter blocks red, passes green, and starts

passing yellow light. The transmitted colour is yellow, blue and green ($a^* < 0, b^* \approx 0$).

7. $\lambda_0 < 650$ nm: The stopband moves into the infrared and the transmitted colour approaches white ($a^* \approx 0, b^* \approx 0$).

To achieve the design goal of maximum colour change (ΔC, Eq. 6.4) with minimal wavelength shift, note the regions where the colour change (Fig. 6.3b) is highest. Two λ_0 regions are of interest: between 450 and 520 nm and between 550 and 600 nm. PCs with λ_0 in these intervals will exhibit large colour changes for small wavelength shifts. Because of scattering and absorption, which occur at shorter λ, the second interval is more appropriate for this work.

6.4 Fabrication

The 1D PC is fabricated following the previously described method (see Sec. 5.3.1), by alternating deposition of high- and low-index sublayers (denoted H and L). The deposition angles corresponding to these layers was chosen to be α_H=60° and α_L=80°. These angles were selected for multiple reasons. First, because depositing at low α creates a dense structure, excessively low deposition angles may inhibit the penetration of water vapour into the deeper layers of the PC and negatively impact the performance of the PC sensor. At 60°, the pores are sufficiently large and the pore network sufficiently open to allow appreciable vapour condensation in the film [220]. A second reason is that near these angles, the surface area of the structured GLAD-film is near its peak [220, 221]. The third reason is that at high α, the deposited structures grow larger and optical scattering becomes detrimental to PC band gap formation. Studying the impact of (α_H,α_L) on sensor performance presents an excellent opportunity to optimize the PC sensor, but is beyond the scope of this thesis.

Twelve and one-half periods were deposited in total creating the layer sequence $(HL)^{12}H$. A two nanometer transition interval between H- and L-layers was incorporated in the motion algorithm to provide sufficent time for stable substrate movement. The H- and L-layer thicknesses were calculated to produce quarter-wave optical path lengths at the design wavelength λ_0 = 560 nm, targeting the wavelength interval described in the previous section.

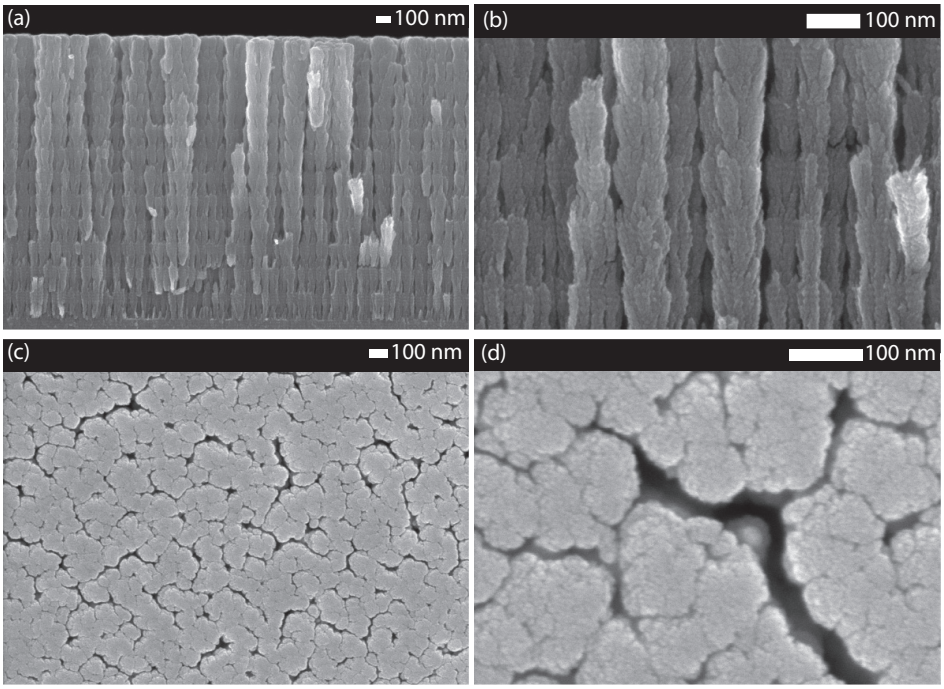

Figure 6.4: SEM images of the 1D PC sensor. (a) and (b) are side-on images of the exposed PC edge taken at magnifications of 40 000 and 110 000. (c) and (d) are top-down images of the film surface taken at magnifications of 50 000 and 200 000. The side-on views show the columnar nature of PC, as well as the periodic density stratification. The porous surface of the PC, allowing water vapour to enter and condense inside the PC, and be seen in the top-down views.

6.5 Structural characterization

Fig. 6.4 shows four SEM images of this PC. Figs. 6.4a and b are images of the PC cross-section taken at different magnifications. The structural stratification characteristic of GLAD-fabricated 1D PCs is evident. This structural variation creates the refractive index contrast responsible for the formation of a reflectance band when the Bragg condition is satisfied. The average thickness of the H- and L-sublayers is measured to be $d_H = 76 \pm 2$ nm and $d_L = 84 \pm 3$ nm. (The uncertainties are equal to one standard deviation.) Also visible is fine structuring on a $\approx$10 nm scale. This structural roughness is created by the motion of the substrate which completes one

rotation every 10 nm of growth. Another source of fine structuring is the bundling of microcolumns, as explained by the evolutionary model of film growth (Sec. 2.2.4). In this model, a given columnar feature is itself composed of smaller, tightly bundled substructres, which in turn are composed of even smaller bundled structures. In the visible wavelength range of interest, these features are practically invisible but may add a weak, Rayleigh scattering contribution to the optical properties of the overall PC.

Figs 6.4c and d show the top surface of the PC at different magnifications. From these SEM images, several observations about the PC porosity can be made. The pore structure that forms in the PC is hierarchical. In Fig. 6.4c, slit-like pores can be seen, roughly 10-20 nm in width and varying in length. These pores chain together and branch-off of one another, forming an intricate, highly interconnected network. Examining the surface at higher magnification (Fig. 6.4d) sees this pattern repeated, although on a smaller scale. In addition to the larger slit-like pores, an equally interconnected and intricate network of smaller slit-like pores is present. Fractal-type scaling such as this has been previously observed in GLAD-fabricated films [222, 223] and can be understood again using the evolutionary growth model. The pores can be viewed as defining "grain boundaries" between bundles of columns. Because the size of the column bundle extends over several length scales from a few nanometers to nearly a micrometer [64], a heirarchial pore network emerges and develops in between the bundles.

The International Union of Pure and Applied Chemistry (IUPAC) defines three pore types, classified based on the pore width w_p [224]: macropores ($w_p > 50$nm), mesopores (2nm $< w_p <$ 50nm), and micropores ($w_p <$ 2nm). Using this nomenclature, the top-most $\alpha_H = 60^\circ$ layer has a pore structure composed of meso- and micropores. However, from the SEM observations the pore sizes continuously span across these ranges and describing the layer as a hierarchical structure of meso- and micropores is more appropriate.

Because the film is terminated by the $\alpha_H = 60^\circ$ layer, the other sublayers cannot be directly imaged top-down. Observations of the internal film structure must therefore be obtained from the high magnification cross-sectional SEM image in Fig. 6.4b. This image examines the film near its thickness midpoint. In the $\alpha_L = 80^\circ$ layers the columnar structure is visible but the

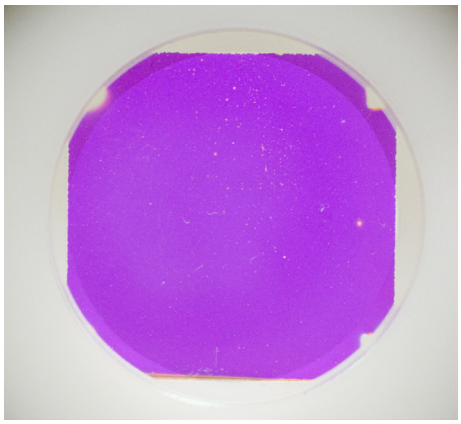

Figure 6.5: A photograph of the colourimetric PC sensor taken at low relative humidity. The colour of the film is determined by the transmitted light. Because the PC reflects green and yellow and passes blue and red wavelengths, the resulting sample colour is magenta.

space between columns is larger than in the $\alpha_L = 60°$ layers. Even so, the spacing is less than 50 nm, meaning that the porous L-layers remain in the mesopore regime.

6.6 Optical characterization

The first optical characterization of the sample, done immediately and unavoidably upon removal from the system, is visual. A photograph of the film is shown in Fig. 6.5. To obtain this image a white screen was placed behind the film, creating a large, diffuse white-light source. The light sources behind the camera were dim, meaning that the camera only captures the transmitted light. The sample is held in a polytetrafluoroethylene (PTFE, Teflon®) mount which was used to set the white point of the photograph in Adobe®Photoshop®CS3.

The optical transmittance $T(\lambda)$ at normal incidence was measured using the spectrophotometer. $T(\lambda)$ was measured in 0.5 nm increments for wavelengths from 400 nm to 1000 nm. The results are shown as data points in Fig. 6.6. The transmittance measurement reveals the presence of a photonic band gap centred at λ_g = 548 $\pm$ 0.5 nm. The band gap is created by constructive and destructive interference of the reflected and transmitted

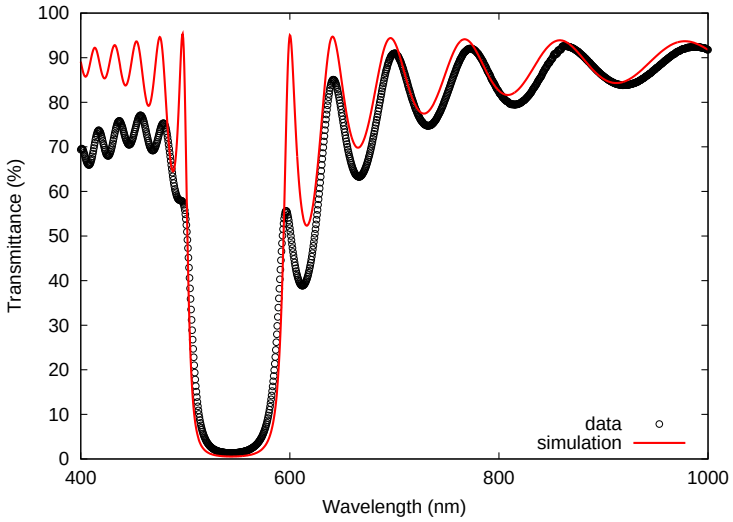

Figure 6.6: Measured (data points) and simulated (red curve) spectral transmittance through a 12.5 period Bragg multilayer. The strongly reduced transmittance, with an 82 nm bandwidth centred at λ_g = 548 nm, corresponds to the destructive and constructive wave interference of a photonic band gap.

waves. The band is blue-shifted by 12 nm from the design wavelength of 560 nm. The bandwidth of the gap is $\Delta\lambda$ = 82 nm, measured between points of 30% transmittance. The magenta colouration of the sample, as seen in Fig. 6.5, can be understood from the transmittance spectrum. The sample blocks green and yellow coloured wavelengths and transmits blue and red coloured wavelengths. The transmitted colour is therefore a mixture of blue and red, which is magenta. The CIE colour values are calculated from the transmittance spectrum: the (X,Y,Z) values are (38.6, 21.0, 75.9), and the (L^*,a^*,b^*) values are (53.0, 72.9, -58.4).

Also shown on Fig. 6.6 is the results of fitted characteristic matrix simulations for this film (solid red curve). The film was modeled as a stack of 25 layers, following the pattern $(HL)^{12.5}H$, with the measured layer thicknesses. The layer index dispersion was specified using a two-term Cauchy equation $n = A + B\lambda^{-2}$. The MSE was minimized by numerically optimizing (via the LM algorithm) the parameter set (A_H, B_H, A_L, B_L). The B values were constrained to be positive, to ensure normal dispersion behaviour. The optimized parameters, with 1σ uncertainty estimates, are A_H = 1.81 $\pm$ 0.01, B_H

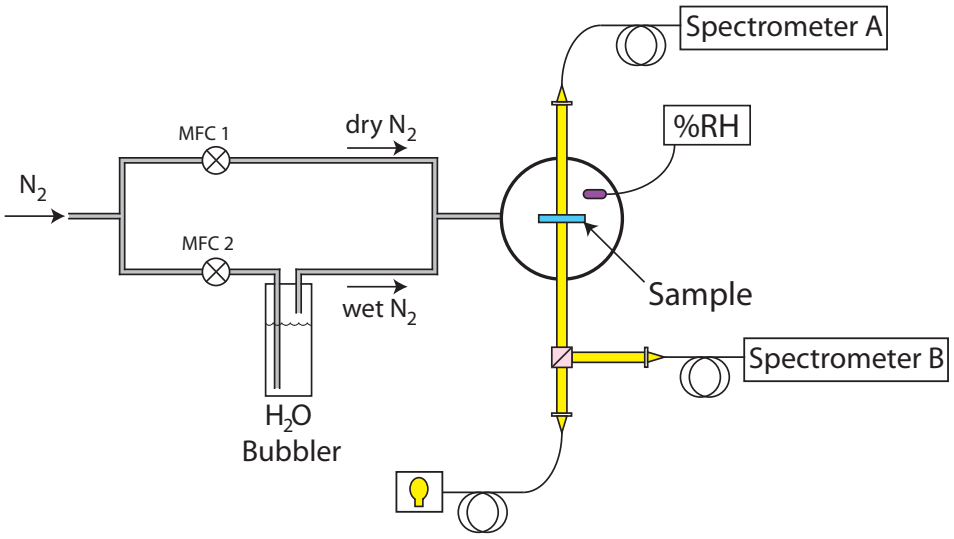

Figure 6.7: Experimental apparatus for measuring the humidity sensitivity of the photonic crystal samples. The flow rates of dry and wet N_2 are set independently by two mass flow controllers (MFC1 and MFC2).

= 0 $\pm$ 0.0044 and A_L = 1.19 $\pm$ 0.02, B_L = 0.066 $\pm$ 0.005. These dispersion parameters correspond to indices of n_H = 1.81 $\pm$ 0.03 and n_L = 1.41 $\pm$ 0.03 at λ = 548 nm. The fit *MSE* is 97.3. Good agreement is observed between the measured and simulated data indicating that the model is a good approximation of the sample. The simulation accurately reproduces the band gap depth and width. The agreement is also good in the interference fringes away from the band gap, particularly at longer wavelengths. At shorter wavelengths, scattering losses lead to poorer fits, although the fringe-period agreement is good.

6.7 PC sensor humidity response

6.7.1 Environmental test chamber

To investigate the operation of this PC as a humidity sensor requires studying the effects of water vapour on the PC sample optical properties. This is accomplished by integrating an optical measurement apparatus into an environmental test chamber capable of controlled humidity changes, shown in Fig. 6.7. The test chamber, developed by Steele *et al.* [28] and based on

an earlier design used by Steele *et al.* [199], recieves a mixture of two gases. One is dry N_2, for which RH$\approx$ 0%. The second is wet N_2, obtained by bubbling dry N_2 gas through a water resevoir. Two mass flow controllers (maximum flow rates of 500 sccm) set the ratio of dry to wet N_2 delivered to the chamber. By varying the flow rates of the two gases, RH control between approximately 3% and 90% was achieved. A single RH test cycle began at a low-RH point, established by a 500 sccm flow of dry N_2 and a zero sccm flow of wet N_2 into the chamber. The dry / wet flow rates were then decremented / incremented by 25 sccm every 300 s until the flow ratio was 0:500 sccm of dry:wet N_2. This creates the high-RH point. The dry / wet flow rates were then incremented / decremented by 25 sccm every 300 s until the starting flow ratio was reached. This flow rate progression constituted a single RH cycle. The test chamber RH was continuously monitored using a commercial RH sensor (Vaisala HMP100), previously calibrated with standard salt solutions [225, 226]. Note that the RH control is an open loop; no feedback is used to reach RH set points.

The chamber was fitted with two windows providing optical access to the sample during testing. The output from a white-light source (Ocean Optics LC-1, tungsten halogen lamp) was collimated and directed onto the sample. The transmitted beam was focused into an optical fibre and sent to a CCD spectrometer (Ocean Optics HR4000; spectrometer A in Fig. 6.7). A beam splitter was placed between the source and sample, allowing a second CCD spectrometer (Ocean Optics USB2000; spectrometer B in Fig. 6.7) to monitor the lamp output. The transmitted signal can then be normalized to a 100%-transmittance reference signal. A computer program logged the measured and reference spectra every 60 s, stamping the data with time and RH. To test the repeatability of PC sample humidity response, transmittance spectra were collected over 28 complete RH cycles.

6.7.2 Measured optical response

Fig. 6.8 shows the measured PC sensor transmittance spectrum at different humidity values during the rising portion of the first humidity cycle. The spectral features (band gap, interference fringes) are observed to shift to longer wavelengths as the RH increases. This is consitent with the understood sensing mechanism. As the humidity increases, water vapour moves

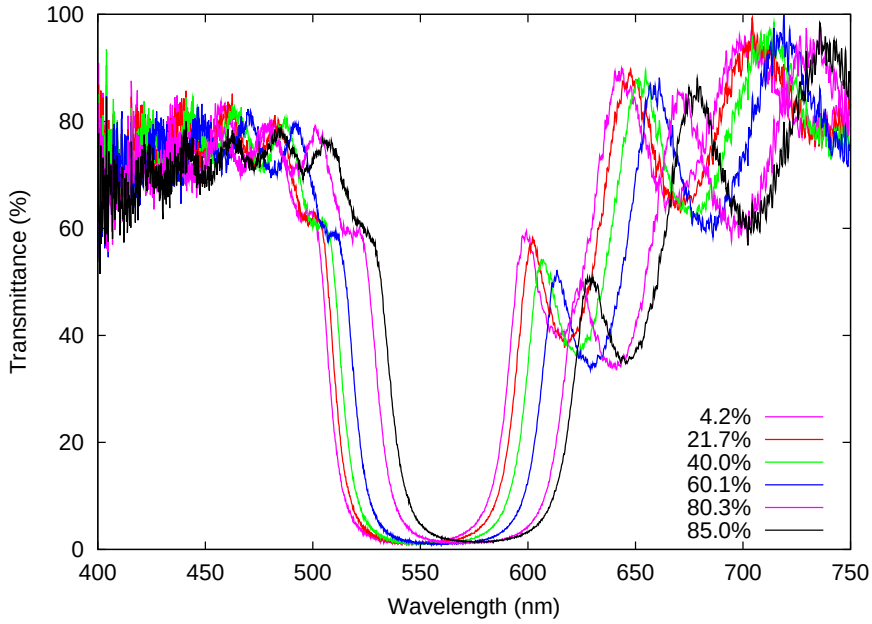

Figure 6.8: Measured transmittance of the PC sensor at different humidity values during the rising portion of the first humidity cycle. The PC band gap shifts to longer wavelengths, consistent with a refractive index increase due to water adsorption in the meso- and micropores of the PC structure.

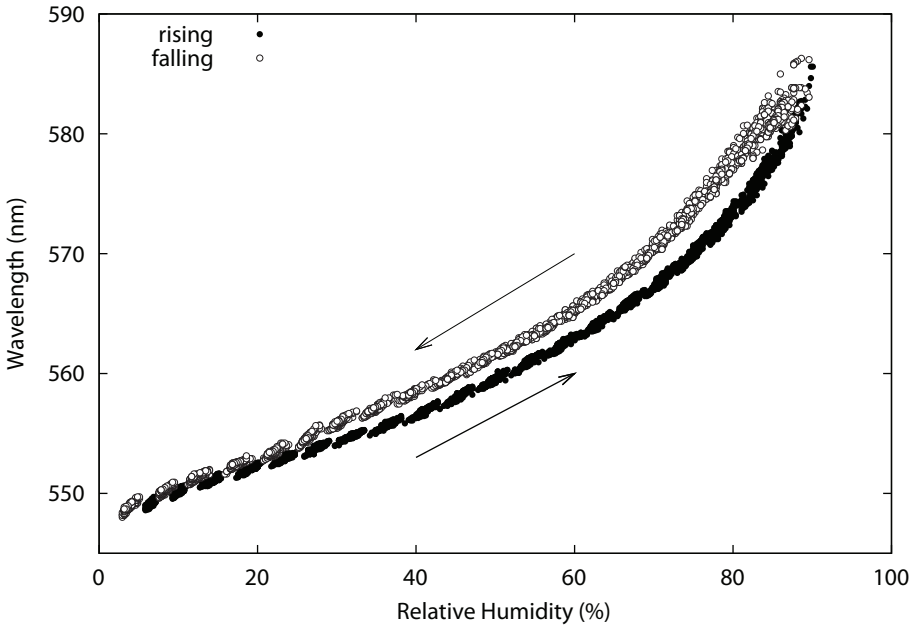

Figure 6.9: Change in the band gap centre wavelength as relative humidity increases (filled circles) and decreases (open circles). The stopband shift changes the PC colour, allowing visual detection of changes in relative humidity.

into the PC pore structure and condenses on the internal surfaces. This increases the average refractive index of the PC sublayers, thus increasing the sublayer optical path lengths and redshifting the Bragg resonance condition repsonsible for the PC stopband.

From the measured transmittance spectra, the band gap centre wavelength λ_g was extracted for all 28 RH cycles (midpoint between 30% transmittance points along the bandedges). Fig. 6.9 shows how λ_g changes with humidity. The λ_g values were divided into two sets depending on whether the humidity was rising (filled points) or falling (open circles).

For the given rates of flow change, 28 cycles corresponds to over 95 hours of testing. Over the measured 28 cycles, the λ_g response curves trace verynearly the same path which demsontrates the repeatability and stability of the PC sensor response. Fig. 6.10a shows λ_g at 50% RH from cycle to cycle. (Because the chamber does not always reach exactly 50% RH, the value of λ_g at 50% was interpolated from the four nearest-neighbour points.) Also

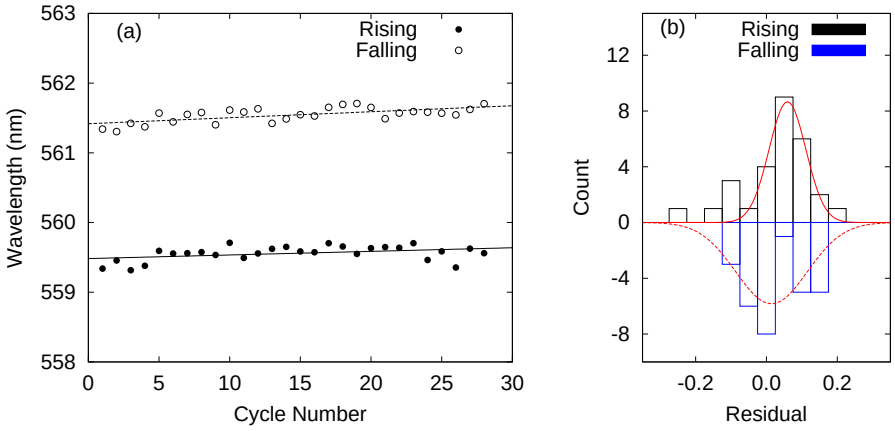

Figure 6.10: The band gap centre wavelength (at 50% relative humidity) exhibits minimal drift from cycle-to-cycle, indicating excellent repeatability.

shown on this figure are linear fits to the data to estimate the λ_g drift. The intercepts are b_{rise} = 559.48 $\pm$ 0.04 nm and b_{fall} = 561.42 $\pm$ 0.03 nm. The slopes of these lines are m_{rise} = (5.2 $\pm$ 2.4) $\times$ 10^{-3} nm/cycle and m_{fall} = (8.6 $\pm$ 2.0) $\times$ 10^{-3} nm/cycle, where one cycle lasts 200 minutes. Extrapolating these drift estimates yields wavelength shifts of 1 nm every 641 $\pm$ 296 (rising) and 398 $\pm$ 90 (falling) hours. This demonstrates the exceptional stability of the PC sensor humidity response.

Fig. 6.10b shows the frequency distributions of the residual ($\lambda_0 - \lambda_{\text{linear fit}}$) at 50% RH for the rising and falling data sets. While there is a time drift in the data, the very small slope associated with this drift means it can be neglected in the following analysis. These histograms therefore estimate the cycle-to-cycle random variation of the PC sensor. A Gaussian distribution (Eq. 3.2) was fit to the histogram. The estimated standard deviations are σ_{rise} = 0.052 $\pm$ 0.007 nm and σ_{fall} = 0.10 $\pm$ 0.03 nm. Although the sample size is small (28 points), the sub-nm standard deviation associated wih the sensor response indicates excellent repeatability.

6.7.3 Colour change of the PC sensor

The CIELAB colour space was previously introduced as a convenient method for calculating colour changes. Therefore, the measured transmittance

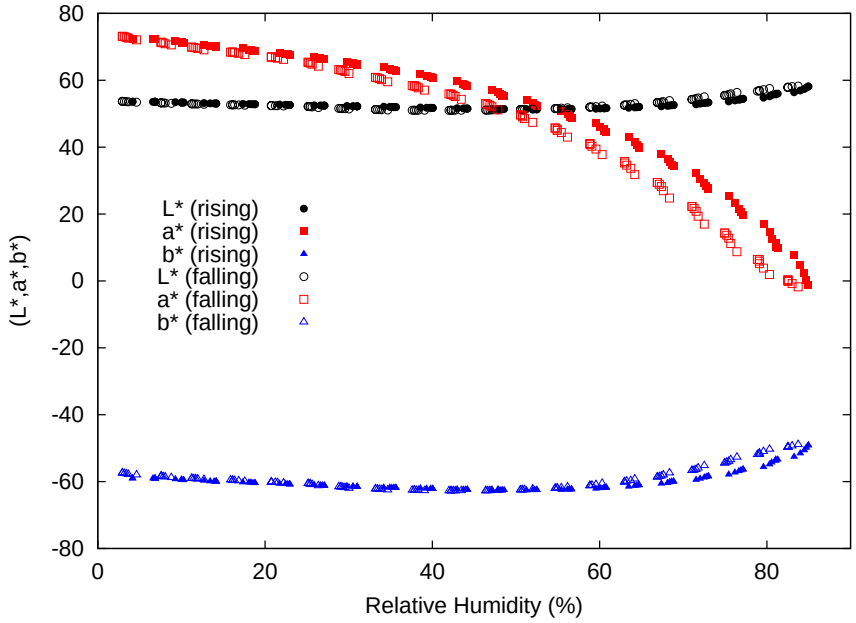

Figure 6.11: The L* (black), a* (red), and b* (blue) colour co-ordinates as a function of chamber relative humidity. The filled and open data points correspond to rising and falling relative humidity values.

spectra were converted to (L^*,a^*,b^*) colour co-ordinates in order to evaluate the performance of the PC sensor in its intended use as a colourimetric sensing device. These (L^*,a^*,b^*) values are shown in Fig. 6.11. Because the observed sensor response is highly repeatable, only the results for a single RH test cycle are shown for clarity of presentation.

At low RH, the colour values of light transmitted through the PC is $a^* > 0$ and $b^* < 0$, which corresponds to a mixture of red and blue (hence the magenta colouration seen in Fig. 6.5). At high RH, the colour values of the transmitted light are $a^* \approx 0$ and $b^* < 0$, a mixture of red, green, and blue. The colour of the mixture is cyan. A photograph of the film at high RH is shown in Fig. 6.12, taken under the same lighting conditions as the photo in Fig. 6.5.

The colourimetric humidity sensitivity of the PC is defined as the colour change (Eq. 6.4) per unit RH change, dC/dRH. Because the RH test chamber is slow respond to RH changes, this calculation uses the measurements taken 300 s after flow rate changes. This avoids sampling the transient re-

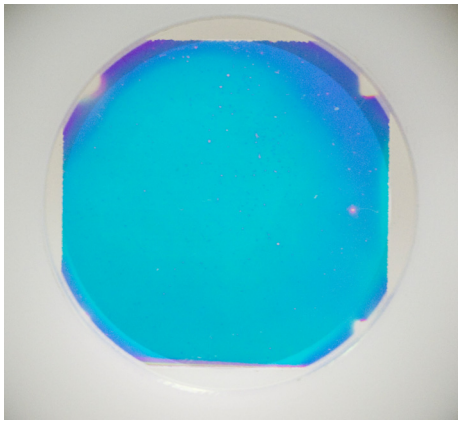

Figure 6.12: A photograph of the colourimetric PC sensor taken at a high relative humidity. The colour of the film is determined by the transmitted light. The PC stopband has shifted to longer wavelengths because water vapour has condensed inside the PC. The PC now reflects yellow and most of the red light while passing blue and green wavelengths. The resulting sample colour is cyan.

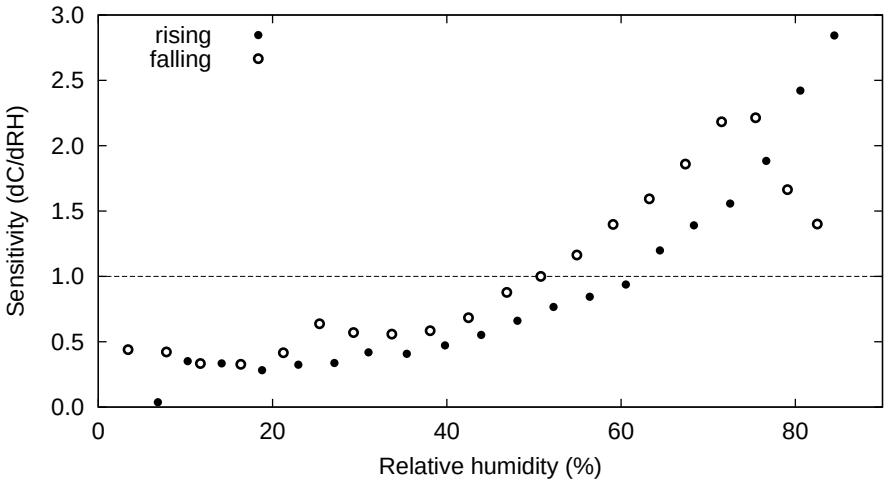

Figure 6.13: The PC sensor sensitivity dC / dRH (colour change per unit relative humidity change) as a function of relative humidity. The dashed line indicates dC / dRH = 1, above which a one-percent RH change is detectable.

sponse of the chamber and isolates the PC response. Fig. 6.13 shows this calculated sensitivity. The PC sensitivity is RH-dependent, exhibiting greater sensitivity at higher RH values. The dashed line on Fig. 6.13 marks for reference the point where dC/dRH is equal to 1. A value of $\Delta C = 1$ corresponds to the approximate threshold of perceptual colour change. Although this depends on both viewing conditions and the observer, it is a good number with which to evaluate the sensor performance. Across the entire measured RH range, the colour change associated with a 3% RH change is percievable. For RH $>$ 60% (rising) or 50% (falling), a 1% change in RH is detectable. This demonstrates the good sensitivity of the PC sensor to a wide range of RH values.

6.8 Hysteresis in the PC sensor response

As previously mentioned, a repeatable hysteresis loop is observed in the PC sensor humidity response. Hysteresis such as this is commonly seen in adsorption isotherms of mesoporous solids [224]. An adsorption isotherm is a measurement of the amount of gas adsorbed by a solid as a function of gas partial pressure (while temperature is kept constant). It has long been recognized that porous solids can take up large volumes of gas by adsorbing gas molecules onto the accessible internal surfaces of the porous solid [211]. The volume of gas adsorbed depends on: the interaction between gas-molecule and solid-surface (mediated by physical van der Waals forces and/or chemical reactions), and the surface and structural geometry of the pores in the solid.

In mesoporous solids (pore sizes between 2 nm and 50 nm), gas adsorption is strongly affected by the phenomenon of capillary condensation (see Sec. 6.1.3). Hysteresis is created by the pore geometry which can break the symmetry between the adsorption and desorption processes. The pore geometry of the PC sensor was discussed in Sec. 6.5. The PC sensors possess cylindrical and slit-like pore structures with a hierarchial range of dimensions. Therefore, water will condense in the PC sensor over a wide range of pressures, resulting in an integrated, smoothly varying response with hysteresis, as is observed.

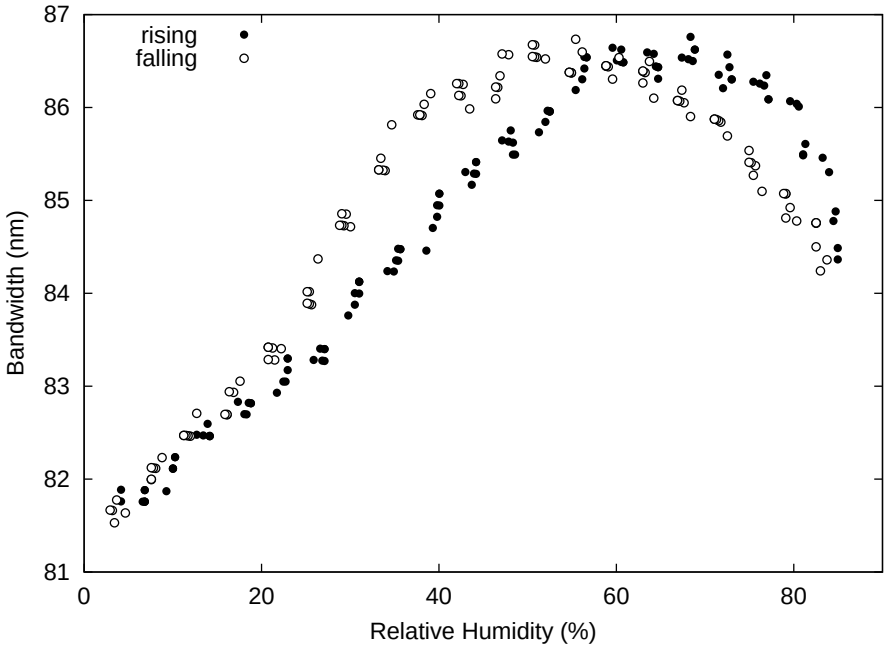

Figure 6.14: The PC band gap width as a function of relative humidity during rising (filled points) and falling (open circles) portions of the humidity cycle.

6.8.1 Wavelength dependent hysteresis

While hysteresis is present at all wavelengths, it has only been shown in the λ_g response. However, intriguing hysteresis behaviour is observed in the bandwidth ($\Delta\lambda$) response, shown in Fig. 6.14. In this plot, $\Delta\lambda$ is shown for rising (dark circles) and falling (open circles) relative humidity. During the adsorption (rising RH) portion of the cycle $\Delta\lambda$ increases with RH, reaching a maximum at approximately 70%. $\Delta\lambda$ then decreases as RH is increased further. As the cycle changes to desorption (decreasing RH), $\Delta\lambda$ increases along a different path, *crossing* the adsorption branch near 60%, and reaching a maximum at approximately 50%. As RH decreases further hystersis is observed until 20%, when the hysteresis loop nearly closes. The end result is a distored figure-eight loop in the $\Delta\lambda$ response curve.

Examining the RH response of the long (red points) and short (blue points) wavelength bandedges (Fig. 6.15) shows that $\Delta\lambda$ cycles in this manner because the RH response is different at these two wavelengths. The

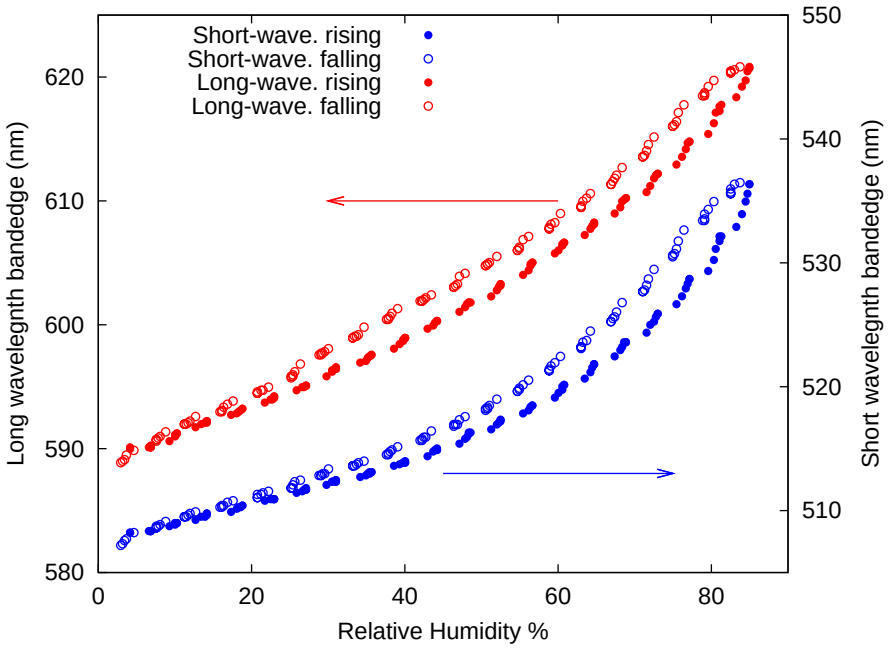

Figure 6.15: Relative humidity dependence of the short-wavelength (blue) and long-wavelength (red) bandedges. Filled and open circles correspond to rising and falling relative humidity values.

long-wavelength bandedge (λ_r) is more sensitive and shows more hysteresis at low RH (<50%) than the short-wavelength bandedge (λ_b). At high RH (>50%) however, the situation is reversed; λ_b is more sensitive and shows greater hysteresis than λ_r. The different RH response curves measured at λ_r and λ_b cause the bandwidth hysteresis to first widen, then close, then widen again, and then close again, as the humidity is cycled.

The difference between the RH responses at λ_b and λ_r originates from the structure of the electric field **E** inside the PC at the bandedges. For freespace wavelengths of λ_b and λ_r, the field propagates in the PC as Bloch modes (Sec. 2.5.1). Both of these Bloch modes have the same spatial wavelength, which is equal to twice the PC structural period. The field of the lower energy mode (λ_r) is concentrated in the high-index regions of the PC, while the field of the higher energy mode (λ_b) is concentrated in the low-index regions.

To confirm this for the PC sensor, the electric field distribution was computed using the same simulation parameters as in Fig. 6.6. This calculation was performed using the characteristic matrix method. Subdividing the PC into J sublayers, the characteristic matrix is given by Eq. 2.14. Once the transmission coefficient is obtained (Eq. 2.19a), it can be used to formulate boundary conditions (Eqs. 2.17 and 2.18) to compute the field z-distributions. The field amplitudes in the q^{th} sublayer, corresponding to z_q, are calculated as

$$\begin{bmatrix} U(z_q) \\ V(z_q) \end{bmatrix} = \left(\prod_{j=q}^{J} \mathbf{M}_j \right) \begin{bmatrix} tA_i \\ \left(\cos\theta \sqrt{\varepsilon_s / \mu_s}\right) tA_i \end{bmatrix} \tag{6.5}$$

where A_i is the amplitude of the incident field. The electric field intensity $|E(z)|^2$, normalized to A_i, is then given by

$$|E(z)|^2 = \frac{U^*(z)U(z)}{A_i^* A_i} \tag{6.6}$$

where * denotes complex conjugation.

The calculation results are presented in Fig. 6.16 which shows the field intensity ($|E|^2$) at (a) 547 nm, (b) 588 nm, and (c) 506 nm. These respectively correspond to the band gap centre wavelength, the long-wavelength bandedge, and the short-wavelength bandedge. Presented on these plots are $|E|^2$ (red curves) superimposed over the refractive index profile $n(z)$ (black line).

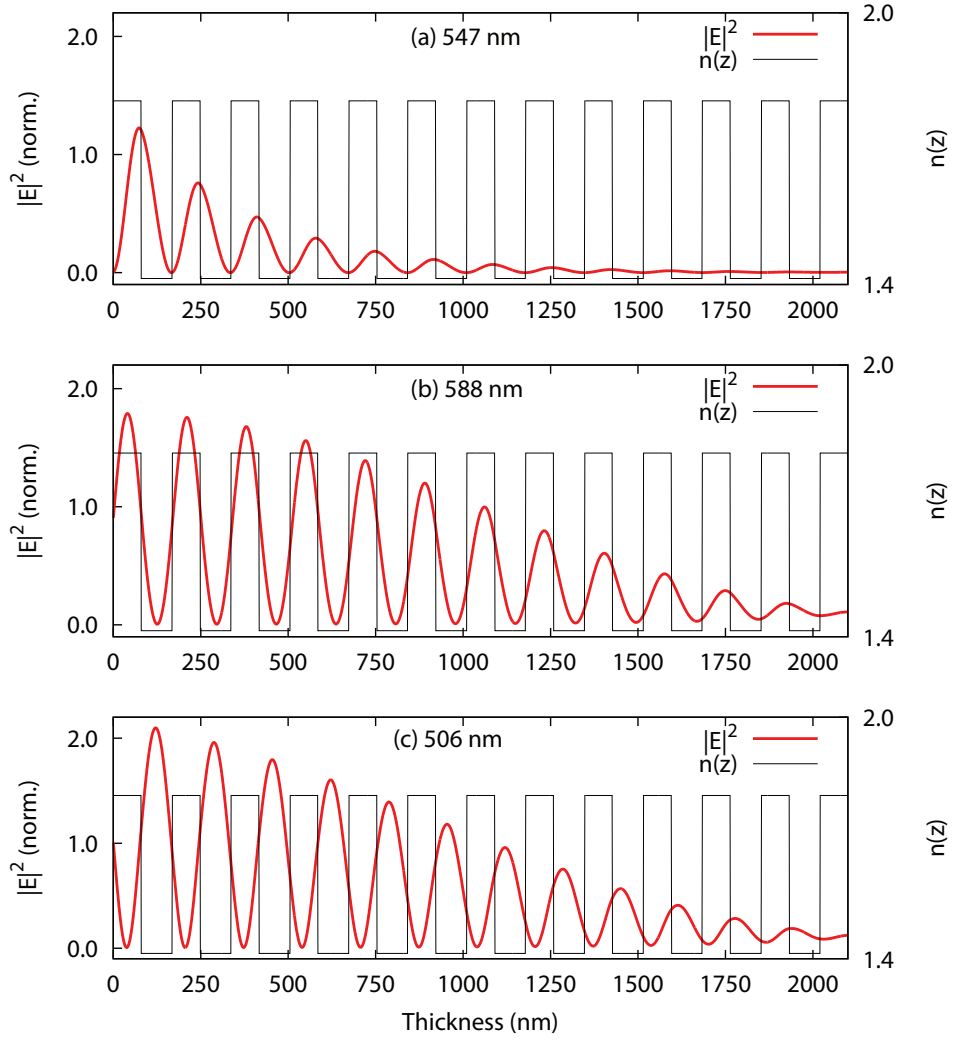

Figure 6.16: The electric field intensity distribution (shown in red) inside the PC at wavelengths of (a) 547, (b) 588, and (c) 506 nm. These wavelengths respectively correspond to the band gap centre, the long-wavelength bandedge, and the short wavelength bandedge. The refractive index profile of the PC is shown in black.

In Fig. 6.16a, the incident field couples to a Bloch mode: the field intensity varies with the same period as the PC. However, because of interference, the mode is evanescent inside the PC and does not propagate. In Figs. 6.16b and c, the field couples to propagating Bloch modes. As expected, at λ_r the field intensity is concentrated primarily in the high-index regions of the PC. At λ_b the field is concentrated in the low-index region.

Because the high- and low-index regions of the PC are structured differently, the bandedge modes sense different pore structures. Therefore, the bandedge modes will have different humidity responses due to differences in capillary condensation. The λ_b mode probes a region with larger pore structures (larger r_m). Because water vapour requires higher p to condense in these pores the λ_b mode is less sensitive to low RH levels, but water quickly condenses at high RH, leading to rapid optical changes. The other bandedge mode, λ_r, senses the smaller pore structures in the high-index regions. In these smaller pores, water begins condensing at lower p, leading to higher sensitivity at low RH values.

6.9 Summary and Conclusions

This chapter examines the design, fabrication, and characterization of a PC RH sensor. Sensing through colourimetric changes is an attractive approach, requiring only visual inspection for sensor readout. Capillary condensation of water vapour in the internal mesopore structure of the PC increases the optical pathlength and shifts the PC spectral features to longer wavelengths. Consequently, the PC colouration is sensitive to the presence of water vapour. This work presents the first use of GLAD in such a sensor design.

Because the PC sensor possesses a heirarchial pore structure, it is sensitive to water over a wide range of RH values. The device is capable of detecting RH changes as small as 3% across the full dynamic range of the sensor. This sensitivity improves to 1% at high RH ($>$50%). Extended testing over multiple RH cycles shows that the sensor response is very stable and repeatable, an important feature for real-world application of the sensor device.

Because this experiment examines only one PC, with sublayers deposited

at α_H=60° and α_L=80°, it would be interesting to examine different (α_H,α_L) combinations and see how it affects the sensor. The results of this work are also extendable to other materials and compatible with surface sensitization methods [227]. Furthermore, this work demonstrates that the total spectral (and hence colour) response of the PC sensor is determined not only by the pore structure but also by the spatial distribution of the fields within the PC. This presents a large parameter space providing an excellent opportunity to tailor and optimize the sensor response. Another possibility is to develop a multiplexed sensor array of PCs responding differently to analyte mixtures. Such a multiplexed sensor could function as an “optical nose” where the presence of analytes is quantified from spectral signatures in the PC response [190].

Chapter 7

Defects in Periodic Structures: Optical Microresonators

A promising approach to enhancing PC functionality is to alter the PC index profile over a small area, essentially creating a localized defect in the periodicity [228–230]. Because the band gap prevents propagation into the surrounding periodic media, light is confined to the defect. This provides new methods for controlling and manipulating the flow of light. Studying engineered PC defect structures is one of the most important disciplines in the PC field with a wide-range of optical devices applications, including lasers [231], waveguides [232], light-emitting diodes [233], sensing [178, 179, 234], and slow-light optics [235].

Defect incorporation in GLAD-fabricated PCs is an unexamined field, presenting an excellent opportunity to realize complex, functional PC devices. This chapter briefly introduces relevant theory on PC defects before examining defect incorporation in GLAD-fabricated periodic multilayers. Several defect architectures are examined, based on $\lambda/2$-defect layers in Bragg PCs and index phase-shifts in rugate PCs. Excellent control and tunability of the defect behaviour is demonstrated. Thesis research presented in this chapter has been published in *Journal of Applied Physics* [236] and *Optics Express* [237].

7.1 Defects in 1D PCs: optical microresonators

Light in a PC defect is effectively confined in a cavity between two PC mirrors. Consequently, when the light is phase-matched to the cavity mode, the electromagnetic field is enhanced through a Fabry-Perot resonance [230]. PC defects are frequently referred to as microresonators since the defect cavity dimension is on the order of a single wavelength. A key parameter of any resonant system is the quality factor Q, defined as the (time-averaged) energy stored in the cavity divided by the energy loss per cycle [2]. In the optical case, this definition describes the balance between energy stored in and the power radiated out of the PC defect.

Exact treatment of PC defects requires complicated simulations, usually involving vectorial solutions of Maxwell's equations in three-dimensions [238, 239]. However, many PC defect characteristics can be explained using a simple harmonic oscillator model. Furthermore, this simplification provides great insight regarding defect mode properties. A damped, oscillating system excited by a periodic driving force is modelled as a second-order differential equation [213]. In an underdamped, near-resonance system, the system's amplitude response $L(\omega)$ follows the Lorentzian equation

$$L(\omega) = I_0 \frac{\gamma}{(\omega - \omega_0)^2 + \gamma^2}, \tag{7.1}$$

and the system's phase response $\vartheta(\omega)$ is given by

$$\vartheta(\omega) = \text{atan}\left(\frac{-\gamma\omega}{\omega_0^2 - \omega^2}\right). \tag{7.2}$$

In these two equations, ω is the driving force frequency, ω_0 is the system resonant frequency, I_0 is the peak amplitude at resonance, and γ is the damping coefficient.

As indicated by Eq. 7.1, the amplitude response is resonantly increased for ω near ω_0. In the relevant case of a PC defect, light propagation through the structure is greatly increased by resonance. Consequently, optical measurements will reveal a Fabry-Perot-type transmittance peak within the PC band gap. The spectral shape of this peak corresponds to Eq. 7.1 [240]. Transmittance is maximized at resonance ($\omega = \omega_0$). The peak FWHM $\Delta\omega$ is

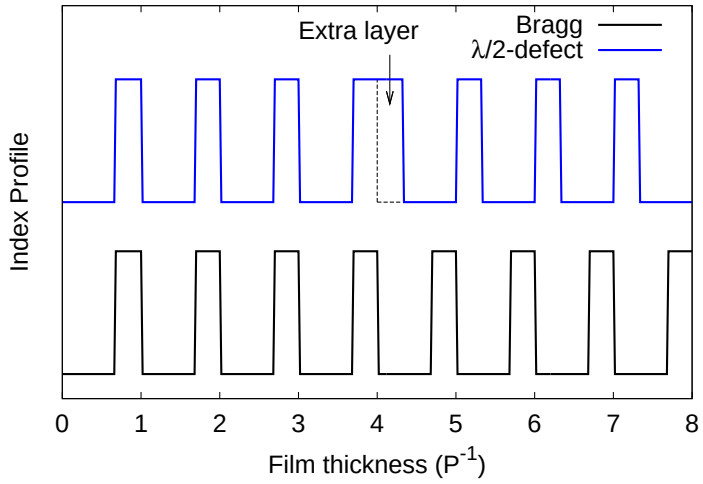

Figure 7.1: Refractive index profiles of a normal Bragg multilayer (black) and a Bragg multilayer with a half-wave layer (blue line).

equal to 2γ. The electromagnetic field energy escapes the defect by (1) penetrating through the finite PC mirror and radiating into freespace, (2) being scattered in a direction not confined by the (1D) PC mirrors, and (3) being lost to material absorption. These three loss mechanisms are parametrized by γ and determine the quality factor of the PC defect:

$$Q = \frac{\omega_0}{2\gamma}. \tag{7.3}$$

The results presented in this chapter are discussed primarily in wavelength (λ) and energy ($\mathcal{E}$) units. These quantities are related to ω in the above equations via $\mathcal{E} = h\omega = hc/\lambda$, where h is Planck's constant. To quickly convert γ between different units, note that $\Delta\omega = 2\gamma$ and

$$Q = \frac{\omega_0}{\Delta\omega} = \frac{\lambda_0}{\Delta\lambda} = \frac{\mathcal{E}_0}{\Delta\mathcal{E}}.$$

7.2 Defect structures in Bragg multilayers

The Bragg multilayer (Sec. 2.5.2) is the simplest 1D PC and has long been used to fabricate high-reflectance all-dielectric mirrors [95]. A defect is incorporated in this structure through the insertion of an extra quarter-wave

layer [241]. Fig. 7.1 illustrates this process. The black line corresponds to a normal Bragg multilayer and the blue line shows the same profile with an extra quarter-wave layer (dashed line) inserted after four periods. Inserting this additional layer causes resonant transmission through the Bragg multilayer, but only over a narrow wavelength range. This structure is commonly used to create distributed feedback (DFB) laser resonators [242, 243], employed in wide-ranging applications.

7.2.1 Sample fabrication and characterization

Realizing this $\lambda/2$-defect multilayer structure using GLAD requires only a slight modification of the substrate motion algorithm discussed in Sec. 5.3.1. An extra H-sublayer was added to the centre of a twelve-period Bragg multilayer. The design parameters α_H, α_L, and λ_0 of this multilayer were 40°, 80°, and 670 nm, respectively. This parameter set corresponds to film L in Table 5.4, providing an unmodified Bragg multilayer for comparison. The film was deposited onto both p-doped Si and B270 glass substrates using the deposition conditions described in Sec. 3.1.4. Samples prepared on Si wafers were cleaved and the exposed edge examined via SEM. The optical transmittance spectrum at normal incidence was measured using the spectrophotometer.

7.2.2 Bragg multilayer defect: Structural properties

Fig. 7.2 shows cross-sectional SEM images of the $\lambda/2$-defect multilayer. Fig. 7.2(a) shows the entire film thickness and the characteristically stratified structure of the Bragg multilayer is clearly visible. After eleven sublayers, an H-sublayer of twice the regular thickness can be seen. This corresponds to the $\lambda/2$-defect layer. Fig. 7.2(b) shows this defect layer at higher magnification. From this SEM image, the defect layer is measured to be 175 ± 20 nm. The estimated defect layer boundaries are indicated, with the dashed lines indicating uncertainty in the sublayer interface location.

7.2.3 Bragg multilayer defect: Optical properties

The measured optical transmittance spectrum of the $\lambda/2$-defect multilayer is presented (solid red line) in Fig. 7.3. Also shown in this figure is the mea-

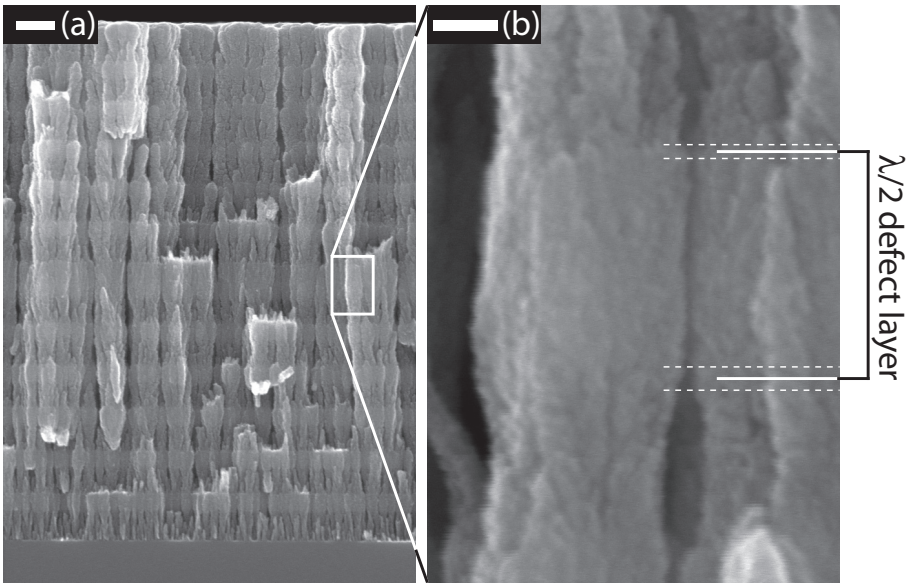

Figure 7.2: Cross-sectional SEM images of a Bragg multilayer with a $\lambda/2$ defect layer in the film centre. (a) shows the entire twelve period film with a 200 nm scale bar. (b) is a close-up, higher resolution image of the defect layer with a 50 nm scale bar.

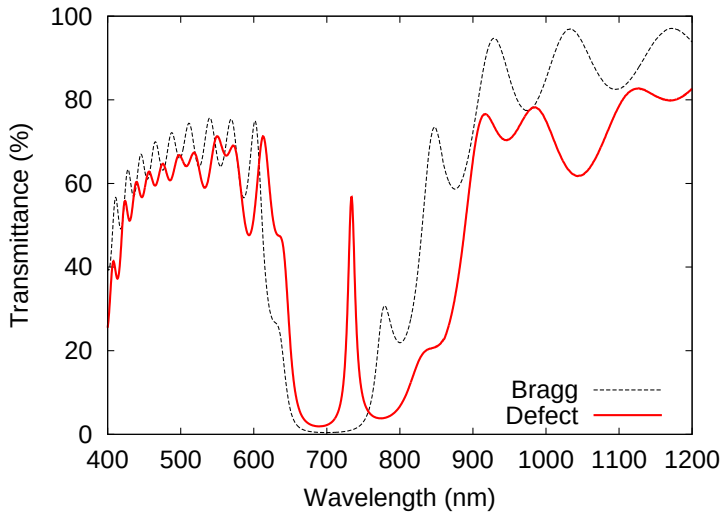

Figure 7.3: Measured optical transmittance spectra of Bragg multilayer structures with (solid red line) and without (dashed black line) a $\lambda/2$-defect layer. The defect layer causes resonant transmittance over a narrow wavelength band within the larger photonic stopband.

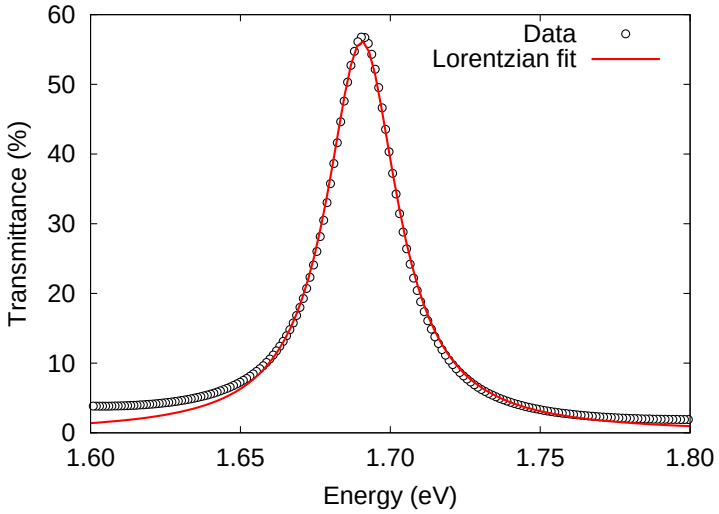

Figure 7.4: Measured optical transmittance of the $\lambda/2$-defect multilayer (data points) plotted in energy units. A Lorentzian function (Eq. 7.1, red line) is fit to the measured data.

sured transmittance of the defect-free Bragg structure (dashed black line). Within the $\lambda/2$-defect multilayer band gap, a narrow band of wavelengths are transmitted through the film. This transmittance peak is absent in the defect-free film spectrum. Over this narrow wavelength band, light incident on the PC couples to the defect layer, is resonantly confined in the defect cavity, and then couples out of the PC at the substrate interface. This result is the first successful realization of $\lambda/2$-defect Bragg filters using the GLAD fabrication approach.

Fig. 7.4 plots the $\lambda/2$-defect multilayer transmittance (data points) in energy units (eV). Eq. 7.1 (with ω converted to E) is fit to the data using the LM algorithm. The Lorentzian function nicely describes the shape of the transmittance pass band. The best-fit curve parameters are $I_0 = 56.2 \pm 0.3$ %, $\mathcal{E}_0 = 1.69053 \pm 0.00009$ eV, and $\gamma = 0.0144 \pm 0.0001$ eV. This corresponds to peak transmittance at a wavelength $\lambda_p = 733.91 \pm 0.04$ nm and a resonance Q-factor of $Q = 58.7 \pm 0.5$.

7.3 Defect structures in rugate multilayers

As previously mentioned, $\lambda/2$-defect layers in Bragg multilayers are commonly used in DFB laser applications and their properties are well-studied. Defects in periodic gradient-index profiles, such as the rugate multilayer, are comparatively unexplored. Likely, this discrepancy is due to the greater difficulty in preparing graded-index multilayers relative to Bragg multilayers. However, the GLAD technique is able to fabricate rugate structures in a straightforward manner as was shown in chapter 5. This provides an excellent opportunity to examine new defect structures.

One method to introduce graded-index defects is with spacing layers, as is done in Bragg multilayers. However, a different approach involves abruptly altering the sinusoidal index profile phase at a single point in the film. Consider the previously described rugate refractive index profile (Eq. 2.27), except with a spatially dependent phase term $\phi(z)$:

$$n(z) = n_a + \frac{1}{2} n_p \sin\left[\frac{2\pi z}{P} + \phi(z)\right]. \tag{7.4}$$

Abruptly shifting the index-profile phase by $\Delta\phi$ at the rugate midpoint corresponds to a phase term

$$\phi(z) = \begin{cases} \phi_0 & \text{if } z < L/2 \\ \phi_0 + \Delta\phi & \text{if } z \geq L/2 \end{cases} \tag{7.5}$$

where ϕ_0 is the initial phase and L is the total film thickness. Fig. 7.5 shows the index profiles of a normal rugate (black line) and a rugate with a $\Delta\phi = \pi$-phase shift (blue line). (For both profiles, $\phi_0 = -\pi/2$.) At $z = 4P$, the phase shift discontinuously changes the index from low ($n_a - n_p/2$) to high ($n_a + n_p/2$).

7.3.1 Sample fabrication and characterization

Fabricating a rugate multilayer with a phase term specified by Eq. 7.5 requires a straightforward modification to the substrate motion algorithm discussed in Sec. 5.2.1. At the deposition midpoint ($z = L/2$), the substrate is positioned at $\alpha_{\max}$. To create the defect, the substrate is rotated to $\alpha_{\min}$.

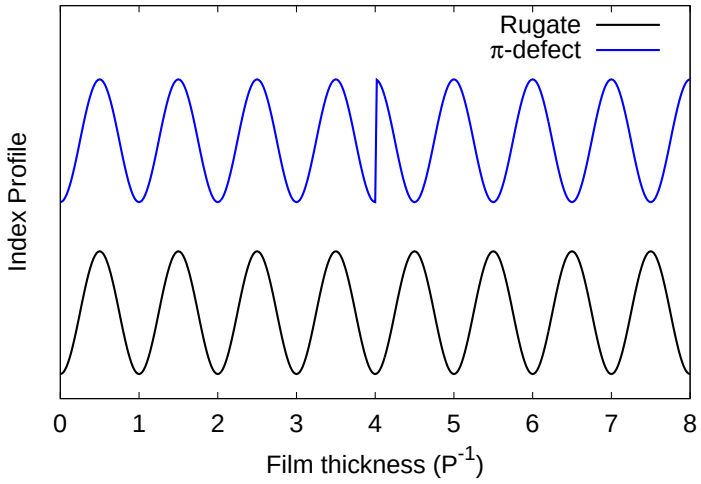

Figure 7.5: Refractive index profiles of a normal rugate filter (black) and a rugate filter with a π-phase shift midway through the film (blue line).

This substrate motion step was performed rapidly to realize the sharpest possible index transition.

A gradient-index multilayer was fabricated using this modified substrate motion algorithm. The film design parameters were the same as film B in Table 5.1 ($\alpha_{\min} = 30^\circ$, $\alpha_{\max} = 80^\circ$, $\lambda_0 = 530$ nm, $L = 16$ periods, $\phi_0 = -\pi/2$). As with Sec. 7.2.1, this provides an unmodified multilayer structure for purposes of comparison. The film was fabricated on p-doped Si and B270 glass substrates. The deposition conditions are described in Sec. 3.1.4. The samples deposited on Si wafers were carefully cleaved and the exposed edge examined via SEM. The sample optical transmittance spectrum was measured at normal incidence using the spectrophotometer.

7.3.2 Phase-shift defect: Structural properties

Fig. 7.6 shows a cross-sectional SEM image of the multilayer taken in the vicinity of the phase-shift defect. The scale bar indicates 200 nm. As was seen in Sec. 5.2.3, the gradient-index varation is achieved by variation of the microcolumn diameter. Over one period, the microstructure smoothly alternates between large-diameter, closely packed columns (corresponding to high refractive index) and smaller-diameter, sparsely packed columns (low

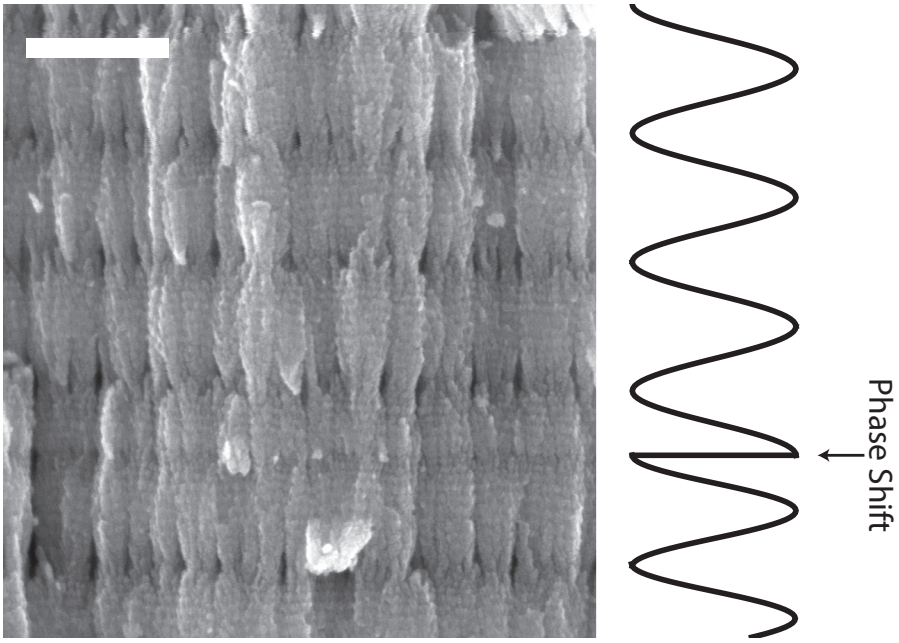

Figure 7.6: An SEM image of the gradient-index multilayer taken in the vicinity of the phase-shift defect. The scale bar indicates 200 nm. The accompanying illustration highlights the sinusoidal structural variation and the phase shift.

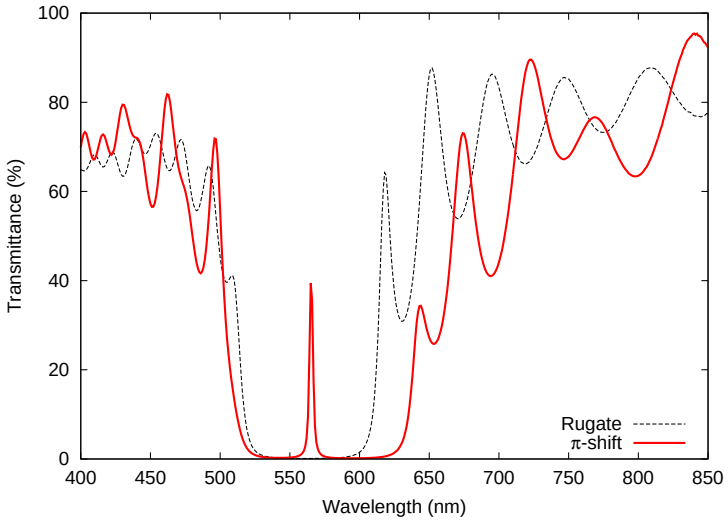

Figure 7.7: Measured optical transmittance spectra of an unmodified rugate multilayer (dashed black line) and a rugate multilayer with a π phase-shift defect (solid red line). The phase-shift causes a narrow wavelength band to be resonantly transmitted through the multilayer.

refractive index). The SEM also reveals a high (spatial) frequency structural variation. This fine structure is caused by the continuous φ rotation (one revolution every 10 nm growth) during deposition. The structural modification caused by the defect can be detected by following the periodic structural variation until a phase change is observed. The diagram to the right of the SEM in Fig. 7.6 is included to illustrate this process and highlight the defect structure. As can be seen from the SEM, the defect is realized by a sudden change from a low- to a high-density structure.

7.3.3 Phase-shift defect: Optical properties

Fig. 7.7 shows the measured optical transmittance spectra of rugate multilayers with (solid red line) and without (dashed black line) a π phase-shift defect. In the former spectrum, a large, spectrally-narrow transmittance peak is observed within the band gap. This transmittance peak is absent in the normal rugate multilayer, indicating the peak is caused by the phase-shift defect.

The transmittance peak is plotted in energy units in Fig. 7.8. Eq. 7.1 (red line) was numerically fit to the data points using the LM algorithm.

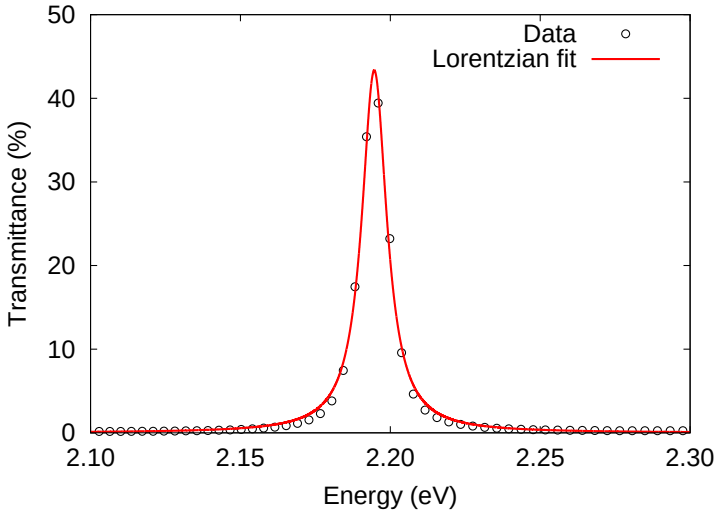

Figure 7.8: Measured optical transmittance of the rugate multiayer with π phase-shift defect (data points) plotted in energy units. A Lorentzian function (Eq. 7.1, red line) is fit to the measured data.

The transmittance peak is well-reproduced by this equation, indicating a Lorentzian resonance response. The best-fit curve parameters are I_0 = 43.3 $\pm$ 0.6, $\mathcal{E}_0$ = 2.19465 $\pm$ 0.00007 eV, and γ = 0.00508 $\pm$ 0.00010 eV. These values correspond to peak transmittance at a wavelength λ_p = 565.33 $\pm$ 0.02 nm and a resonance Q-factor of Q = 216 $\pm$ 4.

This experiment demonstrates that inserting a phase-shift defect in a rugate multilayer creates resonantly enhanced transmittance through the multilayer. The $\lambda/2$ defect layer of Sec. 7.2.3 can be understood as a micro-analog of a Fabry-Perot cavity. However, the phase-shift defect is point-like and does not create an obvious cavity. Therefore, understanding the phase-shift defect resonance requires a somewhat different interpretation.

The interface between two different PC mirrors (in this case, differing in phase) supports a localized surface mode [244]. This is illustrated by Fig. 7.9(a) which presents the calculated electric field intensity distribution at the resonance wavelength λ_p. The calculation method is described in Sec. 6.8.1. The field intensity is normalized to the incident electromagnetic wave. The transmittance peak associated with this resonance is presented in Fig. 7.9(b), where the vertical axis measures %-transmittance. The simulated multilayer index profile is shown in Fig. 7.9(c). As can be seen, the PCs surrounding

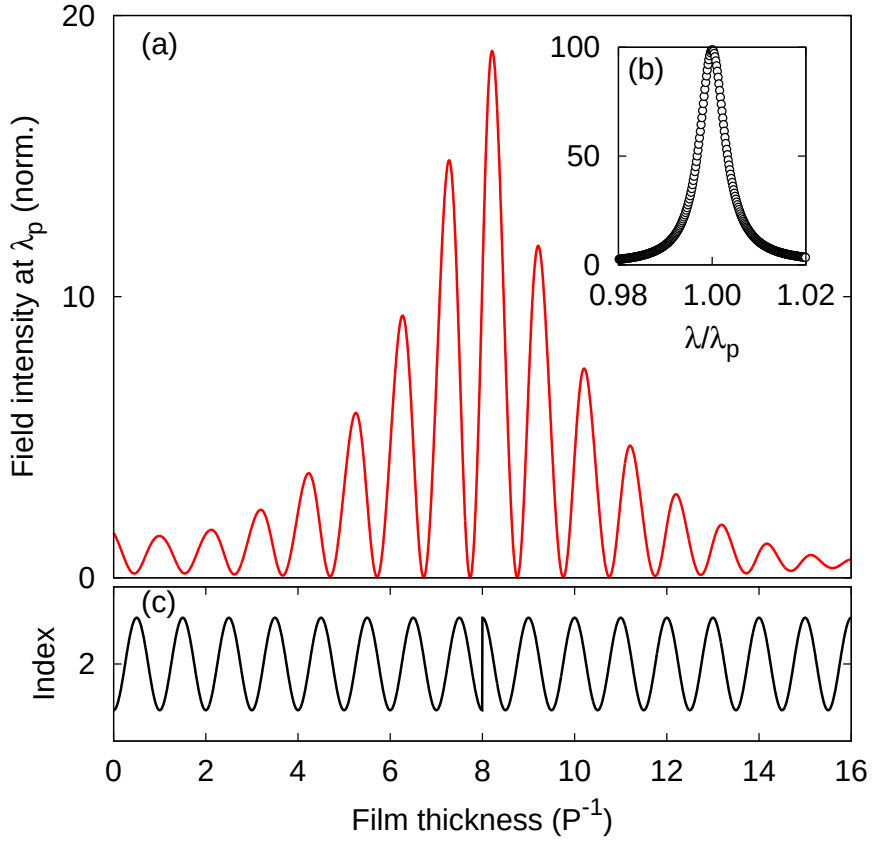

Figure 7.9: Phase-shift defects in rugate multilayers create resonant surface modes. (a) shows the calculated electric field intensity distribution at resonance. The field intensity is normalized to the incident electromagnetic wave. The transmittance peak created by the resonance is shown in (b), where the vertical axis measured %-transmittance. The rugate multilayer index profile, with π-phase shift defect in the film centre, is shown in (c).

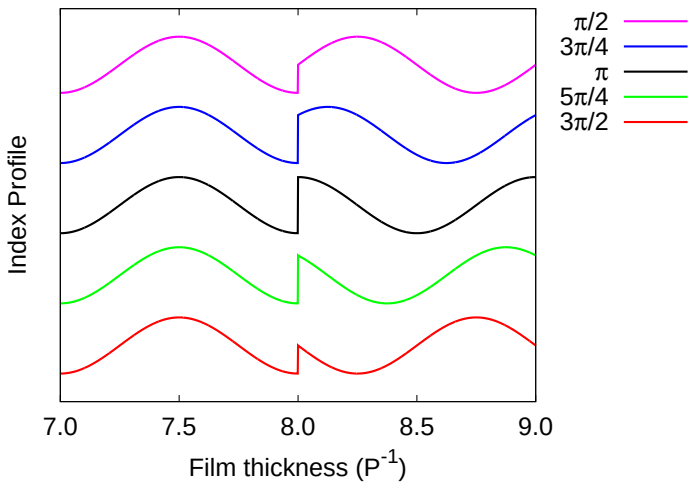

Figure 7.10: The refractive index profiles of rugate multilayers containing defects with different phase-shifts ($\Delta\phi$ in Eq. 7.5). The horizontal axis range is limited to the one period on either side of the defect to allow closer examination of the defect structure.

the defect confine the mode to the interface. At resonance, a standing wave pattern is generated and the modal fields penetrate evanescently into the bounding PCs. Consequently, the light is resonantly transmitted through the PC.

7.4 Controlling phase-shift defects

The defect structure examined in Sec. 7.3 is only a specific case: the phase-shift $\Delta\phi$ in Eq. 7.5 can assume any value between zero and 2π. To examine the effect of $\Delta\phi$ on the defect mode resonance, four 16-period films were fabricated having $\Delta\phi = \pi/2$, $3\pi/4$, $5\pi/4$, and $3\pi/2$. Except for the phase change, the films were prepared in a manner identical to the multilayer fabricated in Sec. 7.3. This provides a set of five multilayers having different $\Delta\phi$ values. The refractive index profiles associated with these defects are shown in Fig. 7.10. To allow closer examination of the defect structures, this figure only shows one period on either side of the defect. Before the defect, the index profiles are all identical. After the defect, the film index transitions to a different point in the sinusoidal variation. The normal-incidence optical

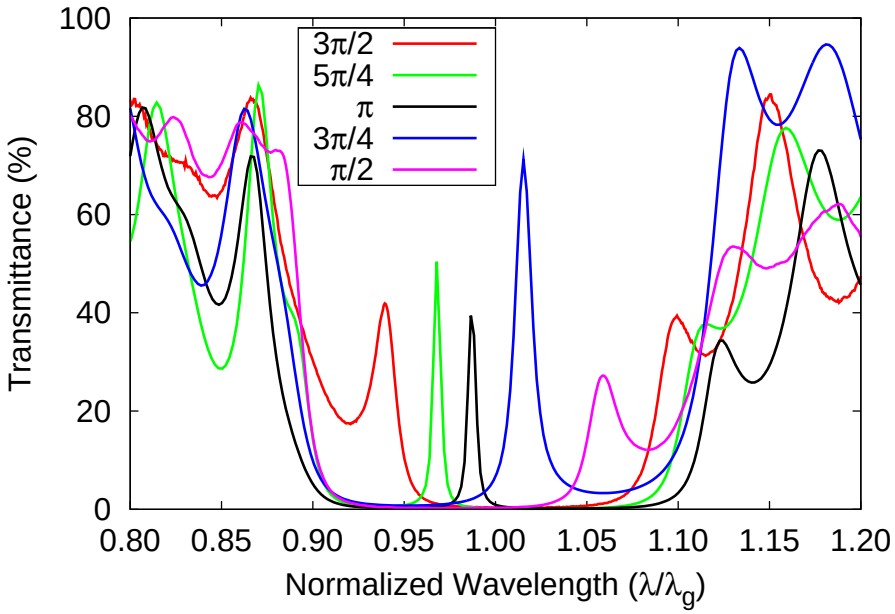

Figure 7.11: Transmittance spectra (normalized to the band gap centre wavelength λ_g) for a set of rugate multilayers with phase defects. The different spectra correspond to phase shifts ranging from $\Delta\phi = \pi/2$ to $3\pi/2$, as indicated by the legend.

transmittance spectrum of each film was measured using the spectrophotometer.

To accompany the fabricated films and verify the experimental results, characteristic matrix calculations were used to simulate a series of multilayers with $\Delta\phi$ from $\pi/2$ to $3\pi/2$ in $\pi/16$ steps. The n_a and n_p parameters of the simulated films were 2.0 and 0.6, respectively. These values were selected based on the results in Table 5.2. For the simulations, the continuous rugate index profile was discretized into one nanometer thick homogenous layers.

7.4.1 Controlling phase-shift defects: Optical properties

Process variability means that the photonic band gaps of each film are spectrally shifted relative to one another by different amounts. Compensating for these shifts is required to allow comparison between the multilayers. Therefore the wavelength units of each spectrum were normalized to the

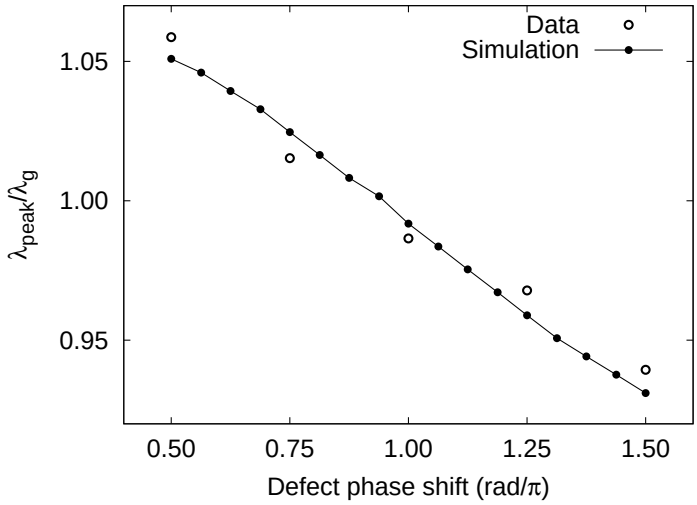

Figure 7.12: The transmittance peak wavelength (λ_p) relative to the band gap centre wavelength (λ_g) for different defect phase-shift values ($\Delta\phi$). Open circles indicate experimentally measured results and filled circles correspond to simulated results.

respective band gap centre wavelength λ_g. These normalized spectra are presented in Fig. 7.11. The different coloured lines correspond to measured spectra for different $\Delta\phi$, as indicated in the figure legend. The normalization shifts each spectrum to the same centre-point, facilitating direct comparison of the data.

As can be seen in Fig. 7.11, the band gap of each multilayer has similar normalized width and a transmittance peak is observed within each band gap. Interestingly, the spectral location λ_p of the transmittance peak occurs at different points within the band gap. Furthermore, λ_p varies systematically with $\Delta\phi$: the peak location decreases as $\Delta\phi$ increases. Fig. 7.12 plots λ_p / λ_g (i.e., the transmittance peak spectral location relative to the band gap centre wavelength) for different $\Delta\phi$. This figure also shows the same quantities measured from the simulated transmittance spectra. Excellent agreement is observed between the experimental data and the simulation. These results indicate that the phase-shift defect mode exhibits a resonance determined by the value of $\Delta\phi$. The position of the defect mode within the stopband can be continuously tuned by changing $\Delta\phi$.

7.5 Coupled phase-shift defects

The resonant confinement of light at a PC defect leads to interesting and useful optical phenomena. The properties of more complicated PC structures with multiple defects are also of significant interest. Positioning two PC defects sufficiently close together permits energy exchange between the localized fields, leading to defect mode splitting [245] and Rabi oscillation [246]. These phenomena are entirely absent in single-defect PCs. Energy coupling between defects creates novel device capabilities and coupled-defect PCs are being actively studied for integrated optical devices [247,248], slow-light optics [249,250], and intriguing experiments in quantum optical systems [251]. Realizing coupled-defect PCs using GLAD is consequently an important extension of the previous results.

7.5.1 Coupled resonators and mode splitting

As discussed in Sec. 7.1 a PC defect acts as an optical microresonator. By extension, the properties of coupled PC defects can be understood by considering the general characteristics of a coupled oscillator system [252, 253]. Consider two coupled harmonic oscillators with natural frequencies ω_a and ω_b. When the oscillator amplitudes are weakly (i.e., linearly) coupled together with a coupling coefficient κ, the normal modes of the coupled system oscillate with frequencies ω_+ and ω_- given by [252]

$$2\omega_\pm = \omega_1 + \omega_2 \pm \sqrt{(\omega_1 - \omega_2)^2 + 4\kappa^2}.$$

The radical term of this equation is equal to the frequency splitting between the two normal modes:

$$\Delta\omega = \omega_+ - \omega_- = \sqrt{(\omega_1 - \omega_2)^2 + 4\kappa^2}. \tag{7.6}$$

Eq. 7.6 shows that two factors influence the mode splitting. The first is a mismatch between the two oscillators, expressed by the detuning between their natural frequencies ω_1 and ω_2. If the detuning is non-zero, complete energy exchange between the resonators is not achieved due to imperfect destructive interference [253]. Maximizing the energy coupling efficiency requires minimizing this resonance detuning.

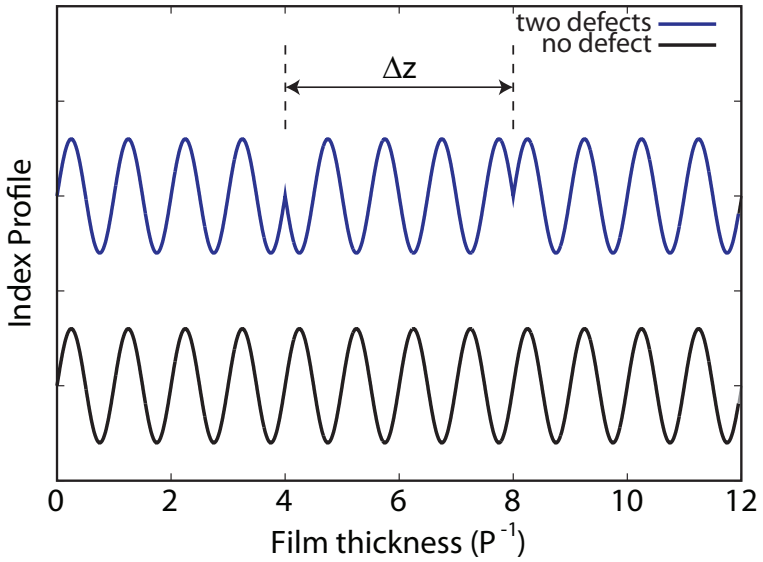

Figure 7.13: Refractive index profile of a rugate multilayer with two π phase-shift defects (blue line). The defects are separated by Δz = 4P as indicated. A rugate index profile with no defects (black line) is shown for comparison.

The second factor is the magnitude of κ. Increased coupling between the resonators causes a larger frequency split between the normal modes of the coupled system. The coupling coefficient κ quantifies the weak coupling between the oscillators. For two coupled optical microresonators, κ represents the interaction between the two defects, proportional to the overlap of the neighbouring localized defect eigenmodes. Away from the defect, the localized field decays exponentially. This field decay can be seen from the corresponding calculated field profile in Fig. 7.9. The coupling interaction between two defect modes is mediated by these evanescent tails. Therefore, κ falls off exponentially with increasing defect separation [252, 254, 255].

7.5.2 Multi-defect rugate multilayer fabrication

Incorporating two phase-shift defects in a rugate multilayer corresponds to the refractive index profile in Eq. 7.4 with a phase term $\phi(z)$ given by

$$\phi(z) = \begin{cases} \phi_0 & \text{if } z < (L - \Delta z)/2 \\ \phi_0 + \Delta\phi & \text{if } (L - \Delta z)/2 \leq z < (L + \Delta z)/2 \\ \phi_0 + 2\Delta\phi & \text{if } z \geq (L + \Delta z)/2. \end{cases} \tag{7.7}$$

This produces a sinusoidal index profile with two $\Delta\phi$ phase-shifts separated by Δz. The defects are centred about the film midpoint $z = L/2$. This index profile is shown (blue line) in Fig. 7.13, for $\Delta\phi = \pi$, $\Delta z = 4P$, and $\phi_0 = 0$. The GLAD realization of this index profile requires only slight modification of the motion algorithm previously developed in Sec. 7.3.1. The phase of the substrate α-variation is now shifted at $(L - \Delta z)/2$, to create the first defect, and at $(L + \Delta z)/2$, to create the second defect. One extra subtlety is introduced when $\phi_0 = 0$, as shown in Fig. 7.13. Whereas in Fig. 7.5 the phase-shift is created by a rapid transition from α_{min} to α_{max}, the phase-shifts in Fig. 7.13 are realized by reversing the direction of the α-variation. Therefore, no rapid substrate motion is required to fabricate the latter defects.

A set of eight films were prepared using this motion algorithm to study multiple phase-shift defects in rugate multilayers. The rugate multilayer design parameters were $\alpha_{\text{min}} = 30^\circ$, $\alpha_{\text{max}} = 80^\circ$, $\lambda_0 = 550$ nm, $L = 16$ periods, $\phi_0 = 0$. Two $\Delta\phi = \pi$ phase-shift defects were inserted in the index profile of each multilayer. In each film, the defects were separated by an integer multiple of periods ($\Delta z = NP$, where $N = 1$ through 8). Films were prepared on p-doped Si and B270 glass. Depositions were performed using the method and conditions described in Sec. 3.1.4. Samples deposited on Si wafers were cleaved and the exposed edge examined via SEM. The optical transmittance spectrum of the samples deposited on glass substrates were measured at normal-incidence using the spectrophotometer.

7.5.3 Structural characterization

Figs. 7.14 (a) and (b) respectively show the multilayer index profile $n(z)$ and a cross-sectional SEM image of the multilayer structure ($\Delta z = 2P$). The structural periodicity is evident and persists over all sixteen periods in the multiayer. The periodicity is created by a cyclic variation in the column diameter, consistent with previous observations of graded-index multilayer structures (see Secs. 5.2.3 and 7.3.2). The cyclical structuring of the columns creates a periodic density gradient and a corresponding sinusoidal index profile.

Fig. 7.14 (c) shows an enlarged section of the SEM in Fig. 7.14 (b) in the vicinity of the phase-shift defects. The phase-shift defect locations are indicated on the image. The defects are separated by two periods. Note that the defect microstructures are different even though they are both created by π phase shifts. While both defects occur at n_a points of the index profile, their points of insertion are 180° out of phase (see Figs. 7.13 and 7.14(a)). The indices around the defects are therefore different. Consequently, the first and second defects are respectively surrounded by low- and by high-density microstructures.

7.5.4 Optical properties of coupled phase-shift defects

Fig. 7.15 shows the transmittance spectra measured for the film with defect separation $\Delta z = 4P$. This graph is representative of the other measurements and it is shown to highlight the important spectral features of the coupled defect system. Note the presence of the photonic band gap, spanning the wavelength interval from 451 nm to 628 nm (measured between points of 40% transmittance). From these points, the band gap centre wavelength is measured to be λ_g = 539.5 nm. The mean band gap centre wavelength (defined the same way) of all eight samples is $\langle\lambda_g\rangle$ = 555 nm $\pm$ 5 nm. This result shows good agreement with the design value of 550 nm and the observed variation is attributed to process fluctuations.

Outside the band gap, interference fringes typical of optical thin films are observed. Each film examined in this study showed similar band gap formation and interference fringes. Indicated on Fig. 7.15 are two transmittance peaks (labelled ω_+ and ω_-). These transmittance peaks correspond to

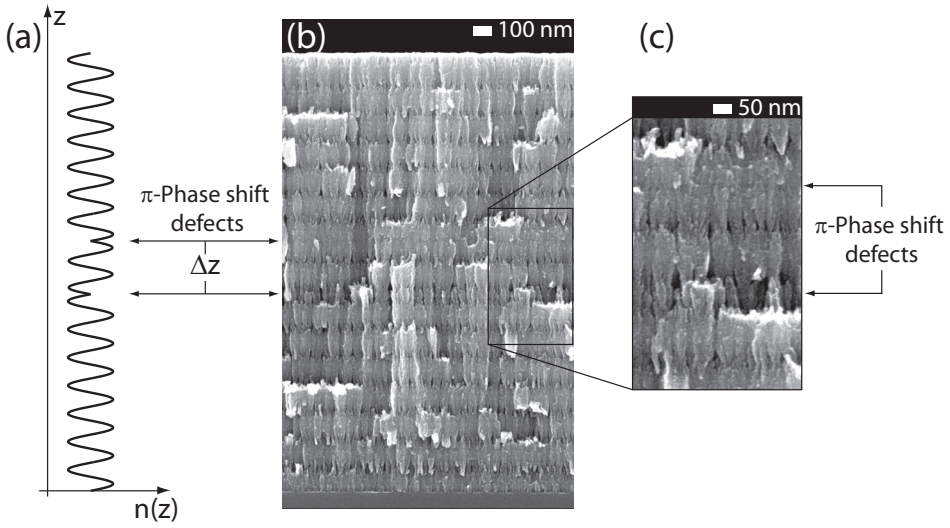

Figure 7.14: (a) The sinusoidal refractive index profile with two phase-shift defects separated by $\Delta z = 2P$. (b) SEM image of a fabricated rugate multilayer containing two π phase-shift defect. (c) Enlarged section of the SEM image showing the defects.

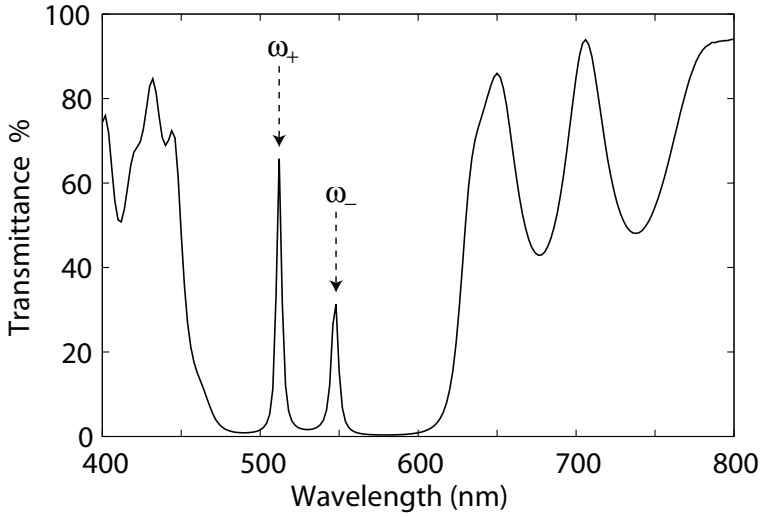

Figure 7.15: Measured optical transmittance spectrum for a rugate multilayer with two π phase-shift defects separated by $\Delta z = 4P$. Two resonant transmittance peaks are observed within the stopband. These correspond to the high (ω_+) and low (ω_-) frequency normal modes of the coupled defect system.

Table 7.1: Resonance peak parameters for the normal modes of coupled phase-shift defects.

Δz (P^{-1})	$\Delta\mathcal{E}$ (eV)	$\mathcal{E}_+$ (eV)	$\mathcal{E}_-$ (eV)	Q_+	Q_-
1	0.383 ± 0.001	2.4623 ± 0.0006	2.0790 ± 0.0004	89 ± 6	83 ± 4
2	0.2715 ± 0.0004	2.4173 ± 0.0001	2.1459 ± 0.0002	138 ± 4	153 ± 5
3	0.201 ± 0.001	2.3021 ± 0.0005	2.1009 ± 0.0007	225 ± 84	126 ± 14
4	0.1565 ± 0.0002	2.4235 ± 0.0001	2.2670 ± 0.0001	133 ± 1	114 ± 2
5	0.1562 ± 0.0004	2.3404 ± 0.0003	2.1842 ± 0.0001	62 ± 2	150 ± 1
6	0.134 ± 0.001	2.3368 ± 0.0002	2.2032 ± 0.0005	94 ± 2	61 ± 3
7	0.097 ± 0.001	2.2558 ± 0.0009	2.1589 ± 0.0001	35 ± 2	105 ± 1
8	0.077 ± 0.002	2.4372 ± 0.0004	2.361 ± 0.002	77 ± 3	39 ± 4

the resonant excitation of the coupled-system normal-modes. The resonant peaks are located at λ_- = 547.3 nm and λ_+ = 512.0 nm with Q-factors of 114 ± 2 and 133 ± 1, respectively. These peak lineshape parameters ($\lambda_\pm$ and $Q_\pm$) were determined by fitting Eq. 7.1 to the data in energy units.

Figs. 7.16 (a)-(d) show the measured transmittance (data points) in the vicinity of the defect modes for defect separations of $\Delta z = 2P$, $3P$, $5P$, and $8P$ periods, respectively. The spectra are plotted in energy units (eV). Lorentzian lineshapes (Eq. 7.1) fit to the measured data are plotted as well (solid line). The other four spectra are omitted for brevity. In every measured spectrum, two transmittance peaks are observed and the Lorentzian function accurately reproduces the resonance lineshapes. The best-fit lineshape parameters ($\mathcal{E}_\pm$, and $Q_\pm$) determined for every film are presented in Table 7.16. The normal mode splitting $\Delta\mathcal{E} = \mathcal{E}_+ - \mathcal{E}_-$ is calculated and presented as well.

As indicated by these parameters, and by Fig. 7.17 which plots $\Delta\mathcal{E}$ against Δz, the normal mode splitting decreases as the defects are moved further apart. Also shown on Fig. 7.17 is the equation

$$\Delta\mathcal{E} = \sqrt{A^2 + 4\left[B\exp\left(C\Delta z\right)\right]^2} \tag{7.8}$$

after curve-fitting to the measured data via the constants A, B, and C. The best-fit parameters are A = (0.08 ± 0.02) eV, B = (0.25 ± 0.02) eV, and C = (-0.32 ± 0.05)P^{-1}. Eq. 7.8 is essentially Eq. 7.6 written in energy units, with

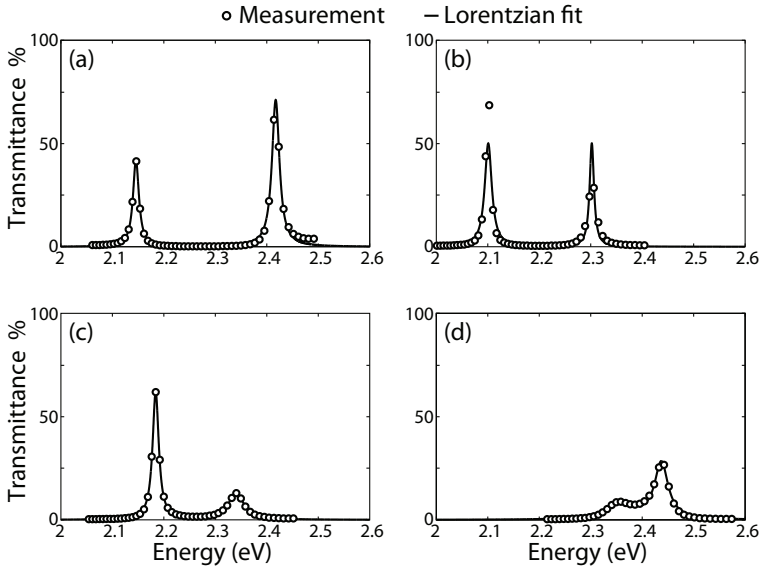

Figure 7.16: Measured transmittance (data points) in the vicinity of the resonant transmittance peaks inside the band gap, plotted in energy units. The spectra correspond to defect separations Δz = (a) $2P$, (b) $3P$, (c) $5P$, and (d) $8P$. Also shown on the spectra are Lorentzian lineshapes fit to the measured data.

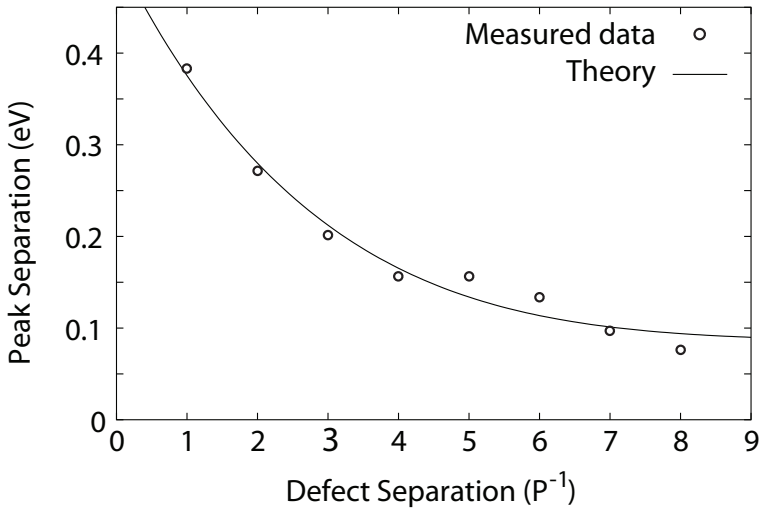

Figure 7.17: The measured normal mode splitting ($\Delta\mathcal{E}$) is plotted as a function of defect separation (Δz). The theoretical curve is Eq. 7.8 in the text after fitting to the data set.

$A = \mathcal{E}_1 - \mathcal{E}_2$ and $[B\exp(C\Delta z)] = \kappa$. The latter relation phenomenologically expresses the exponential-dependence between the coupling strength and the defect separation, discussed in Sec. 7.5.1.

The agreement between the measured data and Eq. 7.8 is excellent, supporting the validity of the coupled-oscillator model for this system. The appearance of two peaks in the measured transmittance can be created by the coupling interaction and/or a mismatch between defect resonances. However, the exponential behavior confirms that defect coupling contributes significantly to the mode splitting in addition to resonance detuning. This indicates the successful realization of coupled-defect PCs using the GLAD technique and that the defect coupling can be tuned through the defect spacing.

The parameter A = (0.08 $\pm$ 0.02) eV found for Eq. 7.8 provides an estimate of the average defect mode detuning across all eight samples. Detuning can be attributed to multiple sources. First, random fabrication errors will detune the resonances. However, this can be mitigated by improved fabrication control. A second source comes from the PC boundaries. Because the PCs are finite, the defect modes leak into freespace at the system boundaries. Since the boundaries are different (one being air/film and the other film/substrate) they introduce different losses and detune the resonances. By increasing the number of periods in the film the defects can be moved further from the film edges, decreasing the boundary influence. Alternatively, the two defect resonances could be intentionally detuned (via $\Delta\phi$ as shown in Sec. 7.4) at the design stage to compensate.

7.6 Anisotropic microresonators I

The optical properties of the defect structures examined thus far have all been polarization-insensitive. However as discussed in Sec. 2.2.1, a unique characteristic of the GLAD process is the ability to fabricate optically anisotropic materials. The polarization-sensitivity arises from structural anisotropy. The structural control and precision provided by the GLAD process allows realization of tunable linearly and circularly birefringent media. Therefore, introducing anisotropic layers as defects in GLAD-fabricated multilayers allows resonant interference effects to be combined with polarization-sensitive

optical characteristics. Novel anisotropic optical microresonators can consequently be realized in a single fabrication step.

Characterizing these anisotropic microresonators demands studying the polarization state of the resonantly transmitted light. While the ellipsometer is capable of many polarimetric measurements, it lacks a retarding optical element after the sample. Without such an element, the full Stokes vector (defined below) can not be determined. A rigorous polarimetric measurement requires constructing a polarimeter [256]. The remainder of Sec. 7.6 examines the polarimeter construction. The next section (Sec. 7.7) presents the anisotropic microresonator fabrication and characterization.

7.6.1 Optical polarization state: Stokes parameters

The electric field of an optical beam with frequency ω can be written as a superposition of two transverse fields $E_x \cos(\omega t + \vartheta_x)$ and $E_y \cos(\omega t + \vartheta_y)$, where E_x and E_y are the instantaneous field amplitudes and ϑ_x and ϑ_y are the instantaneous phase factors. The Stokes parameters of this beam are then [1, 256]

$$S_0 = E_x^2 + E_y^2, \tag{7.9a}$$

$$S_1 = E_x^2 - E_y^2, \tag{7.9b}$$

$$S_2 = 2E_x E_y \cos\left(\vartheta_y - \vartheta_x\right), \tag{7.9c}$$

$$S_3 = 2E_x E_y \sin\left(\vartheta_y - \vartheta_x\right), \tag{7.9d}$$

where the field amplitudes have been suitably time-averaged. The four Stokes parameters define the Stokes vector $\mathbf{S} = [\, S_0\ S_1\ S_2\ S_3\,]^T$, where ^{T} denotes transpose. The Stokes parameters fully characterize the optical beam's polarization state:

1. S_0 is the total beam intensity.
2. S_1 describes the amount of linearly polarized light oriented along the horizontal (x) or the vertical (y).
3. S_2 is the amount of linearly polarized light oriented +45° or -45° from the horizontal.
4. S_3 describes the amount of right or left circularly polarized light.

A main advantage of characterizing light with a Stokes 4-vector, as opposed to a Jones 2-vector, is that unpolarized light can be described using the Stokes approach. For a completely polarized beam, $S_0^2 = S_1^2 + S_2^2 + S_3^2$. An unpolarized beam has $S_0 > S_1 = S_2 = S_3 = 0$. The degree of polarization D_p is defined as

$$D_p = \frac{\sqrt{S_1^2 + S_2^2 + S_3^2}}{S_0}. \tag{7.10}$$

$D_p = 0$ indicates the light is unpolarized and $D_p = 1$ indicates completely polarized light. Values of D_p intermediate between 0 and 1 correspond to a partially-polarized beam.

7.6.2 Stokes parameter measurement: Spectropolarimeter

Polarization characterization amounts to measureing the beam's Stokes vector **S**. This is accomplished using a polarimeter (called a spectropolarimeter when the characterization is wavelength-resolved). Two optical elements are required to measure **S** [256–258]: a phase-retarding optical waveplate and a linear polarizer. Several measurements are taken, with one of the elements rotated between measurements. (Either the waveplate or the polarizer can be rotated; for the present apparatus the waveplate is rotated.) When a beam passes through an optical element, the new Stokes vector is the product of **S** and a 4x4 matrix, known as the element's Mueller matrix **M**. The Mueller matrix for a waveplate, with retardation Φ and rotated to an angle θ_w, is [256]

$$\mathbf{M}_w = \begin{bmatrix} 1 & 0 & 0 & 0 \\ 0 & \cos^2 2\theta_w + \cos\Phi \sin^2 2\theta_w & (1-\cos\Phi)\sin 2\theta_w \cos 2\theta_w & -\sin\Phi \sin 2\theta_w \\ 0 & (1-\cos\Phi)\sin 2\theta_w \cos 2\theta_w & \cos^2 2\theta_w + \cos\Phi \sin^2 2\theta_w & \sin\Phi \cos 2\theta_w \\ 0 & \sin\Phi \sin 2\theta_w & -\sin\Phi \cos 2\theta_w & \cos\Phi \end{bmatrix} \tag{7.11}$$

and for a linear polarizer

$$\mathbf{M}_p = \frac{1}{2}\begin{bmatrix} 1 & \pm 1 & 0 & 0 \\ \pm 1 & 1 & 0 & 0 \\ 0 & 0 & 0 & 0 \\ 0 & 0 & 0 & 0 \end{bmatrix} \tag{7.12}$$

where the ± 1 elements correspond to horizontal and vertical orientations.

The measured intensity is equal to the transmitted Stokes vector's first

element S_0', calculated by cascading $\mathbf{M}_w$ and $\mathbf{M}_p$ together and multiplying by the initial Stokes vector $\mathbf{S}$

$$\mathbf{S}'(\theta_w) = \mathbf{M}_p \mathbf{M}_w(\theta_w)\,\mathbf{S}. \tag{7.13}$$

The input Stokes parameters are recovered by curve-fitting Eq. 7.13 to the measured intensity.

7.6.3 Spectropolarimeter construction: Waveplate characterization

The first step in constructing the spectropolarimeter is to measure the wavelength dependent retardance $\Phi(\lambda)$ of the waveplate[1]. $\Phi(\lambda)$ was determined by placing the waveplate between crossed Glan-Taylor polarizers[2] and measuring the signal intensity as the waveplate was rotated. The optical system is illuminated with unpolarized light, $\mathbf{S} = [\, S_0\ 0\ 0\ 0\,]^T$. Assuming ideal polarizers, a safe approximation given the high-quality (100,000:1 extinction ratio, manufacturer specification) of the polarizers, the transmitted signal is

$$\mathbf{S}'(\lambda, \theta_w) = \mathbf{M}_{p-}\mathbf{M}_w(\theta_w - \theta_m)\,\mathbf{M}_{p+}\mathbf{S}, \tag{7.14}$$

where the +/- subscript refers to horizontal/vertical polarizer alignment and θ_m is the offset between the optomechanical rotation mount and the waveplate fast axis. Carrying out this multiplication leads to

$$\frac{4S_0'}{S_0} = 1 - \cos^2\left[2\left(\theta_w - \theta_m\right)\right] - \cos\Phi(\lambda)\sin^2\left[2\left(\theta_w - \theta_m\right)\right]. \tag{7.15}$$

This measurement was performed with the waveplate mount rotated from 0 to 90° in 10° increments. The Ocean-Optics white-light source was used to illuminate the optical system and the transmitted signal I_D was detected using the Ocean-Optics CCD spectrometer. At every wavelength, Eq. 7.15 was fit to the data by varying the parameters Φ and θ_m. The best-fit Φ and θ_0 parameters are respectively shown in Figs. 7.18(a) and (b).

The retardance values are consistent with the waveplate specifications. A $\Phi = 163.8/\lambda$ dependence (red line in Fig. 7.18a) nicely fits the data.

[1] The waveplate used is a Thorlabs zero-order quartz waveplate, specified to have a quarter-wave retardance at 633 nm.

[2] Thorlabs Glan-Taylor calcite polarizers.

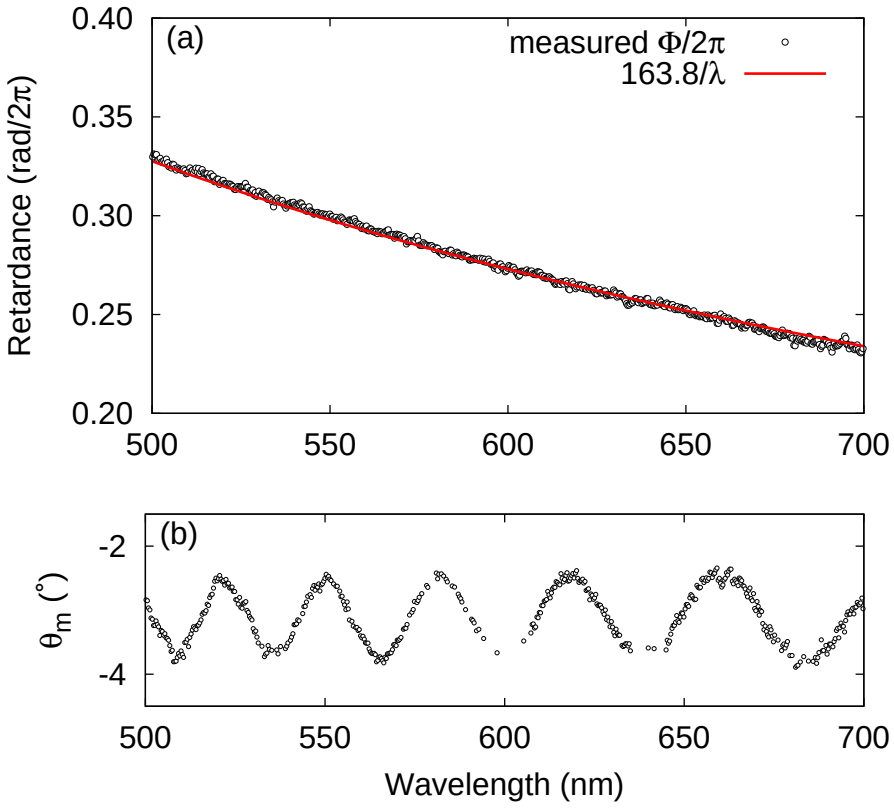

Figure 7.18: The measured wavelength-dependence of (a) the waveplate retardance and (b) the offset θ_m between the optomechanical rotation mount and the waveplate fast axis. The wavelength oscillation of θ_m indicates an internal misalignment in the zero-order waveplate.

The retardance at 633 nm is $0.259/2\pi$, 3.6% from the specified value of $0.25/2\pi$. However, as can be seen in Fig. 7.18(b), θ_m has an oscillatory wavelength-dependence. This indicates the fast axes of the two multi-order waveplates in the zero-order waveplate, which should be at 90°, are misaligned [259–261]. This misalignment negatively impacts the spectropolarimeter accuracy. These multi-order waveplates are inaccessible and realignment is not possible. However, the error can be accounted for by changing 7.14 to

$$\mathbf{S}'(\lambda,\theta_w) = \mathbf{M}_{p-}\mathbf{M}_{w2}(\theta_w - \theta_e - \theta_m + 90^\circ)\,\mathbf{M}_{w1}(\theta_w - \theta_m)\,\mathbf{M}_{p+}\mathbf{S}, \qquad (7.16)$$

where $\mathbf{M}_{w1}$ and $\mathbf{M}_{w2}$ are multi-order waveplates and θ_e is the misalignment. The multi-order waveplates have retardances $\Phi_1(\lambda)$ and $\Phi_2(\lambda)$. Fitting Eq. 7.16 removes the θ_m wavelength variation and yields a misalignment value of θ_e = 0.82°. The measured overall waveplate retardance $\Phi(\lambda) = \Phi_1(\lambda) - \Phi_2(\lambda)$ changes only slightly using this improved model. The retardance is now $0.258/2\pi$ at 633 nm ($\Phi = 163.5/\lambda$), 3.2% from the specified value.

7.6.4 Spectropolarimeter construction: Test cases

The constructed spectropolarimeter is shown in Fig. 7.19. The optical system consists of the collimated lamp output (source), an initial polarizer, the sample under investigation (on a rotation mount), the waveplate characterized in Sec. 7.6.3 (on a rotation mount), an analyzing polarizer, and the CCD spectrometer. In every measurement, the signal was measured for θ_w from 0 to 360°, in 20° increments.

To characterize the spectropolarimeter and confirm it operates as intended, suitable test standards are required. These tests involve preparing a beam of a known polarization state and measuring its Stokes parameters. Three separate test cases were devised, one using unpolarized light ($D_p = 0$), another with polarized light ($D_P = 1$), and a third with partially-polarized light ($0 < D_p < 1$).

The first test case measures the lamp output, which should be unpolarized. This is accomplished by removing the first polarizer and the sample in Fig. 7.19. The measured Stokes parameters (normalized to S_0) of the lamp output are presented in Fig. 7.20. The calculated degree of polarization (Eq.

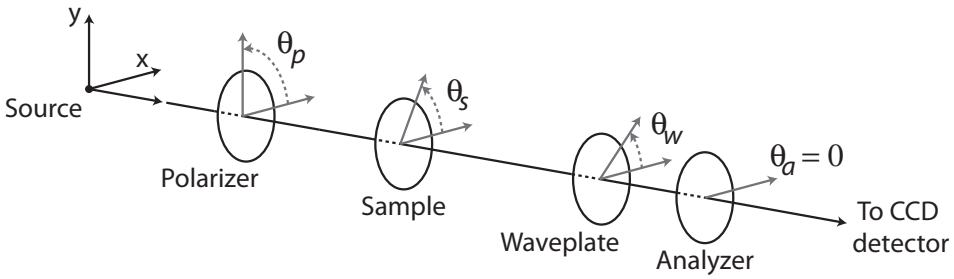

Figure 7.19: Diagram of the optical system in the spectropolarimeter. Light from an (unpolarized) source passes through a polarizer to create a linearly (vertical) polarized beam. The beam is transmitted through the sample (normal-incidence, rotated to an angle θ_s). To measure the polarization state emerging from the sample, the beam is passed through a waveplate (fast axis rotated to θ_w) and an analyzing polarizer (transmission axis colinear to the horizontal). The spectrally-resolved intensity of the beam is then measured using a CCD spectrometer.

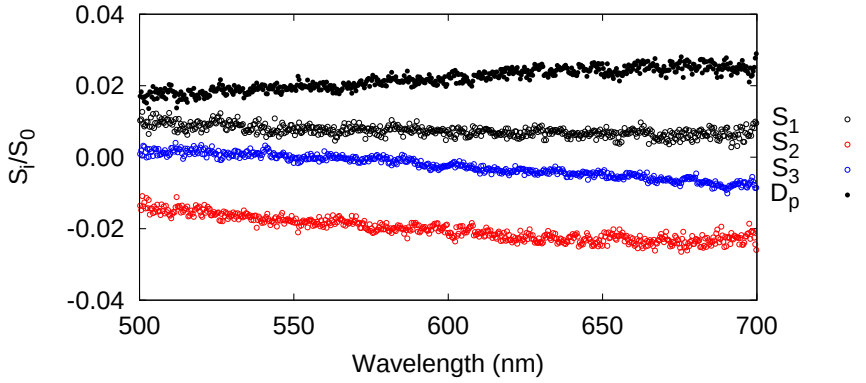

Figure 7.20: The Stokes parameters (normalized to S_0) and the degree of polarization (D_p) measured for the lamp output.

7.10) is also shown. Across the 500 nm to 700 nm wavelength range, the Stokes parameters are all less than (approximately) 0.02. The degree of polarization is less than 0.03. This indicates that the bulb output is almost completely unpolarized. The small polarized portion of the beam could originate from multiple sources. The collection optics (paraboloid mirror, fibre-optic coupling, collimating lens) may introduce some slight polarization component. Measurement artefacts may also arise from non-idealities in the polarizers (finite extinction ratios, non-zero retardance, ellipticity, inhomogeneity, depolarization) and the waveplate (diattenuation, ellipticity, inhomogeneity, depolarization) [262].

For the second test, the first polarizer in Fig. 7.19 was reinserted. Stokes parameter measurements were performed for linearly polarized input beams oriented horizontally, vertically, and at 45° from the horizon, created by rotating the polarizer appropriately. These polarization states correspond to Stokes vectors

$$S_x = S_0 \left[\, 1 \; 1 \; 0 \; 0 \, \right]^T, \tag{7.17a}$$

$$S_y = S_0 \left[\, 1 \; \text{-}1 \; 0 \; 0 \, \right]^T, \tag{7.17b}$$

$$S_{45^\circ} = S_0 \left[\, 1 \; 0 \; 1 \; 0 \, \right]^T. \tag{7.17c}$$

Figs. 7.21(a), (b), and (c) present the measured Stokes parameters (normalized to S_0) for these three polarized input beams. Excellent agreement between the measured values and the expected values (Eqs. 7.17a, b, and c) is observed. The small systematic errors, for example in S_2, can be attributed to misalignment of the polarizer (which is accurate to $\sim 0.5^\circ$).

For the third test, the first polarizer in Fig. 7.19 was removed, and an uncoated B270 glass substrate was inserted. The glass substrate was mounted on a rotatable stage so that the angle of incidence θ_0 could be changed. The substrate rotates so that the *s*- and *p*-polarizations correspond to the *x*- and *y*-polarizations of the spectropolarimeter. For $\theta_0 \neq 0$, the Fresnel coefficients are polarization-dependent and the transmitted light is partially polarized. The Stokes vector of the transmitted beam can be calculated from the Fresnel

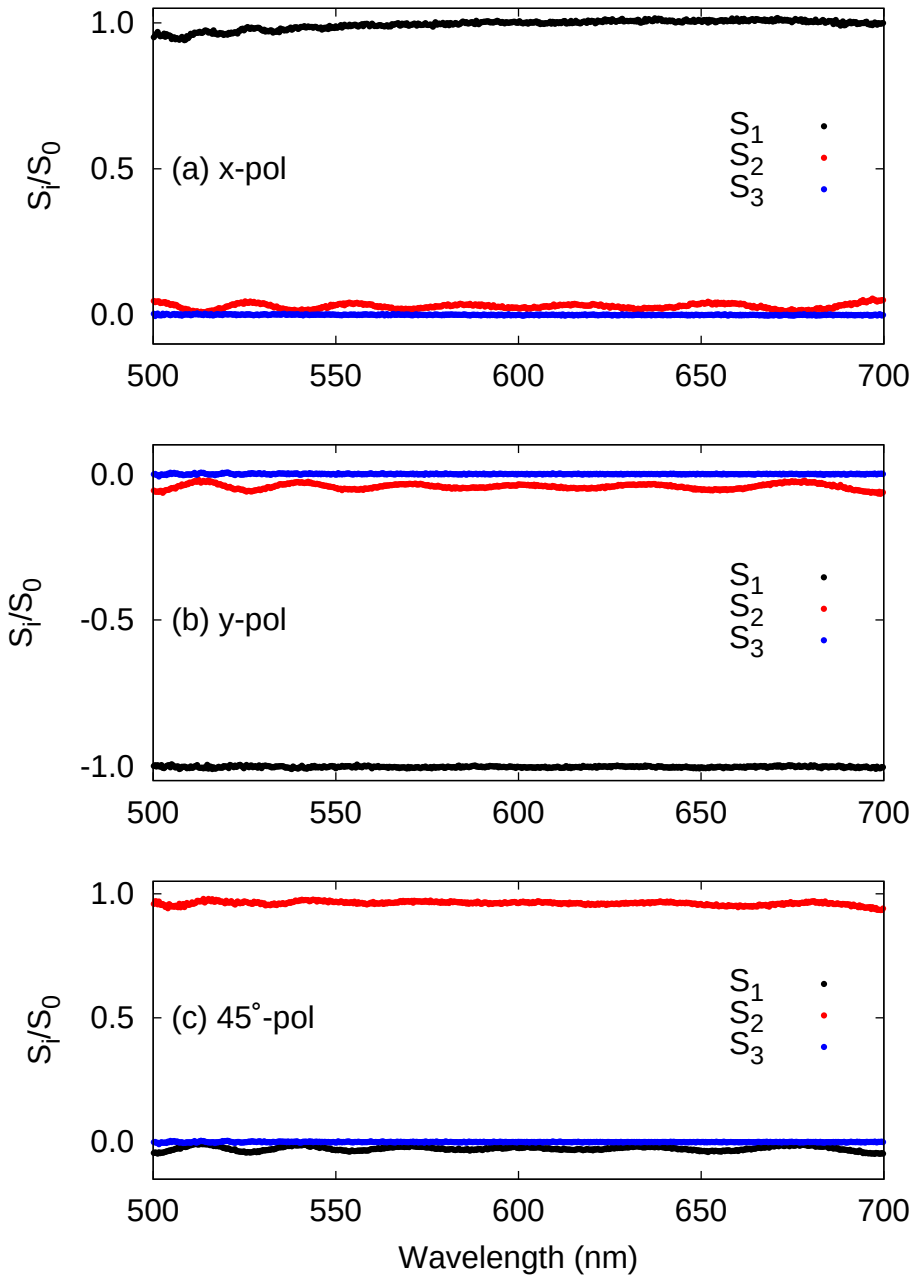

Figure 7.21: The Stokes parameters (normalized to S_0) measured for light linearly polarized along (a) the horizontal, (b) the vertical, and (c) 45° from the horizontal.

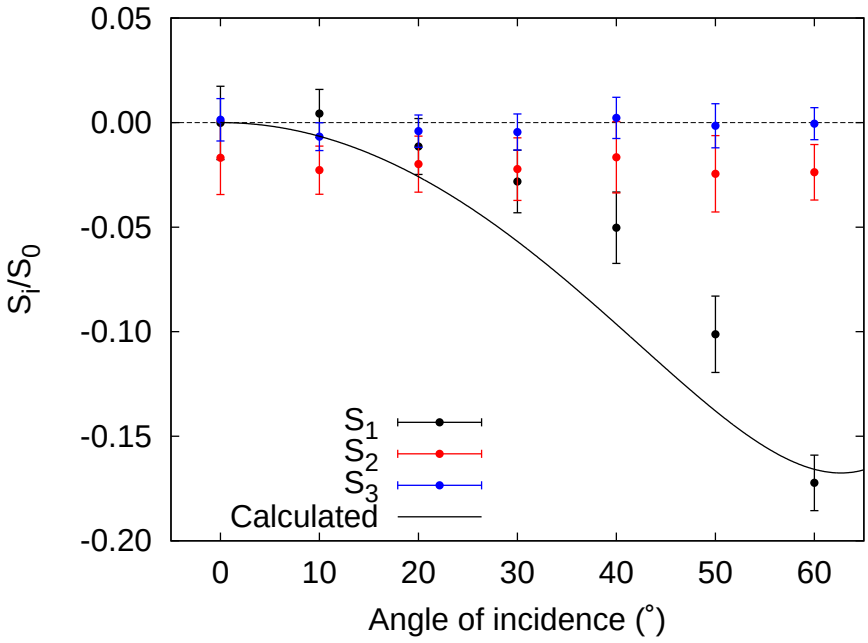

Figure 7.22: The Stokes parameters (normalized to S_0) measured for unpolarized light transmitted through an uncoated piece of glass (b270) at 600 nm. The solid curve is calculated from Eq. 7.18 using $n_{\text{glass}} = 1.54$.

transmission coefficients t to be [256]

$$\mathbf{S}_t = S_0 \cos\theta_0 \begin{bmatrix} (t_{x12}t_{x21})^2 + (t_{y12}t_{y21})^2 \\ (t_{x12}t_{x21})^2 - (t_{y12}t_{y21})^2 \\ 0 \\ 0 \end{bmatrix}, \tag{7.18}$$

where the $_{12}$ and $_{21}$ subscripts refer to the air / glass and glass / air interfaces, and the $_x$ and $_y$ subscripts indicate the polarization. S_0 is the intensity of the incident beam. Because the phase factors of unpolarized light are zero and unchanged upon transmission, S_2 and S_3 are both zero.

Fig. 7.22 shows the measured Stokes parameters for θ_0 = 0 to 60°, in 10° increments, at a wavelength of 600 nm. As θ_0 increases, the transmitted beam becomes increasingly y-polarized ($S_1 < 0$). This is consistent with the S_1 prediction of Eq. 7.18, shown as a solid black line on Fig. 7.22.

These three tests have confirmed the spectropolarimeter operates successfully and can correctly measure the Stokes parameters of a given light

beam. Examining the results in Figs. 7.20, 7.21, and 7.22, the spectropolarimeter is estimated to be accurate to better than 4% (the maximum residual in Fig. 7.22).

7.7 Anisotropic microresonators II

7.7.1 Sample fabrication and characterization

Three 16-period Bragg multilayers were fabricated using the substrate motion algorithm described in Sec. 7.2.1. Each sample had a central $\lambda/2$-defect layer. The defect layers were deposited at α = 60°, 70°, and 80°. To fabricate tilted columns and create polarization anisotropy, the substrate was not rotated during deposition. The H- and L-sublayers were respectively deposited at α_H = 40° and α_L = 80°, and the design wavelength was λ_0 = 600 nm. Samples were prepared on p-doped Si (for SEM characterization) and B270 glass (for optical measurements) substrates. The *x*- and *y*-polarized transmittance spectrum was measured using the ellipsometer operating in intensity mode. For these transmittance measurements, the samples were oriented such that the *y*-polarized field was perpendicular to the deposition plane.

The transmitted light Stokes vector was measured (at normal-incidence) for three different sample orientations, defined via the sample rotation angle θ_s. In the first ($\theta_s = 0$), the deposition plane is perpendicular to the polarimeter *y*-axis (see Fig. 7.19). For the second ($\theta_s = 90°$), the deposition plane is perpendicular to the polarimeter *x*-axis. In the third orientation ($\theta_s = 45°$), the sample is rotated 45° between the previous two orientations. In all three polarimetric measurements, the initial polarizer is oriented at $\theta_p = 45°$. Therefore, equal parts of in-phase, linearly *x*- and *y*-polarized light illuminate the sample (input Stokes vector Eq. 7.17c).

These three alignments correspond to high-symmetry configurations because the tilted columns behave as a biaxial medium [1]. At normal-incidence, the optical axes lie in the substrate plane and are oriented parallel and perpendicular to the deposition plane [77, 147, 263]. In the first and second sample orientations, the *x*- and *y*-polarized fields align colinearly with the optical axes. Therefore, the first two sample orientations are maximally anisotropic, although the optical axes are reversed between the two cases.

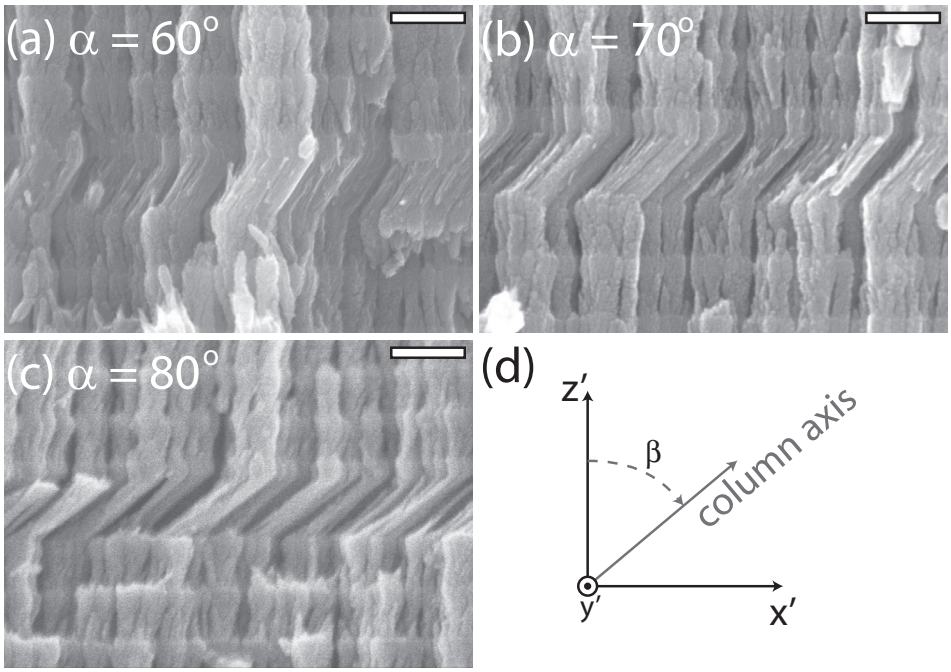

Figure 7.23: Cross-sectional SEM images of $\lambda/2$-defect layers deposited at α = (a) 60°, (b) 70°, and (c) 80°. The scale bars indicate 200 nm. Because the substrate is not rotated during layer deposition, the columnar structures are tilted towards the source. The column axis is tilted to an angle β from the substrate normal, as indicated in (d). The *x*' and *z*' axes define the deposition plane. The *y*' axis is perpendicular to this plane, pointing out of the page.

In the third sample orientation, the *x*- and *y*-polarized fields both align 45° between the optical axes. The anisotropy is therefore minimized.

7.7.2 Structural properties of anisotropic microresonantors

Fig. 7.23 shows cross-sectional SEM images of all three samples taken at the same magnification. Defect layers deposited at α = 60°, 70°, and 80° are respectively shown in (a), (b), and (c). The defect layer thickness are estimated to be 146 nm, 175 nm, and 160 nm (within 20 nm, see Fig. 7.2). The tilted columnar microstructure of the defect layers can be clearly seen. Away from the defect layer the films are composed of vertically oriented columnar microstructures, consistent with previous structural observations. The defect layer columns tilt in the direction of the source. This defines a local coordinate system *x'y'z'* within the structure, as shown in Fig. 7.23d. The col-

Table 7.2: Measured column tilt angles β. Predictions using the tangent rule and Tait's rule are presented as well. Each value carries units of degrees.

α	$\langle\beta\rangle$	Tangent rule [53]	Tait's rule [57]
60	33 ± 2	40.9	45.5
70	43 ± 2	53.9	50.8
80	54 ± 3	70.6	55.6

umn tilt angle β is the angle between the substrate normal (z'-axis) and the column axis. β increases with α, as expected [53, 57]. For each sample, the column tilt was estimated by averaging ten separate β measurements. The results are presented in Table 7.2 with one standard deviation uncertainties. Also shown are the predicted β values using the tangent rule $\tan\alpha = 2\tan\beta$ and Tait's rule $\beta = \alpha - \arcsin[0.5(1-\cos\alpha)]$. As is commonly found in tilt angle measurements [57], the tangent rule provides good agreement for $\alpha \leq 60^\circ$ while Tait's rule is more accurate at greater α values.

7.7.3 Polarization-resolved transmittance

The measured x- and y-polarized light transmittance spectra (T_x and T_y) are shown in Fig. 7.24. The spectra measured for α = 60°, 70°, and 80° defect layers respectively correspond to Figs. 7.24(a, d), (b, e), and (d, f). The red and black lines plot T_x and T_y. The spectra in (a), (b), and (c) are plotted over the entire wavelength range. In each spectrum, a band of decreased transmittance is observed indicating the formation of a photonic band gap. The x- and y-polarized band gaps and bandedges are nearly identical. This polarization-insensitivity is expected since the band gap interference effects originate in the isotropic (at normal-incidence) periodic multilayers surrounding the anisotropic defect layer. For wavelengths outside the band gap, the expected thin film interference fringes are present. The transmittance fringe amplitudes are approximately equal for all three samples and are consistent with previously measured spectra of similar multilayer structures (cf. Fig. 5.14). There is a small difference between the x and y-polarized interference fringes. Since wavelengths outside the band gap propagate through the entire multilayer, the defect layer birefringence

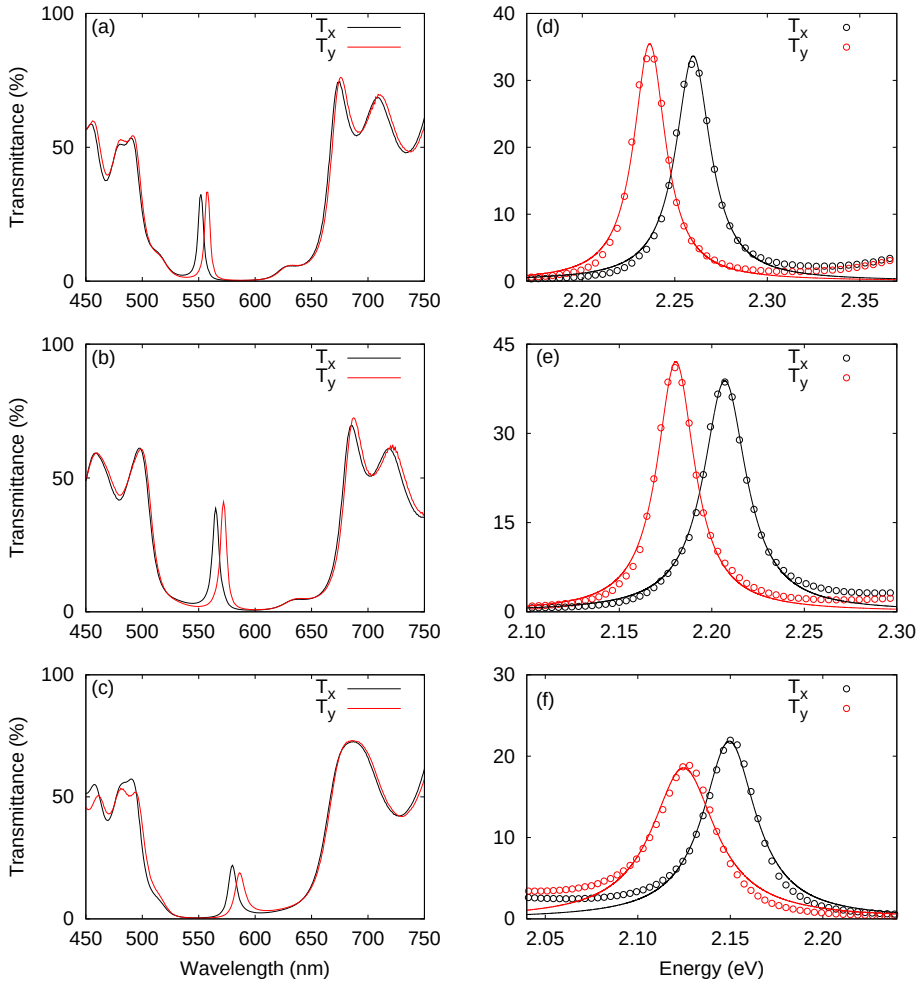

Figure 7.24: Transmittance of linearly x- and y-polarized light (T_x and T_y, respectively). The spectra in (a, d), (b, e), and (c, f) correspond to samples with $\alpha = 60^\circ$, 70°, and 80° defect layers. The spectra in (a), (b), and (c) show the transmittance over the entire measured range, while the spectra in (d), (e), and (f) focus on the transmittance peak and are plotted in energy units (along with best-fit Lorentzian curves).

Table 7.3: Resonance peak parameters.

α (°)	Polarization	I_0 (%)	$\mathcal{E}_0$ (eV)	Q
60	x	33.7 ± 0.8	2.2599 ± 0.0003	99 ± 12
	y	35.5 ± 0.8	2.2364 ± 0.0002	108 ± 10
70	x	38.8 ± 0.6	2.2070 ± 0.0002	78 ± 3
	y	42.1 ± 0.6	2.1805 ± 0.0002	89 ± 5
80	x	21.8 ± 0.6	2.1495 ± 0.0004	62 ± 5
	y	18.6 ± 0.5	2.1247 ± 0.0006	51 ± 4

causes this difference.

A transmittance peak, created by resonant constructive interference in the multilayer, is observed within the band gap of each sample. However, the peak's spectral location is polarization-dependent. The *x*-polarized light transmittance peak, where the field is colinear with the *x*'-axis (Fig. 7.23), always occurs at a shorter wavelength than the *y*-polarized peak. This shift is caused by the defect layer birefringence: the index in the *y*'-direction is greater than the index in the *x*'-direction. The Fabry-Perot resonance condition in an anisotropic resonator is therefore polarization-dependent.

To focus on the resonant transmittance peaks, the spectra are replotted (in energy units) over a narrower spectral range in Figs. 7.24(b), (d), and (d). Also shown on these three plots are Lorentzian curves (Eq. 7.1) fitted to the resonance peaks. The Lorentzian lineshapes show good agreement with the measured transmittance peaks. The best-fit parameters (I_0, $\mathcal{E}_0$, and $Q = \mathcal{E}_0/2\gamma$) are presented in Table 7.3. The resonance shifts between *x*- and *y*-polarized transmittance peaks for the 60°, 70°, and 80° defect layers are 24.8 ± 0.7 meV, 26.5 ± 0.3 meV, and 23.5 ± 0.4 meV, respectively. The greatest shift is observed for the α = 70° defect layer. Since resonance occurs at twice the cavity path length, the layer birefringence Δn can be estimated from the resonance shift (in wavelength units) $\lambda_{0y} - \lambda_{0x}$ and the measured defect layer thicknesses d_{def} as

$$\Delta n = \frac{\lambda_{0y} - \lambda_{0x}}{2d_{\text{def}}}.$$

For the 60°, 70°, and 80° defect layers, the respective Δn values are 0.020 ±

0.003, 0.020 $\pm$ 0.002, and 0.021 $\pm$ 0.003.

7.7.4 Polarization state of the transmitted light

Fig. 7.25 presents the measured Stokes parameters, normalized to S_0. The black, red, and blue data points respectively correspond to S_1/S_0, S_2/S_0, and S_3/S_0. Recall that the input polarization state is ($\mathbf{S} = [\,1\;0\;1\;0\,]^T$). Nine spectra are presented in total:

- (a), (b), and (c) are the 60°, 70°, and 80° samples at θ_s = 0°.
- (d), (e), and (f) are the 60°, 70°, and 80° samples at θ_s = 45°.
- (g), (h), and (i) are the 60°, 70°, and 80° samples at θ_s = 90°.

As discussed in Sec. 7.7.1, symmetries of the defect structure create corresponding symmetries in the measured optical properties. At θ_s = 45° the sample is not birefringent since the *x*- and *y*-polarizations are oriented symmetrically between the optical axes. As a result, the polarization-state remains relatively unchanged upon transmission. (The small changes observed can be attributed to sample misalignment.) However, for θ_s = 0° and 90° the birefringence is maximized and the polarization-state is drastically altered. Furthermore, note the *x*-axis reflection symmetry between the S_2/S_0 and S_3/S_0 data sets at θ_s = 0° and 90°. This symmetry arises because the optical axes are reversed by a 90° sample rotation.

The interplay between birefringence and resonance phenomena causes the polarization-state to change rapidly with wavelength. To analyze the system behaviour, the spectrum in Fig. 7.25(a) will be examined in greater detail. Because all three samples behave similarly, the following analysis and discussion applied separately to each case yields equivalent conclusions. Fig. 7.26(a) and (b) respectively plot the polarization-resolved transmittances and the normalized Stokes parameters of the 60° sample at θ_s = 0° (Figs. 7.24d and 7.25a). The optical measurements are examined by progressing from low to high energy along the horizontal axes of Fig. 7.26. At each of the points labelled 1-7, the transmitted polarization-state can be understood in terms of how the incident 45°-polarized light couples to the *x*- and *y*-polarization resonance modes. The field amplitudes E_x and E_y follow Eq.

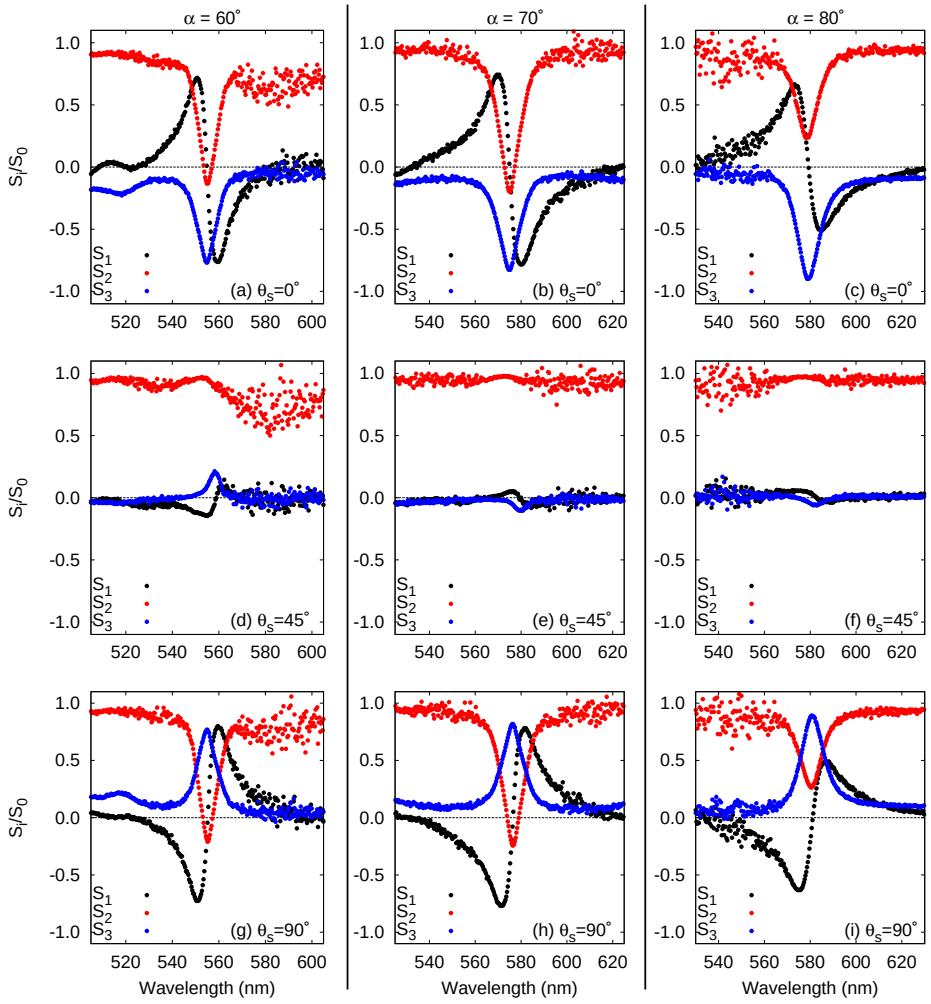

Figure 7.25: The measured Stokes parameters, normalized to S_0, of all three samples in all three orientations. The spectra in the left, centre, and right columns correspond to the α = 60°, 70°, and 80° defect samples. The spectra in the top, middle, and bottom row correspond to θ_s = 0°, 45°, and 90°.

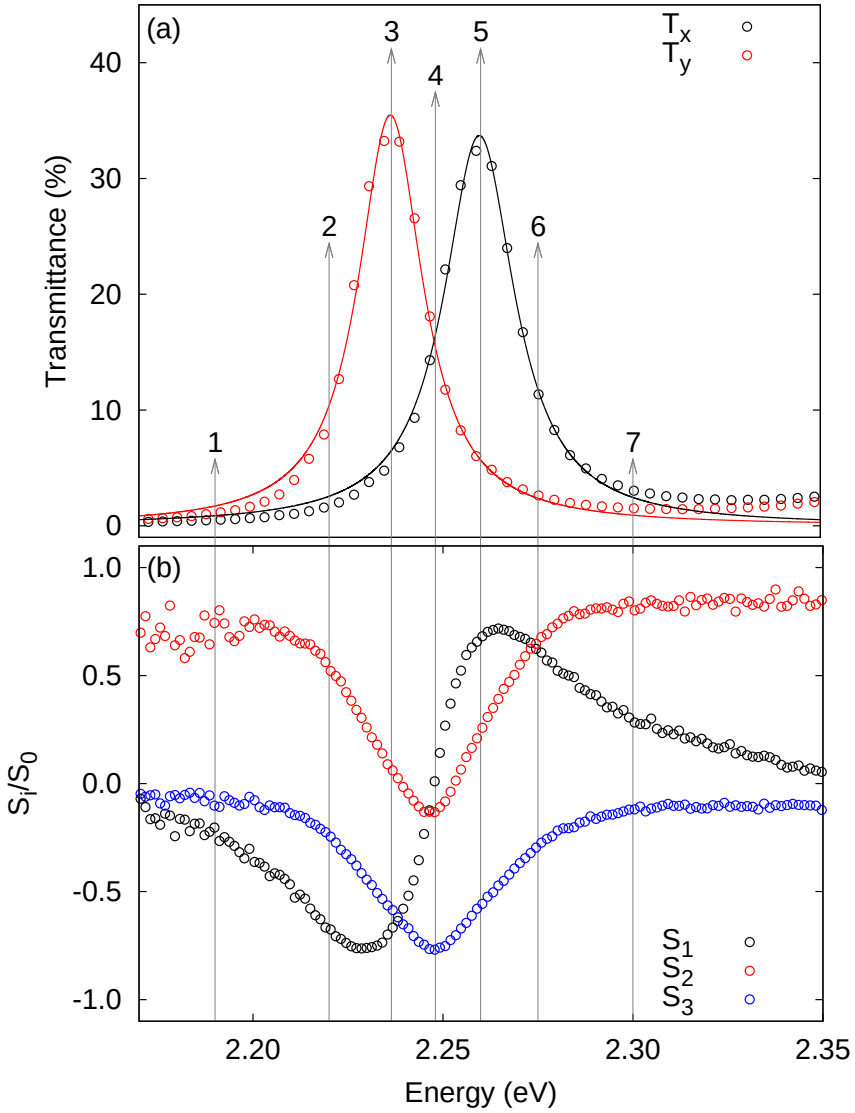

Figure 7.26: (a) The polarization resolved transmittances (T_x and T_y) and (b) the normalized Stokes parameters of the 60° sample at θ_s = 0°.

7.1; the field phases ϑ_y and ϑ_x follow Eq. 7.2. The Stokes paremeters depend on these quantities as described by Eqs. 7.9a-d.

1. As can be seen in Fig. 7.26(a), the incident light is strongly detuned from both resonances and only a small fraction of the light is transmitted through the multilayer. The low-signal levels lead to greater scatter in the measured Stokes parameters. The polarization-state is relatively unchanged upon transmission ($S_2 \approx 1$, $S_2 \approx 0$, $S_3 \approx 0$).

2. The incident light approaches the *y*-polarization resonance but is still far from the *x*-polarization resonance. Therefore, the *y*-polarization is preferentially transmitted, resulting in $E_x^2 < E_y^2$ and $S_1 < 0$ (see Eq. 7.9b). Since the incident *y*-polarized field couples to a resonance mode, the transmitted *y*-polarized light incurs a phase delay according to Eq. 7.2. The *y*-polarization therefore lags the *x*-polarization ($\vartheta_y < \vartheta_x$). As a result, $S_2 < 1$ (Eq. 7.9c) and $S_3 < 0$ (Eq. 7.9d).

3. The incident light is phase-matched to the *y*-polarization resonance and approaches the *x*-polarization resonance. Therefore, $E_x^2 \ll E_y^2$ and $S_1 \approx$ -1 in this region. The *y*-polarization phase delay is now $\pi/2$ and the *x*-polarized light also incurs a small phase delay. The relative phase delay $\Delta\vartheta = \vartheta_y - \vartheta_x$ is large and $S_2 <$ 0.2 and $S_3 <$ -0.5.

4. A particularly notable point is reached: the *x*- and *y*-polarization transmittances, and therefore E_x and E_y, are equal. S_1 is correspondingly zero. S_2 is also nearly zero and S_3 is at its minimum ($\approx$ -0.75). When $S_2 \approx 0$, $S_3/S_2 = \tan(\Delta\vartheta)$ is very large. This implies that $\Delta\vartheta \approx -\pi/2$ and the transmitted light is therefore almost entirely left circularly polarized.

5. The incident light is now phase-matched to the *x*-polarization resonance and is at an energy above the *y*-resonance. Therefore, $E_x^2 \gg E_y^2$ and $S_1 \approx 1$. Note that between this point and point 3, a spectral distance of 23.5 meV (5.8 nm), S_1 changes from -1 to 1. This illustrates the rapid spectral variation of the transmitted polarization state. There is still an appreciable relative phase delay between the *x*- and *y*-polarizations, as indicated by the S_2 and S_3 values.

6. The incident light is slightly detuned above the x-resonance and far above the y-resonance. In the transmitted beam, $E_x^2 > E_y^2$ and consequently $0 < S_1 < 1$. The y-polarization phase delay is now fixed at $\approx \pi$ and the x-polarization phase delay is approaching this value as well. The relative phase delay is therefore small. S_2 is returning to 1 and S_3 is returning to zero.

7. The incident light is strongly detuned above both resonances and both transmittances are low. The resonance-induced phase delays are both π and the relative phase delay is zero. Other than the π phase changes, the polarization-state is unchanged upon transmission ($S_2 \approx 1$, $S_2 \approx 0$, $S_3 \approx 0$).

In naturally occuring birefringent materials, such as quartz and calcite, a relative phase delay develops between ordinary and extraordinary rays due to optical path length differences. In this manner, linear polarizations develop circularity ($0 < |\Delta\vartheta| < \pi$, $S_3 \neq 0$) upon transmission through the thickness of the birefringent medium.

In an anisotopic defect layer however, birefringence combines with resonance producing a new effect. The defect birefringence breaks the resonator polarization-symmetry: at a given wavelength, there is a difference between the x- and y-polarization resonance-induced phase delays. The relative phase delay is therefore not merely determined by the polarization-dependent optical path length (as in a normal birefringent medium) but is now a function of the resonator Q-factor as well (Eq. 7.2). Given the small thickness (< 200 nm) and birefringence ($\Delta n \approx 0.02$) of the defect layers, the expected birefringence-induced phase difference is small. However, the resonance-induced phase difference is much more significant and the transmitted light is highly circular ($S_3 \rightarrow 1$). It is consequently termed giant resonance-induced birefringence, to distinguish it from regular birefringence effects.

7.8 Summary and Conclusions

When light is confined to a PC defect, new and useful optical effects are created by optical-wave resonances. These effects can be manipulated by

tuning the defect structure, allowing the design and fabrication of more advanced PC devices. The first examination of defect incorporation and engineering in GLAD-fabricated PCs has been presented in this chapter. The results of these investigations have advanced the level of sophistication and functionality of GLAD-fabricated PC devices.

Basic defect structures, $\lambda/2$-layers in Bragg multilayers and π phase-shift defects in rugate multilayers, were successfully realized and shown to exhibit the proper Lorentzian resonance behaviour. The phase-shift defect is a relatively unexamined defect structure and its properties were explored in detail using measurement and simulation. The value of the phase shift was demonstrated to be a key determinant of defect resonance, providing a means to control PC device properties. It was also demonstrated that the precision of the GLAD technique is sufficient to control defect-defect interaction in multi-defect PC architectures. This is an important capability given that new coupling-based optical phenomena are created upon incorporating additional defects.

Achieving truly novel devices requires integrating the unique properties offered by GLAD into PC device design. To achieve this goal, anisotropic defect layers were introduced into Bragg PCs and a specialized, polarization-measurement apparatus was constructed. The combination of birefringence and resonance leads to new polarization-sensitive optical properties, including giant resonance-induced birefringence and large polarization-state dispersion. These polarization effects may find use in designing novel polarization optics components not realizable with natural materials.

Chapter 8

Summary, Conclusions, and Future Recommendations

8.1 Thesis summary and conclusions

GLAD is an advanced PVD technique that enables the single-step, bottom-up fabrication of nanostructured materials. It is an enormously flexible fabrication technique, adaptable to many different material systems and applications. GLAD harnesses ballistic shadowing during film deposition to create self-assembled nanocolumnar architectures. The optical properties of these nanomaterials, composed of subwavelength structural inhomogeneities, can be understood through homogenization approaches, such as the Maxwell-Garnett and Bruggeman effective medium theories. These approximations reveal that, for lossless dielectrics, there is a monotonic relationship between the nanomaterial relative density and the refractive index. Because the relative density can be controlled using GLAD, the optical properties of GLAD-fabricated nanomaterials can be engineered with great precision. This provides a route towards more complex optical devices.

GLAD-enabled refractive index control of TiO_2 optical nanomaterials was studied at length in chapter four. Indices and deposition ratios were measured across a wide α range, providing the calibration data required for the design of complicated optical structures. Two different optical models were developed to examine the fabricated films. The first approximates the film as a homogenous material layer. It is shown to provide a good, first-order representation of the TiO_2 nanostructures prepared in this work. Prior

studies of GLAD-fabricated optical films have implemented such a model. However, the second model developed in this work has not been previously implemented in GLAD research. This new model improves upon the homogenous layer approach by allowing the refractive index to change with film thickness, with the index variation approximated by a linear gradient. Superior agreement between experimental and simulated results is obtained using the second model, demonstrating that it provides a more complete picture of these optical nanomaterials.

In chapter five, the optical nanomaterial results of chapter four were used to realize 1D PC devices. By dynamically varying α during deposition, the refractive index profile of the deposited material can be tuned. Periodic α variation leads to periodic refractive index profiles, creating PC structures. Two types of PCs were examined: Bragg and rugate multilayers. The former is based on a discretely varying index periodicity while the latter has a continuously varying periodic index. Several rugate multilayer structures were designed and fabricated. The rugate-PC band gap was controlled by tuning design parameters such as period and index contrast. An apodized version of the rugate PC, where the index profile is modified by a squared-Gaussian envelope function, was successfully fabricated as well. Excellent control over PC structural and optical properties is demonstrated by this work, surpassing previous reports in the literature.

After the rugate investigations, a large set of Bragg PCs were fabricated. An optical modeling technique, similar to those used in chapter four, was implemented to thoroughly examine the Bragg PC optical properties. The model developed approximates the Bragg PC high- and low-index sublayers as homogeneous layers. The simulation accurately reproduced salient features of the measured optical spectra, including band gap depth, width, and shape. Additionally, good agreement between the data and model is observed in the interference fringes outside the bandgap. The optical simulations reveal that this preliminary model is less accurate for thicker films, an observation supported by a detailed analysis of band-gap-parameter thickness scaling. Possible factors explaining the discrepancy were suggested. Incorporating these factors into new models is an important step towards an improved understanding of the PC optical properties.

In extending these PC results towards device-level research, it is im-

portant to target applications benefitting from unique GLAD advantages. Because GLAD-fabricated nanomaterials have greatly increased surface areas, they exhibit excellent environmental sensitivity and are commonly investigated for sensing devices. Developing the PC structures for sensing applications is correspondingly an attractive objective.

Chapter six presented the fabrication and characterization of a PC designed to measure RH. The sensor was designed to change colour as water vapour condensed in the internal PC pore structure. Maximizing the device sensitivity required translating the PC transmittance spectrum into the quantitative CIE colour space. The design was then optimized, producing the greatest possible colour change per unit wavelength shift. Measurements demonstrated excellent sensor performance. The device was capable of measuring 3% RH changes over the full RH range. RH changes as small as 1% could be visually detected at high RH (>50%). The band gap shifted less than 1 nm during over 90 hours of testing. Interesting hysteresis behaviour is observed in the sensor response. Numerical simulations show that the electric-field spatial distribution is strongly wavelength-dependent. Consequently, the electric field concentrates within distinct pore geometries at different wavelengths. Because capillary condensation, and hence refractive index change, is linked to the detailed pore structure, the optical response and the sensor hysteresis is wavelength-dependent. Controlling the spatial distribution of the field could be exploited to tune the sensor response.

Having successfully fabricated PC structures using GLAD, realizing the next generation of GLAD PCs requires creating more advanced PC devices. A prominent approach to enhancing PC functionality is to incorporate intentional defects to the index periodicity. This creates resonantly-confined states within the PC band gap that can be engineered to realize new optical behaviour. Chapter seven examined the theory, design, and GLAD-fabrication of PCs with a range of defect structures. Half-wavelength spacing layers in Bragg PCs were created and characterized. The properties of phase-shift defects in rugate PCs were explored in detail. Controlled defect interaction in multi-defect PCs was achieved as well. The unique polarization-sensitive properties of anisotropic PC defects were examined using a custom-built spectropolarimeter. The success of these results demonstrates the precision and flexibilty of the GLAD technique in fabricat-

ing advanced photonic devices. The results of this chapter present a new level of sophistication in GLAD optical research.

8.2 Recommendations for future research

The new results and capabilities presented in this thesis suggest several research opportunities and directions. An improved theoretical understanding of the optics of GLAD-fabricated nanostructures would be of major benefit. All the optical models used in GLAD-optics research thus far are elementary. In addition to refractive index gradients (as examined in chapter 4), other important optical effects need to be considered. Optical scattering by the nanostructures is universally neglected in analysis, as is the roughness of the air-nanostructure interface. GLAD-fabricated structures are inhomogeneous in several respects: the planar arrangement is disordered; the nanostructures are of many different sizes; the nanostructure surface is mesoscopically rough. Preliminary results implementing advanced modeling (finite-difference time-domain and frequency-domain methods) to simulate GLAD-fabricated PCs have been reported [175, 264]. While developing these theoretical techniques, new experimental research must be performed to accurately verify model predictions. Further research requires well-designed experimentation, accurate optical characterizations, new measurement techniques, and precise sample fabrication. A close partnership between theoretical and experimental work is essential.

In chapter six, a promising colourimetric PC sensor was developed. The spectral properties of this PC sensor were optimized for colour change. However, there remains a large parameter space which could be investigated to further improve the sensor performance. Only one deposition angle pair (60°, 80°) was examined. Using other α combinations to optimize the pore geometry and sensor response should be investigated. Additionally, the work could be extended to other materials (e.g. Al_2O_3) whose surface properties may lead to improved sensing characteristics. Because the spatial distribution of the electric field contributes to the optical changes, adjusting the PC design could also be used to engineer the sensor response.

In parallel with these optimization studies, continued investigation of this PC device should examine additional sensor characteristics. These in-

clude the sensor time-response, non-normal incidence spectral behaviour, and behaviour in liquid environments. Additionally, examining the effect of temperature on sensor response would be crucial as temperature strongly affects gas adsorption / desorption kinetics as well as relative humidity. Building on these results, demonstrating sensor response to other interesting analytes, such as volatile organic gases and biochemical compounds, would be a major accomplishment. The device could then be developed into a multiplexed sensor array. Such a device would be capable of colourimetric detection and discrimination of a wide range of compounds.

The realization of PC defects is an important step forward in GLAD optical devices. Continuation of this work could progress in several directions. Improving the resonator properties is an immediate goal. The fabricated defects have moderate quality factors (ranging from 35 to 225), and the maximum resonant transmittances are also sub-optimal ($T < 75\%$). Improved performance can be achieved by minimizing resonator loss and assuring the equivalency of the PC mirrors on both sides of the defect. This will require correcting fabrication and design inaccuracies and optimizing the device structure to engineer these PC defects into high-performance devices. Again, when targeting applications for these PC defect structures, it is important to leverage GLAD advantages. Sensing is always an attractive option and has been examined in preliminary studies [199]. Future work in this area will benefit from improved resonator performance.

Further research on the interesting and novel properties of anisotropic resonators is highly recommended. Examining the basic design parameter space (defect α, design wavelength in the UV / visible / NIR, number of PC periods) is an obvious starting point, as is demonstrating control over defect splitting, Q, and giant resonance-induced birefringence. It will be useful for device design to implement modeling techniques capable of handling anisotropic media, such as 4x4 matrix [160] or FDTD calculations. Increasing the number of anisotopic defects in the PC presents interesting options. Anisotropic defect coupling will be highly polarization-sensitive, and the interaction could be engineered by tuning the orientation of neighbouring defects. Advanced polarization optics could subsequently be realized, such as polarization spectroscopy elements, polarization-routing circuits, polarization-sensitive optical-delay components, and complicated dispersion filters.

By inventing and engineering new devices using GLAD-fabricated optical nanomaterials, this thesis has increased the optical capabilities of GLAD as an economic, bottom-up nanofabrication method. The core results of this thesis highlight the exciting prospects of optical nanomaterials: creating structured materials with engineered properties and providing unprecedented control over light. Given the ubiquitous scope of optical science, the pursuit of optical nanomaterials will continue to be a major topic in scientific research and technological development.

References

[1] M. Born and E. Wolf, *Principles of Optics*. Cambridge, UK: Cambridge University Press, 7^{th} ed., 1999.

[2] J. D. Jackson, *Classical Electrodynamics*. Hoboken, US: Wiley, 3^{rd} ed., 1998.

[3] W. Cai and V. Shalaev, *Optical Metamaterials: Fundamentals and Applications*. New York, US: Springer, 2010.

[4] J. D. Joannopoulos, S. G. Johnson, J. N. Winn, and R. D. Meade, *Photonic Crystals: Molding the flow of light*. New Jersey, US: Princeton University Press, 2^{nd} ed., 2008.

[5] J. D. Joannopoulos, P. R. Villeneuve, and S. Fan, "Photonic crystals: putting a new twist on light," *Nature*, vol. 386, pp. 143–149, 1997.

[6] A. Chutinan and S. John, "Light localization for broadband integrated optics in three dimensions," *Physical Review B*, vol. 72, p. 161316, 2005.

[7] T. Baba, "Slow light in photonic crystals," *Nature Photonics*, vol. 2, no. 8, pp. 465–473, 2008.

[8] R. W. Boyd and D. J. Gauthier, "Controlling the Velocity of Light Pulses," *Science*, vol. 326, pp. 1074–1077, 2009.

[9] S. Kawata, Y. Inouye, and P. Verma, "Plasmonics for near-field nano-imaging and superlensing," *Nature Photonics*, vol. 3, no. 7, pp. 388–394, 2009.

[10] J. B. Pendry, D. Schurig, and D. R. Smith, "Controlling Electromagnetic Fields," *Science*, vol. 312, pp. 1780–1782, 2006.

[11] H. Chen, C. T. Chan, and P. Sheng, "Transformation optics and metamaterials," *Nature Materials*, vol. 9, no. 5, pp. 387–396, 2010.

[12] J. V. Sanders, "Colour of precious opal," *Nature*, vol. 204, pp. 1151–1153, 1964.

[13] P. Vukusic and J. R. Sambles, "Photonic structures in biology," *Nature*, vol. 424, pp. 852–855, 2003.

[14] B. D. Gates, Q. Xu, M. Stewart, D. Ryan, C. G. Willson, and G. M. Whitesides, "New approaches to nanofabrication: molding, printing, and other techniques," *Chemical Reviews*, vol. 105, no. 4, pp. 1171–1196, 2005.

[15] G. M. Whitesides and J. P. Mathias, "Molecular self-assembly and nanochemistry: A chemical strategy for the synthesis of nanostructures," *Science*, vol. 254, pp. 1312–1319, 1991.

[16] R. H. F. *et al.*, "Long range interactions in nanoscale science," *Reviews of Modern Physics*, vol. 82, no. 2, pp. 1887–1944, 2010.

[17] X. Wang, J. Zhuang, Q. Peng, and Y. Li, "A general strategy for nanocrystal synthesis," *Nature*, vol. 437, pp. 121–124, 2005.

[18] Y. X. *et al.*, "One-Dimensional Nanostructures: Synthesis, Characterization, and Applications," *Advanced Materials*, vol. 15, no. 5, pp. 353–389, 2003.

[19] Z. F. Ren, Z. P. Huang, J. W. Xu, J. H. Wang, P. Bush, M. P. Siegal, and P. N. Provencio, "Synthesis of large arrays of well-aligned carbon nanotubes on glass," *Science*, vol. 282, pp. 1105–1107, 1998.

[20] N. C. Seeman and A. M. Belcher, "Emulating biology: Building nanostructures from the bottom up," *Proceedings of the National Academy of Sciences of the United States of America*, vol. 99, pp. 6451–6455, 2002.

[21] M. T. Taschuk, M. M. Hawkeye, and M. J. Brett, "Glancing angle deposition," in *Handbook of Deposition Technologies for Films and Coatings: Science, Applications and Technology* (P. M. Martin, ed.), Oxford, UK: Elsevier, 3^{rd} ed., 2010.

[22] M. M. Hawkeye and M. J. Brett, "Glancing angle deposition: Fabrication, properties, and applications of micro- and nanostructured thin films," *Journal of Vacuum Science and Technology A*, vol. 25, no. 5, pp. 1317–1335, 2007.

[23] T. Motohiro and Y. Taga, "Thin film retardation plate by oblique deposition," *Applied Optics*, vol. 28, no. 13, pp. 2466–2482, 1989.

[24] N. O. Young and J. Kowal, "Optically active fluorite films," *Nature*, vol. 183, pp. 104–105, 1959.

[25] K. Robbie, M. J. Brett, and A. Lakhtakia, "Chiral sculptured thin films," *Nature*, vol. 384, p. 616, 1996.

[26] I. Hodgkinson and Q. H. Wu, "Inorganic chiral optical materials," *Advanced Materials*, vol. 13, no. 12-13, pp. 889–897, 2001.

[27] K. D. Harris, J. R. McBride, K. E. Nietering, and M. J. Brett, "Fabrication of porous platinum thin films for hydrocarbon sensor applications," *Sensors and Materials*, vol. 13, no. 4, pp. 225–234, 2001.

[28] J. J. Steele, M. T. Taschuk, and M. J. Brett, "Nanostructured metal oxide thin films for humidity sensors," *IEEE Sensors Journal*, vol. 8, no. 8, pp. 1422–1429, 2008.

[29] K. Robbie, A. J. P. Hnatiw, M. J. Brett, R. I. MacDonald, and J. N. McMullin, "Inhomogeneous thin film optical filters fabricated using glancing angle deposition," *Electronics Letters*, vol. 33, no. 14, pp. 1213–1214, 1997.

[30] S. R. Kennedy and M. J. Brett, "Porous broadband antireflection coating by glancing angle deposition," *Applied Optics*, vol. 42, no. 22, pp. 4573–4579, 2003.

[31] E. Ritter, "Deposition of oxide films by reactive evaporation," *Journal of Vacuum Science and Technology*, vol. 3, no. 4, pp. 225–226, 1966.

[32] S. I. Shah, G. H. Jaffari, E. Yassitepe, and B. Ali, "Evaporation: Processes, bulk microstructures, and mechanical properties," in *Handbook of Deposition Technologies for Films and Coatings: Science, Applications and Technology* (P. M. Martin, ed.), Oxford, UK: Elsevier, 3rd ed., 2010.

[33] L. I. Maissel and R. Glang, eds., *Handbook of thin film technology*. New York, US: McGraw-Hill, 1970.

[34] B. Lewis and D. S. Campell, "Nucleation and initial-growth behavior of thin film deposits," *Journal of Vacuum Science and Techbology*, vol. 4, no. 5, pp. 209–218, 1967.

[35] C. Ratsch and J. A. Venables, "Nucleation theory and the early stages of thin film growth," *Journal of Vacuum Science and Techology A*, vol. 21, no. 5, pp. S96–S109, 2003.

[36] R. W. Vook, "Structure and growth of thin films," *International Metals Review*, vol. 27, pp. 209–245, 1982.

[37] K. Reichelt, "Nucleation and growth of thin films," *Vacuum*, vol. 38, no. 12, pp. 1083–1099, 1988.

[38] J. A. Venables, G. D. T. Spiller, and M. Hanbücken, "Nucleation and growth of thin films," *Reports on Progress in Physics*, vol. 47, pp. 399–459, 1984.

[39] J. A. Venables, "Atomic process in crystal growth," *Surface Science*, vol. 299/300, pp. 798–817, 1994.

[40] B. A. Movchan and A. V. Demchishin, "Study of the structure and properties of thick vacuum condensates of nickel, titanium, tungsten, aluminum oxide and zirconium oxide," *Fizika Metallov i Metallovedenie*, vol. 28, no. 4, pp. 653–660, 1969.

[41] H. T. G. Hentzell, C. R. M. Grovenor, and D. A. Smith, "Grain-structure variation with temperature for evaporated metal-films," *Journal of Vacuum Science and Technology A*, vol. 2, pp. 218–219, 1984.

[42] J. V. Sanders, *Chemisorption and Reactions on Metal Films*. Academic Press, 1971.

[43] J. A. Thornton, "High-rate thick-film growth," *Annual Review of Materials Science*, vol. 7, pp. 239–260, 1977.

[44] A. Kundt, "Ueber doppelbrechung des lichtes in metallschiten, welche durch zerstäuben einer kathode hergestellt sind," *Annalen der Physik*, vol. 27, pp. 59–71, 1886.

[45] F. Kaempf, "Gröβe und ursache der doppelbrechung in kundtschen spiegelnund erzeugung von doppelbrechung in metallspiegeln durch zug," *Annalen der Physik*, vol. 26, pp. 308–333, 1905.

[46] C. Maurin, "Dichroïsme, birèfringence et conductibilité de lames métalliques minces obtenues par pulvérisation cathodique," *Comptes Rendus Hebdomadaires des Séances de l'Académie des Sciences*, vol. 142, pp. 870–872, 1906.

[47] C. Bergholm, "Uber doppelbrechung in kathodenzerstäubten metallschichten," *Annalen der Physik*, vol. 43, pp. 1–23, 1914.

[48] T. G. Knorr and R. W. Hoffman, "Dependence of geometric magnetic anisotropy in thin iron films," *Physical Review*, vol. 113, pp. 1039–1046, 1959.

[49] D. O. Smith, "Anisotropy in permalloy films," *Journal of Applied Physics*, vol. 30, pp. S264–S265, 1959.

[50] D. O. Smith, M. S. Cohen, and G. P. Weiss, "Oblique-incidence anisotropy in evaporated permalloy films," *Journal of Applied Physics*, vol. 31, pp. 1755–1762, 1960.

[51] E. W. Pugh, E. L. Boyd, and J. F. Freedman, "Angle-of-indicence anisotropy in evaporated nickel-iron films," *IBM Journal of Research and Development*, vol. 4, no. 2, pp. 163–172, 1960.

[52] V. Kamberský, Z. Málek, Z. Frait, and M. Ondris, "The dependence of the uniaxial magnetic anisotropy in evaporated films on the angle of incidence," *Czechoslovak Journal of Physics,* vol. 11, no. 3, pp. 171–178, 1961.

[53] J. M. Nieuwenhuizen and H. B. Haanstra, "Microfractography of thin films," *Philips Tech. Review*, vol. 27, pp. 87–91, 1966.

[54] A. G. Dirks and H. J. Leamy, "Columnar microstructure in vapor-deposited films," *Thin Solid Films*, vol. 47, pp. 219–233, 1977.

[55] S. Lichter and J. Chen, "Model for columnar microstructure of thin solid films," *Physical Review Letters*, vol. 56, pp. 1396–1399, 1986.

[56] P. Meakin, "Ballistic deposition onto inclined surfaces," *Physical Review A*, vol. 38, pp. 994–1004, 1988.

[57] R. N. Tait, T. Smy, and M. J. Brett, "Modeling and characterization of columnar growth in evaporated-films," *Thin Solid Films*, vol. 226, pp. 196–201, 1993.

[58] I. J. Hodgkinson, Q. H. Wu, and J. Hazel, "Empirical equations for the principal refractive indices and column angle of obliquely deposited films of tantalum oxide, titanium oxide, and zirconium oxide," *Applied Optics*, vol. 37, pp. 2653–2659, 1998.

[59] S. R. Kennedy and M. J. Brett, "Advanced techniques for the fabrication of square spiral photonic crystals by glancing angle deposition," *Journal of Vacuum Science and Technology B*, vol. 22, no. 3, pp. 1184–1190, 2004.

[60] K. D. Harris, D. Vick, T. Smy, and M. J. Brett, "Column angle variations in porous chevron thin films," *Journal of Vacuum Science and Technology A*, vol. 20, no. 6, pp. 2062–2067, 2002.

[61] A. C. van Popta, J. C. Sit, and M. J. Brett, "Optical properties of porous helical thin films," *Applied Optics*, vol. 43, no. 18, pp. 3632–3639, 2004.

[62] B. Dick, M. J. Brett, and T. Smy, "Investigation of substrate rotation at glancing incidence on thin-film morphology," *Journal of Vacuum Science and Technology B*, vol. 21, no. 6, pp. 2569–2575, 2003.

[63] K. Robbie, C. Shafai, and M. J. Brett, "Thin films with nanometer-scale pillar microstructure," *Journal of Materials Research*, vol. 14, no. 7, pp. 3158–3163, 1999.

[64] R. Messier, A. Giri, and R. Roy, "Revised structure zone model for thin film physical structure," *Journal of Vacuum Science & Technology A: Vacuum, Surfaces, and Films*, vol. 2, pp. 500–503, 1984.

[65] R. Landauer, "Electrical conductivity in inhomogeneous media," *AIP Conference Proceedings*, vol. 40, pp. 2–45, 1978.

[66] D. E. Aspnes, "Optical properties of thin films," *Thin Solid Films*, vol. 89, pp. 249–262, 1982.

[67] D. J. Bergman, "The dielectric constant of a composite material - a problem in classical physics," *Physics Reports*, vol. 43, pp. 377–407, 1978.

[68] C. Brosseau, "Modelling and simulation of dielectric heterostructures: a physical survey from a historical perspective," *Journal of Physics D*, vol. 39, pp. 1277–1294, 2006.

[69] J. C. M. Garnett, "Colours in metal glasses and metallic films," *Philosophical Transactions of the Royal Society of London*, vol. 203, pp. 385–420, 1904.

[70] D. A. G. Bruggeman, "Berechnung verschiedener physikalischer konstanten von heterogenen substanzen. i. dielecktrizität konstanten und leitfäkigkeiten der mischkörper aus isotropen substanzen," *Annalen der Physik*, vol. 24, pp. 636–664, 1935.

[71] D. E. Aspnes, "Local-field effects and effective medium theory: a microscopic perspective," *American Journal of Physics*, vol. 50, no. 8, pp. 704–709, 1982.

[72] G. A. Niklasson, C. G. Granqvist, and O. Hunderi, "Effective medium models for the optical properties of inhomogeneous materials," *Applied Optics*, vol. 20, no. 1, pp. 26–30, 1981.

[73] R. W. Cohen, G. D. Cody, M. D. Coutts, and B. Abeles, "Optical properties of granular silver and gold films," *Physical Review B*, vol. 8, no. 8, pp. 3689–3701, 1973.

[74] S. Berthier, "Anisotropic effective medium theories," *Journal de Physique I*, vol. 4, no. 2, pp. 303–318, 1994.

[75] G. B. Smith, "Theory of angular selective transmittance in oblique columnar thin-films containing metal and voids," *Applied Optucs*, vol. 29, no. 25, pp. 3685–3693, 1990.

[76] G. W. Mbise, D. L. Bellac, G. A. Niklasson, and C. G. Granqvist, "Angular selective window coatings: theory and experiments," *Journal of Physics D*, vol. 30, pp. 2103–2122, 1997.

[77] J. Gospodyn and J. Sit, "Characterization of dielectric columnar thin films by variable angle Mueller matrix and spectroscopic ellipsometry," *Optical Materials*, vol. 29, no. 2-3, pp. 318–325, 2006.

[78] F. L. Galeener, "Submicroscopic-void resonance: the effect of internal roughness on optical absorption," *Physical Review Letters*, vol. 27, no. 7, pp. 421–423, 1971.

[79] G. Mie, "Beiträge zur optik trüber medien, speziell kolloidaler metallösungen," *Annalen der Physik (4)*, vol. 25, pp. 377–445, 1908.

[80] P. Debye, "Der lichtdruck auf kugeln von beliebigem material," *Annalen der Physik (4)*, vol. 30, pp. 57–136, 1909.

[81] D. Stroud and F. P. Pan, "Self-consistent approach to electromagnetic wave propagation in composite media: application to model granular metals," *Physical Review B*, vol. 17, no. 4, pp. 1602–1610, 1978.

[82] W. G. Egan and D. E. Aspnes, "Finite-wavelength effectis in composite media," *Physical Review B*, vol. 26, no. 10, pp. 5313–5320, 1982.

[83] W. Lamb, D. M. Wood, and N. W. Ashcroft, "Long-wavelength electromagnetic propagation in heterogeneous media," *Physical Review B*, vol. 21, no. 6, pp. 2248–2266, 1980.

[84] G. B. Airy, "On the phenomena of Newton's Rings when formed between transparent Substances of different refractive Powers," *Philosophical Magazine, Series 3*, vol. 2, pp. 20–30, 1833.

[85] C. Fabry and A. Perot, "Théorie et applications d'une nouvelle méthode de spectroscopie interférentielle," *Annales de Chimie et de Physique*, vol. 16, pp. 115–144, 1899.

[86] H. Fizeau, "Recherches sur les modifications que subit la vitesse de la lumière dans le verre et plusieurs autres corps solides sous l'influence de la chaleur," *Annales de Chimie et de Physique*, vol. 66, pp. 429–481, 1862.

[87] F. Abelès, "Recherche sur la propagation des ondes électromagnétiques sinuso idales dans les milieux stratifiés: Application aux couches minces," *Annales de Physique*, vol. 5, pp. 596–640, 1950.

[88] L. Rayleigh, "On the maintenance of vibrations by forces of double frequency, and on the propagation of waves through a medium endowed with a periodic structure," *Philosophical Magazine (5)*, vol. 24, no. 147, pp. 145–159, 1887.

[89] L. Rayleigh, "On the reflection of light from a regularly stratified medium," *Proceedings of the Royal Society of London A*, vol. 93, no. 655, pp. 565–577, 1917.

[90] W. L. Bragg, *The Crystalline State*, vol. 1. London, UK: G. Bell and Sons, 1933.

[91] F. Bloch, "Über die quantenmechanik der elektronen in kristallgittern," *Zeitschrift für Physik*, vol. 52, no. 7-8, pp. 555–600, 1928.

[92] E. Yablonovitch, "Inhibited spontaneous emission in solid-state physics and electronics," *Physical Review Letters*, vol. 58, no. 20, pp. 2059–2062, 1987.

[93] S. John, "Strong localization of photons in certain disordered dielectric superlattices," *Physical Review Letters*, vol. 58, no. 23, pp. 2486–2489, 1987.

[94] C. López, "Materials aspects of photonic crystals," *Advanced Materials*, vol. 15, no. 20, pp. 1679–1704, 2004.

[95] H. A. Macleod, *Thin-Film Optical Filters*. Bristol, UK: Institute of Physics Publishing, 3^{rd} ed., 2001.

[96] W. H. Southwell, "Spectral response calculations of rugate filters using coupled-wave theory," *Journal of the Optical Society of America*, vol. 5, no. 9, pp. 1558–1564, 1988.

[97] B. T. Sullivan, G. A. Clarke, T. Akiyama, N. Osborne, M. Ranger, J. A. Dobrowolski, L. Howe, A. Matsumoto, Y. Song, and K. Kikuchi, "High-rate automated deposition system for the manufacture of complex multilayer coatings," *Applied Optics*, vol. 39, no. 1, pp. 157–167, 2000.

[98] J. A. Dobrowolski and D. Lowe, "Optical thin-film synthesis program based on use of Fourier-transforms," *Applied Optics*, vol. 17, no. 19, pp. 3039–3050, 1978.

[99] A. V. Tikhonravov, M. K. Trubetskov, and G. W. DeBell, "Application of the needle optimization technique to the design of optical coatings," *Applied Optics*, vol. 35, no. 28, pp. 5493–5508, 1996.

[100] A. V. Tikhonravov, M. K. Trubetskov, and G. W. DeBell, "Optical coating design approaches based on the needle optimization technique," *Applied Optics*, vol. 46, no. 5, pp. 704–710, 2007.

[101] H. A. Macleod, "Monitoring of optical coatings," *Applied Optics*, vol. 20, no. 1, pp. 82–89, 1981.

[102] B. T. Sullivan and J. A. Dobrowolski, "Deposition error compensation for optical multilayer coatings. 1. Theoretical description," *Applied Optics*, vol. 31, no. 19, pp. 3821–3835, 1992.

[103] B. T. Sullivan and J. A. Dobrowolski, "Deposition error compensation for optical multilayer coatings. 2. Experimental results - sputtering system," *Applied Optics*, vol. 32, no. 13, pp. 2351–2360, 1993.

[104] W. J. Gunning, R. L. Hall, F. J. Woodberry, W. H. Southwell, and N. S. Gluck, "Codeposition of continuous composition rugate filters," *Applied Optics*, vol. 28, no. 14, pp. 2945–2948, 1989.

[105] M. F. Ouellette, R. V. Lang, K. L. Yan, R. W. Bertram, R. S. Owles, and D. Vincent, "Experimental studies of inhomogeneous coatings for optical applications," *Journal of Vacuum Science and Technology A*, vol. 9, no. 3, pp. 1188–1192, 1991.

[106] L. Martinu and D. Poitras, "Plasma deposition of optical films and coatings: a review," *Journal of Vacuum Science and Technology A*, vol. 18, no. 6, pp. 2619–2645, 2000.

[107] R. Vernhes, O. Zabeida, J. E. Lemberg-Saphieha, and L. Martinu, "Single-material inhomogenous optical filters based on microstructural gradients in plasma-deposited silicon nitride," *Applied Optics*, vol. 43, no. 1, pp. 97–103, 2004.

[108] E. P. Donovan, D. V. Vechten, A. D. F. Kahn, C. A. Carosella, and G. K. Hubler, "Near infrared rugate filter fabrication by ion beam assisted deposition of $si_{(l-x)}n_x$ films," *Applied Optics*, vol. 28, no. 14, pp. 2940–2944, 1989.

[109] G. Korotcenkov and B. K. Cho, "Porous Semiconductors: Advanced Material for Gas Sensor Applications," *Critical Reviews in Solid State and Materials Sciences*, vol. 45, pp. 1–37, 2010.

[110] S. Y. Choi, M. Mamak, G. von Freymann, N. Chopra, and G. A. Ozin, "Mesoporous Bragg Stack Color Tunable Sensors," *Nano Letters*, vol. 6, no. 11, pp. 2456–2461, 2006.

[111] Y. Fink, A. M. urbas, M. G. Bawendi, J. D. Joannolpoulos, and E. L. Thomas, "Block copolymers as photonic bandgap materials," *Journal of Lightwave Technology*, vol. 17, no. 11, pp. 1963–1969, 1999.

[112] F. A. Grant, "Properties of rutile (titanium dioxide)," *Reviews of Modern Physics*, vol. 31, no. 3, pp. 646–674, 1959.

[113] J. R. DeVore, "Refractive indices of rutile and sphalerite," *Journal of the Optical Society of America*, vol. 41, no. 6, pp. 416–419, 1951.

[114] W. L. Bond, "Measurement of the refractive incides of several crystals," *Journal of Applied Physics*, vol. 36, no. 5, pp. 1674–1677, 1965.

[115] U. Diebold, "The surface science of titanium dioxide," *Surface Science Reports*, vol. 48, no. 5-8, pp. 53–229, 2003.

[116] G. Pfaff and P. Reynders, "Angle-dependent optical effects deriving from submicron structures of films and pigments," *Chemical Reviews*, vol. 99, pp. 1963–1981, 1999.

[117] B. L. Diffey and P. M. Farr, "Sunscreen protection against UVB, UVA and blue light: an *in vivo* and *in vitro* comparison," *British Journal of Dermatology*, vol. 124, no. 3, pp. 258–263, 1991.

[118] B. O'Regan and M. Grätzel, "A low-cost, high-efficiency solar cell based on dye-sensitized colloidal TiO_2 films," *Nature*, vol. 353, pp. 737–740, 1991.

[119] A. L. Linsebigler, G. Lu, and J. T. Yates, "Photocatalysis on TiO_2 surfaces: principles, mechanisms, and selected results," *Chemical Reviews*, vol. 95, no. 3, pp. 735–758, 1995.

[120] Y. Matsumoto, M. Murakami, T. Shono, T. Hasegawa, T. Fukumura, M. Kawasaki, P. Ahmet, T. Chikyow, S. ya Koshihara, and H. Koinuma, "Room-temperature ferromagnetism in transparent transition metal-doped titanium dioxide," *Science*, vol. 291, pp. 854–856, 2001.

[121] D. B. Strukov, G. S. Snider, D. R. Stewart, and R. S. Williams, "The missing memristor found," *Nature*, vol. 453, pp. 80–83, 2008.

[122] J. J. Yang, M. D. Pickett, X. Li, D. A. A. Ohlberg, D. R. Stewart, and R. S. Williams, "Memristive switching mechanism for metal/oxide/metal nanodevices," *Nature Nanotechnology*, vol. 3, pp. 429–433, 2008.

[123] A. R. Armstrong, G. Armstrong, J. Canales, R. García, and P. G. Bruce, "Lithium-ion intercalation into TiO_2-B nanowires," *Advanced Materials*, vol. 17, no. 7, pp. 862–865, 2005.

[124] M. Wagemaker, A. P. M. Kentgens, and F. M. Mulder, "Equilibrium lithium transport between nanocrystalline phases in intercalated TiO_2 anatase," *Nature*, vol. 418, pp. 397–399, 2002.

[125] G. Hass, "Optical film materials and their applications," *Journal of Vacuum Science and Technology*, vol. 4, pp. 71–79, 1967.

[126] H. K. Pulker, G. Paesold, and E. Ritter, "Refractive indices of TiO_2 films produced by reactive evaporation of various titanium-oxygen phases," *Applied Optics*, vol. 15, no. 12, pp. 2986–2991, 1976.

[127] H. Selhofer, E. Ritter, and R. Linsbod, "Properties of titanium dioxide films prepared by reactive electron-beam evaporation from various starting materials," *Applied Optics*, vol. 41, pp. 756–762, 2002.

[128] H. W. Lehmann and K. Frick, "Optimizing deposition parameters of electron beam evaporated TiO_2 films," *Applied Optics*, vol. 27, no. 23, pp. 4920–4924, 1988.

[129] J. M. B. *et al.*, "Comparison of the properties of titanium dioxide films prepared by various techniques," *Applied Optics*, vol. 28, no. 15, pp. 3303–3317, 1989.

[130] K. N. Rao, "Influence of deposition parameters on optical properties of TiO_2 films," *Optical Engineering*, vol. 41, no. 9, pp. 2357–2364, 2002.

[131] M. J. Colgan, B. Djufors, D. G. Ivey, and M. J. Brett, "Effects of annealing on titanium dioxide structured films," *Thin Solid Films*, vol. 466, pp. 92–96, 2004.

[132] B. Karunagaran, R. T. R. Kumar, D. Mangalaraj, S. K. Narayandass, and G. M. Rao, "Influence of thermal annealing on the composition and structural parameters of DC magnetron sputtered titanium dioxide thin films," *Crystal Research and Technology*, vol. 37, no. 12, pp. 1285–1292, 2002.

[133] G. Tian, L. Dong, C. Wei, J. Huang, H. He, and J. Shao, "Investigation on microstructure and optical properties of titanium dioxide coatings annealed at various temperature," *Optical Materials*, vol. 28, pp. 1058–1063, 2006.

[134] A. C. van Popta, J. Cheng, J. C. Sit, and M. J. Brett, "Birefringence enhancement in annealed TiO_2 thin films," *Journal of Applied Physics*, vol. 102, p. 013517, 2007.

[135] S. M. Purcell, M. W. Horn, and A. Lakhtakia, "Blue-shifting of circular bragg phenomenon by annealing of chiral sculptured thin films," *Optics Express*, vol. 14, no. 17, pp. 8001–8012, 2006.

[136] K. Levenberg, "A method for the solution of certain non-linear problems in least squares," *The Quarterly of Applied Mathematics*, vol. 2, pp. 164–168, 1944.

[137] D. W. Marquardt, "An algorithm for least-squares estimation of nonlinear parameters," *Journal of the Society for Industrial and Applied Mathematics*, vol. 11, no. 2, pp. 431–441, 1963.

[138] W. H. Press, S. A. Teukolsky, W. T. Vetterling, and B. P. Flannery, *Numerical Recipes: The Art of Scientific Computing*. Cambridge, UK: Cambridge University Press, 3rd ed., 2007.

[139] P. R. Bevington and D. K. Robinson, *Data Reduction and Error Analysis for the Physical Sciences*. New York, US: McGraw-Hill, 3rd ed., 2003.

[140] J. P. Borgogno, B. Lazarides, and E. Pelletier, "Automatic determination of the optical constants of inhomogeneous thin films," *Applied Optics*, vol. 21, no. 22, pp. 4020–4029, 1982.

[141] D. P. A. *et al.*, "Multiple determination of the optical constants of thin-film coating materials," *Applied Optics*, vol. 23, no. 20, pp. 3571–3596, 1984.

[142] F. Abelès, "Methods for determining optical parameters of thin films," in *Progress in Optics* (E. Wolf, ed.), vol. 2, Amsterdam, NL: Elsevier, 1963.

[143] K. Kaminska, T. Brown, G. Beydaghyan, and K. Robbie, "Vacuum evaporated porous silicon photonic interference filters," *Applied Optics*, vol. 42, pp. 4212–4219, 2003.

[144] M. F. Schubert, J.-Q. Xi, J. K. Kim, and E. F. Schubert, "Distributed Bragg reflector consisting of high- and low-refractive-index thin film layers made of the same material," *Applied Physics Letters*, vol. 90, p. 141115, 2007.

[145] J. K. Kim, S. Chhajed, M. F. Schubert, E. F. Schubert, A. J. Fischer, M. H. Crawford, J. Cho, H. Kim, and C. Sone, "Light-Extraction Enhancement of GaInN Light-Emitting Diodes by Graded-Refractive-Index Indium Tin Oxide Anti-Reflection Contact," *Advanced Materials*, vol. 40, pp. 801–804, 2008.

[146] Y. Zhong, Y. Shin, C. Kim, B. Lee, E. Kim, Y. Park, K. Sobahan, C. Hwangbo, Y. Lee, and T. Kim, "Optical and electrical properties of indium tin oxide thin films with tilted and spiral microstructures prepared by oblique angle deposition," *Journal of Materials Research*, vol. 23, no. 9, pp. 2500–2505, 2008.

[147] B. Szeto, P. C. P. Hrudey, J. Gospodyn, J. C. Sit, and M. J. Brett, "Obliquely deposited tris(8-hydroxyquinoline) aluminium (Alq3) biaxial thin films with negative in-plane birefringence," *Journal of Physics A*, vol. 9, pp. 457–462, 2007.

[148] D. Schmidt, A. C. Kjerstad, T. Hofmann, R. Skomski, E. Schubert, and M. Schubert, "Optical, structural, and magnetic properties of cobalt nanostructure thin films," *Journal of Applied Physics*, vol. 105, p. 113508, 2009.

[149] D. Schmidt, B. Booso, T. Hofmann, E. Schubert, A. Sarangan, and M. Schubert, "Monoclinic optical constants, birefringence, and dichroism of slanted titanium nanocolumns determined by generalized ellipsometry," *Applied Physics Letters*, vol. 94, p. 011914, 2009.

[150] J.-Q. Xi, J. K. Kim, and E. F. Schubert, "Silica Nanorod-Array Films with Very Low Refractive Indices," *Nano Letters*, vol. 5, no. 7, pp. 1385–1387, 2005.

[151] K. Starbova, J. Dikova, and N. Starbov, "Structure related properties of obliquely deposited amorphous a-As2S3 thin films," *Journal of Non-Crystalline Solids*, vol. 210, pp. 261–266, 1997.

[152] P. Bhardwaj, P. K. Shishoda, and R. M. Mehra, "Photo-induced changes in optical properties of As_2S_3 and As_2Se_3 films deposited at normal and oblique incidence," *Journal of Materials Science*, vol. 38, pp. 937–940, 2003.

[153] S. Wang, X. Fu, G. Xia, J. Wang, J. Shao, and Z. Fan, "Structure and optical properties of ZnS thin films grown by glancing angle deposition," *Applied Surface Science*, vol. 252, pp. 8734–8737, 2006.

[154] S. Wang, G. Xia, X. Fu, H. He, J. Shao, and Z. Fan, "Preparation and characterization of nanostructured ZrO2 thin films by glancing angle deposition," *Thin Solid Films*, vol. 515, pp. 3352–3355, 2007.

[155] S. Wang, G. Xia, H. He, K. Yi, J. Shao, and Z. Fan, "Structural and optical properties of nanostructured TiO_2 thin films fabricated by glancing angle deposition," *Journal of Alloys and Compounds*, vol. 431, no. 1-2, pp. 287–291, 2007.

[156] P. Bhardwaj, P. K. Shishoda, and R. M. Mehra, "Optical and electrical properties of obliquely deposited a-$GeSe_2$ films," *Journal of Materials Science*, vol. 42, pp. 1196–1201, 2007.

[157] X. Xiao, G. Dong, C. Xua, H. He, H. Qi, Z. Fan, and J. Shao, "Structure and optical properties of Nb_2O_5 sculptured thin films by glancing angle deposition," *Applied Surface Science*, vol. 255, pp. 2192–2195, 2008.

[158] G. E. Jellison, "Generalized ellipsometry for materials characterization," *Thin Solid Films*, vol. 450, pp. 42–50, 2004.

[159] M. Schubert, "Another century of ellipsometry," *Annalen der Physik (Leipzig)*, vol. 15, no. 7-8, pp. 480–497, 2006.

[160] D. D. Berreman, "Optics in stratified and anisotropic media: 4x4-matrix formulation," *Journal of the Optical Society of America*, vol. 62, no. 4, pp. 502–510, 1972.

[161] M. Schubert, "Polarization-dependent optical parameters of arbitrarily anisotropic homogeneous layered systems," *Physical Review B*, vol. 53, no. 8, pp. 4265–4274, 1996.

[162] M. M. Hawkeye and M. J. Brett, "Controlling the optical properties of nanostructured TiO_2 thin films," *Physica Status Solidi A*, vol. 206, no. 5, pp. 940–943, 2009.

[163] A. V. Tikhonravov, M. K. Trubetskov, M. A. Kokarev, T. V. Amotchkina, A. Duparré, E. Quesnel, D. Ristau, and S. Günster, "Effect of systematic errors in spectral photometric data on the accuracy of determination of optical parameters of dielectric thin films," *Applied Optics*, vol. 42, no. 13, pp. 2555–2560, 2002.

[164] D. F. Edwards, "Silicon," in *Handbook of Optical Constants of Solids* (E. D. Palik, ed.), vol. 1, San Diego, US: Academic Press, 1998.

[165] A. V. Tikhonravov, M. K. Trubetskov, B. T. Sullican, and J. A. Dobrowolski, "Influence of small inhomogeneities on the spectral characteristics of single thin films," *Applied Optics*, vol. 36, no. 28, pp. 7188–7198, 1997.

[166] M. Harris, H. A. Macleod, S. Ogura, E. Pelletier, and B. Vidal, "The relationship between optical inhomogeneity and film structure," *Thin Solid Films*, vol. 57, pp. 173–178, 1979.

[167] D. Mergel, D. Buschendorf, S. Eggert, R. Grammes, and B. Samset, "Density and refractive index of TiO_2 films prepared by reactive evaporation," *Thin Solid Films*, vol. 371, pp. 218–224, 2000.

[168] D. R. Lide, ed., *CRC Handbook of Chemistry and Physics*. Boca Raton, US: CRC Press, 90^{th} ed., 2010.

[169] H. E. Bennett and J. O. Porteous, "Relation Between Surface Roughness and Specular Reflectance at Normal Incidence," *Journal of the Optical Society of America*, vol. 51, no. 2, pp. 123–129, 1961.

[170] J. Strong, "On a method of decreasing the reflection from nonmetallic substances," *Journal of the Optical Society of America*, vol. 26, no. 1, pp. 73–74, 1936.

[171] A. McPhun, Q. Wu, and I. Hodgkinson, "Birefringent rugate filters," *Electronics Letters*, vol. 34, no. 4, pp. 360–361, 1998.

[172] K. Kaminska, M. Suzuki, K. Kimura, Y. Taga, and K. Robbie, "Simulating structure and optical response of vacuum evaporated porous rugate filters," *Journal of Applied Physics*, vol. 95, no. 6, pp. 3055–3062, 2004.

[173] K. Robbie, Y. Cui, C. Elliott, and K. Kaminska, "Oxidation of evaporated porous silicon rugate filters," *Applied Optics*, vol. 45, no. 32, pp. 8298–8303, 2006.

[174] K. Kaminska and K. Robbie, "Birefringent omnidirectional reflector," *Applied Optics*, vol. 43, no. 7, pp. 1570–1576, 2004.

[175] K. V. Tabunshchyk, M. M. Hawkeye, A. Kovalenko, and M. J. Brett, "Three-dimensional simulation of periodically structured thin films with uniaxial symmetry," *Journal of Physics D*, vol. 40, pp. 4936–4942, 2007.

[176] W. H. Southwell, "Using apodization functions to reduce sidelobes in rugate filters," *Applied Optics*, vol. 28, no. 23, pp. 5091–5094, 1989.

[177] F. Vratny and F. Micale, "Reflectance spectra of non-stoichiometric titanium oxide, niobium oxide, and vanadium oxide ," *Transactions of the Faraday Society*, vol. 59, pp. 2739–2749, 1963.

[178] A. M. Armani and K. J. Vahala, "Heavy water detection using ultra-high-Q microcavities.," *Optics letters*, vol. 31, no. 12, pp. 1896–1898, 2006.

[179] A. M. Armani, R. P. Kulkarni, S. E. Fraser, R. C. Flagan, and K. J. Vahala, "Label-free, single-molecule detection with optical microcavities.," *Science*, vol. 317, pp. 783–787, 2007.

[180] T. Sünner, T. Stichel, S.-H. Kwon, T. W. Schlereth, S. Höfling, M. Kamp, and A. Forchel, "Photonic crystal cavity based gas sensor," *Applied Physics Letters*, vol. 92, p. 261112, 2008.

[181] P. A. Snow, E. K. Squire, P. S. J. Russell, and L. T. Canham, "Vapor sensing using the optical properties of porous silicon Bragg mirrors," *Journal of Applied Physics*, vol. 86, no. 4, pp. 1781–1784, 1999.

[182] P. Allcock and P. A. Snow, "Time-resolved sensing of organic vapors in low modulating porous silicon dielectric mirrors," *Journal of Applied Physics*, vol. 90, no. 10, pp. 5052–5058, 2001.

[183] Y. Y. Li, F. Cunin, J. R. Link, T. Gao, R. E. Betts, S. H. Reiver, V. Chin, S. N. Bhatia, and M. J. Sailor, "Polymer replicas of photonic porous silicon for sensing and drug delivery applications," *Science*, vol. 299, no. 5615, pp. 2045–2047, 2003.

[184] M. S. Salem, M. J. Sailor, K. Fukami, T. Sakka, and Y. H. Ogata, "Sensitivity of porous silicon rugate filters for chemical vapor detection," *Journal of Applied Physics*, vol. 103, no. 8, p. 083516, 2008.

[185] V. Mulloni and L. Pasevi, "Porous silicon microcavities as optical chemical sensors," *Applied Physics Letters*, vol. 76, pp. 2523–2525, 2000.

[186] L. D. Stefano, L. Moretti, I. Rendina, and A. M. Rossi, "Time-resolved sensing of chemical species in porous silicon optical microcavity," *Sensors and Actuators B*, vol. 100, pp. 168–172, 2004.

[187] B. V. Lotsch and G. A. Ozin, "Photonic Clays: A New Family of Functional 1D Photonic Crystals," *ACS Nano*, vol. 2, no. 10, pp. 2065–2074, 2008.

[188] S. Colodrero, M. Ocana, A. R. González-Elipe, and H. Míguez, "Response of nanoparticle-based one-dimensional photonic crystals to ambient vapor pressure," *Langmuir*, vol. 24, pp. 9135–9139, 2008.

[189] B. V. Lotsch and G. A. Ozin, "Clay Bragg Stack Optical Sensors," *Advanced Materials*, vol. 20, pp. 4079–4084, 2008.

[190] L. D. Bonifacio, D. P. Puzzo, S. Breslav, B. M. Willey, A. McGeer, and G. A. Ozin, "Towards the photonic nose: A novel platform for molecule and bacteria identification," *Advanced Materials*, vol. 22, no. 12, pp. 1351–1354, 2009.

[191] I. M. Krieger and F. M. O'Neill, "Diffraction of light by arrays of colloidal spheres," *Journal of the American Chemical Society*, vol. 90, no. 12, pp. 3114–3120, 1968.

[192] A. van Blaaderen, R. Ruel, and P. Wiltzius, "Template-directed colloidal crystallization," *Nature*, vol. 385, pp. 321–324, 1997.

[193] K. Lee and S. A. Asher, "Photonic crystal chemical sensors: pH and ionic strength," *Journal of the American Chemical Society*, vol. 122, pp. 9534–9537, 2000.

[194] I. Tokarev and S. Minko, "Stimuli-responsive hydrogel thin films," *Soft Matter*, vol. 5, pp. 511Ű–524, 2009.

[195] Y.-J. Lee and P. V. Braun, "Tunable inverse opal hydrogel pH sensors," *Advanced Materials*, vol. 15, pp. 563–566, 2003.

[196] V. L. Alexeev, A. C. Sharma, A. V. Goponenko, S. Das, I. K. Lednev, C. S. Wilcox, D. N. Finegold, and S. A. Asher, "High ionic strength glucose-sensing photonic crystal," *Analytical Chemistry*, vol. 75, pp. 2316–2323, 2003.

[197] T. Endoa, Y. Yanagidaa, and T. Hatsuzawa, "Colorimetric detection of volatile organic compounds using a colloidal crystal-based chemical sensor for environmental applications," *Sensors and Actuators B*, vol. 125, pp. 589–595, 2007.

[198] A. Lakhtakia, M. W. McCall, J. A. Sherwin, Q. H. Wu, and I. J. Hodgkinson, "Sculptured-thin-film spectral holes for optical sensing of fluids," *Optics Communications*, vol. 194, no. 1-3, pp. 33–46, 2001.

[199] J. J. Steele, A. C. van Popta, M. M. Hawkeye, J. C. Sit, and M. J. Brett, "Nanostructured gradient index optical filter for high-speed humidity sensing," *Sensors and Actuators B*, vol. 120, no. 1, pp. 213–219, 2006.

[200] R. J. Martín-Palma, V. Torres-Costa, and C. G. Pantano, "Distributed Bragg reflectors based on chalcogenide glasses for chemical optical sensing," *Journal of Physics D: Applied Physics*, vol. 42, p. 055109, Mar. 2009.

[201] G. K. Kiema and M. J. Brett, "Electrochemical characterization of carbon films with porous microstructures," *Journal of The Electrochemical Society*, vol. 150, no. 7, p. E342, 2003.

[202] Y.-J. Liu, H. Y. Chu, and Y.-P. Zhao, "Silver nanorod array substrates fabricated by oblique angle deposition: morphological, optical, and SERS characterizations," *The Journal of Physical Chemistry C*, vol. 114, no. 18, pp. 8176–8183, 2010.

[203] D. A. Gish, F. Nsiah, M. T. Mcdermott, and M. J. Brett, "Localized Surface Plasmon Resonance Biosensor Using Silver Nanostructures Fabricated by Glancing Angle Deposition," *Analytical Chemistry*, vol. 79, no. 11, pp. 4228–4232, 2007.

[204] L. W. Bezuidenhout and M. J. Brett, "Ultrathin layer chromatography on nanostructured thin films.," *Journal of chromatography A*, vol. 1183, no. 1-2, pp. 179–185, 2008.

[205] S. R. Jim, M. T. Taschuk, G. E. Morlock, L. W. Bezuidenhout, W. Schwack, and M. J. Brett, "Engineered anisotropic microstructures for ultrathin-layer chromatography," *Analytical chemistry*, vol. 82, no. 12, pp. 5349–5356, 2010.

[206] N. Yamazoe and Y. Shimizu, "Humidity Sensors: principles and applications," *Sensors and Actuators*, vol. 10, pp. 379–398, 1986.

[207] R. Fenner and E. Zdankiewicz, "Micromachined Water Vapor Sensors: A Review of Sensing Technologies," *IEEE Sensors Journal*, vol. 1, no. 4, pp. 309–317, 2001.

[208] Z. M. Rittersma, "Recent achievements in miniaturised humidity sensors: a review of transduction techniques," *Sensors and Actuators A*, vol. 96, pp. 196–210, 2002.

[209] T. Morimoto, M. Nagao, , and F. Tokuda, "The Relation between the Amounts of Chemisorbed and Physisorbed Water on Metal Oxides," *The Journal of Physical Chemistry*, vol. 73, no. 1, pp. 243–248, 1969.

[210] J. C. Owens, "Optical refractive index of air: dependence on pressure, temperature and composition," *Applied Optics*, vol. 6, no. 1, pp. 51–59, 1967.

[211] S. J. Gregg and K. S. W. Sing, *Adsorption, Surface Area and Porosity*. London, UK: Academic Press, 2^{nd} ed., 1982.

[212] J. C. Maxwell, "On colour vision," *Nature*, vol. 4, pp. 13–16, 1871.

[213] R. P. Feynman, R. B. Leighton, and M. Sands, *The Feynman Lectures on Physics*, vol. 1. Reading, US: Addison-Wesley, 1963.

[214] A. D. Broadbent, "A critical review of the development of the CIE1931 RGB color-matching functions," *Color Research & Application*, vol. 29, no. 4, pp. 267–272, 2004.

[215] J. Schanda, "CIE colorimetry," in *Colorimetry: Understanding the CIE system* (J. Schanda, ed.), pp. 25–78, Hoboken, US: Wiley, 2007.

[216] T. Smith and J. Guild, "The C.I.E. colorimetric standards and their use," *Transactions of the Optical Society*, vol. 33, no. 3, p. 73, 1931.

[217] K. Witt, "Cie color difference metrics," in *Colorimetry: Understanding the CIE system* (J. Schanda, ed.), pp. 79–100, Hoboken, US: Wiley, 2007.

[218] R. G. Kuehni, "Color difference formulas: An unsatisfactory state of affairs," *Color Research & Application*, vol. 33, no. 4, pp. 324–326, 2008.

[219] D. B. Judd, D. L. MacAdam, G. Wyszecki, H. W. Budde, H. R. Condit, S. T. Henderson, and J. L. Simonds, "Spectral distribution of typical daylight as a function of correlated color temperature," *Journal of the Optical Society of America*, vol. 54, no. 8, pp. 1031–1040, 1964.

[220] K. M. Krause, M. T. Taschuk, K. D. Harris, D. A. Rider, N. G. Wakefield, J. C. Sit, J. M. Buriak, M. Thommes, and M. J. Brett, "Surface area characterization of obliquely deposited metal oxide nanostructured thin films," *Langmuir*, vol. 26, no. 6, pp. 4368–76, 2010.

[221] M. Suzuki and Y. Taga, "Numerical study of the effective surface area of obliquely deposited thin films," *Journal of Applied Physics*, vol. 90, no. 11, pp. 5599–5605, 2001.

[222] R. Messier and J. Yehoda, "Geometry of thin-film morphology," *Journal of Applied Physics*, vol. 58, no. 10, pp. 3739–3746, 1985.

[223] P. Meakin, "Fractal scaling in thin film condensation and material surfaces," *Critical Reviews in Solid State and Materials Sciences*, vol. 13, pp. 143–189, 1986.

[224] K. S. W. Sing, D. H. Everett, R. A. W. Haul, L. Moscou, R. A. Pierotti, J. Rouquérol, and T. Siemieniewska, "Reporting physisorption data for gas / solid systems," *Pure and Applied Chemistry*, vol. 57, no. 4, pp. 603–619, 1985.

[225] L. Greenspan, "Humidity fixed points of binary saturated aqueous solutions," *Journal of Research of the National Bureau of Standards*, vol. 81A, no. 1, pp. 89–96, 1977.

[226] J. J. Steele, *Nanostructured thin films for humidity sensing*. PhD thesis, University of Alberta, 2006.

[227] S. F. Tsoi, E. Fok, J. C. Sit, and J. G. C. Veinot, "Surface functionalization of porous nanostructured metal oxide thin films fabricated by glancing angle deposition," *Chemistry of Materials*, vol. 18, no. 22, pp. 5260–5266, 2006.

[228] R. D. Meade, K. D. Brommer, A. M. Rappe, and J. D. Joannopoulos, "Photonic bound states in periodic dielectric materials," *Physical Review B*, vol. 44, no. 24, pp. 13772–13774, 1991.

[229] E. Yablonovitch, T. J. Gmitter, R. D. Meade, A. M. Rappe, K. D. Brommer, and J. D. Joannopoulos, "Donor and acceptor modes in photonic

band structure," *Physical Review Letters*, vol. 67, no. 24, pp. 3380–3383, 1991.

[230] P. Lalanne, C. Sauvan, and J. P. Hugonin, "Photon confinement in photonic crystal nanocavities," *Laser and Photonics Review*, vol. 2, no. 6, pp. 514–526, 2008.

[231] O. Painter, R. K. Lee, A. Scherer, A. Yariv, J. D. O'Brien, P. D. Dapkus, and I. Kim, "Two-dimensional photonic band-gap defect mode laser," *Science*, vol. 284, pp. 1819–1821, 1999.

[232] S. G. Johnson, P. R. Villeneuve, S. Fan, and J. D. Joannopoulos, "Linear waveguides in photonic-crystal slabs," *Physical Review B*, vol. 62, no. 12, pp. 8212–8222, 2000.

[233] S. Noda, M. Fujita, and T. Asano, "Spontaneous-emission control by photonic crystals and nanocavities," *Nature Photonics*, vol. 1, pp. 449–458, 2007.

[234] E. Chow, A. Grot, L. W. Mirkarimi, M. Sigalas, and G. Girolami, "Ultracompact biochemical sensor built with two-dimensional photonic crystal microcavity," *Optics letters*, vol. 29, no. 10, pp. 1093–1095, 2004.

[235] T. Tanabe, M. Notomi, E. Kuramochi, A. Shinya, and H. Taniyama, "Trapping and delaying photons for one nanosecond in an ultrasmall high-Q photonic-crystal nanocavity," *Nature Photonics*, vol. 1, pp. 49–52, 2007.

[236] M. M. Hawkeye and M. J. Brett, "Narrow bandpass optical filters fabricated with one-dimensionally periodic inhomogeneous thin films," *Journal of Applied Physics*, vol. 100, p. 044322, 2006.

[237] M. M. Hawkeye, R. Joseph, J. C. Sit, and M. J. Brett, "Coupled defects in one-dimensional photonic crystal films fabricated with glancing angle deposition," *Optics Express*, vol. 18, no. 12, pp. 13220–13226, 2010.

[238] Y. Akahane, T. Asano, B.-S. Song, and S. Noda, "High-Q photonic nanocavity in a two-dimensional photonic crystal," *Nature*, vol. 425, pp. 944–947, 2003.

[239] D. Englund, I. Fushman, and J. Vučkovič, "General recipe for designing photonic crystal cavities," *Optics Express*, vol. 12, no. 16, pp. 5961–5975, 2005.

[240] Y. Xu, Y. Li, R. K. Lee, and A. Yariv, "Scattering-theory analysis of waveguide-resonator coupling," *Physical Review E*, vol. 62, no. 5, pp. 7389–7404, 2000.

[241] H. A. Macleod, "Thin film narrow band optical filters," *Thin Solid Films*, vol. 34, pp. 335–342, 1976.

[242] H. Kogelnik and C. V. Shank, "Coupled-wave theory of distributed feedback lasers," *Journal of Applied Physics*, vol. 23, no. 5, pp. 2327–2335, 1972.

[243] H. A. Haus and C. V. Shank, "Antisymmetric taper of distributed feedback lasers," *IEEE Journal of Quantum Electronics*, vol. 12, no. 9, pp. 532–539, 1976.

[244] P. Yeh, A. Yariv, and C.-S. Hong, "Electromagnetic propagation in periodic stratified media. I. General theory," *Journal of the Optical Society of America*, vol. 67, no. 4, pp. 423–438, 1977.

[245] A. Yariv, Y. Xu, R. K. Lee, and A. Scherer, "Coupled-resonator optical waveguide: a proposal and analysis," *Optics Letters*, vol. 24, no. 11, pp. 711–713, 1999.

[246] E. Centeno and D. Felbacq, "Rabi oscillations in bidimensional photonic crystals," *Physical Review B*, vol. 62, no. 15, pp. 10101–10108, 2000.

[247] J. K. S. Poon, K. Scheuer, and A. Yariv, "Designing coupled-resonator optical waveguide delay lines," *Journal of the Optical Society of America B*, vol. 21, no. 9, pp. 1665–1673, 2004.

[248] G. T. Paloczi, Y. Huang, A. Yariv, , and S. Mookherjea, "Polymeric Mach-Zehnder interferometer using serially coupled microring resonators," *Optics Express*, vol. 11, no. 21, pp. 2666–2671, 2003.

[249] M. F. Yanik and S. Fan, "Stopping light all optically," *Physical Review Letters*, vol. 92, no. 8, p. 083901, 2004.

[250] M. Notomi, E. Kuramohi, and T. Tanabe, "Large-scale arrays of ultrahigh-Q coupled nanocavities," *Nature Photonics*, vol. 2, no. 12, pp. 741–747, 2008.

[251] M. J. Hartmann, F. G. S. L. B. ao, and M. B. Plenio, "Strongly interacting polaritons in coupled arrays of cavities," *Nature Physics*, vol. 2, no. 12, pp. 849–855, 2006.

[252] H. A. Haus and W. Huang, "Coupled-mode theory," *Proceedings of the IEEE*, vol. 79, no. 10, pp. 1505–1518, 1991.

[253] K. A. Atlasov, K. F. Karlsson, A. Rudra, B. Dwir, and E. Kapon, "Wavelength and loss splitting in directly coupled photonic-crystal defect microcavities," *Optics Express*, vol. 16, no. 20, pp. 16255–16264, 2008.

[254] A. L. Reynolds, U. Peschel, F. Lederer, P. J. Roberts, T. F. Krauss, and P. J. I. de Maggt, "Coupled defects in photonic crystals," *IEEE Transactions on Microwave Theory and Technology*, vol. 49, no. 10, pp. 1860–1867, 2001.

[255] K. Guven and E. Ozbay, "Coupling and phase analysis of cavity structures in two-dimensional photonic crystals," *Physical Review B*, vol. 71, no. 8, p. 085108, 2005.

[256] D. Goldstein, *Polarized Light*. Boca Raton, US: CRC Press, 2^{nd} ed., 2003.

[257] H. Berry, G. Gabrielse, and A. Livingston, "Measurement of the Stokes parameters of light," *Applied Optics*, vol. 16, no. 12, pp. 3200–3205, 1977.

[258] B. Schaefer, E. Collett, R. Smyth, D. Barrett, and B. Fraher, "Measuring the Stokes polarization parameters," *American Journal of Physics*, vol. 75, no. 2, pp. 163–168, 2007.

[259] E. A. West and M. H. Smith, "Polarization errors associated with birefringent waveplates," *Optical Engineering*, vol. 34, no. 6, pp. 1574–1580, 1995.

[260] B. Boulbry, B. Bousquet, B. LeJeune, Y. Guern, and J. Lotrian, "Polarization errors associated with zero-order achromatic quarter-wave plates in the whole visible spectral range," *Optics Express*, vol. 9, no. 5, pp. 225–235, 2001.

[261] B. Boulbry, B. LeJeune, F. Pellen, J. Cariou, and J. Lotrian, "Identification of error parameters and calibration of a double-crystal birefringent wave plate with a broadband spectral light source," *Journal of Physics D*, vol. 35, pp. 2508–2515, 2002.

[262] R. A. Chipman, "Precision polarimetry of polarization components," *Proceedings of SPIE*, vol. 1746, pp. 49–60, 1992.

[263] I. J. Hodgkinson, F. Horowitz, H. A. Macleod, M. Sikkens, and J. J. Wharton, "Measurement of the principal refractive indices of thin films deposited at oblique incidence," *Journal of the Optical Society of America A*, vol. 2, no. 10, pp. 1693–1697, 1985.

[264] V. Leontyev, N. G. Wakefield, K. Tabunshchyk, J. C. Sit, M. J. Brett, and A. Kovalenko, "Selective transmittance of linearly polarized light in thin films rationally designed by FDTD and FDFD theories and fabricated by glancing angle deposition," *Journal of Applied Physics*, vol. 104, no. 10, pp. 2477–2480, 2008.

Appendix A

Assembled Single Layer Data

In chapter 4, the data presentation was crafted by balancing completeness with brevity. Consequently, the $n(\alpha)$ and $D(\alpha)$ calibration data sets were presented in graphical form and only a representative selection of measured and simulated spectra were provided. This appendix presents the chapter 4 results in full form. For reference and archival purposes, Table A.1 contains the measured D values and the slab and GRIN model best-fit parameters. The plots in Fig. A.1 show every measured and fitted reflectance spectrum, allowing closer inspection of the data-simulation agreement.

Table A.1: The measured and calculated parameters for single-layer TiO_2 films fabricated in this thesis. d' is the QCM measured deposited thickness, D is the deposition ratio (Eq. 3.1), A and B are the Cauchy dispersion coefficients (Eq. 4.1), the $_{slab}$ and $_{GRIN}$ subscripts refer to the respective thin film model, and Δn is the relative index inhomogeneity (Eq. 4.4).

Film	$\alpha(^\circ)$	d'(nm)	D	A_{slab}	B_{slab} (μm^2)	A_{GRIN}	B_{GRIN} (μm^2)	Δn
m=1	40	250	1.18 ± 0.04	2.066 ± 0.007	0.056 ± 0.002	1.949 ± 0.002	0.0569 ± 0.0003	0.0123 ± 0.0002
2	60	150	1.01 ± 0.03	1.90 ± 0.02	0.023 ± 0.005	1.6890 ± 0.0007	0.0444 ± 0.0001	0.00790 ± 0.00002
3	70	200	0.91 ± 0.03	1.661 ± 0.007	0.017 ± 0.002	1.5673 ± 0.0006	0.0278 ± 0.0001	0.00360 ± 0.00001
4	75	200	0.86 ± 0.02	1.416 ± 0.005	0.018 ± 0.001	1.286 ± 0.003	0.0364 ± 0.0005	0.0032 ± 0.0001
5	80	125	1.0 ± 0.2	1.28 ± 0.04	0.00 ± 0.01	1.5109 ± 0.0004	0.0229 ± 0.0001	-0.01600 ± 0.00001
6	86	150	0.88 ± 0.09	1.12 ± 0.02	0.020 ± 0.006	1.3049 ± 0.0005	0.0095 ± 0.0001	-0.01140 ± 0.00002
7	40	515	1.29 ± 0.02	2.012 ± 0.005	0.056 ± 0.001	1.799 ± 0.007	0.0487 ± 0.0004	0.065 ± 0.002
8	50	520	1.21 ± 0.02	1.946 ± 0.005	0.047 ± 0.001	1.761 ± 0.004	0.0439 ± 0.0003	0.051 ± 0.001
9	60	500	1.16 ± 0.02	1.790 ± 0.003	0.0422 ± 0.0007	1.701 ± 0.003	0.0383 ± 0.0003	0.0262 ± 0.0008
10	65	575	1.02 ± 0.02	1.694 ± 0.003	0.0340 ± 0.0007	1.603 ± 0.002	0.0326 ± 0.0002	0.0260 ± 0.0006
11	70	620	0.94 ± 0.02	1.601 ± 0.002	0.0264 ± 0.0004	1.554 ± 0.001	0.0261 ± 0.0001	0.0129 ± 0.0003
12	75	660	0.88 ± 0.02	1.454 ± 0.001	0.0211 ± 0.0003	1.430 ± 0.002	0.0216 ± 0.0002	0.0067 ± 0.0004
13	78	680	0.78 ± 0.01	1.444 ± 0.001	0.0200 ± 0.0003	1.429 ± 0.002	0.0187 ± 0.0003	0.0055 ± 0.0005
14	80	633	0.75 ± 0.02	1.197 ± 0.009	0.015 ± 0.002	1.25 ± 0.01	0.013 ± 0.002	-0.011 ± 0.001
15	81	500	1.1 ± 0.3	1.287 ± 0.002	0.0153 ± 0.0004	1.284 ± 0.002	0.0151 ± 0.0004	0.0011 ± 0.0006
16	83	700	0.67 ± 0.04	1.190 ± 0.007	0.010 ± 0.002	1.232 ± 0.008	0.007 ± 0.002	-0.0081 ± 0.0007
17	83	780	0.68 ± 0.01	1.284 ± 0.001	0.0170 ± 0.0003	1.279 ± 0.002	0.0169 ± 0.0003	0.0016 ± 0.0003
18	85	725	0.62 ± 0.04	1.133 ± 0.007	0.010 ± 0.002	1.230 ± 0.007	0.004 ± 0.001	-0.0198 ± 0.0009

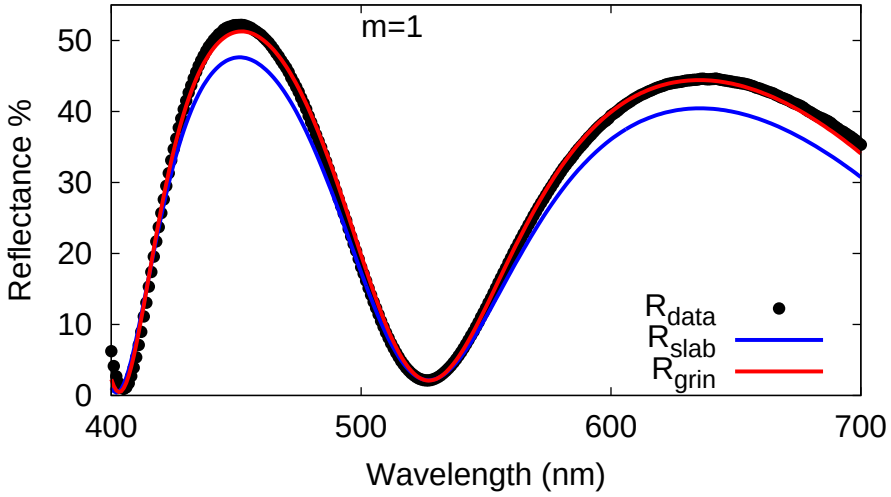

Figure A.1: The measured (black points), slab-model (blue line), and GRIN-model (red line) reflectances for all the single-layer TiO_2 nanostructured films listed in Table A.1. The figure is continued below.

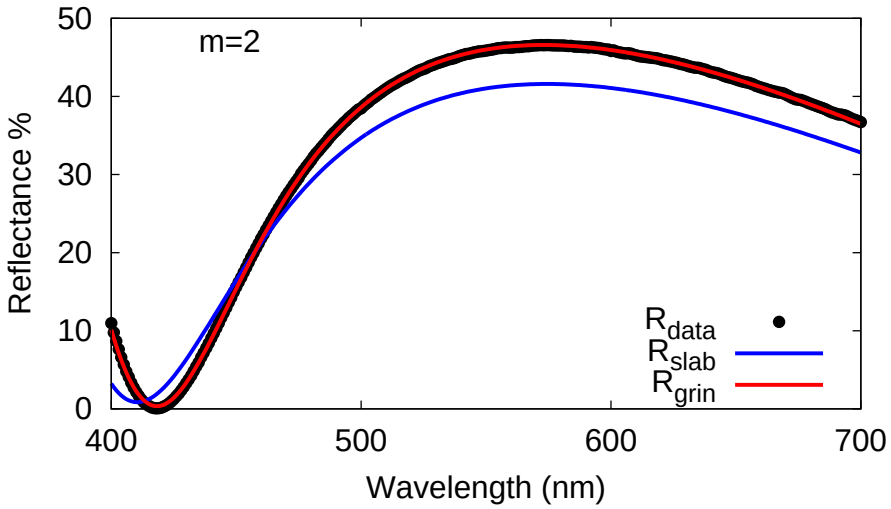
m=2
Reflectance %
Wavelength (nm)
R_data
R_slab
R_grin
0
10
20
30
40
50
400
500
600
700

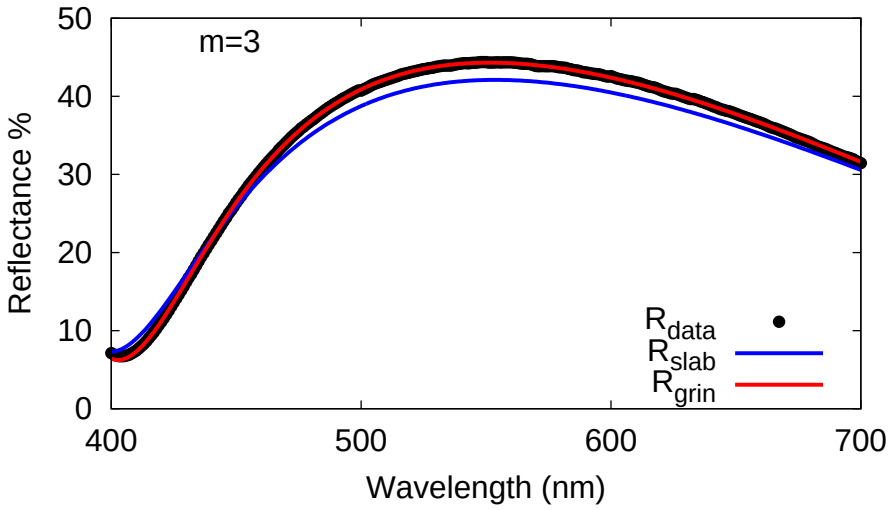
m=3
Reflectance %
Wavelength (nm)
R_data
R_slab
R_grin
0
10
20
30
40
50
400
500
600
700

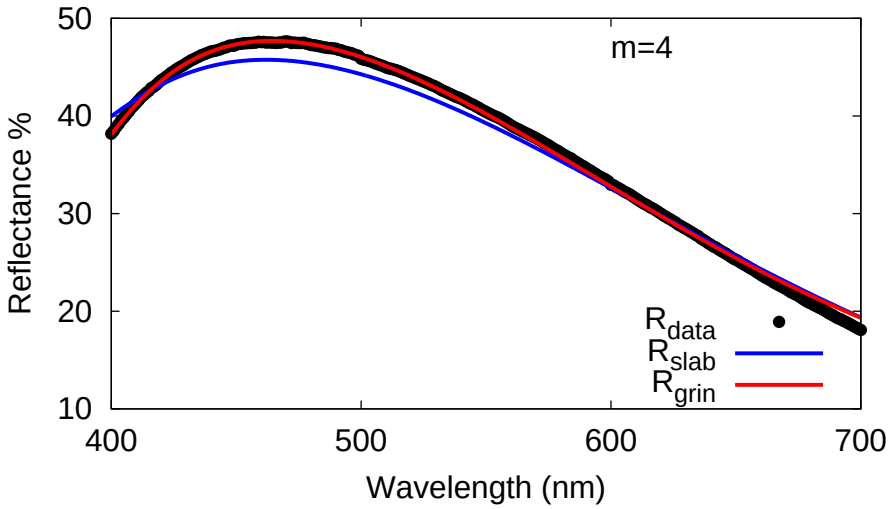
m=4
Reflectance %
Wavelength (nm)
50
40
30
20
10
400
500
600
700
R_data
R_slab
R_grin

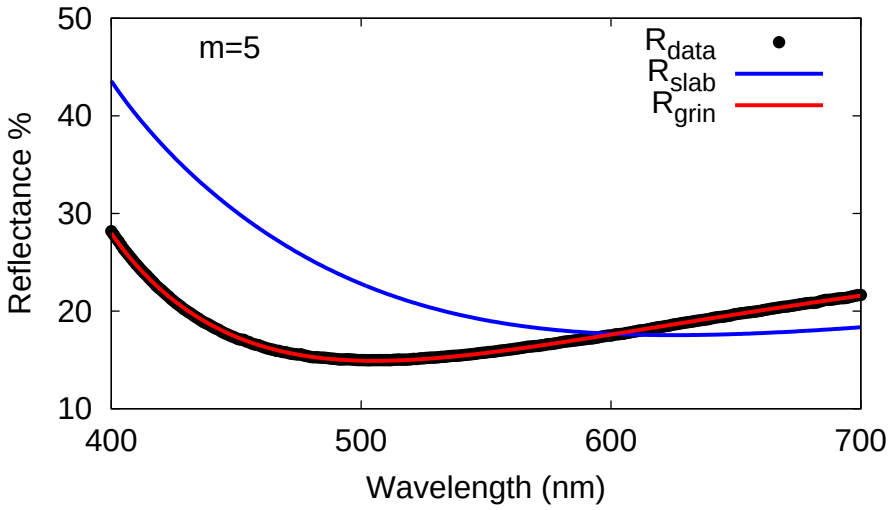
m=5
Reflectance %
Wavelength (nm)
50
40
30
20
10
400
500
600
700
R_data
R_slab
R_grin

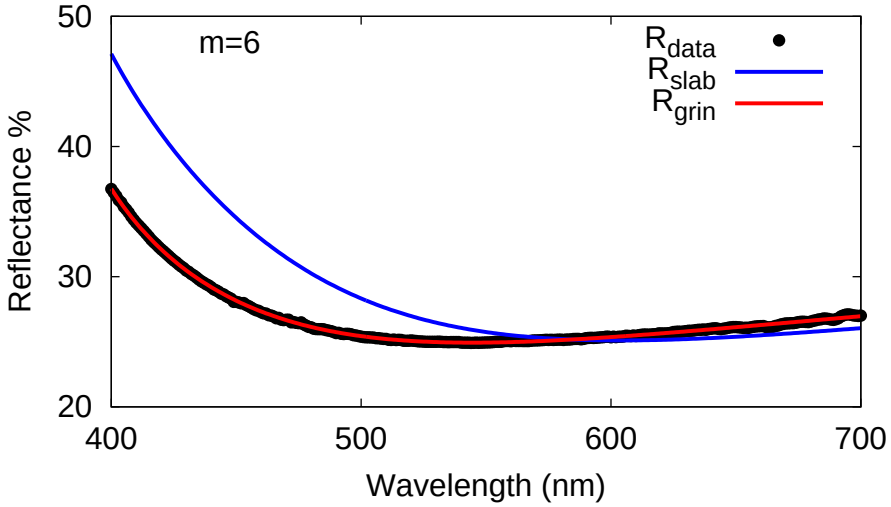
m=6
R_{data}
R_{slab}
R_{grin}
Reflectance %
Wavelength (nm)
50
40
30
20
400
500
600
700

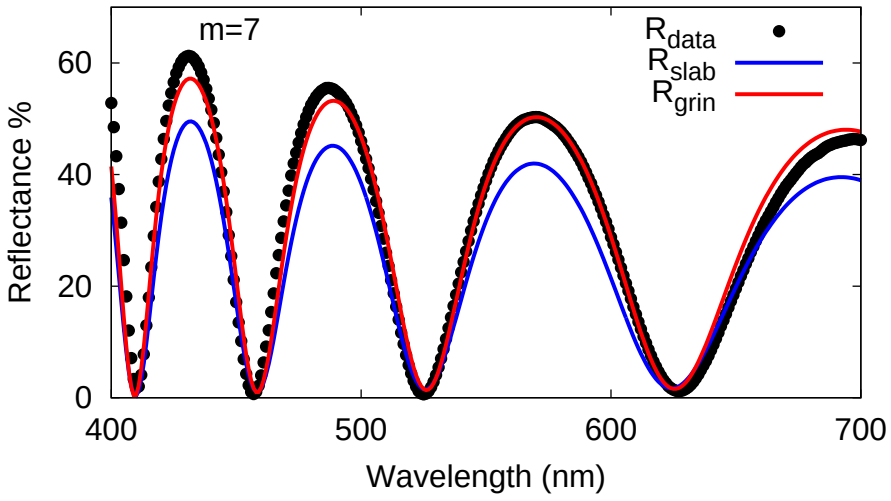
m=7
R_{data}
R_{slab}
R_{grin}
Reflectance %
Wavelength (nm)
60
40
20
0
400
500
600
700

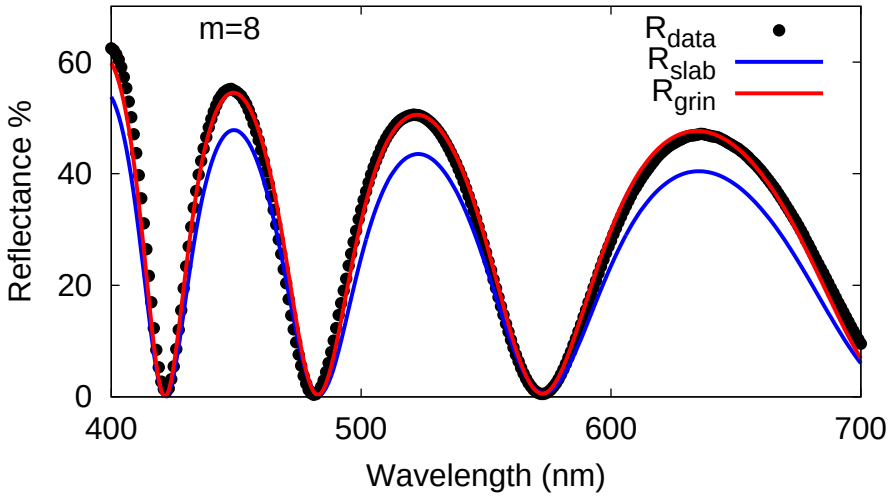
m=8
R_data
R_slab
R_grin
Reflectance %
0
20
40
60
400
500
600
700
Wavelength (nm)

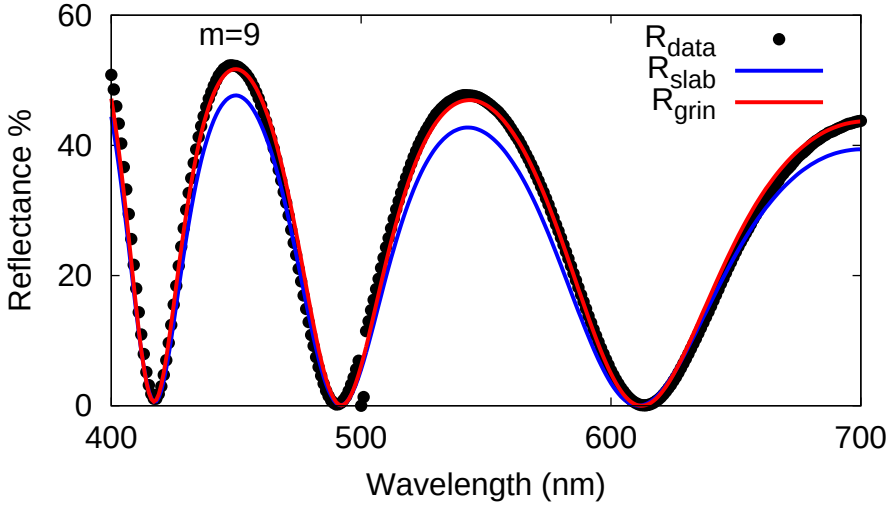
m=9
R_data
R_slab
R_grin
Reflectance %
0
20
40
60
400
500
600
700
Wavelength (nm)

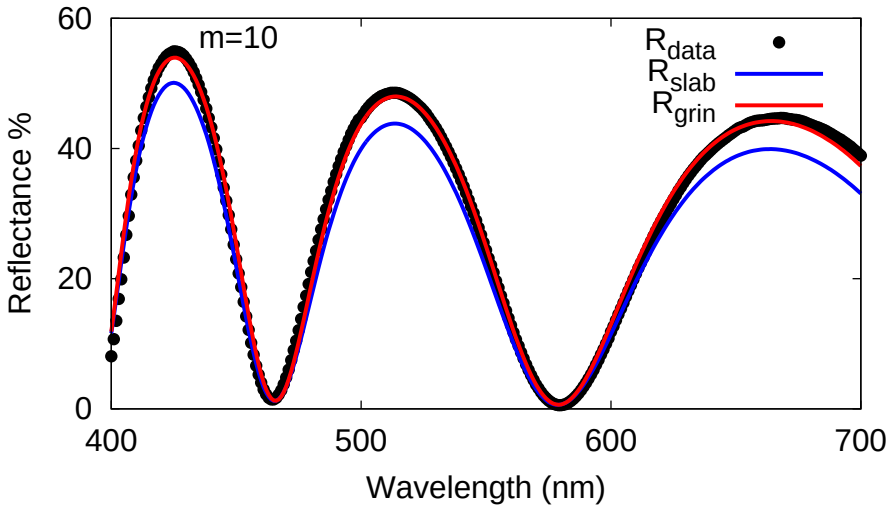
m=10
R_data
R_slab
R_grin
Reflectance %
Wavelength (nm)
0
20
40
60
400
500
600
700

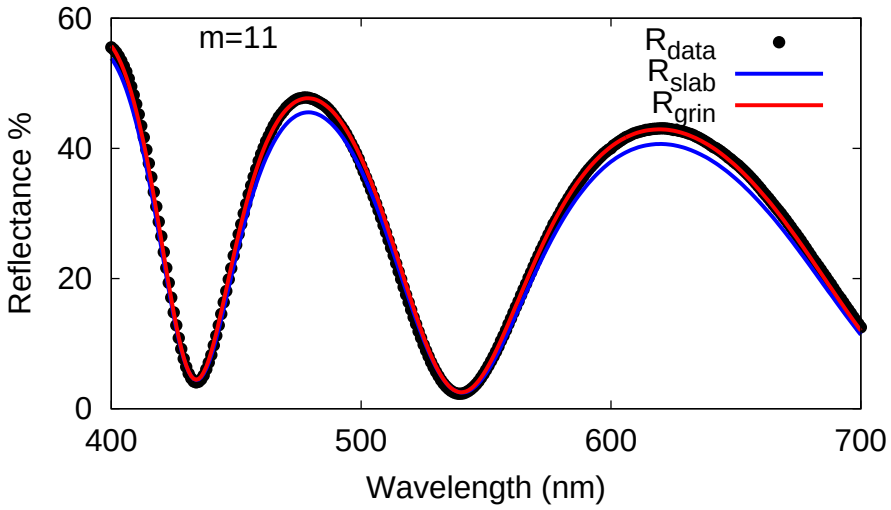
m=11
R_data
R_slab
R_grin
Reflectance %
Wavelength (nm)
0
20
40
60
400
500
600
700

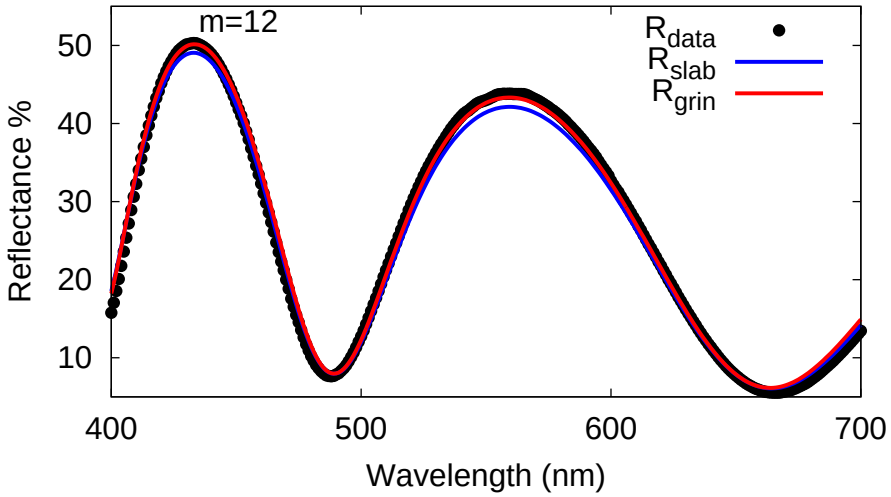
m=12
R_data
R_slab
R_grin
Reflectance %
50
40
30
20
10
400
500
600
700
Wavelength (nm)

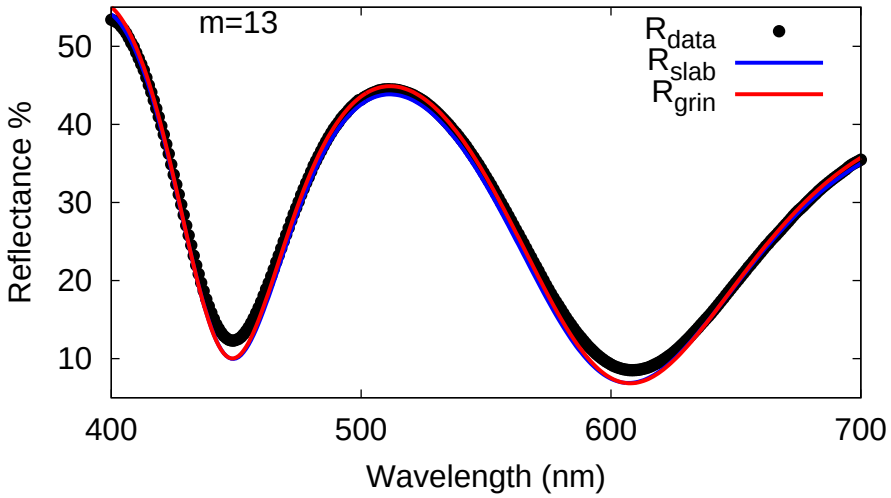
m=13
R_data
R_slab
R_grin
Reflectance %
50
40
30
20
10
400
500
600
700
Wavelength (nm)

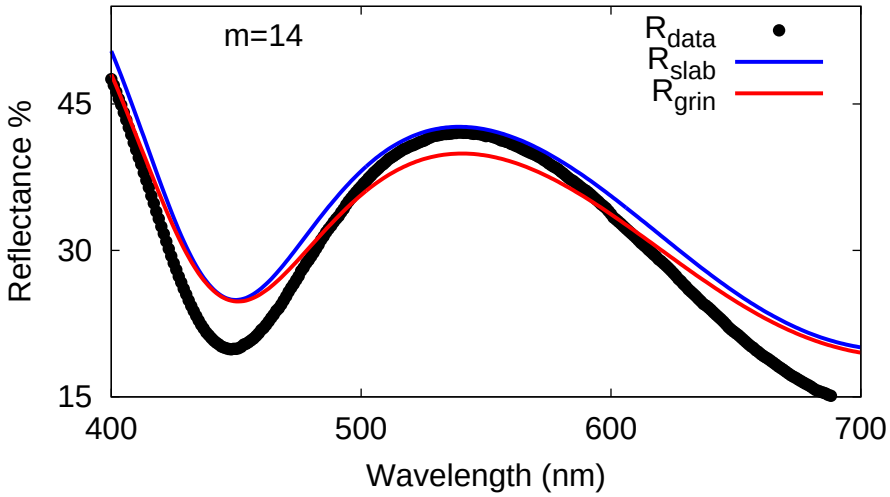
m=14
R_data
R_slab
R_grin
Reflectance %
45
30
15
400
500
600
700
Wavelength (nm)

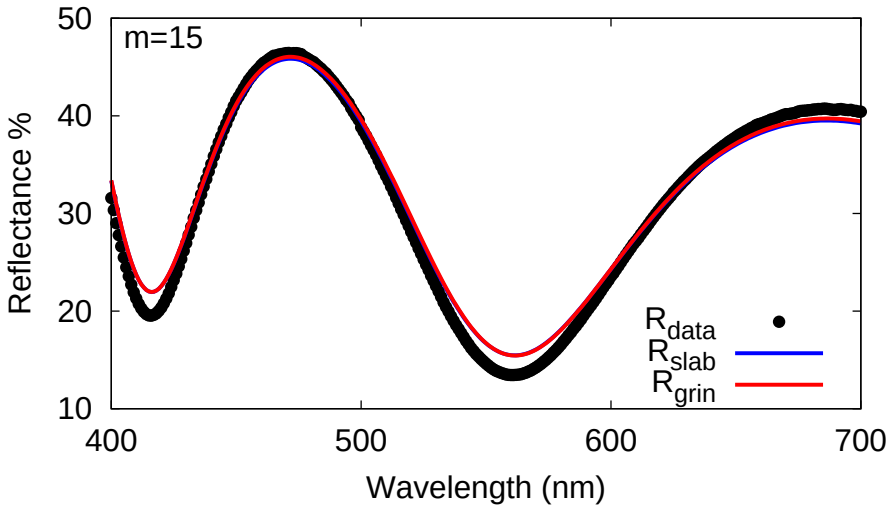
m=15
R_data
R_slab
R_grin
Reflectance %
50
40
30
20
10
400
500
600
700
Wavelength (nm)

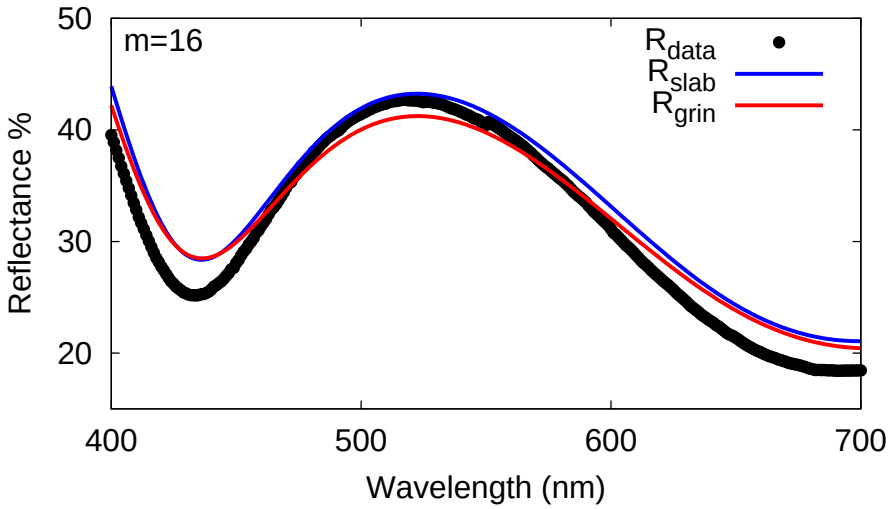
m=16
R_data
R_slab
R_grin
Reflectance %
50
40
30
20
400
500
600
700
Wavelength (nm)

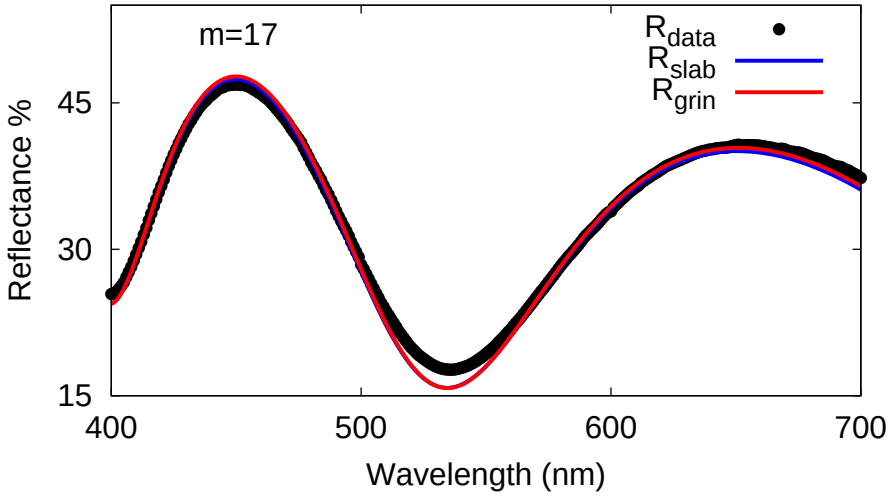
m=17
R_data
R_slab
R_grin
Reflectance %
45
30
15
400
500
600
700
Wavelength (nm)

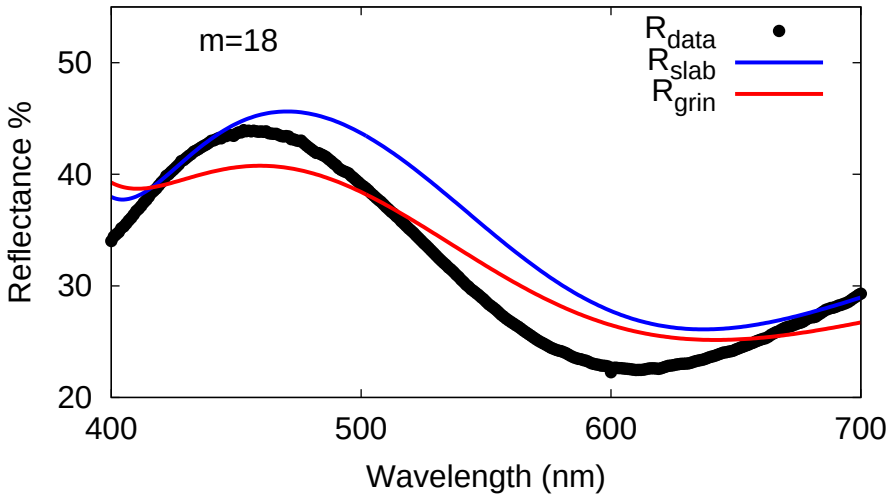
m=18
R_data
R_slab
R_grin
Reflectance %
50
40
30
20
400
500
600
700
Wavelength (nm)

Appendix B

Assembled Bragg Multilayer Data

For space reasons, only a representative selection of the complete Bragg-multilayer data set was provided in chapter 5. This appendix presents the data set in its entirety. Table B.1 contains the measured sublayer deposition ratios and the best-fit Cauchy dispersion parameters. The plots in Fig. B.1 show every measured and fitted transmittance spectrum, allowing closer inspection of the data-simulation agreement.

Table B.1: The measured and calculated parameters for every Bragg multilayer fabricated in this thesis. The $_L$ and $_H$ subscript denote the low- and high-index sublayer. $\langle D \rangle$ and σ_D are the average and standard deviation of the measured sublayer deposition ratios. A and B are the sublayer Cauchy dispersion coefficients (Eqs. 5.3a and b).

Film	α_L	α_H	$\langle D_L \rangle$	σ_{DL}	$\langle D_H \rangle$	σ_{DH}	A_L	B_L (μm^2)	A_H	B_H (μm^2)
A	78	45	0.71	0.08	1.20	0.04	1.34 ± 0.02	0.032 ± 0.007	1.93 ± 0.01	0.021 ± 0.005
B	78	45	0.63	0.04	1.28	0.10	1.51 ± 0.04	0.000 ± 0.02	2.01 ± 0.03	0.01 ± 0.01
C	78	45	0.61	0.04	1.16	0.11	1.32 ± 0.02	0.000 ± 0.009	1.847 ± 0.008	0.027 ± 0.004
D	78	45	0.63	0.02	1.37	0.15	1.29 ± 0.01	0.000 ± 0.006	1.718 ± 0.004	0.045 ± 0.002
E	78	45	0.62	0.03	1.23	0.08	1.25 ± 0.02	0.05 ± 0.01	1.93 ± 0.01	0 ± 0.007
F	78	45	0.65	0.06	1.21	0.08	1.34 ± 0.02	0 ± 0.008	1.860 ± 0.008	0.029 ± 0.004
G	80	40	0.64	0.04	1.10	0.05	1.30 ± 0.02	0 ± 0.007	1.907 ± 0.003	0.026 ± 0.001
H	80	40	0.69	0.09	1.19	0.11	1.272 ± 0.009	0 ± 0.004	1.837 ± 0.003	0.0202 ± 0.0009
J	80	40	0.71	0.11	1.45	0.15	1.12 ± 0.02	0.051 ± 0.009	1.80 ± 0.01	0 ± 0.006
K	80	40	0.63	0.05	1.28	0.07	1.33 ± 0.01	0 ± 0.005	1.811 ± 0.005	0.069 ± 0.002
L	80	40	0.67	0.09	1.52	0.13	1.06 ± 0.03	0.09 ± 0.01	1.85 ± 0.01	0 ± 0.009
M	80	40	0.63	0.11	1.43	0.08	1.20 ± 0.03	0.07 ± 0.01	1.92 ± 0.01	0 ± 0.008
N	80	60	0.64	0.06	1.14	0.09	1.462 ± 0.009	0 ± 0.002	1.767 ± 0.006	0.012 ± 0.002
P	80	60	0.57	0.04	1.00	0.08	1.08 ± 0.02	0.097 ± 0.004	1.771 ± 0.009	0.051 ± 0.003
Q	80	60	0.64	0.06	1.18	0.12	1.03 ± 0.02	0.097 ± 0.006	1.75 ± 0.01	0 ± 0.005
R	80	60	0.59	0.05	1.16	0.07	0.95 ± 0.01	0.121 ± 0.002	1.782 ± 0.001	0 ± 0.0003

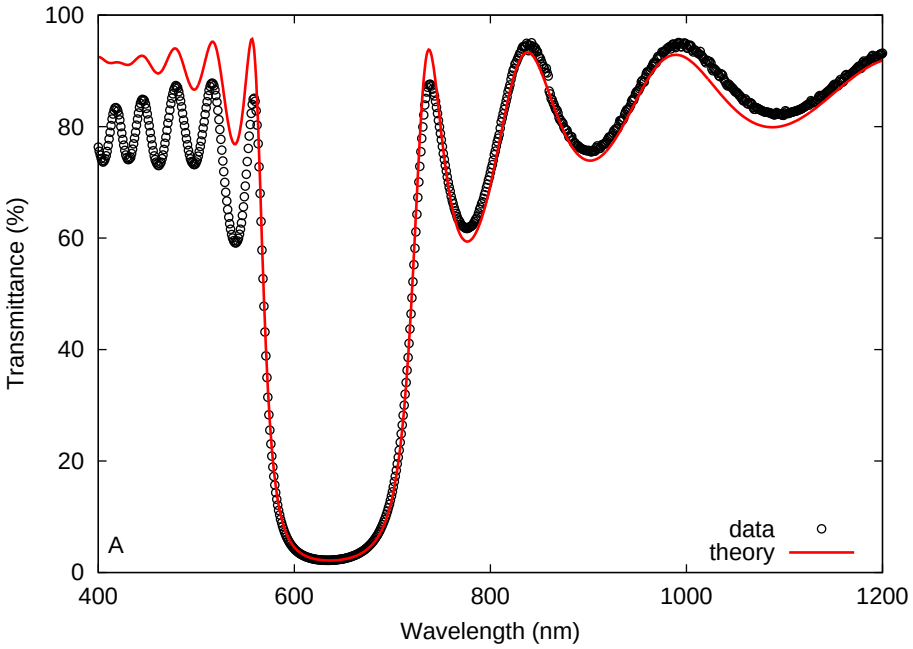

Figure B.1: The measured (black points) and simulated (red line) transmittances for each TiO_2 nanostructured Bragg multilayer listed in Table B.1. The figure is continued below.

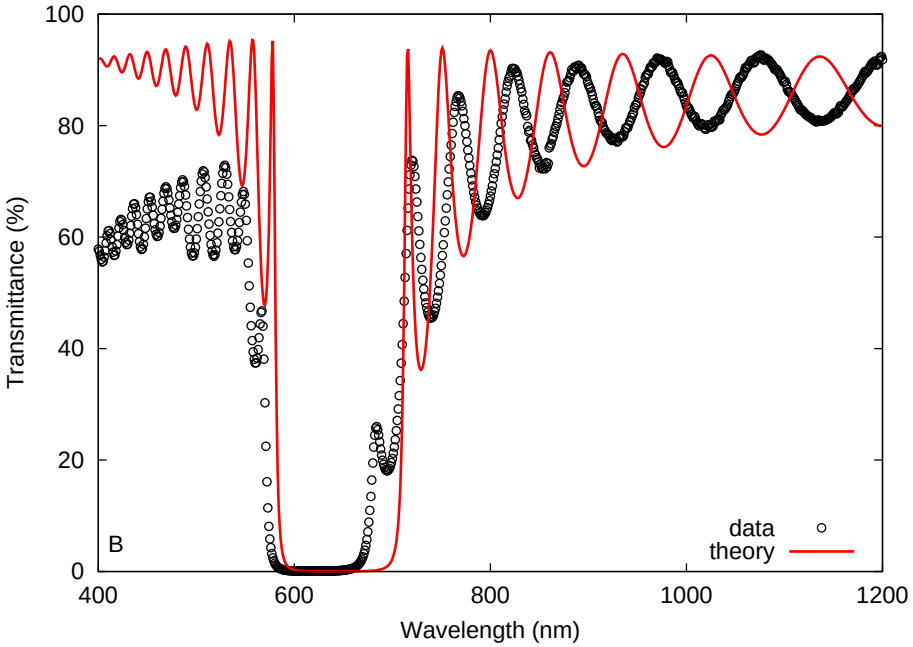
100
80
60
40
20
0
400
600
800
1000
1200
Transmittance (%)
Wavelength (nm)
B
data
theory

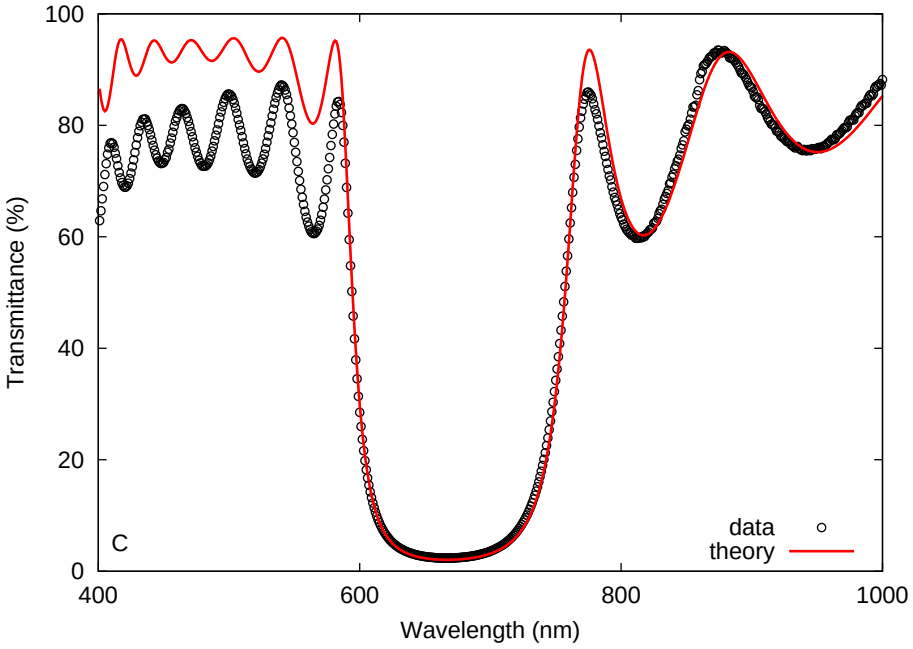
100
80
60
40
20
0
400
600
800
1000
Transmittance (%)
Wavelength (nm)
C
data
theory

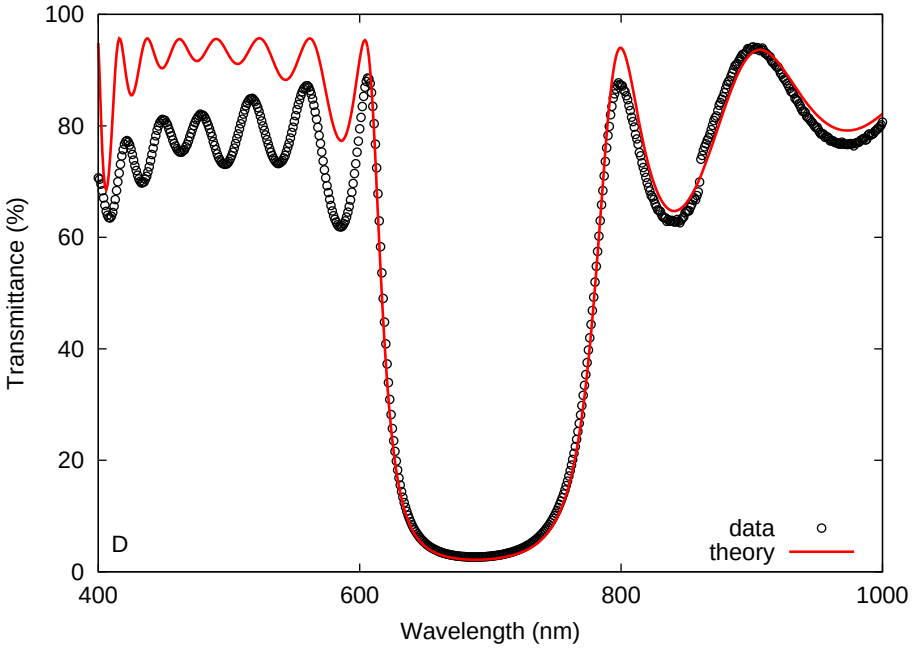
100
80
60
40
20
0
400
600
800
1000
Transmittance (%)
Wavelength (nm)
D
data
theory

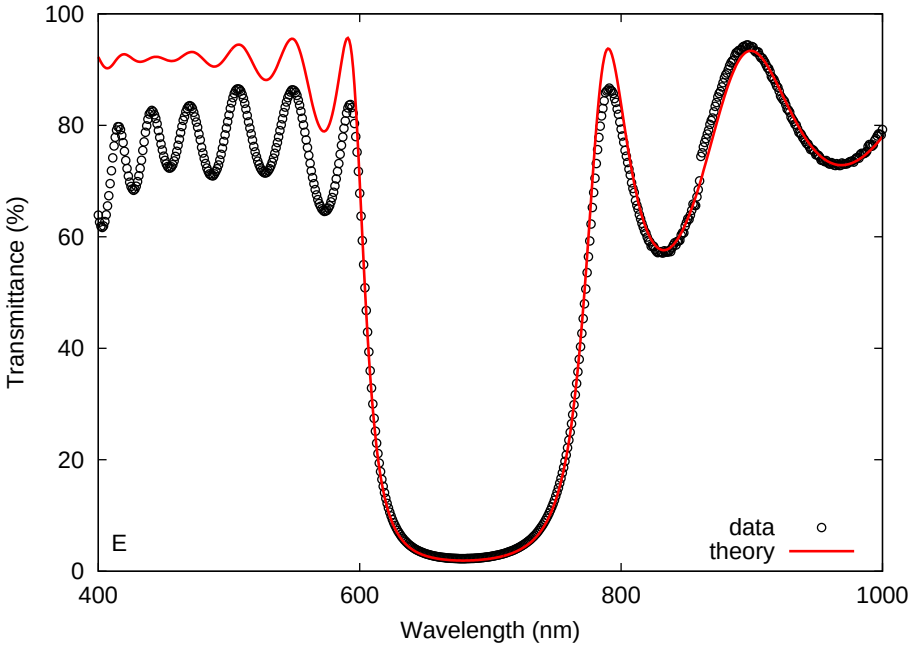
100
80
60
40
20
0
400
600
800
1000
Transmittance (%)
Wavelength (nm)
E
data
theory

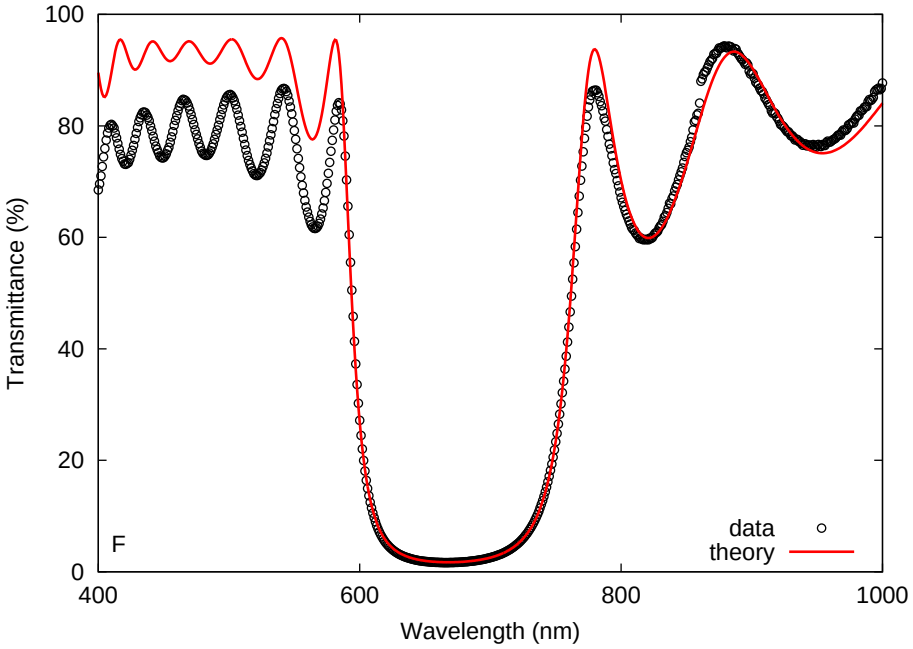
100
80
60
40
20
0
400
600
800
1000
Transmittance (%)
Wavelength (nm)
F
data
theory

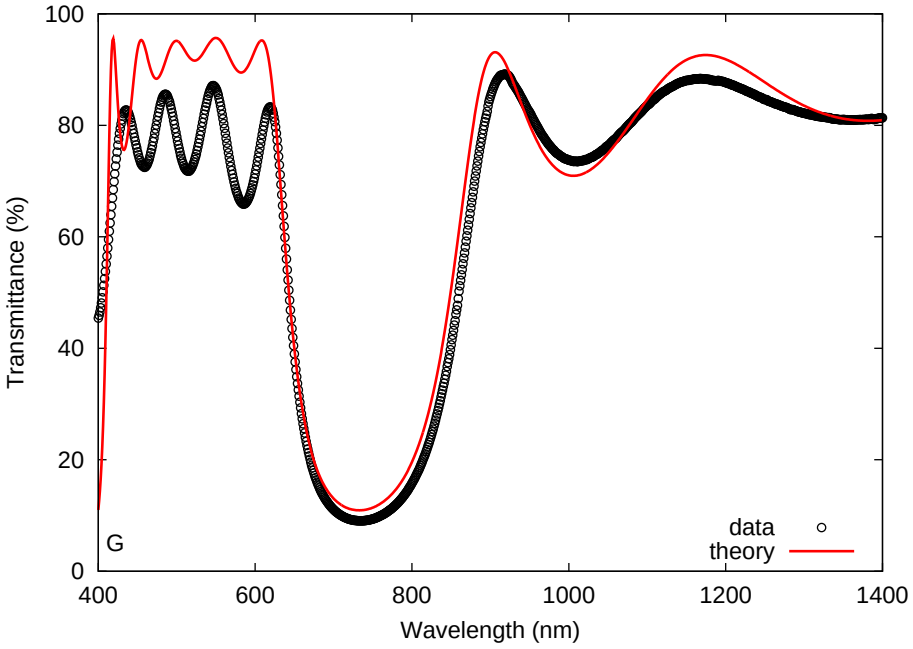
100
80
60
40
20
0
Transmittance (%)
400
600
800
1000
1200
1400
Wavelength (nm)
G
data
theory

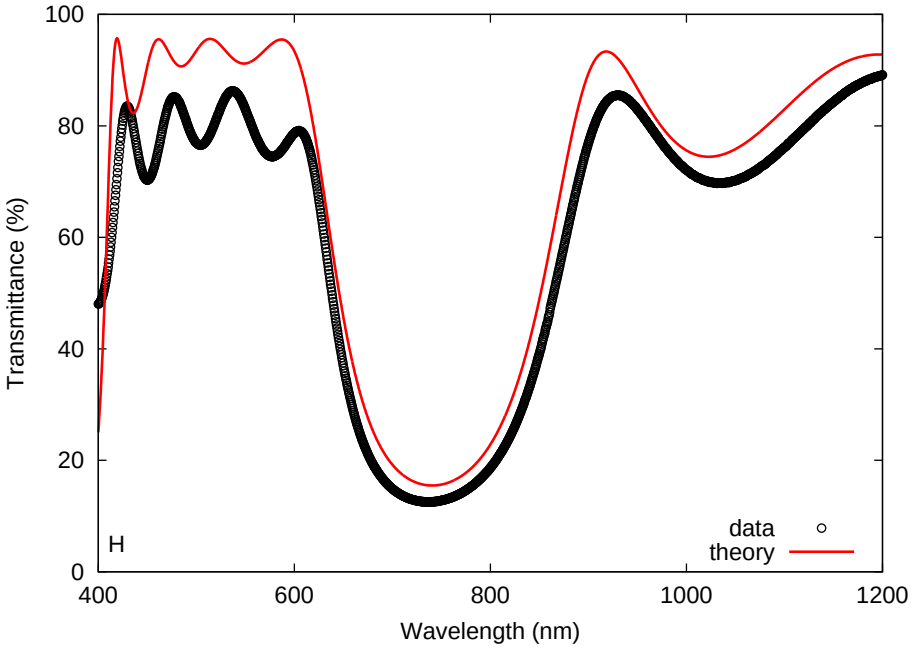
100
80
60
40
20
0
Transmittance (%)
400
600
800
1000
1200
Wavelength (nm)
H
data
theory

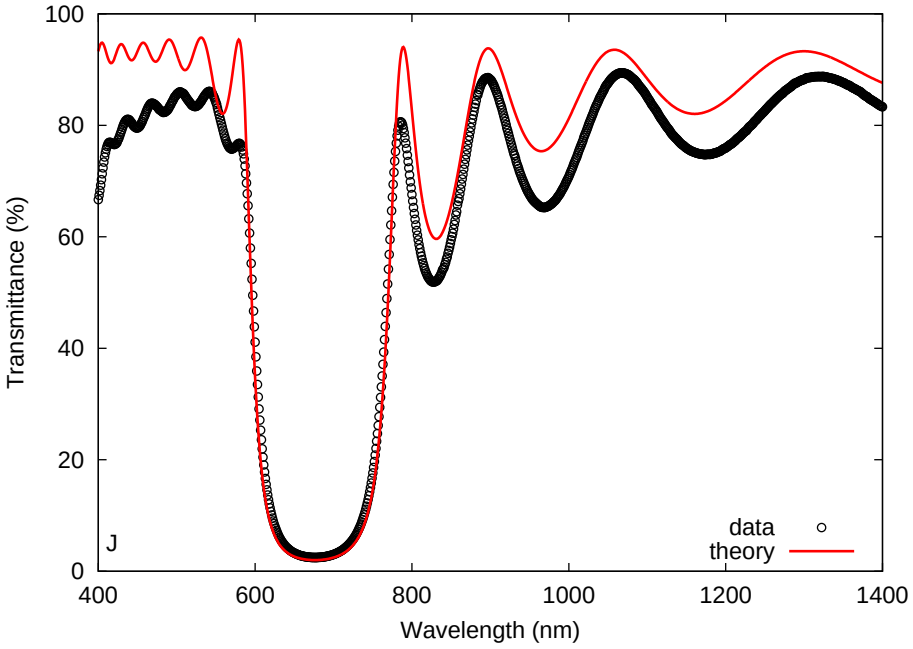
100
80
60
40
20
0
Transmittance (%)
400
600
800
1000
1200
1400
Wavelength (nm)
J
data
theory

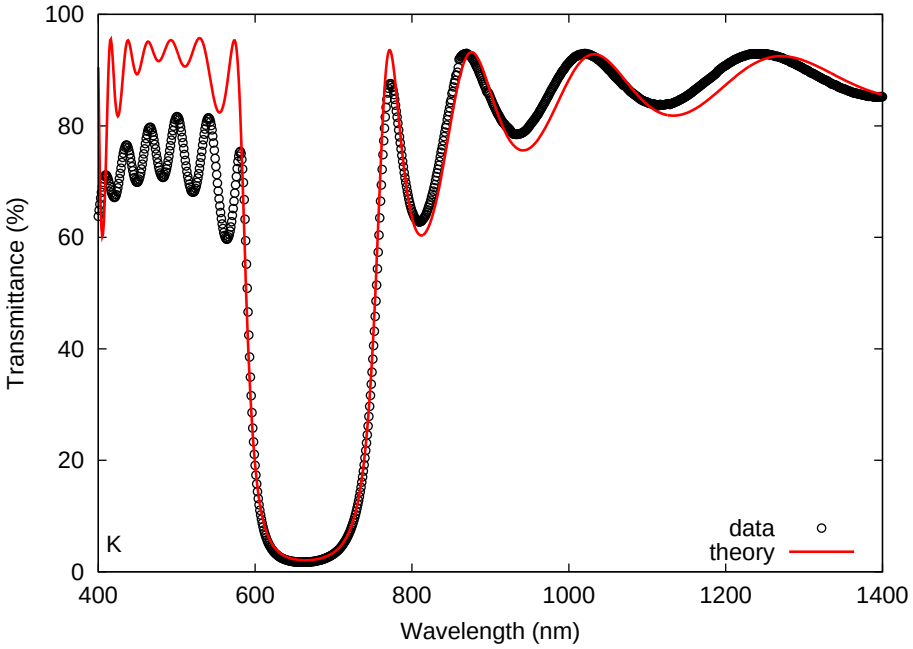
100
80
60
40
20
0
Transmittance (%)
400
600
800
1000
1200
1400
Wavelength (nm)
K
data
theory

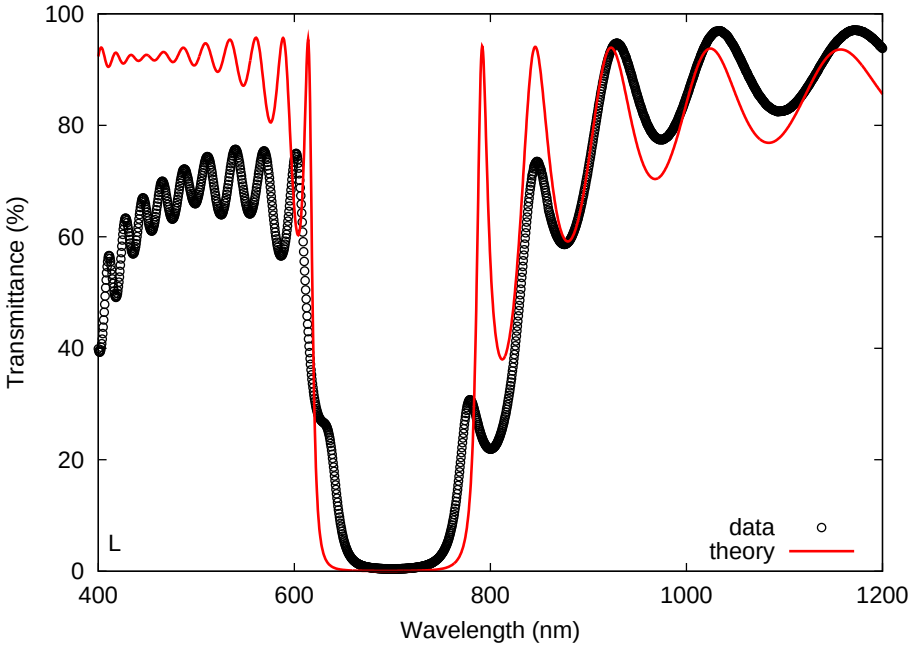
100
80
60
40
20
0
Transmittance (%)
400
600
800
1000
1200
Wavelength (nm)
L
data
theory

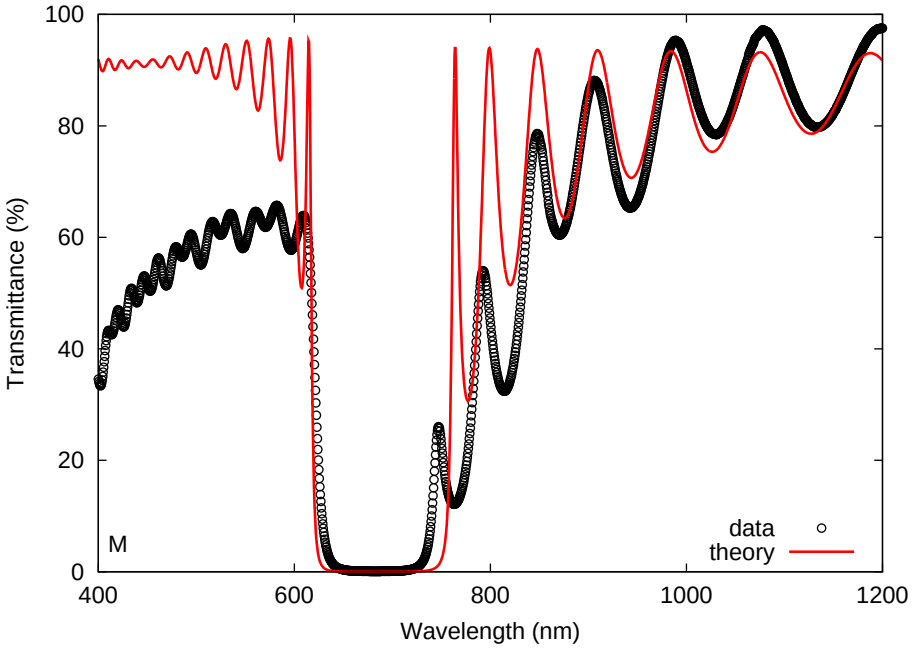
100
80
60
40
20
0
Transmittance (%)
400
600
800
1000
1200
Wavelength (nm)
M
data
theory

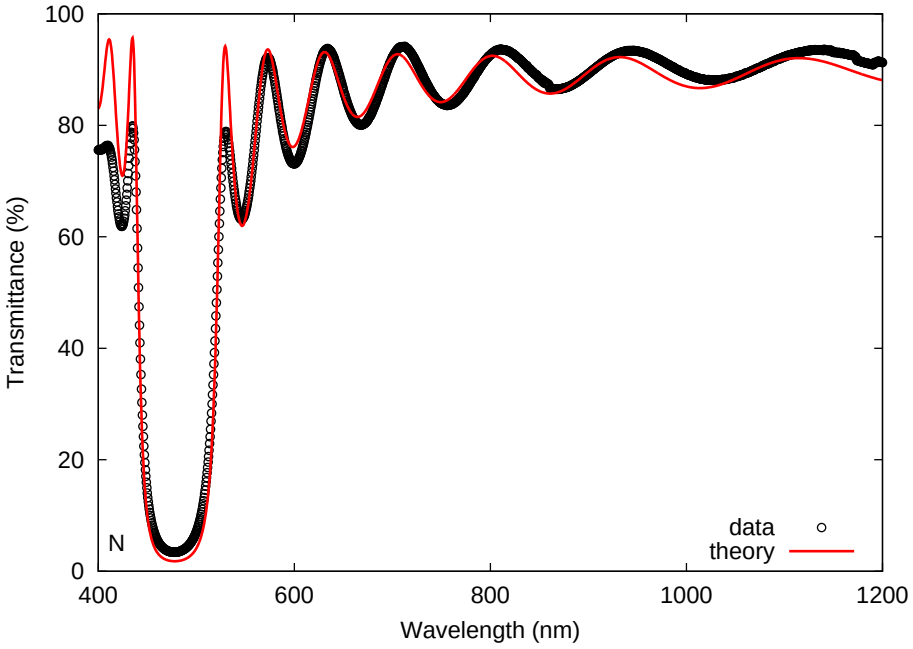
100
80
60
40
20
0
Transmittance (%)
400
600
800
1000
1200
Wavelength (nm)
N
data
theory

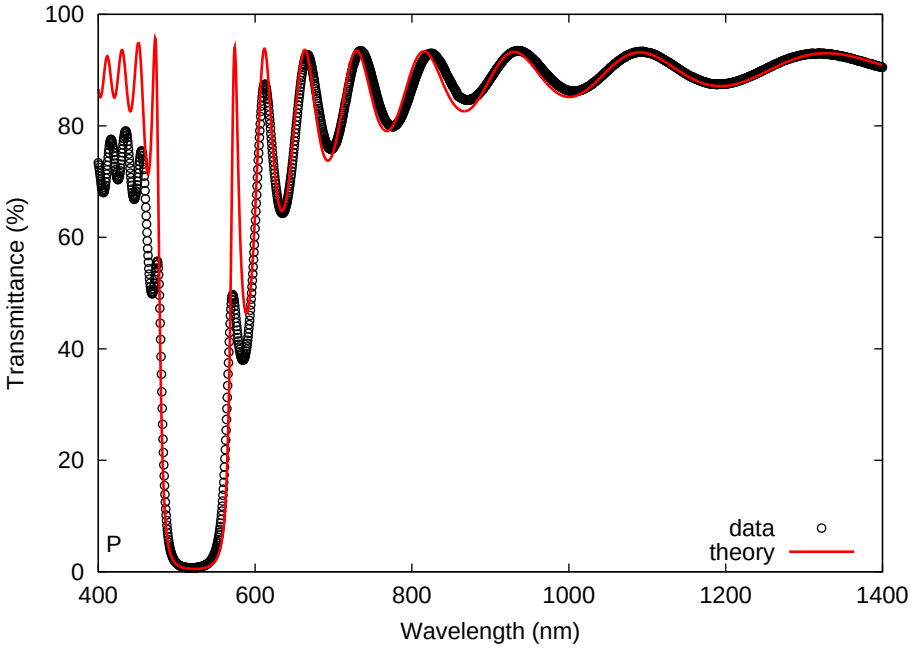
100
80
60
40
20
0
Transmittance (%)
400
600
800
1000
1200
1400
Wavelength (nm)
P
data
theory

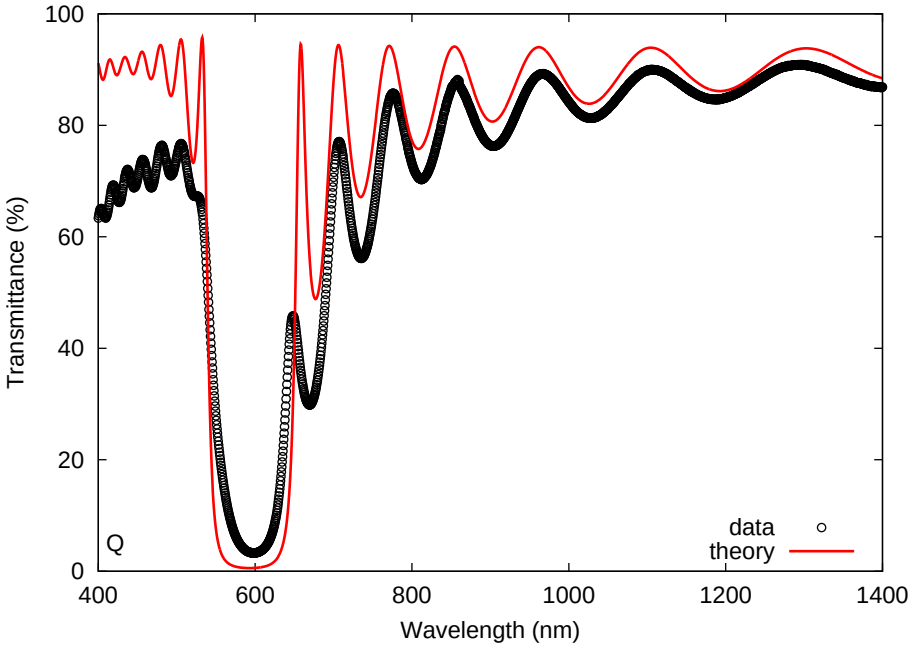
100
80
60
40
20
0
400
600
800
1000
1200
1400
Transmittance (%)
Wavelength (nm)
Q
data
theory

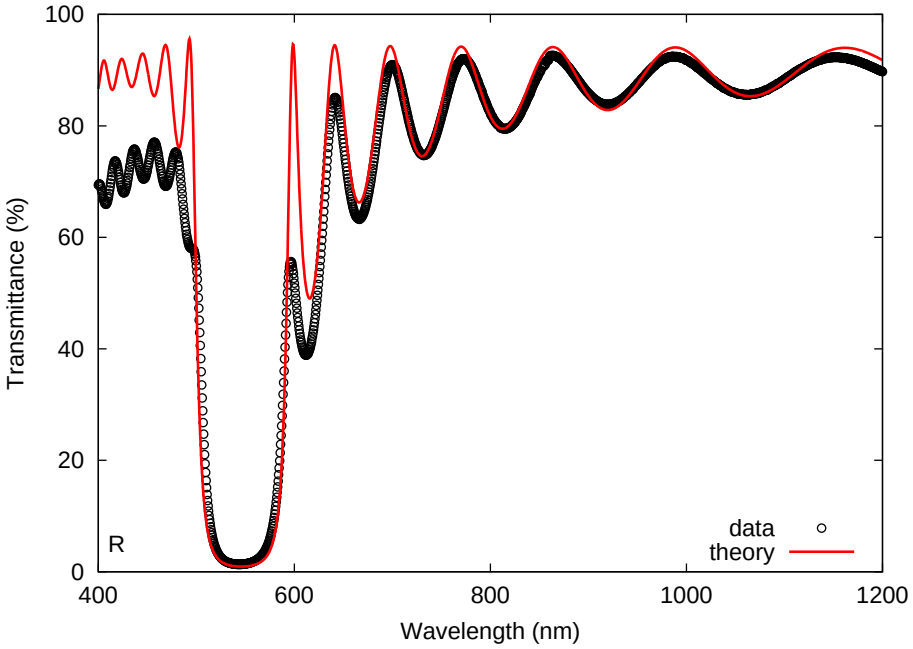
100
80
60
40
20
0
400
600
800
1000
1200
Transmittance (%)
Wavelength (nm)
R
data
theory